RADIO POLARIZATION STUDIES OF THE SOLAR CORONA AT LOW FREQUENCIES

A Thesis
Submitted for the Degree of
Doctor of Philosophy (Technology)

Submitted by

SASIKUMAR RAJA K

Department of Applied Optics & Photonics
University College of Technology
University of Calcutta

October 2014

Dedicated to,
My Father, Mother, Brother and Sister.

yac-cakshur esha savita sakala-grahanam

raja samasta-sura-murtir asesha-tejah

yasyajnaya bhramati sambhrita-kala-chakro

govindam adi-purusham tam aham bhajami

(Language: Sanskrit)

Translation

The Sun who is the king of all the planets, full of infinite effulgence, the image of the good soul, is as the eye of this world. I adore the primeval Lord Govinda in pursuance of whose order the Sun performs his journey mounting the wheel of time.

(Book courtesy: Sri Brahma Samhita)

Acknowledgements

First and Foremost, I would like to acknowledge Prof. R. Ramesh for suggesting the research topic. His patience and consistent technical/scientific discussions made me possible to accomplish this work.

I would like to express sincere gratitude to Dr. C. Kathiravan from whom I learned the designing aspects of the antennas, RF components and many other techniques involved in building the interferometric arrays. I also thank him for his care and affection at Gauribidanur Radio Observatory (GRO), India, which made my stay pleasant there. I extend my sincere thanks to Shri. M.S. SundaraRajan for teaching me the digital techniques.

I profoundly thank all my teachers in the Department of Applied Optics and Photonics, University of Calcutta (CU), India who taught me in M. Tech. My sincere gratitude to Prof. Ajay Ghosh and Prof. Kallol Battacharya for their kind help and efficiently dealing with the official correspondences in addition to their teaching courses. Specifically, I would like to express my sincere thanks to the excellent teachers Prof. L. N. Hazra, Prof. Amitabha Basuray, Prof. A. K. Chakraborty, Prof. S. K. Sarkar, Prof. A. K. Datta, Prof. Mina Ray and Prof. R. Chakraborty. Their friendly nature enabled me to approach them and interact. I also thank my teachers from Indian Institute of Astrophysics (IIA) and other members from CU whose excellent teaching made me to understand the basics of astronomy and astrophysics and many engineering aspects which are related to the course. My sincere thanks to Prof. A. Satya Narayanan for very variable discussions which I had with him.

I profusely thank Mr. Indrajit V. Barve and Mr. M. Rajalingam for their kind cooperation and help at GRO. I would like to express my sincere thanks to my colleagues Mr. P. Kishore, Mr. K. Hariharan, Mr. V. Mugundhan, Ms. M. Anna Lakshmi, Ms. Sargam Mulay for their friendly and helping nature. My deep sense of appreciation to the working staff at GRO for their help in building the array and its maintenance, love and affection.

It is my duty to thank the members of Board of Graduate Studies (IIA) and the administration department (IIA and CU) for their kind help in dealing with the official formalities. I am extremely thankful to library and computer center staff members (specially Mr. Ashok kumar) at IIA and CU for their timely help and resolving the related issues.

Specially I would like to thank Mr. Anwar Saheb, Mr. P.V. Nakkeeran (BARC) and staff members of Raman Research Institute (RRI) at GRO for their kind cooperation. My special thanks to the observers Mr. Nagendra Kumar, Mr. Naveen Kumar, Mr. R. Rajesh and Mr. K. Santosh for their all time possible help. I owe my sincere thanks to my teachers at M.Sc level, Dr. D. Baba Basha and Dr. S.A.K. Jilani without whose help and encouragement I might have not been to IIA.

I would like to thank my friends and colleagues at IIA and CU for being friendly to me and for their help when ever it is needed. Since I cannot mention all names here I would like to give special thanks to few of them are: Mr. Manjunath Hegde, Mr. D.V.S. Phanindra, Dr. Girjesh Gupta, Mr. Krishna Prasad, Dr. Bharath Kumar, Dr. G. Uday Kumar, Dr. S. Ramya, Mr. A. B. Sudhakar Reddy, Mr. Pradeep Chitta, Mr. N. Venkata Suresh, Mr. Sajal kumar Dhara, Dr. Ananth C. Pradhan, Dr. Tapan Mishra, Dr.Veeresh Singh, Mr. P. Chandra Sekhar, Mr. Narsi Reddy, Mr. Hemanth Pruthvi, Mr. Subhamoy Chatterjee, Mr. V. Sreekanth Reddy, Mr. Tarun Kumar Sharma, Mr. Mayuresh Sarpotdar, Ms. P. Ramya, Ms. Amanpreet Kaur, Mr. Ravi Pawase and Mr. Rajendra Bahadur Singh. Thank you all for being friendly to me.

I am deeply indebted to my father Shri K. Krishnappa and my mother Smt. K. Narasamma who are constant inspiration, support and strength without whose love and blessings, I might not have completed this work. I would like to thank my brother Mr. K. Rajasekhar and sister Ms. K. Drakshayani for their constant support, love and encouragement. I would like to thank my brother-in-law Mr. V. Madhusudana and the young chap, my nephew Mr. V. Praneeth Swasan for their moral support. I thank my uncles Shri. M. Srinivasulu and Shri. R. Ramakrishnappa for their kind help and suggestions.

Acknowledgments will never end if I keep mentioning and I would like to stop here by thanking all my teachers, friends, cousins, relatives, classmates and others who helped me directly or indirectly throughout my career.

K. Sasikumar Raja

Abstract

The radio telescopes that are presently in operation specifically to study the Sun are limited. We have: (1) the Nobeyama radioheliograph in Japan operating at 17 and 34 GHz; (2) the Nançay radioheliograph in France which observes in the frequency band 150-450 MHz; and (3) the Gauribidanur radioheliograph (30-150 MHz) operated by Indian Institute of Astrophysics at Gauribidanur Radio Observatory near Bangalore. Since the electron density (N_e) and hence the plasma frequency (f_p) decreases radially outward in the solar atmosphere, the radio emission at different frequencies originate from different heights. For example, 30-150 MHz emission is generally emitted over the height range of $\approx 1-2$ solar radii above the photosphere. The above frequency range is well suited for observations of enhanced radio emission (both thermal and non-thermal) from the solar corona. Presently, it is difficult to observe the white light emission from the solar corona in the above height range even with space coronagraphs because of various practical difficulties. Radio observations play a useful role to understand the different coronal phenomenon along with observations from space at different wavelengths. To have a better understanding, it is essential to have polarization information in addition to imaging and spectral observations. The existing observations with the Gauribidanur radioheliograph (GRAPH) and Gauribidanur Low-frequency Solar Spectrograph (GLOSS) are limited to two-dimensional imaging (Stokes I) and one-dimensional spectral mode (Stokes I), respectively.

The recently commissioned one-dimensional Gauribidanur Radio Interference Polarimeter (GRIP) is in operation in both Stokes I and V modes. As part of building the array, I have been involved in design and fabrication of antennas, analog and digital receiver systems. I also carried out different test measurements like characterization of antennas, phase equalization of coaxial cables, radiation pattern measurements, RF network cabling in

the field/receiver room and other interferometric measurements. The GRIP consists of 40 frequency independent antennas (log periodic dipoles, LPDs) mounted independently in 0^o and 90^o orientation (with respect to the terrestrial north) for the measurement of polarized radio emission from the solar corona over the frequency range 30-150 MHz. LPDs were used because of the broad frequency coverage. The observations are limited to the circularly polarized radio emission (Stokes V) that arises due to propagation effects and also due to the non-thermal emission mechanisms which occurs frequently in the solar corona. Any linearly polarized emission (Stokes Q and Stokes U) that is generated at the source region cannot be observed over the typical observing bandwidths (kHz/MHz) used in radio astronomy, since the same are depolarized due to Faraday rotation in the solar corona and Earth's ionosphere. I was involved in the design/development and fabrication of the associated front-end analog electronics, back-end digital receiver system, and the data acquisition/observational/data analysis software.

Weak non-thermal radio activity are often noticed in the solar atmosphere. But their energy budget and the strength of the associated magnetic field were not established. Observations with the GRIP indicate that the estimated energy of the frequently observed type I radio bursts are $\approx 10^{21}$ erg. These are the weakest energy releases reported in the solar atmosphere as on date and they belong to the category of picoflares which is one of the suggested mechanisms to heat the solar corona. We also estimated the associated magnetic field and it is in the range $\approx 200 - 1000$ mG.

At present, measurements of coronal magnetic fields in white light are not possible due to various practical difficulties. By making use of indirect radio methods, the magnetic field strengths of corona is possible to estimate. Using the polarization observation of the group of type III radio bursts the magnetic field strength of the solar corona was estimated in different approaches. Firstly, the limb events whose degree of circular polarization (dcp) is less than 15% was selected. It is known that such events are due to the harmonic emissions which give the clue to estimate the magnetic field. On the other hand using

quasi-periodicity of the mentioned events, the magnetic field was estimated at 1.3 $R_{\odot}$ (80 MHz). These estimated results are consistent with the existing empirical models and other reported observations.

Type IVm radio bursts occurs in association with coronal mass ejections (CMEs) and the source moves in the solar atmosphere with approximate speed of CME. Using GRIP, a CME associated moving type IV burst was observed at 40 and 80 MHz. A weak circularly polarized radio emission was observed in both the frequencies. Observationally it was identified that origin of type IVm burst was due to the gyrosynchrotron emission. Hence by knowing the dcp and emission mechanism the associated magnetic field strength was estimated at height of ≈ 1.9 and 2.2 $R_{\odot}$.

Occultation studies of the Crab nebula by the solar corona was carried out in the polarimetric mode. We expected to observe circularly polarized radiation, since there could be possible density inhomogeneities (with associated magnetic field) in the line of sight. But we did not observe any such emission. It is possible that the polarized signal, if any were present, was too weak to detect. However the observations lead to scattering studies at different heights in the lower heliosphere. Observationally it was known that the flux density of the Crab nebula decreases during its ingress and regains during egress. The flux density vanished when the Crab nebula was close to solar disk, (in mid June) $\approx 5\ R_{\odot}$. Based on the occultation observations in years 2011 and 2013, level of turbulence (C_N^2) at different height in the corona was estimated. It was found that the estimates of $C_N^2(r)$ were higher compared to the similar reports from VLBI observations. Using the estimated C_N^2 values the angular broadening measurements was carried out and the results are consistent with earlier empirical equations.

We designed and fabricated a cross-polarized log periodic dipole (CLPD) antenna system to study the circularly polarized radio emission from the solar atmosphere. The performance study of the CLPD was carried out and found that for commercially available CLPDs are having the isolation > -20 dB which are not suitable to have a precise polar-

ization measurements. Our designed CLPD has the isolation as low as < -40 dB. Using a narrow bandwidth ($\approx 65 - 85$ MHz) CLPD, two element interferometric polarimeter was constructed and observed the circularly polarized radio emissions from the solar corona. By designing the broad band CLPD with improved isolation, it can be used in building the imaging instruments to have the polarized two-dimensional maps of the solar corona. Also they can be used as feeds for dish antennas.

List of Publications

List of my publications till date are given below. It is written in the format: title, authors, journal, volume number, page number, year of publication.

1. *Low-frequency radio observations of picoflare category energy releases in the solar atmosphere,* R. Ramesh, **K. Sasikumar Raja**, C. Kathiravan and A. Satya Narayanan, Astrophysical Journal, 762, 6, 2013.

2. *Design and performance of a low-frequency cross-polarized log-periodic dipole antenna*, **K. Sasikumar Raja**, C. Kathiravan, R. Ramesh, M. Rajalingam and Indrajit V. Barve, Astrophysical Journal Supplement Series, 207, 5, 2013.

3. *Low-frequency observations of transient quasi-periodic radio emission from the solar atmosphere*, **K. Sasikumar Raja** and R. Ramesh, Astrophysical Journal, 775, 6, 2013.

4. *An estimate of the magnetic field strength associated with a solar coronal mass ejections from the low-frequency radio observations*, **K. Sasikumar Raja**, R. Ramesh, K. Hariharan, C. Kathiravan, T. J. Wang, Astrophysical Journal (Accepted for publication).

5. *An estimate of the density turbulence in the near-Sun solar wind from low-frequency radio observations of the occultation of the Crab nebula by the solar corona*, **K. Sasikumar Raja** and R. Ramesh, Astrophysical Journal (In preparation).

List of Presentations

Oral Presentations

1. *Low-frequency observations of transient quasi-periodic radio emission from the solar atmosphere,* presented in Regional Conference on Radio Science, January 2-5, 2014, Pune, India.

2. *Design and performance study of meter wavelength cross-polarized log-periodic dipole antenna to observe the polarized radio emissions from the solar atmosphere,* presented in Regional Conference on Radio Science, January 2-5, 2014, Pune, India.

Poster Presentations

1. *Polarization studies of the type I storm bursts at low frequencies,* presented in 30th meeting of Astronomical Society of India, February 20-22, 2013,Trivandrum, India.

2. *Low-frequency radio observations of picoflare category energy releases in the solar atmosphere,* presented in 39th COSPAR scientific assembly, July 14-22, 2012, Mysore, India.

Awards/Honors Received

1. First prize in Student Paper Competition Award in Regional Conference on Radio Science, was organized by Indian Committee for International Radio Science Union (INC-URSI), 2014, Pune, India.

2. Best poster award in Astronomical Society of India meeting, 2013, Trivandrum in the discipline of Sun and Solar System.

3. Life member of Astronomical Society of India since 26 July 2013, (Membership ID: L2089).

Contents

List of Figures

List of Tables

Chapter 1

Introduction

The Sun is a source of energy for all living beings on the Earth and a cosmic laboratory for the plasma, nuclear, and atomic and molecular physicists. The Sun is of increased interest to the astronomers because of its closeness to the Earth and influence on solar terrestrial activities. The dominant magnetism of the Sun makes it more dynamic in nature. The Sun was formed $\approx$ 4.6 billion years ago and at this epoch, the Sun is a normal main-sequence star of spectral class G2V and its apparent and absolute stellar magnitudes are $\approx$ -26.74 and 4.8 respectively. The Sun follows a 11 year cycle in which the number of sunspots reaches a maximum (solar maximum) and then declines to a minimum number (solar minimum). Many of the solar phenomena correlates with this solar cycle. Also, polarity of the Sun's magnetic field flips once in two solar cycles (22 years) which is called solar magnetic cycle or Hale cycle [Hale et al., 1919].

1.1 Solar interior

The solar interior is divided primarily into three layers as shown in the Figure 1.1: The core, the radiative zone and the convective zone. Heat is generated by nuclear fusion

reactions at the center of the Sun called the core where Helium ($^4He_2$) is formed from the Hydrogen ($^1H_1$) by proton-proton cycle which is shown below.

$$4\ {}^1\mathrm{H}_1 \longrightarrow\ {}^4\mathrm{He}_2 + 2\mathrm{e}^+ + 2\nu + 26.7\ \mathrm{MeV}$$

In the above reaction, ≈ 26.7 MeV energy is released in the form of high-frequency γ-rays and two neutrinos (denoted by ν with energy ≈ 0.5 MeV). These neutrinos are tiny and can escape from the solar interior. They provide direct diagnostics of the Sun's core. The neutrino flux suggests that the temperature of the core is $\approx 12 \times 10^6$ K [Priest, 1982, pp13]. The core is $\approx 25\%$ of the visible disk of the Sun (radius $= 1\ R_\odot \approx 6.96 \times 10^5$ km). The density of the core is ≈ 150 g cm^{-3} which is about 10 times more than the density of the gold (Au).

Radiative zone extends over the range $\approx 0.25 - 0.70\ R_\odot$ i.e. from the outer layer of the core to the interface layer or the tachocline. In this zone the energy is transported in the form of radiation. Although the photons travel at the speed of light, they bounce several times in the dense material. Due to this it takes about a million years for an individual photon to reach the tachocline. The density in the radiative zone is ≈ 0.2 g cm^{-3}, which is less than the density of the water (≈ 1 g cm^{-3}).

Outer most layer of the solar interior is the convective zone which is at a depth of $\approx 0.3\ R_\odot$ from the solar surface. Temperature at the base of this zone is $\approx 2 \times 10^6$ K. The energy transport in this zone is via convection. The convective motions carry heat very rapidly to the solar surface. The surface temperature of the Sun (photosphere) ≈ 5800 K.

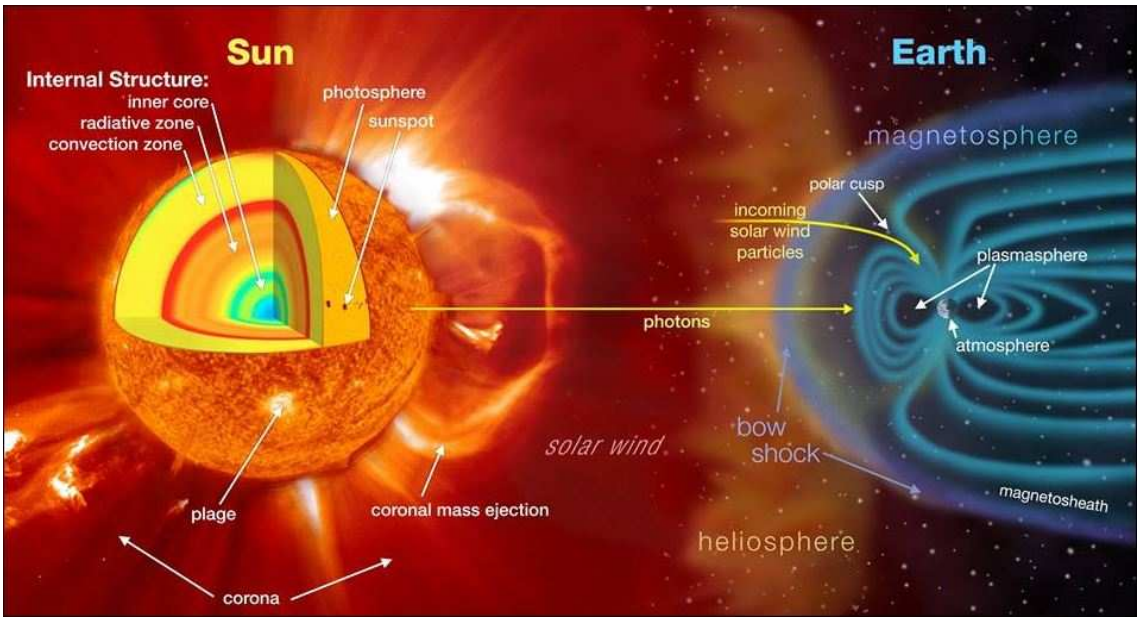

Fig. 1.1: The Figure shows the different layers of the Sun and its influences on the space weather and Earth. Image Credit: http://svs.gsfc.nasa.gov/goto?30481

.

1.2 Solar atmosphere

The solar atmosphere is categorized into four distinct regions: the photosphere, the chromosphere, the transition region and the corona. The density in the Sun decreases with increasing height from the surface. As a consequence the emissivity also decreases. Most of the visible radiation originates from a thin spherical layer of thickness ≈ 300 km. This layer is called the photosphere and is the source of the continuous solar spectrum. The spectrum also includes dark Fraunhofer lines over the continuous solar spectrum which arises due the selective absorption by the atoms and molecules present in the region of the formation of photosphere spectrum.

Above the photosphere, there is another spherical layer with thickness of ≈ 2000 km with temperature of $\approx 10^4$ K. It is called the chromosphere and is observed mainly during the total solar eclipse when the Moon occults the bright photosphere. In the chromosphere the density drops from $\approx 10^{16}$ cm^{-3} (density of photosphere) to $\approx 10^{14}$ cm^{-3}. Outside of eclipses, the chromosphere can be observed using the H_α (6563 A°) and Ca

K (3934 A^o) spectral lines. Radio observations at millimeter wavelengths correspond to the observations of the lower chromosphere. Centimeter observations originate at middle and upper chromosphere. For example, 1.4 GHz observations originate at the top of the chromosphere.

From the top of the chromosphere, temperature gradually increases from $\approx 10^4$ K to 10^5 K within a thickness of ≈ 100 km and this region is called the 'transition region'. This region is observed in strong EUV resonance lines of heavy ions of Fe XV, Mg IX, Ne VII, O VI and O IV. These lines originate at different temperatures. In the radio band, decimeter wavelength observations originate at the heights where the transition region exists.

Immediately after the transition region, a tenuous plasma region with temperature of $\approx 1 \times 10^6$ K exists. It extends millions of kilometers outwards and merges with inter planetary medium. This layer is called the 'corona' which is further divided into three distinct layers: 1. lower corona within $\approx 1.2\ R_\odot$, 2. middle corona which lies between ≈ 1.3 and $3\ R_\odot$, and 3. outer corona which extends outwards from $\approx 3\ R_\odot$. The Sun and its corona can be observed at almost all wavelengths of electromagnetic spectrum using different observing techniques. Each wavelength of observation corresponds to a specific height of the solar atmosphere. For example, the photosphere is observable at visual wavelengths, the chromosphere is observable in H_α and microwave frequencies. Solar corona can be observed in soft X-rays (SXR), hard X-rays (HXR), extreme ultra-violet (EUV), ultra-violet (UV), γ-ray, infra-red (IR), and radio frequencies. While centimeter and decimeter wavelengths observations are used to probe the lower corona, the middle corona is observed at meter and the decameter wavelengths. The outer corona is observed over the frequencies corresponding to hectometer and kilometer wavelengths. The latter observations need to be carried out from space since the Earth's ionosphere reflects the radiation back into space at very low frequencies $\lesssim 10$ MHz.

The solar corona is 10^{-6} times fainter than the photosphere at visible wavelengths

and rapidly decreases to 10^{-9} times within 1 $R_{\odot}$ from the solar limb. So ground based white light observations of solar corona is possible only during a total solar eclipse when the Moon occults the photosphere. Such observations are limited because the solar eclipses that can seen from Earth are a rare phenomenon, occur at different locations, times and also lasts only a few minutes. The solar corona can be observed at visible wavelengths using a coronagraph in which the photosphere is occulted by an artificial occulter. Coronagraphic observations are usually carried out from the space to avoid the scattering effects in the Earth's atmosphere. Microwave and radio observations of the chromosphere and corona can be carried out from ground. SXR, HXR, EUV observations of the solar atmosphere need to be carried out using space borne instrumentation, since the Earth's atmosphere is opaque to the above radiation. Low-frequency radio observations of the solar corona can be used to understanding the long standing mysteries like coronal heating, coronal magnetic fields, coronal mass ejections etc. More details on solar interior and solar atmosphere are found in Priest [1982], Stix [2002].

1.3 Observations of solar corona

Space missions to understand the solar corona started with the satellite series Orbital Solar Observatory (OSO-1 to OSO-8) which carried instruments for observations in EUV, SXR and HXR. Multi wavelength (White light, X-ray, EUV and UV) observations began with launch of Skylab which was followed by Solar Maximum Mission (SMM) and Hintori. The instruments onboard the latter two missions operated at the following wavelengths: γ-ray, HXR, SXR EUV, UV and Infra Red (IR) and White light. Many interesting results on the solar corona were obtained with the Yohkoh mission. The latter had instruments that operated at SXR, HXR and γ-ray wavelengths. Major solar mission, called the Solar Heliospheric Observatory (SOHO), jointly built by European Space Agency (ESA) and National Aeronautical Space Administration (NASA) was launched in the nineties. The

spacecraft had instruments to study helio seismology, solar atmosphere and to monitor the solar wind. Some of the instruments are Solar Ultraviolet Measurements of Emitted Radiation (SUMER) telescope, Coronal Diagnostic Spectrometer (CDS), Extreme Ultraviolet Coronagraph Spectrometer (UVCS) and Large Angle Spectroscopic COronagraph (LASCO). LASCO has the coronagraphs known as C1, C2 and C3 which operate in the range $1.1-3\ R_{\odot}$, $2-6\ R_{\odot}$ and $3.7-32\ R_{\odot}$ respectively [Brueckner et al., 1995, Fleck et al., 1995, Domingo et al., 1995]. Out of the above listed three coronagraphs, C1 is presently not operational. Transition Region And Coronal Explorer (TRACE) is another telescope which works in the EUV, UV, White light, H I Lyman α and C IV. It provides high spatial resolution images. (Reuven) Ramaty High Energy Solar Spectroscopic Imager (RHESSI) was launched to study the physics of particle acceleration. Review on these instruments with references are given in Aschwanden [2004], Golub and Pasachoff [2009]. POLAR [Silvio Orsi, 2010], Interball [GalÊźperin et al., 1995], Advanced Composition Explorer (ACE) [Stone et al., 1998], Solar TErrestrial RElations Observatory (STEREO) and Solar Dynamics Observatory (SDO) [Pesnell et al., 2012] etc, are few more missions which are currently in operation. STEREO employs two nearly identical space-based observatories: one ahead of Earth in its orbit (STEREO/A) and the other behind (STEREO/B). STEREO has different instruments: (1) Sun-arth Connection Cornal and Heliospheric Investigation (SECCHI) whose primary science target is to observe the 3-D evolution of CMEs from close to solar surface through the corona and interplanetary medium including the impacts of CMEs on Earth. (2) SWAVES is aimed to study the interplanetary radio bursts. (3) In-situ Measurements of Particles And CME Transients (IMPACT) and (4) PLasma And Super Thermal Ion Composition (PLASTIC) [Kaiser, 2005, Kaiser et al., 2008].

Ground based observations of the solar corona is possible at optical and radio regimes of the electromagnetic spectrum. Coronal observations from the ground is carried out at high altitude sites like the Mauna Loa Solar Observatory (MLSO), Hawaii which is oper-

ated by High Altitude Observatory of Boulder, Colorado [Fisher et al., 1981, Golub and Pasachoff, 2009]. Interferometric imaging instruments in the radio domain were developed/used to observe the corona. Few of them are Culgoora radioheliograph, in Australia [Wild, 1967], Nançay radioheliograph, France [Kerdraon and Delouis, 1997], the Very Large Array in New Mexico [Murdin, 2000], Owens Valley Radio Observatory in California [Gary et al., 2011], RATAN-600 in Russia [Korolkov and Pariiskii, 1979], Nobeyama radioheliograph at Nobeyama Radio Observatory in Japan [Nakajima et al., 1994], Clark lake heliograph [Erickson et al., 1982], and Gauribidanur Radioheliograph [Ramesh et al., 1998] etc. The recently commissioned, Murchison Widefield Array (MWA), located at the Murchison Radio-astronomy Observatory (MRO) in Western Australia is also used to observe the corona [Lonsdale et al., 2009]. Space based spectral radio observations at less than 14 MHz are carried out using URAP-Ulysses [Stone et al., 1992], WAVES-WIND [Bougeret et al., 1995], WAVES-STEREO [Kaiser, 2005, Rucker et al., 2005] etc. Several ground based radio spectrometers located at different longitude zones are used to observe the spectral signature of the transient emissions in the corona [Kondo et al., 1994, Ebenezer et al., 2001, Gorgutsa et al., 2001, Benz et al., 2009].

1.4 Solar flares

Sudden and rapid brightening in the solar atmosphere is defined as a flare[1]. A flare is a highly concentrated explosive release of energy in the solar atmosphere. In general they are categorized into three phases: (1) a preflare stage which lasts few minutes. (2) an impulsive/flash phase which lasts about 5 minutes. This is the most energetic phase of the flare. The flare intensity suddenly increases during the impulsive phase. (3) The main phase of a flare (after the impulsive phase) lasts for several minutes to hours depending on its intensity. Various radio bursts (see section-1.7) are generated during the different

[1]http://hesperia.gsfc.nasa.gov/sftheory/flare.htm

phases of a flare. High energy particles are also release from the Sun during intense flares [McLean and Labrum, 1985, pp54]. Note that all flares not necessarily follow all the phases.

The large flares have energy $\approx 10^{33}$ erg. In the optical regime the solar flares are classified based on the flare area and brilliance. An Sf is the smallest and faintest flare. The flare area is represented by either S or 1 or 2 or 3 or 4 depending on whether apparent area is less than either 200 or 500 or 1200 or 2400 or greater than 2400 millionths of the solar disk. The flare brilliance is represented by either f or n or b depending on whether the flare is faint or normal or bright. In this classification, Sf event is the smallest and faintest flare, where as 4b is the largest and brightest flare. Solar flares are also classified A, B, C, M, X based on their X-ray intensity. into different types: The letter 'A' signifies the weakest energy whereas 'X' highest. Each letter represents different number: $A = 1{\times}10^{-8}$, $B = 1 \times 10^{-7}$, $C = 1 \times 10^{-6}$, $M = 1 \times 10^{-5}$, and $X = 1 \times 10^{-4}$ W m^{-2}. Also each class is divided into a logarithmic scale from 1 to 9. For example, M1 to M9, X1 to X9 etc. Note that energy of the A2 flare is twice as an A1 flare and so on. Solar flares can radiate strong radiation at radio wavelengths [Bastian et al., 1998b]. The solar flares can accelerate electrons to nonthermal energies and capable of producing high brightness temperatures [White et al., 2001, Fletcher et al., 2011].

1.5 Coronal mass ejections

Coronal mass ejection (CME) is a huge balloon shaped bubble of gas that is ejected from the Sun and expands as it propagates away from the Sun. They are caused by instabilities in the solar magnetic fields which are constantly evolving. While majority of the CMEs are associated with the solar flares and eruptive prominences, some of them occur in the absence of both. A typical CME can eject $\approx 10^{14}$ g of coronal material [Carley et al., 2012] and they can reach Earth in 1-5 days of time depending on its speed. The CMEs

propagate through the ambient corona with speeds of $\approx 10 - 3300$ km s^{-1}. The energy involved in this expulsion is $\approx 10^{30} - 10^{32}$ erg [Gosling et al., 1974, Gopalswamy and Kundu, 1992, Ramesh et al., 2003, Gopalswamy, 2004, Hudson et al., 2006, Mittal and Narain, 2009, Vourlidas et al., 2002, 2011].

The CMEs that propagate towards the Earth are called 'halo' CMEs or Earth directed events. Halo CMEs look bigger than the Sun as they appear as a 'halo' of bright coronal emission around the Sun. They can cause geomagnetic storms, disrupt global communication and navigation networks, satellite and power grid failure [Aschwanden, 2004]. The CMEs consists of mainly three parts when they propagate: the leading edge, the cavity and the core of the CME [Howard, 2011] which are shown in the Figure 1.2.

1.6 Solar wind

The outflow of the stream of energized charged particles (electrons and protons) from the Sun is called solar wind. The source of the solar wind is the 1 million degree kelvin corona. It has been identified that the solar wind speed is high wherever the magnetic field lines of force are open. Essentially this is the case for the coronal holes. The solar wind speed is high for the coronal holes (800 km s^{-1}) and low for the coronal streamers (300 km s^{-1}). Note that the solar wind expands in all directions and is shown in the Figure 1.1. For more details on solar wind see Stix [2002].

1.7 Radio Sun

In radio astronomy, the basic problems of the solar physics are dealt separately for the sake of convenience by dividing them into following categories: (1) solar interior, (2) solar atmosphere, and (3) origin of transient solar phenomena and solar activity, which include the influences on space weather. Also the radiation from the solar atmosphere can be

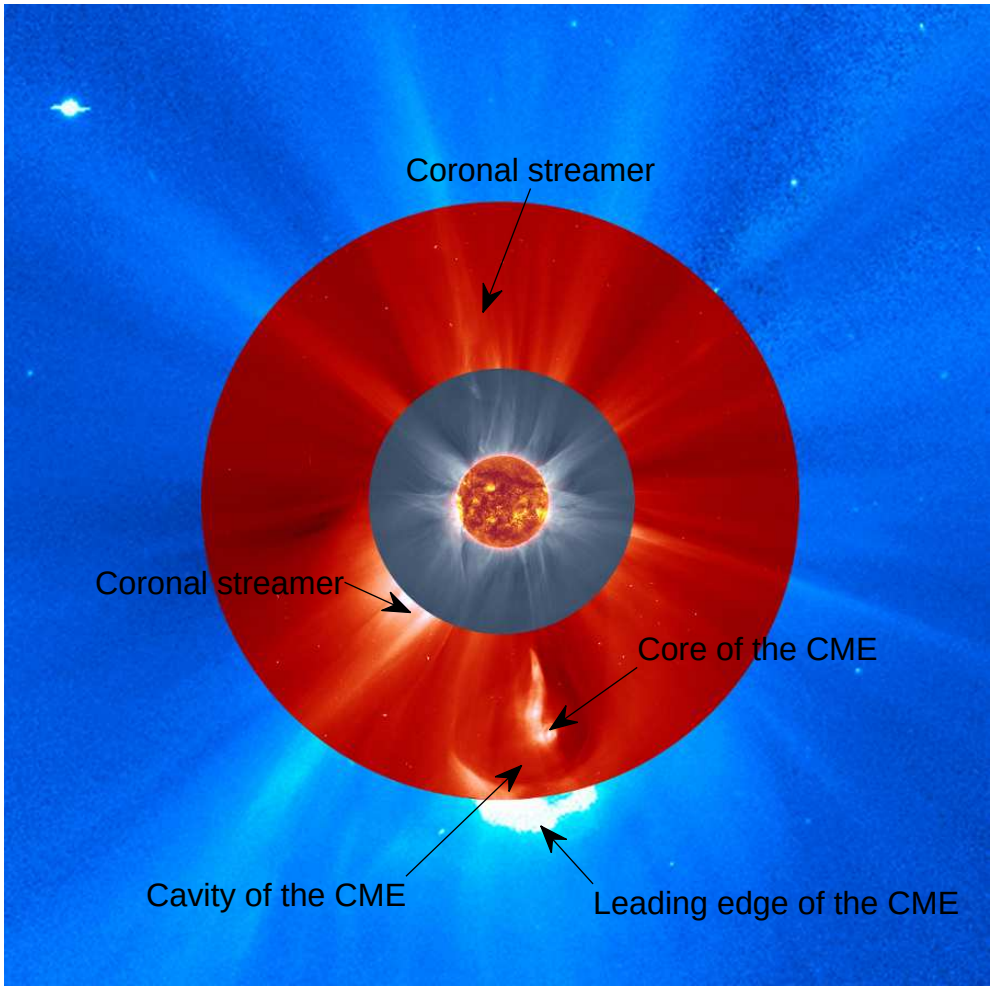

Fig. 1.2: The Figure shows the composite image of the solar corona observed with different instruments and frequencies. Propagation of coronal mass ejections and other streamers are clearly seen in the images which signify the multi-frequency observations. The solar disk shown in the image is observed at EUV 30.4 nm and 17.4 nm using SDO/AIA, NASA and PROBA-2/SWAP, ESA/ROB respectively. $1-3\ R_{\odot}$ grey image is observed using the ground based observations during the eclipse at Gabon and Uganda. $2-6\ R_{\odot}$, $4-33\ R_{\odot}$ red/blue color images are obtained in white LASCO C2, C3 respectively, on-board SOHO instruments. This image shows the significance of importance of the observations of the solar corona at different wavelengths. The image also shows the core, the cavity and the leading edge of the CME observed on 3 November 2013. Image Credit: http://www.esa.int/spaceinimages/Images/2013/12/Multiwavelength_solar_view

.

broadly classified into two categories. (1) 'undisturbed' or 'quiet' Sun and (2) 'disturbed' or 'active' Sun.

1.7.1 'Undisturbed' Sun

The Sun is said to be 'undisturbed' if there is no contribution from the transient events to the observed brightness distribution. In this case, the Sun is viewed as a static, spherically symmetric gaseous hot ball. Radio emission from the 'undisturbed' Sun follow the Rayleigh Jeans law,

$$B_Q(T) = \frac{2f^2kT}{4\pi^2c^2} \tag{1.1}$$

where as $B_Q(T)$ is called the brightness temperature, T is the temperature, f is the frequency of observation, k is the Boltzmann constant, c is the velocity of light. The radiation from the 'undisturbed' Sun consists of two components: (1) A steady background component which is due to the absence of any localized sources like: sunspots, plages, active regions, filaments, prominences and other transient disturbances like solar flares. In other words, the emission below which the solar flux never falls for periods of months or years are said to be quiet Sun radiation and caused by the thermal emission of the solar atmosphere [Kundu, 1965]. (2) The slowly varying component (S-component) which originates from the high density regions of corona called 'coronal condensations'. This component is also due to the thermal emission whose temperature is $\approx 2 \times 10^6$ K, which exist over sunspots and chromospheric plage regions. The intensity of the radio radiation changes slowly from day to day and has the period of about 27 days. At optical wavelength the 'quiet' Sun is very clearly defined. Note that at radio wavelengths, in general, no contribution from the active regions are present when the sunspot cycle is in minimum phase. During the periods of sunspot cycle maximum, S-component has to be distinguished separately from the 'quiet' Sun. S-component is observed primarily at centimeter wavelengths ($\approx 1 - 100$ cm) with broad spectral peak at ≈ 10 cm [Kundu,

1965, Krueger, 1979, Burke and Tapping, 1995].

1.7.2 'Disturbed' Sun

The radiation in the presence of discrete sources like active regions, transient flares, prominences, coronal mass ejections etc, are more compared to the 'undisturbed' Sun. These discrete sources are associated with radio bursts. These radio bursts are non-thermal in nature and brightness temperature (T_b) often exceeds $\approx 10^7$ K. The radiation from the 'disturbed' Sun is also known as rapidly varying component or R-component. Photospheric sunspots, filaments and plages erupt, and release energy in the order of $\approx 10^{33}$ erg. Such eruptions lead to dynamic radio emission in the solar corona. During this period the solar corona is no longer symmetrically spherical. Depending on the location of the active regions the shape of the corona changes.

On meter wavelengths the bursts appear for few seconds to hours, and sometimes continue as storms which fade after few hours to days. Such highly varying radio emissions come under the category of R-component. Depending the morphology of the spectrogram/drifting speeds of the radio bursts, Wild et al. [1963] classified the radio bursts into five principle types: (a) type I bursts/noise storms, (b) type II bursts/slow drift bursts, (c) type III bursts/fast drift bursts, (d) type IV bursts/broad band continuum emissions and (e) type V/continuum meter wave emissions. Apart from these, there exist a few more complex bursts like: J burst, U burst etc. The ratio $\Delta f/\Delta t$ classify different types of the bursts as mentioned above [Wild et al., 1963, Wild and Smerd, 1972, Dulk, 1985, Bastian et al., 1998a], where Δf is the bandwidth over the radio burst propagated through the corona and Δt is duration of the bursts lasted. The classification of the different solar radio bursts and their morphology is shown in the Figure 1.3.

(a) **Type I bursts/Noise storms**: Noise storms are frequently observed radio bursts in the solar corona at meter wavelengths. Noise storms are the slowly varying ($\approx$

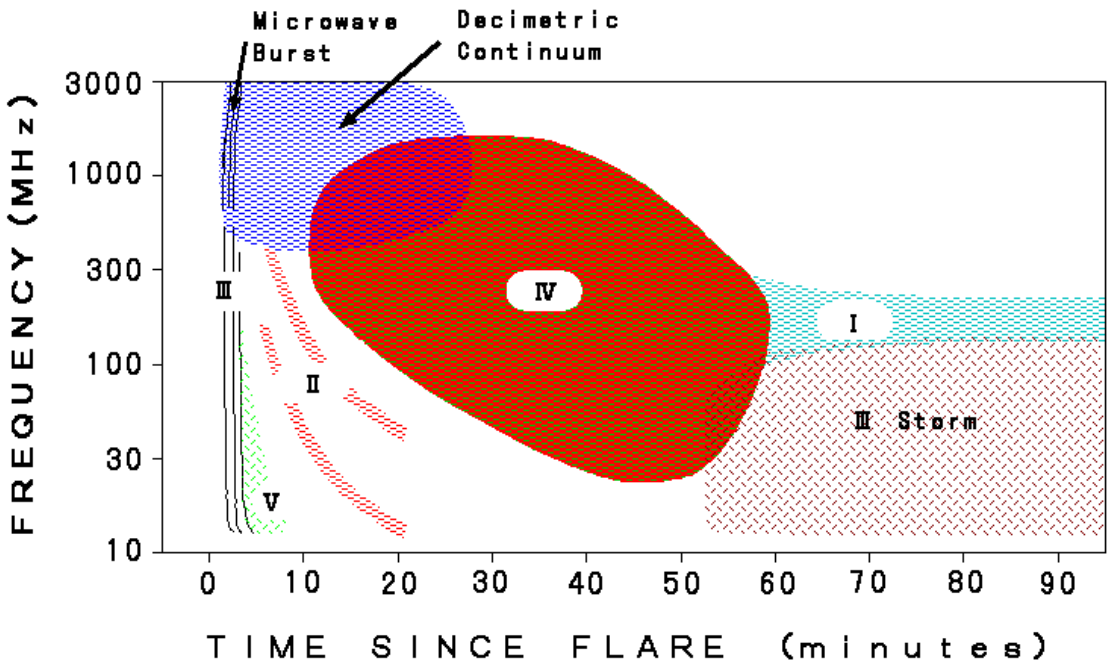

Fig. 1.3: This cartoon describe about the radio bursts which are frequently seen in the solar atmosphere. Note that the classification of the solar radio bursts is done based on their drifting speeds and morphology in the spectrograms. Image Credit: http://Sunbase.nict.go.jp/solar/denpa/hiras/types.html

5 MHz s^{-1}) broad band enhanced radio emissions over which series of narrow-band ($\Delta f/f \approx 0.025$), short duration ($\approx$ 1 s) spikes are superposed. Noise storms are strongly circularly polarized emissions and originate due to the plasma oscillations in the solar atmosphere. These bursts are generally observed in the frequency range of $\approx 50 - 500$ MHz [McLean and Labrum, 1985, pp415] .

(b) **Type II bursts/Slow drifting bursts**: Type II bursts are the slowly drifting ($\approx$ 1 MHz s^{-1}) bursts in the solar corona. In other words the source drifts with a speed of $\approx$ 1000 km s^{-1}. These bursts are due to magnetohydrodynamic shocks which occur in the solar atmosphere and last for few minutes. These bursts are observed in frequency range of $\approx$ 40-240 MHz. Type II bursts emit radiation at distinct bands with a frequency ratio of $\approx$ 2:1. These are called 'fundamental' and 'harmonic' emissions which simultaneously originate from a single source. Polarization measurements of type II bursts were carried out by Komesaroff [1958], Akabane and Cohen [1961] and these bursts can be either unpolarized or weakly polarized. The weak polarization of these bursts are due to the dispersion effects in the solar corona caused by inhomogeneous magnetic field in the vicinity of the shock waves [McLean and Labrum, 1985, pp333].

(c) **Type III bursts/Fast drifting bursts**: Type III bursts are the fast drifting bursts ($\approx$ 100 MHz s^{-1}) in the solar corona. They are due to electrons which stream along the open magnetic field lines with a source velocity of $100,000$ km s^{-1} and excite plasma oscillations. Type III bursts are classified into three types: isolated type III bursts, groups of type III bursts and type III storms. These are weak circularly polarized bursts with a degree of circular polarization (dcp) $\lesssim 50\%$. The weak polarization of these bursts are due to the dispersion effects in the solar corona caused by inhomogeneous magnetic field in the vicinity of the shock waves [McLean and Labrum, 1985, pp289].

(d) **Type IV bursts/Broad-band continuum emissions**: Type IV bursts are smooth varying continuum emissions. They are weakly polarized and occur at centimeter, decameter and meter wavelengths. Origin of these bursts is still uncertain and is believed that they may originate due to gyro-synchrotron emission mechanisms. These bursts may last for 10 minutes to few hours. Type IV bursts are classified into two types (1) Stationary type IV bursts which are also called flare continuum. (2) Moving type IV bursts in which the source propagates with the speed of mass ejections [McLean and Labrum, 1985, pp361].

(e) **Type V bursts/Continuum meter wave emissions**: These are the continuum emissions that last for few seconds to few minutes. These bursts are seen mostly at meter-wavelengths followed by type III bursts. Type V bursts are generally observed in the frequency (< 200 MHz). The dcp of the type V bursts is $\lesssim 0.1$. First time Wild et al. [1959] classified type IV bursts based on the wide spectra, long duration and mainly their association with the type III bursts [McLean and Labrum, 1985, pp325].

Apart from these, some more complex bursts often seen in the solar radio spectrograms are U-type and J-type bursts. U-bursts initially resemble the type III bursts, and later the frequency drifts in reverse direction which appears as an inverted 'U' in the dynamic solar radio spectrum. The J-bursts are similar to the U-bursts provided they do not show the reverse stroke [McLean and Labrum, 1985, pp322] .

S. No.	Type	Event Characteristics	Associated phenomenon	E.M	Δ f (MHz)	Δ t	dcp (%)
1	Type I	Narrow band, short duration spikes superposed over a continuum emission	Active regions, flares, Eruptive prominences	PE	50-500 MHz	Single burst ≈ 1s Noise storm: few hours to days	≈ 50 – 100%
2	Type II	Slow drifting 1 MHz s^{-1}, Second harmonics	Flares, MHD shocks, proton emissions	PE	20-150 MHz	3-30 mins	≈ 50%
3	Type III	Fast drifting 20 MHz s^{-1} occurs as isolated, groups, storms Second harmonics	Active regions, flares	PE	10 kHz-1 GHz	Isolated≈ 1 – 3 s Groups ≈ 1 – 10 mins Storms ≈ mins-hours	F≈ 50% H$\lesssim$ 30%
4	Type IVs	Smoothly varying broad band continuum	Flares, Proton emissions	GS	20 MHz-2 GHz	Hours-days	≈ 50%
5	Type IVm	Smoothly varying broad band continuum Slow drifting	Eruptive prominences MHD shocks	GS	20-400 MHz	30-120 mins	increases from low to ≈ 100%
5	Type V	Smooth, short lived continuum emission follows Type III groups/storms	Active regions, flares	PE	10-200 MHz	1-3 mins	very low (< 10%)

Table 1.1: Radio bursts/emissions are briefly discussed in the Table. EM: Emission mechanisms, PE: Plasma emission, GS: Gyrosynchrotron emission. For more details refer Kundu [1965], McLean and Labrum [1985].

1.8 Radio emission from solar corona

1.8.1 Bremsstrahlung emission

The solar corona and the chromosphere have fully ionized plasma in which the electrons move freely. Emission due to the deviation of trajectory of free electrons under the influence of a proton is called free-free emission or Bremsstrahlung. Free electrons in an ionized plasma are accelerated by the electric field intensity (E) but motion of the ions are negligible. The equation of the motion of the electrons is

$$m_e \dot{v} = -eEe^{-i\omega t} \tag{1.2}$$

Solution of the equation 1.2 is,

$$v = -i\frac{eE}{m_e \omega} \tag{1.3}$$

From the equation 1.3 following conclusions can be made. It is known that mass of the ion (m_i) is greater than mass of the electron [i.e., $m_i \gtrsim 2 \times 10^3 \ m_e$], therefore from the equation 1.3 it is clear that velocity of the electrons in the medium is higher than ions. So velocity of the ions are negligible or considered as stable particles [Rohlfs and Wilson, 2004]. Therefore, passage of electron close to the proton loses its energy by radiation. In such cases, electron undergoes a hyperbolic path and sometimes moves in elliptical orbit after the interaction. In the latter case, the electron is said to be captured and the phenomenon is called free-bound transition. Free-bound transitions seen in lower chromosphere and the radiation is observable in the X-ray domain. Due to the random motions of the electrons in a media, state of polarization varies from one electron to another which results in randomly polarized emission. Such free-free interaction emits the radiation in EUV, SXR and radio frequencies. These type of interactions slow down the electrons in the medium. In the solar atmosphere, radiation due to the interaction of

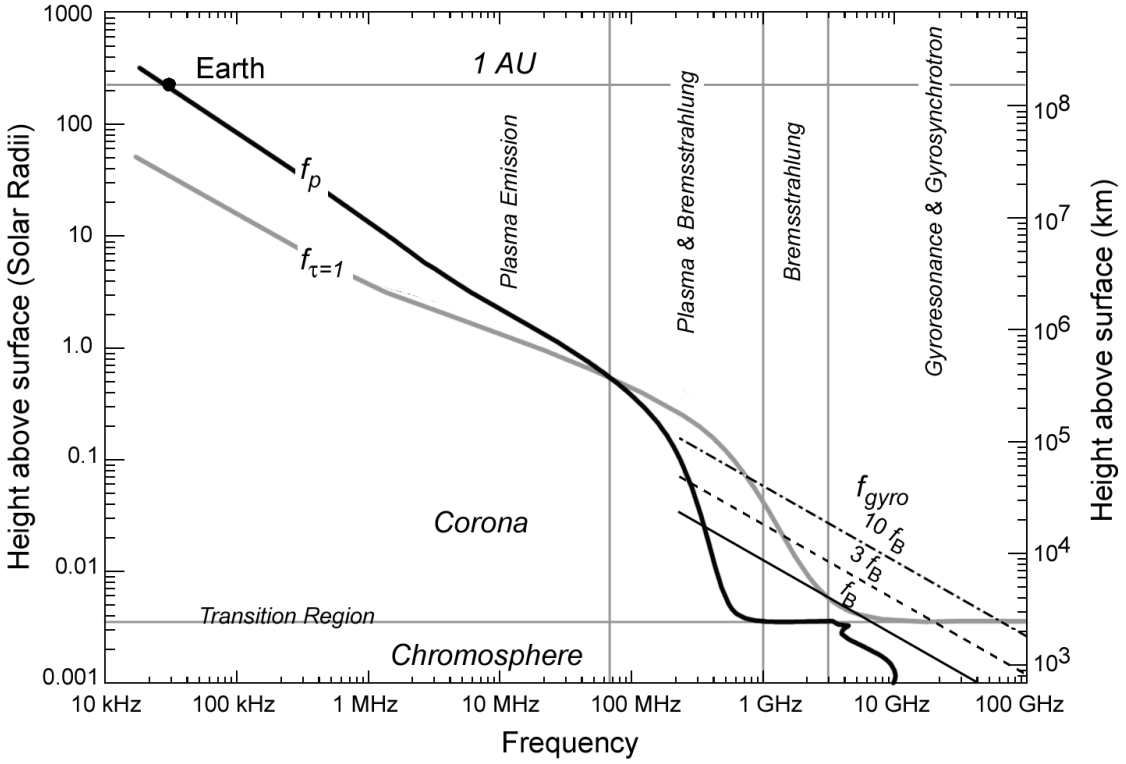

Fig. 1.4: The plot describe the possible emission mechanisms at different height in the solar atmosphere. At a sufficient height (in general, at meter wavelengths) the magnetic field is considered very weak so that the gyrofrequency (f_B) is negligible and plasma frequency (f_p) dominates. At microwave frequencies, gyroresonance and gyrosynchrotron emission are dominant. In meter wavelengths, the plasma emission and bremsstrahlung mechanisms are highly possible. It is clearly represented that microwave frequencies correspond to the chromospheric heights, where as meter wavelengths corresponds to solar corona. The existing instruments at Gauribidanur Radio Observatory work in the frequency range of 150-30 MHz. At those frequencies, the radio emission originates at a heliocentric distance of $\approx\ 1.1 - 1.8\ R_\odot$ ($\approx 765 - 1252$ Mm). Image Credit: Gary and Hurford [2004]

electrons with the protons are called the bremsstrahlung emission or free-free emission. In the solar atmosphere, the medium is highly ionized. The plasma is filled with enormous number of free electrons and protons. Therefore, the free-free interaction of these electrons and protons are highly possible which results in the radio radiation. The radiation from the quiet Sun, active regions, corona holes and coronal streamers are due to the thermal bremsstrahlung emission mechanism [Rybicki and Lightman, 1986, McLean and Labrum, 1985, Aschwanden, 2005].

1.8.2 Gyromagnetic emission

In the presence of magnetic field, the particles in the medium spiral along the magnetic field lines, therefore the name gyromagnetic emission. Depending on speed of rotation of the particles, the originated emissions are broadly classified into three categories. (1) If the electrons gyrate with non-relativistic speeds in the presence of magnetic fields, such emissions are called gyroresonance/cyclotron/magneto bremsstrahlung emission [Aschwanden, 2005, p.227]. (2) When the mildly relativistic particles gyrate in the presence of the magnetic field, such emissions are termed as gyrosynchrotron emissions (3) In some cases, the particles gyrate close to relativistic speeds which are called synchrotron emissions. All the three emission mechanisms are non-coherent emissions [Gary and Keller, 2004, Rybicki and Lightman, 1986, McLean and Labrum, 1985].

(i) **Gyroresonance/Cyclotron emission:** Due to the thermal agitation, the electrons follow a hyperbolic trajectory. If there exists a magnetic field in the medium, the electron will be subjected to travel along the magnetic field lines. In such cases, electrons spiral around the magnetic field line of force and traverse in a helical trajectory. The frequency of the rotation is called gyromagnetic frequency (f_B) and is given by

$$f_B = \frac{eB}{2\pi mc} \tag{1.4}$$

where m is the mass of the electron [$\approx 9.10 \times 10^{-28}$ g], e is the charge of the electron [$\approx 4.8 \times 10^{-10}$ esu], c is the velocity of the light [3×10^{10} cm s^{-1}], and B is the magnetic field in [G]. Substituting these parameters in equation 1.4, gives the gyromagnetic frequency (f_B) in [Hz].

$$f_B[\text{Hz}] = 2.8 \times B\ [\text{G}] \tag{1.5}$$

Equation 1.5 is useful in estimating either gyrofrequency or the magnetic field by knowing any one of them. When the electron rotates along the field lines, it undergoes a centrifugal acceleration which emits the electromagnetic radiation at the gyromagnetic frequency f_B. Such a radiation is circularly polarized. Sense of polarization follows the sense of rotation of the electron. In the plane of orbit, it shows a linear polarization. Gyroresonance emission is concentrated at the fundamental frequency and at harmonics $f/f_B < 10$.

(ii) **Gyrosynchrotron emission:** This emission results due to the gyro motion of the mildly relativistic electrons in the presence of a magnetic field. The equations 1.4 and 1.5 hold good for gyrosynchrotron emission also. The gyrosynchrotron emission is strong at harmonic numbers $10 < f/f_B < 100$.

(iii) **Synchrotron emission:** In the presence of magnetic field, the hot electrons in the solar corona cause this radiation. Brightness temperature may exceed 10^{11} K. Gyromagnetic emission occur in the Sun because of the presence of the electrons which traverse with the speed of few tenths of light velocity. But, it is possible that there exist electrons that traverse with a speed close to the speed of light. Such an ultra speed electron produces an electromagnetic radiation called synchrotron emission. Even though emission mechanism is similar to the gyroresonance and gyrosynchrotron, synchrotron emission produces linearly polarized radio emission. In certain cases, synchrotron emission can cause circular polarization. Origin of some of type IV bursts are believed to be due to synchrotron emission mechanism.

Most of the linearly polarized radio emissions from the stellar sources like Cygnus A, Centaurus A, pulsars, etc are due to synchrotron emission [Rybicki and Lightman, 1986].

Note that all of the above mentioned emission mechanisms are incoherent in nature.

1.8.3 Plasma emission

When the ionized medium is in equilibrium, they obey Maxwell's distribution law. If there is a perturbation in such equilibrium, very complex phenomenon occurs which give rise to radio emission. Such perturbations are very much possible in the solar atmosphere. Electron temperature of the solar corona rarely exceeds $\approx 10^7$ K. During solar activity, brightness temperatures in the solar corona is of the order of $\approx 10^{10} - 10^{11}$ K are observed. Such emissions are due to the nonthermal mechanism. Solar atmosphere is a neutrally ionized medium. Any perturbation in such medium causes plasma oscillations. The emission process occur in two stages (1) the electrons in the solar corona accelerate aftermath of transient events like solar flare. (2) the accelerated electrons interact with the plasma particles which convert them into the transverse electromagnetic radiation at either its characteristic frequency, called plasma frequency [f_p] or its harmonic frequency [$2f_p$]. Plasma frequency can be estimated using the following formula [Rybicki and Lightman, 1986, McLean and Labrum, 1985],

$$f_p = \frac{e}{2\pi}\sqrt{\frac{N_e}{\epsilon_o m}} \tag{1.6}$$

where, N_e is the electron density of the medium [m^{-3}], e is the charge of the electron [$\approx 1.60217\times10^{-19}$ C], m is the mass of the electron [$\approx 9.1\times10^{-31}$ kg], ϵ_o is the permittivity of the free space [$\approx 8.8542 \times 10^{-12}$ F m^{-1}]. By substituting the above parameters in

equation 1.6 gives,

$$f_p[\mathrm{Hz}] \approx 8.98 \times \sqrt{N_e[\mathrm{m}^{-3}]} \tag{1.7}$$

$$\approx 8.98 \times 10^3 \sqrt{N_e[\mathrm{cm}^{-3}]} \tag{1.8}$$

Noise storms (type I), type II and type III bursts are due to plasma radiation. Other coherent emission mechanism is a cyclotron maser [Dulk and Melrose, 1982].

1.9 Polarization states of different emission mechanisms

Different emission mechanisms show different state of polarizations. Few of them is listed in the Table 1.2.

S. No	Emission mechanism	State of polarization
1	Synchrotron emission	linear
2	Non-thermal gyrosynchrotron emission	circular
3	Thermal-gyro-synchrotron emission	circular
4	Gyroresonance emission	circular
5	Cyclotron maser emission	circular
6	Plasma emission	random
7	Bremsstrahlung emission	random

Table 1.2: Polarization state of different emission processes which are frequently observed in solar atmosphere at radio frequencies.

1.10 Radio wave propagation in the solar corona

In an ionized medium, the electric field of an electromagnetic wave force the electrons and ions to oscillate. In the absence of the collisions, the net effect of the movement of electrons correspond to the change in refractive index. In the absence of the magnetic field,

radio waves propagating in the medium undergo (1) bending due to changes of refractive index (2) absorptive attenuation [Kundu, 1965]. If the medium is homogeneous and non-conducting (specific conductivity, $\sigma = 0$) then the refractive index of such medium is defined in Rohlfs and Wilson [2004] as,

$$n = \frac{c}{v} = \sqrt{\epsilon\mu} = \frac{c}{\omega}k \tag{1.9}$$

where n is the refractive index of the medium, c is the velocity of light, v is the velocity of the wave, ϵ and μ are the permittivity and permeability of the medium respectively, $k = 2\pi/\lambda$ is the wave number, $\omega = 2\pi/T$ is the angular frequency, T is the time period of the wave.

If the medium is dissipative, and $\sigma \neq 0$ then from the dispersion equation of the harmonic wave propagation, by assuming $\epsilon \approx 1$ and permeability $\mu \approx 1$, the refractive index equation can be written as

$$n = \sqrt{1 - \frac{f_p^2}{f^2}} \tag{1.10}$$

where n is the refractive index of the plasma, f_p is the plasma frequency which is described in equation 1.6 and f is the frequency of the observation.

Equation 1.10 is very significant in radio astronomy and the following conclusions can be made: (1) $f > f_p$, then the refractive index is real and wave can propagate through the medium. In this case $n < 1$, so that refraction is opposite to that which occurs when the wave enters denser medium. (2) $f = f_p$, then the refractive index becomes zero. It is known that electron density decreases in the solar atmosphere with increasing height. Therefore, from equation 1.7, it is clear that the plasma frequency also decreases radially outward. Figure 1.5 shows the decrease of the plasma frequency from $\approx 1.1 - 1.8\ R_\odot$. Hence, radiation in the corona originates over a thin layer in which $f = f_p$. In the solar corona, the perturbations occur due to the solar flares, CME, high velocity jets, shock waves etc, and they accelerate the particles to the outer atmosphere. The radio radiation

originated due to such disturbances are observed first at high frequencies and then they drift towards the lower frequencies. (3) $f < f_p$, then the refractive index is imaginary and the wave will not propagate through the medium, but reflects back. Therefore, in an isotropic media, different frequencies of observations correspond to different heights/layers in the solar corona. Lower the frequency of observation higher the layer in the solar corona that can be observed.

1.11 Magneto-ionic theory in the solar corona

According to the magneto-ionic theory, wave propagating relative to the magnetic field splits into two characteristic polarized waves (1) ordinary mode (o-mode) which will not be affected by the magnetic field and passes through the line of sight and (2) extraordinary mode (e-mode/x-mode) which is affected by the magnetic field and refracts with an angle to the o-mode. These two modes propagate with different velocities and undergo different amount of absorptions. Such a phenomenon is called birefringence. When a linearly/randomly polarized wave propagates through the ionized plasma in the presence of magnetic fields it undergoes birefringence which causes the split radiation into two opposite circularly polarized modes: (1) left circular polarization (LCP) and (2) right circular polarization (RCP). Dispersion equations and the refractive indices of the magnetized plasma are discussed in many plasma physics text books [Aschwanden, 2005, Ratcliffe, 1969, Ginzburg et al., 1971, Chen, 1974, Schmidt, 1979, Lang, 1980, Benz, 1993, Sturrock, 1994].

1.12 Solar coronal density models

As per equation 1.7, the electron density decreases radially outwards in the solar atmosphere from the photosphere, therefore the plasma frequency. To estimate the electron

density at different heights many models were developed based on different observations. Close to the photosphere, coronal density models have been derived from eclipse observations at visible wavelengths. Some of them which provide densities from 1 to 3 $R_\odot$ are: Baumbach-Allen model [Baumback, 1937, Allen, 1947], Newkirk density model [Newkirk, 1961], Saito model [Saito et al., 1977], Hybrid density model etc. At low corona, $\lesssim 1.1 R_\odot$, the density gradient is very steep. Baumback [1937] was the first to develop expression to estimate the electron density. Saito et al. [1977] determined the density from 2.2 to 5.5 $R_\odot$ using the white light coronagraph data of Skylab. Newkirk's density model is well suited for the operating frequency range of instruments at GRO. Newkirk's density model is developed based on eclipse observations. Variation of the electron density in the quiet corona is determined using the expression 1.11

$$N(R) = N_o \times D \times 10^{4.32/R} \tag{1.11}$$

N_o is 4.2×10^4, R is the distance from the center of the Sun in units of solar radius. $D \approx 0.1$ to 0.5 for a coronal hole, ≈ 2 for an active region, ≈ 10 for a dense streamer, and ≈ 1 for quiet corona. The simulated density profile with frequency and radius in the range $1.8 - 1.1\ R_\odot$ is shown in Figure 1.5. Newkirk density model at large heights slightly deviates with the other models [Pohjolainen et al., 2007, Mann et al., 1999, 2003].

1.13 Polarization and Stokes parameters

Christian Huygens was the first to suggest that light is not a scalar quantity based on his experiments. Newton also suspected that light has 'sides'. The vectorial nature of an electromagnetic wave is called polarization. Experiments of Fresnel and Arago led to the discovery that light has two transverse components which are perpendicular to each other. A brief review of the polarization is described in this section and more details are

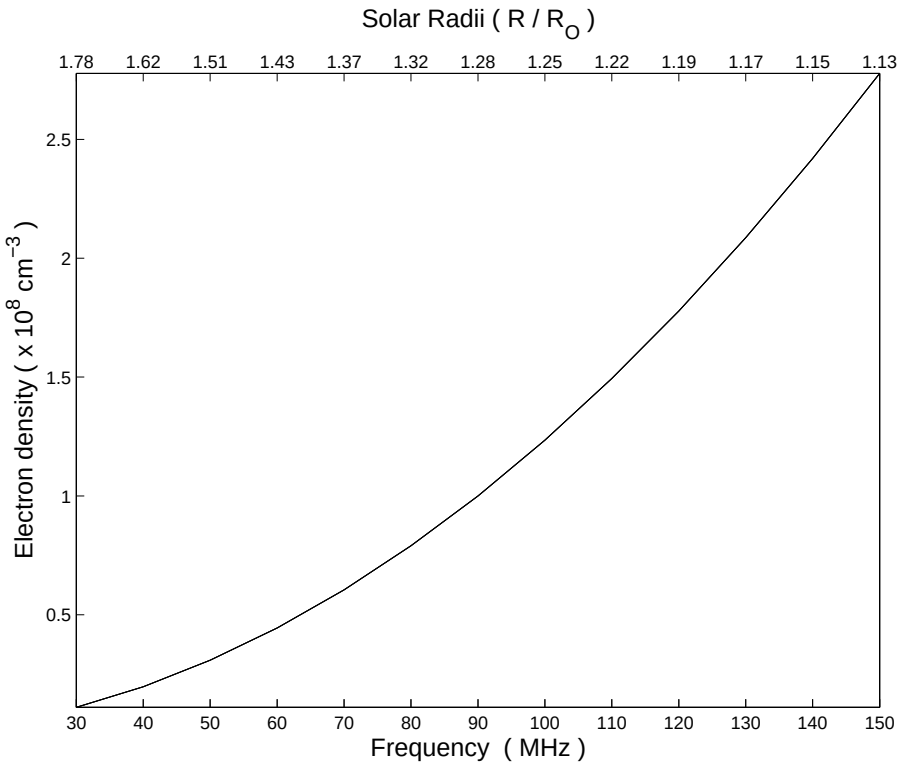

Fig. 1.5: One fold Newkirk's density model in the plasma frequency range of 150-30 MHz.

found in Collett [1934]. If the electromagnetic wave is propagating in the z direction, then the two components of the electromagnetic waves are as follows,

$$E_x(z,t) = E_{ox}cos(\tau + \delta_x) \tag{1.12}$$

$$E_y(z,t) = E_{oy}cos(\tau + \delta_y) \tag{1.13}$$

where $E_x(z,t)$ and $E_y(z,t)$ are the electric field components in x and y directions respectively. E_{ox} and E_{oy} are the maximum amplitudes, δ_x and δ_y are the initial phases respectively and τ is the $\omega t + kz$ is the propagator. Here, ω is the angular frequency, t is the time, k is the wave number of the propagating wave. As the field propagates, $E_x(z,t)$ and $E_y(z,t)$ give the resultant vector of electromagnetic wave. Using the equations 1.12

and 1.13 it is possible to derive the equation 1.14.

$$\frac{E_x^2}{E_{ox}^2} + \frac{E_y^2}{E_{oy}^2} - 2\frac{E_x}{E_{ox}}\frac{E_y}{E_{oy}}cos\delta = sin^2\delta \tag{1.14}$$

where $\delta = \delta y - \delta x$. Equation 1.14 is identified as equation of ellipse, which means that the locus of electric field vector when the electromagnetic wave propagates will be ellipse. Different combinations of the fields (equation 1.12 and 1.13) produces different polarization states of the propagating wave. For the sake of completeness, few cases are discussed briefly here. (1) If the $E_{oy} = 0$ and $E_{ox} \neq 0$ then the linear horizontally polarized electromagnetic wave results and vice-versa, (2) If $\delta = 0$ or π, it is possible to show that the resultant wave will be linearly polarized but oriented in $\pm 45^o$. (3) If $\delta = \pi/2$ or $3\pi/2$ and $E_{ox} = E_{oy} = E_o$ then the polarization ellipse reduces to the equation of a circle, which means that a circularly polarized electromagnetic wave results, which plays an important role in estimating magnetic field at low frequency radio astronomy. Note that if $\delta = \pi/2$, then it is said to be left circularly polarization and $\delta = 3\pi/2$ right circular polarization results. Therefore, linear and circular polarization are different cases of the elliptically polarized wave. If the path traced out by the electric field vector continuously changes randomly, such waves are called randomly polarized or 'unpolarized' waves [Christiansen and Hoegbom, 1969, pp21].

Therefore, orientation of the electric field vector of a propagating electromagnetic wave describes different states of polarization. Although, equation 1.14 is an idealized expression which is having some practical limitations. The equation is valid only for a completely polarized wave which is not the case in most of the practical applications. Therefore, the four Stokes parameters were proposed by George Gabriel Stokes which are sufficient to represent any state of the electromagnetic wave. The four Stokes parameters

are represented using a stokes vector ($\vec{S}$)

$$\vec{S} = \begin{pmatrix} I \\ Q \\ U \\ V \end{pmatrix}$$

where I is the total intensity, Q represents linear polarization oriented either in 0° or 90°, U represents the linear polarization oriented in either 45° or 135° and V represents circular polarization; either right circularly polarization (RCP) or left circular polarization (LCP).

In radio astronomy, polarized radio emissions from the solar corona and other radio celestial sources can be observed using different antennas. For example, using linearly polarized antennas mounting in 0^o or 90^o horizontal linear or vertical linear polarized emissions are observed. By mounting the same in $\pm 45^o$ linearly polarized but oriented $\pm 45^o$ can be observed. Left or right circularly polarized emissions can also be observed using suitable helical antennas. Because of obvious reasons (few of them mentioned in this thesis), linearly polarized antennas are sufficient to study the four Stokes parameters and reasonably preferred to observe the circularly polarized emissions including the total intensity.

1.14 Thesis outline

Chapter-1 mainly describes the introduction to the further chapters. In this chapter solar interior, solar atmosphere, radio bursts, their classification, emission mechanism and propagation of radio waves in the solar corona are described.

Chapter-2 is about the Gauribidanur radio interference polarimeter (GRIP) which was recently constructed at Gauribidanur radio observatory. In this chapter, constructed

interferometric array, analog and digital receiver system, different errors present in the interferometric arrays and calibration techniques of the array are described.

Chapter-3 describes the noise storms observed with GRIP. Total energy radiated by the noise storms are estimated, which are in the category of picoflare energies. Using such picoflares coronal heating is explained.

Chapter-4 is primarily about the estimation of magnetic fields in the solar atmosphere using the polarization observations of group of type III harmonic bursts and based on their quasi-periodicities. The results obtained with different approaches were consistent with the theoretical models.

Chapter-5 is about the estimation of the magnetic field of the solar corona based on observations of the type-IV bursts which are associated with the coronal mass ejections observed using GRIP.

Chapter-6 describes about the scattering studies of the solar corona using Crab nebula occultation technique. In this chapter, method of estimation of level of turbulence and angular broadened source sizes are estimated.

Chapter-7 is about the newly fabricated cross-polarized log-periodic dipole antenna system. Using such antennas two element interference polarimeter was built and observations of the radio emissions on the Sun in both Stokes I and V are discussed.

Chapter-8 explains the summary and conclusions of the work carried out. Also, future scope of the work that is possible with the constructed GRIP is described in this chapter.

References

K. Akabane and M. H. Cohen. Polarization Measurements of Type III Bursts and Faraday Rotation in the Corona. ApJ, 133:258, January 1961. doi: 10.1086/147021.

C. W. Allen. Interpretation of Electron Densities from Corona Brightness. MNRAS, 107: 426, 1947.

M. J. Aschwanden. *Physics of the Solar Corona. An Introduction*. Praxis Publishing Ltd, August 2004.

M. J. Aschwanden. *Physics of the Solar Corona. An Introduction with Problems and Solutions (2nd edition)*. December 2005.

T. S. Bastian, A. O. Benz, and D. E. Gary. Radio Emission from Solar Flares. ARA&A, 36:131–188, 1998a. doi: 10.1146/annurev.astro.36.1.131.

T. S. Bastian, A. O. Benz, and D. E. Gary. Radio Emission from Solar Flares. ARA&A, 36:131–188, 1998b. doi: 10.1146/annurev.astro.36.1.131.

S. Baumback. Strahlung, Ergiebigkeit und Elektronendichte der Sonnenkorona. *Astronomische Nachrichten*, 263:121, July 1937.

A. O. Benz, editor. *Plasma astrophysics: Kinetic processes in solar and stellar coronae*, volume 184 of *Astrophysics and Space Science Library*, 1993.

A. O. Benz, C. Monstein, H. Meyer, P. K. Manoharan, R. Ramesh, A. Altyntsev, A. Lara, J. Paez, and K.-S. Cho. A World-Wide Net of Solar Radio Spectrometers: e-CALLISTO. *Earth Moon and Planets*, 104:277–285, April 2009. doi: 10.1007/s11038-008-9267-6.

J.-L. Bougeret, M. L. Kaiser, P. J. Kellogg, R. Manning, K. Goetz, S. J. Monson, N. Monge, L. Friel, C. A. Meetre, C. Perche, L. Sitruk, and S. Hoang. Waves: The Radio and Plasma Wave Investigation on the Wind Spacecraft. Space Sci. Rev., 71:231–263, February 1995. doi: 10.1007/BF00751331.

G. E. Brueckner, R. A. Howard, M. J. Koomen, C. M. Korendyke, D. J. Michels, J. D. Moses, D. G. Socker, K. P. Dere, P. L. Lamy, A. Llebaria, M. V. Bout, R. Schwenn, G. M. Simnett, D. K. Bedford, and C. J. Eyles. The Large Angle Spectroscopic Coronagraph (LASCO). Sol. Phys., 162:357–402, December 1995. doi: 10.1007/BF00733434.

I. E. Burke and K. F. Tapping. Imaging the sun at 21 cm: Budgetting the S-component. Sol. Phys., 157:295–314, March 1995. doi: 10.1007/BF00680623.

E. P. Carley, R. T. J. McAteer, and P. T. Gallagher. Coronal Mass Ejection Mass, Energy, and Force Estimates Using STEREO. ApJ, 752:36, June 2012. doi: 10.1088/0004-637X/752/1/36.

F. F. Chen. *Introduction to plasma physics*. 1974.

W. N. Christiansen and J. A. Hoegbom. *Radiotelescopes*. 1969.

Edward Collett. *Polarized light : fundamentals and applications*. Marcel Dekker, 1934.

A. E. Covington. Micro-Wave Solar Noise Observations During the Partial Eclipse of November 23, 1946. Nature, 159:405–406, March 1947. doi: 10.1038/159405a0.

V. Domingo, B. Fleck, and A. I. Poland. The SOHO Mission: an Overview. Sol. Phys., 162:1–37, December 1995. doi: 10.1007/BF00733425.

G. A. Dulk. Radio emission from the sun and stars. ARA&A, 23:169–224, 1985. doi: 10.1146/annurev.aa.23.090185.001125.

G. A. Dulk and D. B. Melrose. On the effects of electron-cyclotron masers during flares. *Advances in Space Research*, 2:185–185, 1982. doi: 10.1016/0273-1177(82)90196-X.

E. Ebenezer, R. Ramesh, K. R. Subramanian, M. S. SundaraRajan, and C. V. Sastry. A new digital spectrograph for observations of radio burst emission from the Sun. A&A, 367:1112–1116, March 2001. doi: 10.1051/0004-6361:20000540.

W. C. Erickson, M. J. Mahoney, and K. Erb. The Clark Lake Teepee-Tee telescope. ApJS, 50:403–419, December 1982. doi: 10.1086/190831.

R. R. Fisher, R. H. Lee, R. M. MacQueen, and A. I. Poland. New Mauna Loa coronagraph systems. Appl. Opt., 20:1094–1101, March 1981. doi: 10.1364/AO.20.001094.

B. Fleck, V. Domingo, and A. I. Poland. The SOHO mission. Sol. Phys., 162, December 1995.

L. Fletcher, B. R. Dennis, H. S. Hudson, S. Krucker, K. Phillips, A. Veronig, M. Battaglia, L. Bone, A. Caspi, Q. Chen, P. Gallagher, P. T. Grigis, H. Ji, W. Liu, R. O. Milligan, and M. Temmer. An Observational Overview of Solar Flares. Space Sci. Rev., 159: 19–106, September 2011. doi: 10.1007/s11214-010-9701-8.

I.U.I. GalÊźperin, T. Muliïÿăaïÿąrchik, J.P. Thouvenin, Russian Space Agency, Institut kosmicheskikh issledovaniĭ (Akademiiïÿăaïÿą nauk SSSR), and Centre national d'études spatiales (France). *Interball: Mission and Payload*. RSA, Russian Space Agency, 1995.

D. E. Gary and G. J. Hurford. Radio Spectral Diagnostics. In D. E. Gary and C. U. Keller, editors, *Astrophysics and Space Science Library*, volume 314 of *Astrophysics and Space Science Library*, page 71, September 2004. doi: 10.1007/1-4020-2814-8_4.

D. E. Gary and C. U. Keller, editors. *Solar and Space Weather Radiophysics - Current Status and Future Developments*, volume 314 of *Astrophysics and Space Science Library*, September 2004.

D. E. Gary, G. J. Hurford, G. M. Nita, S. M. White, S. D. Tun, G. D. Fleishman, and J. M. McTiernan. The Expanded Owens Valley Solar Array. In *AAS/Solar Physics Division Abstracts #42*, page 102, May 2011.

V. L. Ginzburg, J. B. Sykes, and R. J. Tatler. *The propagation of electromagnetic waves in plasmas.* 1971.

L. Golub and J. M. Pasachoff. *The Solar Corona*. October 2009.

N. Gopalswamy. A Global Picture of CMEs in the Inner Heliosphere. In G. Poletto and S. T. Suess, editors, *The Sun and the Heliosphere as an Integrated System*, volume 317 of *Astrophysics and Space Science Library*, page 201, November 2004.

N. Gopalswamy and M. R. Kundu. Estimation of the mass of a coronal mass ejection from radio observations. ApJ, 390:L37–L39, May 1992. doi: 10.1086/186366.

R. V. Gorgutsa, A. A. Gnezdilov, A. K. Markeev, and D. E. Sobolev. An upgrade of the izmiran's solar digital radio spectrograph: First results. *Astronomical and Astrophysical Transactions*, 20:547–549, October 2001. doi: 10.1080/10556790108213597.

J. T. Gosling, E. Hildner, R. M. MacQueen, R. H. Munro, A. I. Poland, and C. L. Ross. Mass ejections from the sun - A view from SKYLAB. J. Geophys. Res., 79:4581–4587, November 1974. doi: 10.1029/JA079i031p04581.

G. E. Hale, F. Ellerman, S. B. Nicholson, and A. H. Joy. The Magnetic Polarity of Sun-Spots. ApJ, 49:153, April 1919. doi: 10.1086/142452.

T. Howard, editor. *Coronal Mass Ejections*, volume 376 of *Astrophysics and Space Science Library*, 2011. doi: 10.1007/978-1-4419-8789-1.

H. S. Hudson, J.-L. Bougeret, and J. Burkepile. Coronal Mass Ejections: Overview of Observations. Space Sci. Rev., 123:13–30, March 2006. doi: 10.1007/s11214-006-9009-x.

M. L. Kaiser. The STEREO mission: an overview. *Advances in Space Research*, 36: 1483–1488, 2005. doi: 10.1016/j.asr.2004.12.066.

M. L. Kaiser, T. A. Kucera, J. M. Davila, O. C. St. Cyr, M. Guhathakurta, and E. Christian. The STEREO Mission: An Introduction. Space Sci. Rev., 136:5–16, April 2008. doi: 10.1007/s11214-007-9277-0.

A. Kerdraon and J.-M. Delouis. The Nançay Radioheliograph. In G. Trottet, editor, *Coronal Physics from Radio and Space Observations*, volume 483 of *Lecture Notes in Physics, Berlin Springer Verlag*, page 192, 1997. doi: 10.1007/BFb0106458.

M. Komesaroff. Polarization Measurements of the Three Spectral Types of Solar Radio Burst. *Australian Journal of Physics*, 11:201, June 1958. doi: 10.1071/PH580201.

T. Kondo, T. Isobe, S. Igi, S.-i. Watari, and M. Tokumaru. The new solar radio observation system at hiraiso. *Communications Research Laboratory Review*, 40:85, March 1994.

D. V. Korolkov and I. N. Pariiskii. The Soviet RATAN-600 radio telescope. S&T, 57: 324–329, April 1979.

A. Krueger. *Introduction to solar radio astronomy and radio physics.* 1979.

M. R. Kundu. *Solar radio astronomy.* 1965.

K. R. Lang. *Astrophysical Formulae. A Compendium for the Physicist and Astrophysicist.* 1980.

C. J. Lonsdale, R. J. Cappallo, M. F. Morales, F. H. Briggs, L. Benkevitch, J. D. Bowman, J. D. Bunton, S. Burns, B. E. Corey, L. Desouza, S. S. Doeleman, M. Derome, A. Deshpande, M. R. Gopala, L. J. Greenhill, D. E. Herne, J. N. Hewitt, P. A. Kamini, J. C. Kasper, B. B. Kincaid, J. Kocz, E. Kowald, E. Kratzenberg, D. Kumar, M. J. Lynch, S. Madhavi, M. Matejek, D. A. Mitchell, E. Morgan, D. Oberoi, S. Ord, J. Pathikulangara, T. Prabu, A. Rogers, A. Roshi, J. E. Salah, R. J. Sault, N. U. Shankar, K. S. Srivani, J. Stevens, S. Tingay, A. Vaccarella, M. Waterson, R. B. Wayth, R. L. Webster, A. R. Whitney, A. Williams, and C. Williams. The Murchison Widefield Array: Design Overview. *IEEE Proceedings*, 97:1497–1506, August 2009. doi: 10.1109/JPROC.2009.2017564.

G. Mann, F. Jansen, R. J. MacDowall, M. L. Kaiser, and R. G. Stone. A heliospheric density model and type III radio bursts. A&A, 348:614–620, August 1999.

G. Mann, A. Klassen, H. Aurass, and H. T. Classen. Development of shocks waves in the solar corona and the interplanetary space. In M. Velli, R. Bruno, F. Malara, and B. Bucci, editors, *Solar Wind Ten*, volume 679 of *American Institute of Physics Conference Series*, pages 612–615, September 2003. doi: 10.1063/1.1618669.

D. J. McLean and N. R. Labrum. *Solar radiophysics: Studies of emission from the sun at metre wavelengths.* 1985.

N. Mittal and U. Narain. On some properties of coronal mass ejections in solar cycle 23. New A, 14:341–346, April 2009. doi: 10.1016/j.newast.2008.10.004.

P. Murdin, editor. *Very Large Array, National Radio Astronomy Observatory.* November 2000. doi: 10.1888/0333750888/4358.

H. Nakajima, M. Nishio, S. Enome, K. Shibasaki, T. Takano, Y. Hanaoka, C. Torii, H. Sekiguchi, T. Bushimata, S. Kawashima, N. Shinohara, Y. Irimajiri, H. Koshiishi, T. Kosugi, Y. Shiomi, M. Sawa, and K. Kai. The Nobeyama radioheliograph. *IEEE Proceedings*, 82:705–713, May 1994.

G. Newkirk, Jr. The Solar Corona in Active Regions and the Thermal Origin of the Slowly Varying Component of Solar Radio Radiation. ApJ, 133:983, May 1961. doi: 10.1086/147104.

W. D. Pesnell, B. J. Thompson, and P. C. Chamberlin. The Solar Dynamics Observatory (SDO). Sol. Phys., 275:3–15, January 2012. doi: 10.1007/s11207-011-9841-3.

S. Pohjolainen, L. van Driel-Gesztelyi, J. L. Culhane, P. K. Manoharan, and H. A. Elliott. CME Propagation Characteristics from Radio Observations. Sol. Phys., 244:167–188, August 2007. doi: 10.1007/s11207-007-9006-6.

E. R. Priest. *Solar magneto-hydrodynamics*. 1982.

R. Ramesh, K. R. Subramanian, M. S. Sundararajan, and C. V. Sastry. The Gauribidanur Radioheliograph. Sol. Phys., 181:439–453, August 1998. doi: 10.1023/A:1005075003370.

R. Ramesh, C. Kathiravan, A. S. Narayanan, and E. Ebenezer. Metric observations of transient, quasi-periodic radio emission from the solar corona in association with a "halo" CME and an "EIT wave" event. A&A, 400:753–758, March 2003. doi: 10.1051/0004-6361:20030019.

J. A. Ratcliffe. *Magneto-ionic theory*. 1969.

K. Rohlfs and T. L. Wilson. *Tools of radio astronomy*. 2004.

H. O. Rucker, W. Macher, G. Fischer, T. Oswald, J. L. Bougeret, M. L. Kaiser, and K. Goetz. Analysis of spacecraft antenna systems: Implications for

STEREO/WAVES. *Advances in Space Research*, 36:1530–1533, 2005. doi: 10.1016/j.asr.2005.07.060.

G. B. Rybicki and A. P. Lightman. *Radiative Processes in Astrophysics*. June 1986.

K. Saito, A. I. Poland, and R. H. Munro. A study of the background corona near solar minimum. Sol. Phys., 55:121–134, November 1977. doi: 10.1007/BF00150879.

G. Schmidt. *Physics of High Temperature Plasmas*. 1979.

Silvio Orsi. POLAR: A Space-borne X-Ray Polarimeter for Transient Sources. *ArXiv e-prints*, December 2010.

M. Stix. *The sun: an introduction*. 2002.

E. C. Stone, A. M. Frandsen, R. A. Mewaldt, E. R. Christian, D. Margolies, J. F. Ormes, and F. Snow. The Advanced Composition Explorer. Space Sci. Rev., 86:1–22, July 1998. doi: 10.1023/A:1005082526237.

R. G. Stone, J. L. Bougeret, J. Caldwell, P. Canu, Y. de Conchy, N. Cornilleau-Wehrlin, M. D. Desch, J. Fainberg, K. Goetz, and M. L. Goldstein. The Unified Radio and Plasma wave investigation. A&AS, 92:291–316, January 1992.

P. A. Sturrock. *Plasma Physics, An Introduction to the Theory of Astrophysical, Geophysical and Laboratory Plasmas*. 1994.

A. Vourlidas, D. Buzasi, R. A. Howard, and E. Esfandiari. Mass and energy properties of lasco cmes. In A. Wilson, editor, *Solar Variability: From Core to Outer Frontiers*, volume 506 of *ESA Special Publication*, pages 91–94, December 2002.

A. Vourlidas, R. A. Howard, E. Esfandiari, S. Patsourakos, S. Yashiro, and G. Michalek. Erratum: Comprehensive analysis of coronal mass ejection mass and energy properties over a full solar cycle. ApJ, 730:59, March 2011. doi: 10.1088/0004-637X/730/1/59.

D. F. Webb and T. A. Howard. Coronal Mass Ejections: Observations. *Living Reviews in Solar Physics*, 9:3, June 2012. doi: 10.12942/lrsp-2012-3.

S. M. White, M. R. Kundu, V. I. Garaimov, and T. Yokoyama. The Physical Properties of a Flaring Coronal Loop. *AGU Spring Meeting Abstracts*, page 42, May 2001.

J. P. Wild. The radioheliograph and the radio astronomy programme of the Culgoora Observatory. *Proceedings of the Astronomical Society of Australia*, 1:38, November 1967.

J. P. Wild and S. F. Smerd. Radio Bursts from the Solar Corona. ARA&A, 10:159, 1972. doi: 10.1146/annurev.aa.10.090172.001111.

J. P. Wild, K. V. Sheridan, and G. H. Trent. The transverse motions of the sources of solar radio bursts. In R. N. Bracewell, editor, *URSI Symp. 1: Paris Symposium on Radio Astronomy*, volume 9 of *IAU Symposium*, page 176, 1959.

J. P. Wild, S. F. Smerd, and A. A. Weiss. Solar Bursts. ARA&A, 1:291, 1963. doi: 10.1146/annurev.aa.01.090163.001451.

Chapter 2

Gauribidanur radio interference polarimeter

Observations of the polarized radiation from the Sun to understand its magnetic field is one of the challenging tasks in observational solar physics. In the case of the solar photosphere, chromosphere and to a limited height in the inner corona ($\lesssim 0.1\ R_{\odot}$) magnetic field strengths are usually estimated through emission line observations (optical wavelengths) and gyroresonance observations (cm wavelengths), respectively. Faraday rotation observations of the linearly polarized radio emission from the extra galactic radio sources are used to estimate the magnetic fields in the outer corona. As for as the middle corona is concerned, only extrapolated values of the photospheric measurements are usually adopted. In this chapter the newly constructed Gauribidanur Radio Interference Polarimeter (GRIP) to estimated the magnetic field in the middle corona is discussed. Note that to represent a state of polarization of any electromagnetic wave four Stokes parameters (I, Q, U and V) are required. Here I is the total intensity, Q and U represent the linear polarization and V corresponds to the circular polarization. All Stokes parameters can be measured with linearly polarized antennas at radio wavelengths. Linear

polarization (Q and U) is generally not detectable at low frequencies due to the Faraday effects introduced by the solar corona and Earth's ionosphere over the frequency band observation [Hatanaka, 1956, Grognard and McLean, 1973]. Therefore we restricted to study to the circularly polarized radio emission.

2.1 Interferometry and aperture synthesis

Angular resolution ($\theta \approx \lambda/D$) of a telescope will be better if the aperture size (D) of the telescope is larger, for the observations at wavelength (λ). At radio frequencies, since the wavelength is very large compared to the rest of the electromagnetic spectrum, to achieve high angular resolution it is required to build a telescope with large aperture size of few kilometers. Building a continuous aperture telescope to that extent is not possible due to economical and mechanical difficulties. Interferometric techniques in which one can synthesize the aperture to obtain better angular resolution as well as sensitivity are used. Interferometers can be designed for a desired resolution and collecting area which is not possible with the continuous aperture telescopes. GRIP is a interferometric array which is designed to measure circularly polarized emissions (Stokes V) and the total intensity (Stokes I) of the radio emission from the corona.

2.2 Log-periodic dipole antenna

Numerous applications of electromagnetics in real life necessitate to build different type of antennas. It is always demanded to design a broadband antennas with simple, compact, lightweight and economically feasible structures. In the cases where the extended bandwidth is $\approx$ 40:1 or more, they are referred as frequency independent antennas. It is challenging to design such antennas without altering the characteristics like impedance, radiation patterns, polarization properties, but with increased operating frequency. One

such frequency independent antenna is the log periodic dipole (LPD) antenna which was introduced by Duhamel and Isbell [1957]. The structure of the LPD is shown in Figure 7.1 and the designing procedure is discussed in section 7.2 [Kraus, 1950, Balanis, 2005]. The LPD consists of the number of dipoles of different sizes, separated by different distances along the transmission lines (booms) as shown in Figure 2.1. Note that the elements are arranged in crisscross fashion or mechanically introducing the 180^o phase between the adjacent elements of the LPD. The mechanical phase reversal produces a phase progression, therefore the radiation beams in the direction of the short arms. Otherwise it produces the end-fire beam. The input impedance of a LPD antenna repeats with frequency. Impedance of the LPDA as a function of logarithm of the frequency is periodic (not necessarily sinusoidal), hence the name log periodic. Mathematically the variation of the impedance with frequency in the case of LPDs can be expressed as,

$$f_n = f_{n+1} \star k \tag{2.1}$$

$$log(f_{n+1}) = log(f_n) + log(1/k) \tag{2.2}$$

Also radiation pattern, directivity, beamwidth and side lobe levels etc shows the similar variations. Note that LPD is designed by maintaining the constant apex angle α with a fixed scaling factor (k). The scaling factor decides the dimension of the LPD and is related as follows,

$$\frac{L_{n+1}}{L_n} = \frac{S_{n+1}}{S_n} = k \tag{2.3}$$

where L_{n+1}, L_n are the lengths of the $n+1$ and n dipoles respectively and S_{n+1}, S_n are the distances from the $n+1$, n dipoles to the respective adjacent dipoles (see Figure 7.1). The scaling factor (k) of the LPD used in the GRIP was ≈ 1.12 and the apex angle α was $\approx 28^o$. The thickness of the boom and diameter of the arms are 25 mm and 13 mm

respectively. The calculated spacing between the two booms is ≈ 2 cm for the impedance 50 Ω [Balanis, 2005, Ramesh et al., 1998, Ramesh, 1998b, Sasikumar Raja et al., 2013].

The signal is 'tapped' from the top of the LPD using a coaxial cable. The LPD is designed using the circular aluminum pipes (for the 'arms') and square/rectangular aluminum pipes for the support structure or the 'boom'. In general the outer layer of the coaxial cable is connected the 'boom' through which the coaxial cable is brought to the lower end of the LPD. The center lead is connected to the one of the 'booms' of the LPD as shown in the Figure 2.1. To match the impedance of the antenna, the two booms are shorted at their lower end using a U shaped aluminum plate called 'stub'. The LPDs in the GRIP have been designed to work in the frequency range ≈ 30-150 MHz. Note that impedance of the designed LPD is maintained 50 Ω in order to match the impedance of the coaxial cables used in the GRIP array (50 Ω). The total length of each 'boom' is ≈ 5.6 m and the other specifications are given in Table 2.1.

2.3 Performance study of the LPDA

We measured the LPD and the results are discussed in the following sections. More information on these parameters can be found in section 7.3 [Kraus, 1950, Balanis, 2005, Shevgaonkar, 2005, Huang and Boyle, 2008].

2.3.1 VSWR measurements

Theoretically, when the load impedance match with the characteristic impedance of a transmission line, the input signal completely delivered to the load. If there is a mismatch of impedance between the load and characteristic impedance of the transmission line, a fraction of the input signal (voltage or current) reflects back and cause the reduction in amplitude. Superposition of such forward and backward traveling waves in the

Table 2.1: Dimensions of the LPD antenna used in GRIP.

Dipole number	Length of the arm (cm)	Spacing between the dipoles (cm)	Frequency of a dipole (MHz)
1	275	54.8	27
2	245	48.7	31
3	218.5	43.4	34
4	194.5	38.6	39
5	173	34.4	43
6	154.5	30.6	49
7	137.5	27.2	55
8	122.5	24.2	61
9	109	21.6	69
10	97	19.2	77
11	87	17.1	86
12	77	15.2	97
13	68.5	13.8	109
14	62	12	120
15	55	10.7	136
16	49	9.5	153
17	44	8.5	170
18	39	7.6	192
19	35	6.7	214

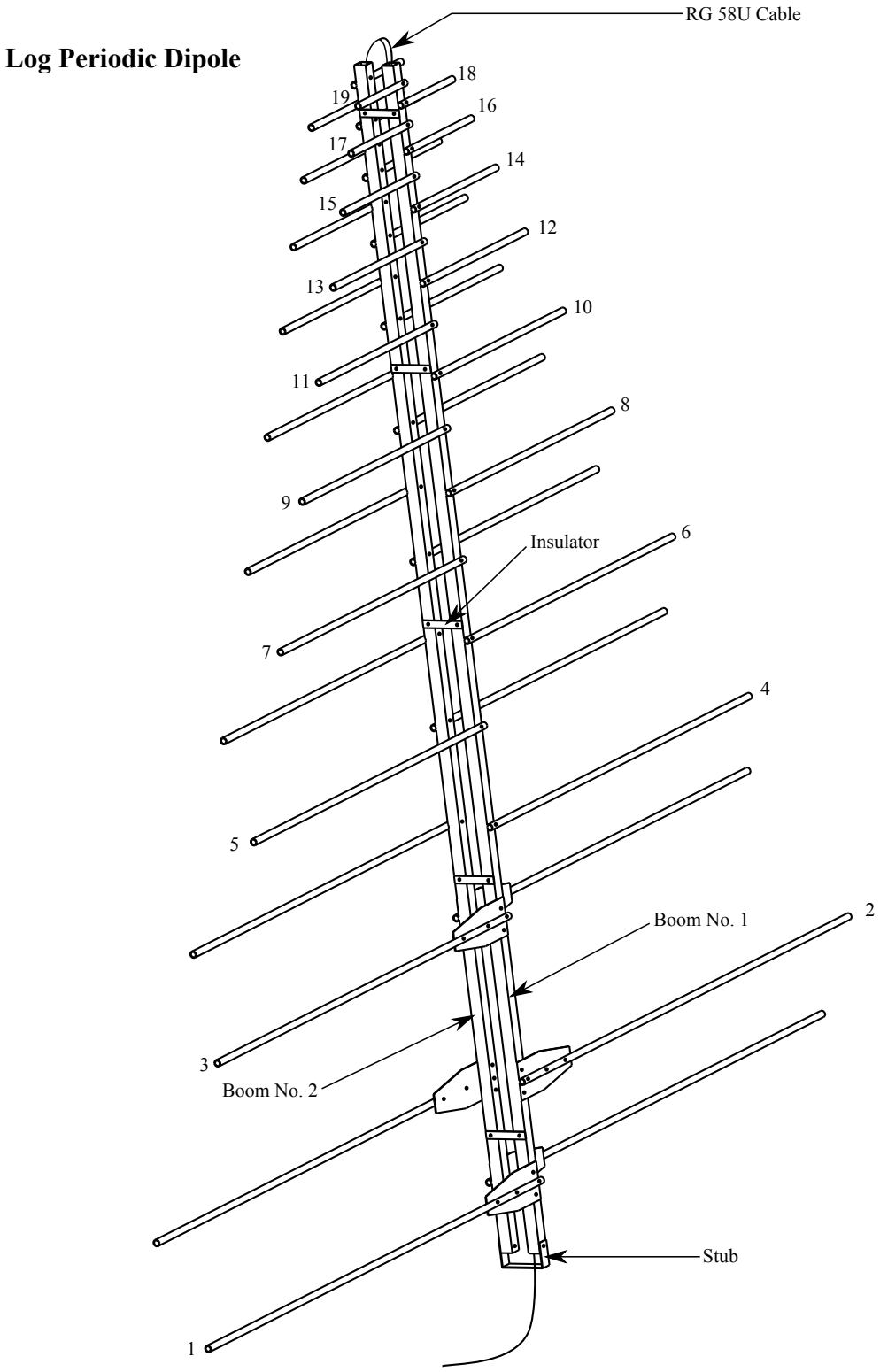

Fig. 2.1: Schematic diagram of a log-periodic dipole antenna used in the GRIP array is shown in the Figure.

transmission line cause the standing waves. This phenomenon can be represented mainly in terms of (1) reflection coefficient (Γ), which represents the amplitude of the reflected wave and is the ratio of the amplitude of the reflected wave to the incident wave. Note that higher the Γ represents more reflection. (2) return loss (L_{rl}), which is the reflection coefficient converted in dB scale or in percentage. (3) Voltage standing wave ratio (VSWR) which is defined as the ratio between the maximum voltage (V_{max}) and minimum voltage (V_{min}) of the standing wave. Note that VSWR is constant at any point for the loss less transmission line and is defined as,

$$VSWR = \frac{|V|_{max}}{|V|_{min}} = \frac{1 + |\Gamma|}{1 - |\Gamma|} \tag{2.4}$$

By knowing the VSWR, return loss (L_{rl}) can be measured in dB and percentage using the expressions 2.5 and 2.6 respectively.

$$|\Gamma| \ [dB] = \frac{VSWR - 1}{VSWR + 1} \tag{2.5}$$

$$L_{rl} \ [\%] = 100 * |\Gamma|^2 \tag{2.6}$$

The VSWR of the LPDs used in GRIP were measured using the vector network analyzer and the VSWR plot with respect to frequency is shown in Figure 2.2. The top panel of the Figure 2.2 shows VSWR of the LPD used in GRIP and middle and lower panels shows the return loss (L_{rl}) in dB scale and percentage respectively. Note that if the VSWR is high, the return loss will be high. For example, if the VSWR is $\lesssim 2$, then the return loss will be $\lesssim 10\%$. From the Figure 2.2, it is clearly noticeable that the VSWR $\lesssim 2.5$ (i.e. return loss $\lesssim 18\%$) in the frequency of operation $30 - 150$ MHz of the LPD which is used in the GRIP. Note that VSWR varies from '1' (since always $V_{max} > V_{min}$) to '∞' (when $V_{min} = 0$). VSWR of '1' and '∞' indicates the maximum power transfer efficiency and no power delivery to the load respectively.

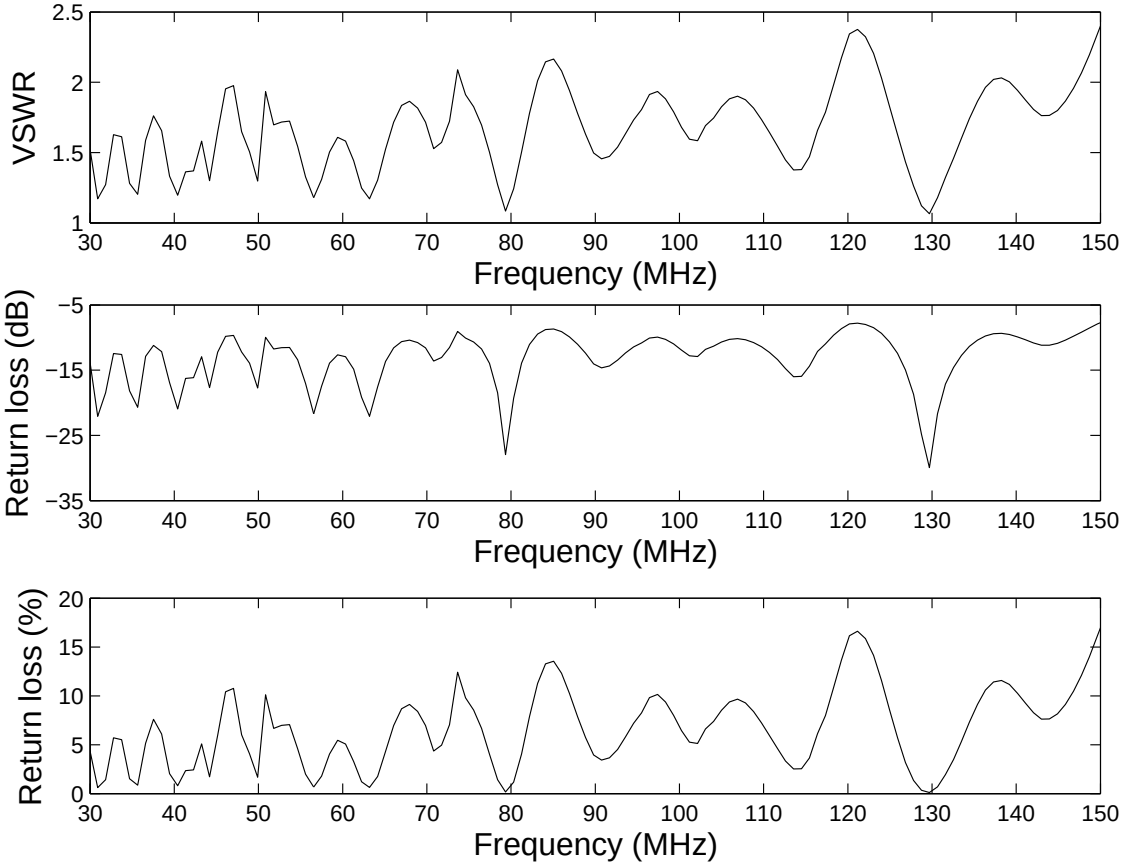

Fig. 2.2: The top panel shows the variation of the VSWR with frequency of the LPD antenna used in the GRIP. The middle and lower panels show the return loss variation in dB scale and in percentage respectively.

2.3.2 Radiation pattern measurements

For a linearly polarized antennas, performance is often described in terms of its principal E and H-plane patterns. The E-plane is defined as, the plane containing the electric field vector and the direction of maximum radiation. The H-plane is a plane containing the magnetic-field vector and the direction of maximum radiation [Balanis, 2005]. Also these E-plane and H-plane measurements can be measured at different distances from which one can understand the propagation of the radiation. It is known that, far-field region is the region of the field of an antenna where the angular field distribution is essentially independent of the distance from the antenna. Far-field region exists approximately at a distance r_{ff} and is expressed as

$$r_{ff} \geq 2l^2/\lambda \tag{2.7}$$

where the l is the largest dimension of the LPD which is $\approx$ 5.6 m and at 80 MHz ($\lambda = 3.75$ m), therefore r_{ff} is $\approx$ 17 meters.

To measure the E-plane of the LPD both transmitting and receiving antennas were mounted on a pole of length $\approx$ 6 meters and separated by a distance of $\approx$ 25 m which is greater than the theoretical far field region. Note that both the LPDs are mounted in horizontal orientation i.e. the arms of the LPDs were mounted parallel to the ground plane. CW signal at different frequencies were transmitted using a signal generator. The level was $\approx$ 15 dBm. The signal level was noted using a spectrum analyzer at the receiver end and the experiment is repeated for all azimuthal angles of the receiving LPD. The Figure 2.5 shows the radiation pattern of the E-plane at 80 MHz measured using the setup described. The peak power of the received signal ≈ -28 dBm. This is less than the expected power (≈ -10 dBm) calculated using the formula [Blake and Long, 2009],

$$P_r = \frac{P_t \; A_{et} \; A_{er}}{R^2 \; \lambda^2} \tag{2.8}$$

where, P_t, P_r are the transmitted and received power from the antennas (in units of dBm), A_{et}, A_{er} are the effective collecting areas of the transmitted and received antennas [$0.6 \times \lambda^2$], R is the distance between the transmitted and received antennas [25 meters] and λ is the wavelength of the transmitted/received signal. The reduced strength of the received signal is likely due to the ground reflections and attenuation in the RF cables.

The half power beam width (HPBW)/field of view (FOV) of the E-plane (θ) were found $\approx 75^o$ for the LPDs. Also the complete experiment was repeated for different frequencies from 50 to 150 MHz and noticed that the HPBW is constant over all the frequencies which is desirable. The radiation pattern measurement setup is shown in the Figure 2.3.

The H-plane pattern was measured using the similar setup discussed above (E-plane setup) provided both the transmitting and receiving antennas were mounted in vertical direction i.e. the arms of the LPDs were mounted perpendicular to the ground plane. The experimental setup of the H-plane measured is shown in the Figure 2.4. The CW signal of level 15 dBm was transmitted and noted the signal at receiving antenna. Similar to E plane pattern in Figure 2.3, here also the received power is less by $\approx 10 - 15$ dBm. Figure 2.6 shows the measured radiation pattern using the setup shown in Figure 2.4. It was found that the HPBW of H-plane (ϕ) was $\approx 105^o$ and is invariant over the frequency of operation of the LPD. Note that such a broad beam enable us to observe the Sun for all declinations over a year of time.

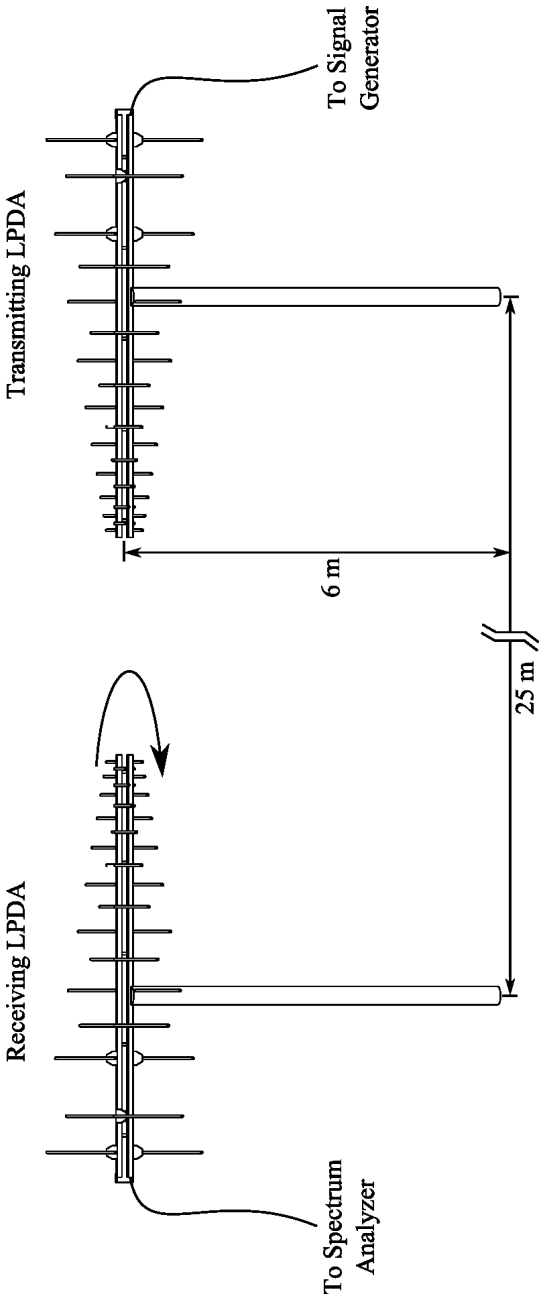

Fig. 2.3: The Figure shows the setup to measure the radiation pattern in the E-plane. In this setup the arms of the both transmitting and receiving antennas are mounted parallel to the ground plane (horizontally mounted). A spot frequency signal is transmitted using transmitter and recorded the readings using the receiver antenna for every angle in azimuthal direction.

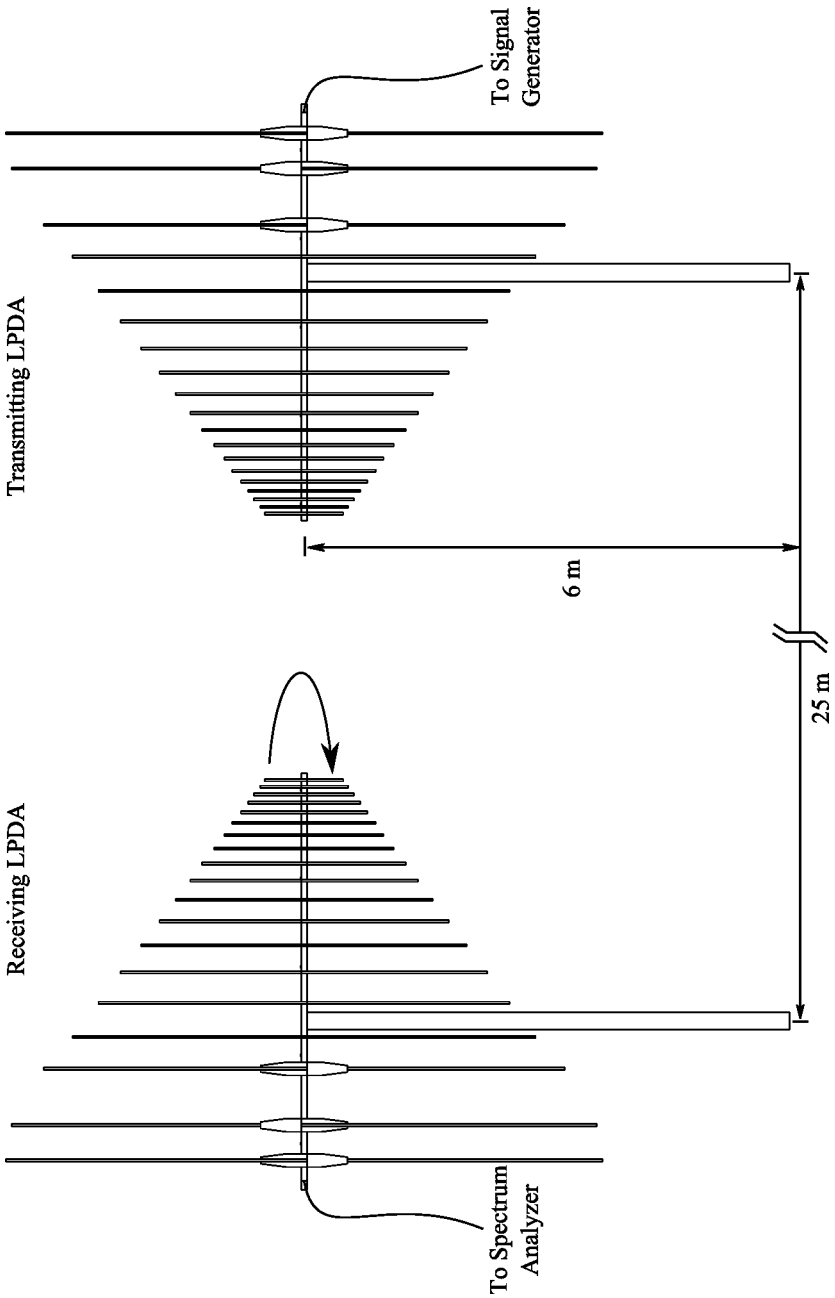

Fig. 2.4: The Figure shows the setup to measure the radiation pattern in the H-plane. In this setup the arms of the both transmitting and receiving antennas are mounted perpendicular to the ground plane (vertically mounted). A spot frequency signal is transmitted using transmitter and recorded the readings using the receiver antenna for every angle in azimuthal direction.

2.3.3 Estimation of antenna parameters

Isotropic radiator is an imaginary, loss less antenna that radiates uniformly in all directions. In practice, all antennas have some degree of non uniformity. Therefore they radiate more power in one direction than others. Such antennas are defined as directional antennas. Although the total power radiated by the isotropic and directional antenna is same, isotropic antenna transmits the power in all directions uniformly. But directional antennas radiates less power in some direction and rest of the concentrated power in one direction. LPD is an example of directional antenna. Directivity is a quantity that measures the concentrated radiated power per unit solid angle in a specific direction and is dependent on radiation patterns.

In the present case, measured HPBW of the E-plane and H-plane of the LPD were 1.3 and 1.8 radians. Therefore the solid angle/beam area corresponding to the LPD was $\Omega = \theta\phi \approx 2.34$ sr. The directivity/directional gain (G) which is the ratio to the maximum radiation in any specific direction to the average radiation in all directions observed in far field region of the antenna was estimated using the expression 2.9. The estimated directional gain of the antenna was ≈ 7 dBi. The gain estimated with respect to the isotropic radiator is referred as absolute gain and its unit is dBi. Also using the expression 2.10 the effective collecting area was estimated. The effective collecting area (A_e) of the LPD was $\approx 0.6 \times \lambda^2$.

$$G = 10\log_{10}(4\pi/\Omega) \tag{2.9}$$

$$A_e = (G/4\pi)\lambda^2 \tag{2.10}$$

where λ is the wavelength of operation.

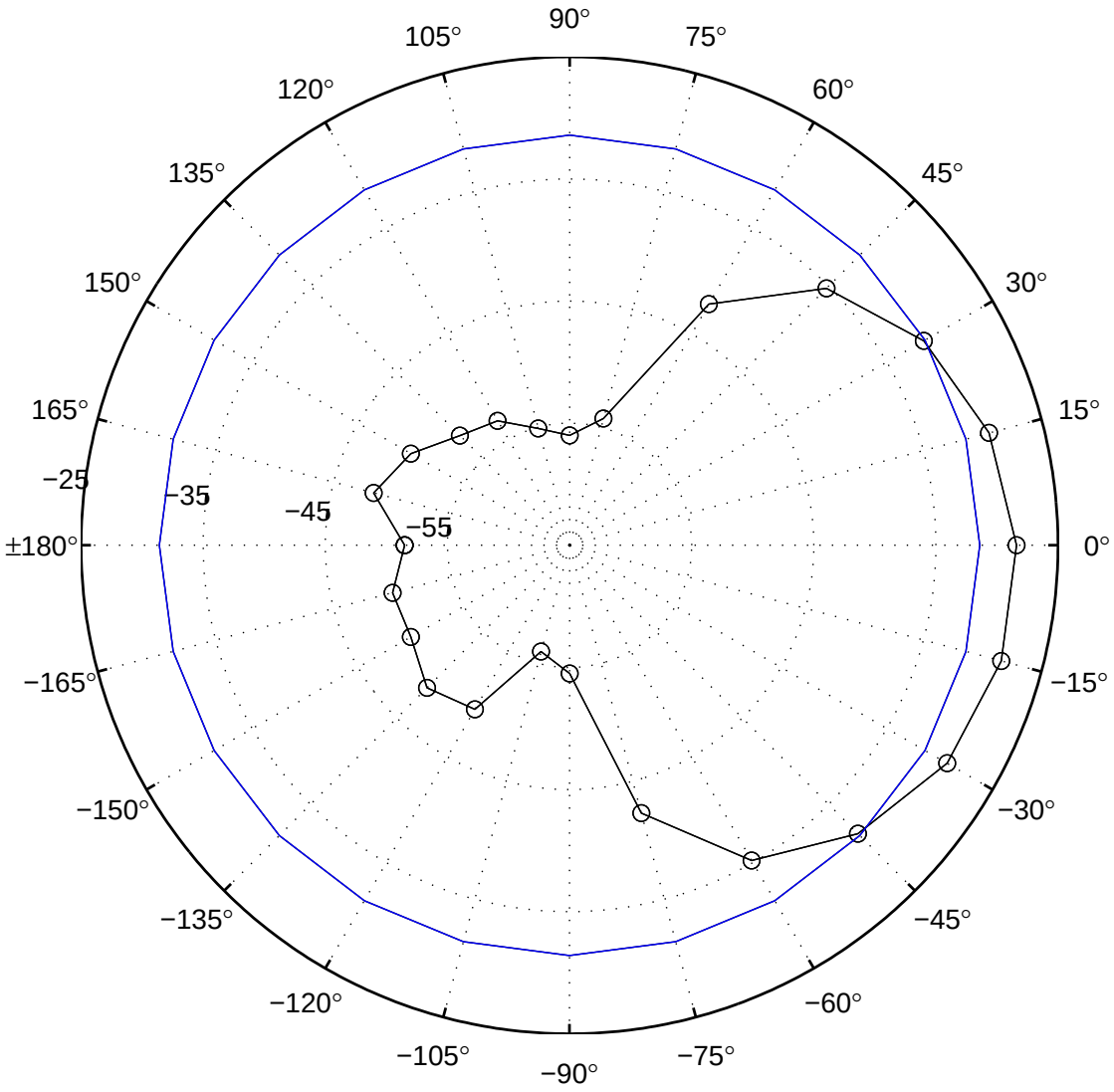

Fig. 2.5: The E-plane of the LPD antenna which is used in GRIP at 80 MHz is shown in the Figure. It is noticeable that there exists a back lobe in E-plane, but there are no other minor lobes seen. The blue circle represents ≈ -31 dBm power level. It intersects the pattern at $\approx 30^o$ and $\approx 45^o$. This gives the HPBW of $\approx 75^o$ for the pattern.

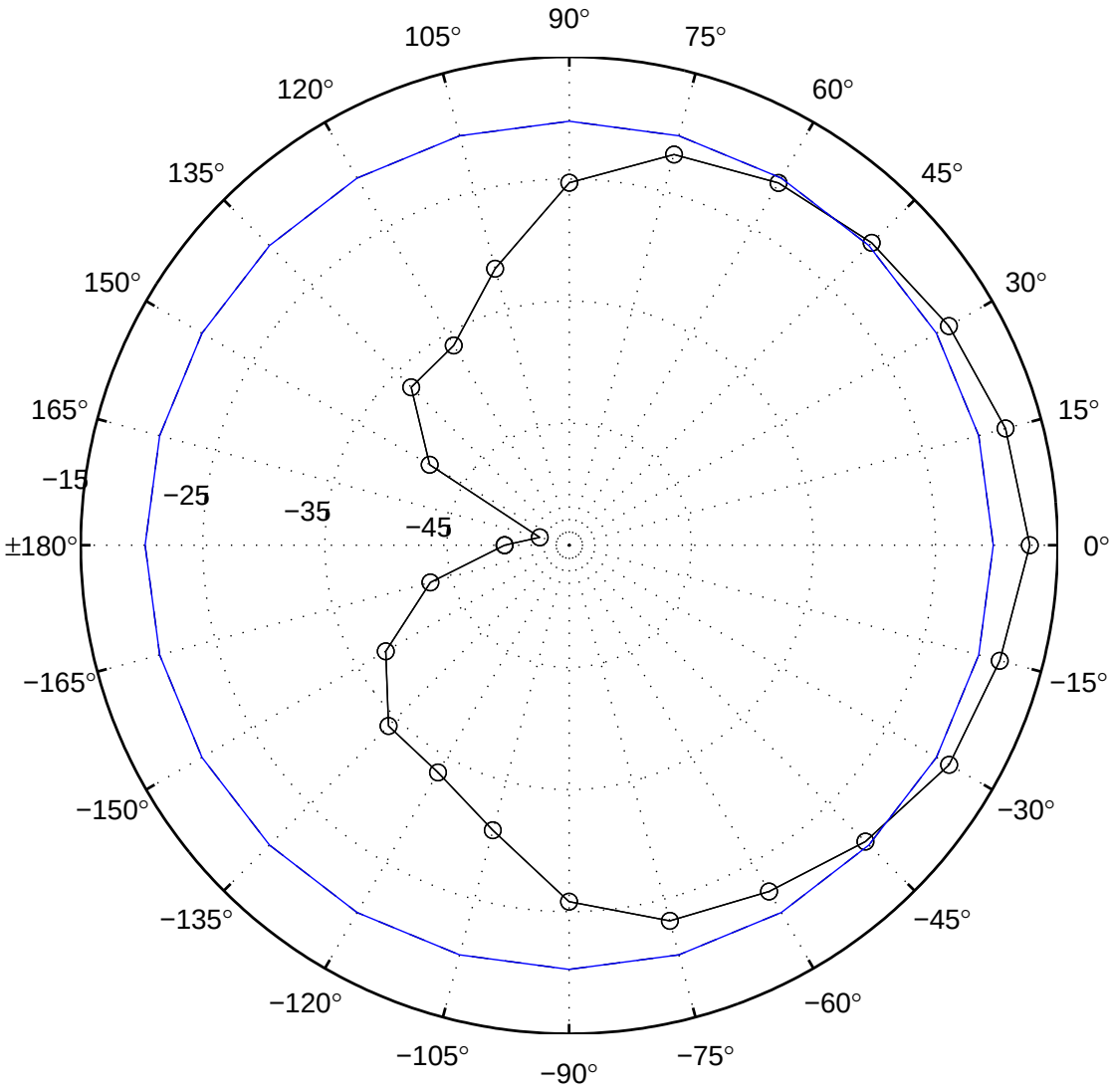

Fig. 2.6: The H-plane of the LPD antenna which is used in GRIP at 80 MHz is shown in the Figure. Also it is noticeable that there are no minor lobes are present in H-plane. The blue circle represents ≈ -20 dBm power level (the maximum received power is ≈ -17 dBm). It intersects the pattern at $\approx 60^o$ and $\approx 45^o$. This gives the HPBW of $\approx 105^o$ for the pattern.

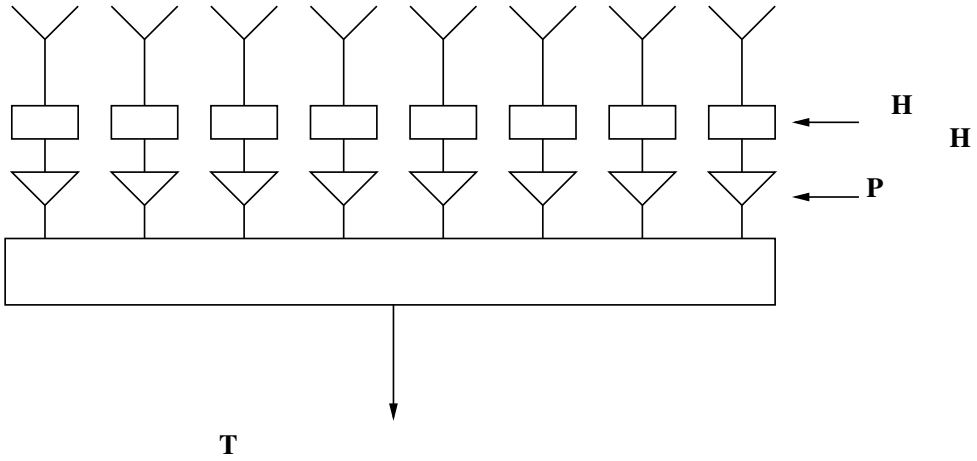

Fig. 2.7: Schematic of a group configuration among the existing 5 groups in GRIP

2.4 Group configuration

GRIP is an array of 40 linearly polarized log-periodic dipole antennas (LPDs) along East-West direction. The adjacent antennas are separated by 10 meters. Each antenna output is high pass filtered using filter whose cut-off frequency is $\approx$ 50 MHz to suppress spurious signals at low-frequencies so that the immediately following amplifier may not saturate. The filtered output is amplified using a pre-amplifier whose gain is $\approx$ 28 dBm. In the same way, the signals from all the antennas in the group are brought to the group center using co-axial cables of $\approx$ 50 meter length (for each antenna) and added using a 8-way power combiner which is shown in Figure 2.7. The combined output is given to the 2-way power combiner which is shown in Figure 2.8 [Ramesh et al., 1998, 2008]. Individual normalized far-field array pattern of an array of antennas can be expressed as,

$$E_n(\phi) = E_0 \frac{sin\ (n\psi/2)}{n\ sin(\psi/2)} \tag{2.11}$$

Where $E_n(\phi)$ is the normalized array field pattern, E_0 is the maximum electric field, n is the number of antenna elements and $\psi = 2\pi d_\lambda\ sin(\phi) + \delta$, $d_\lambda = d/\lambda$ is the distance between the two antennas (in wavelengths), λ is the wavelength of observation, ϕ is the

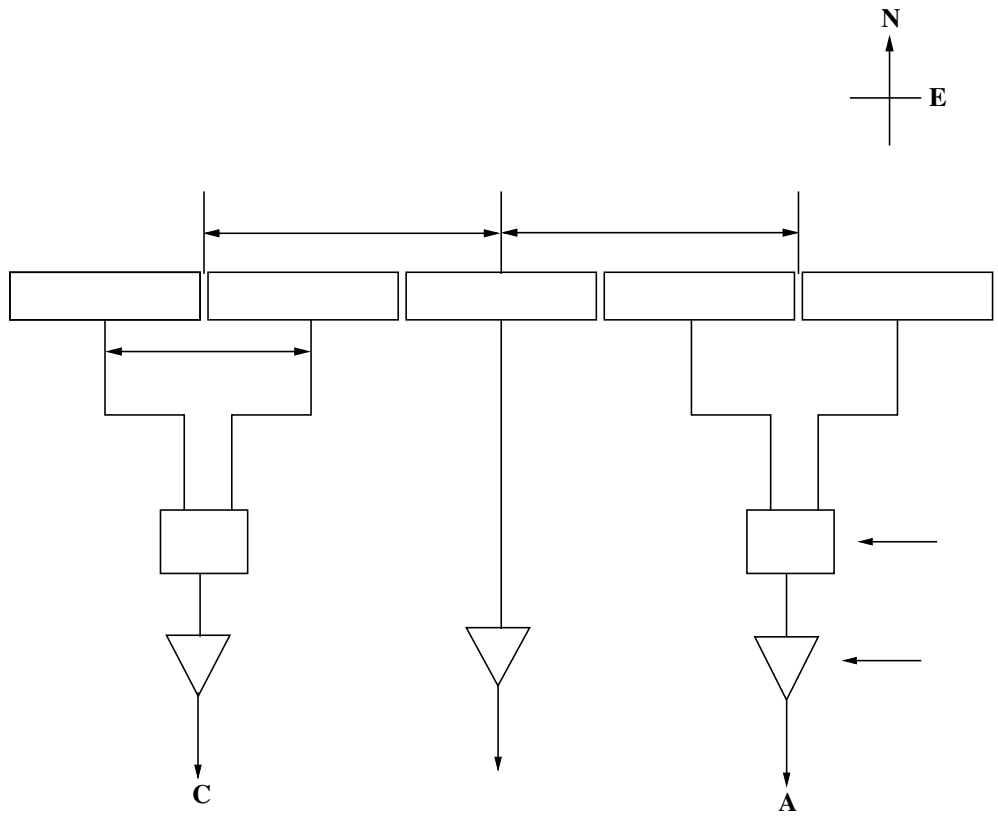

Fig. 2.8: Schematic layout of the GRIP is shown in the Figure.

hour angle, δ is the progressive phase in the array and d is the baseline length between adjacent antennas. Since the output of the every antenna is simply added, it forms a adding interferometer. The power pattern of such array is square of the normalized far-field pattern, $E(\phi)$ is given by,

$$P(\phi) = |E(\phi)|^2 = |E_n(\phi)|^2(1 + cos(\psi)) \tag{2.12}$$

2.5 GRIP Configuration

In GRIP there exist 5 groups and each group consists of 8 antennas. Total length of each group is 70 meters and the total length of the GRIP is 390 meters.

Fig. 2.9: Image shows the GRIP array. The first antenna belong to the group-2 and then onwards next 8 antennas belong to group-3. Note that in the first antenna, arms are aligned in North-South direction where as in group-3, arms of the antennas are aligned in East-West direction. From the second antenna onwards next 8 antenna belongs to group-3 and from there next 16 antennas belongs to the major group-C (group-4 + group-5). Every antenna is placed 10 meters apart from its adjacent antenna in the GRIP. The white boxes shown in the array are the group centers in which power combiners, group amplifier, DC power supply etc are kept.

The 8-way power combiner outputs of group 1 and 2 are added using a 2-way combiner and then amplified using a wide-band amplifier called a group amplifier with gain of $\approx$ 34 dB. In the same fashion, the group 4 and 5 are combined and amplified with a group amplifier. The former combination forms a major group A and the latter one is called a major group C. In group 3, output of 8 antennas are added using a 8-way power combiner and then amplified using a group amplifier and the output is named as B. Note that in the present configuration, the major groups A and C outputs are contributed by 16 antennas where as it is only 8 antennas in group B. In group A, arms of the LPDs are oriented in North-South fashion (0^o) and in the case of group B and C, the LPDs are mounted such that arms of the antennas are oriented along East-West direction (90^o). The signals from A, B and C are brought to the receiver building using a low-loss RF cables which are about 500 meters in length and buried at around one meter depth to avoid fluctuations of phase due to temperature gradient.

The antenna pattern of A, B and C are expressed in the following fashion,

$$E_A = E_0 \frac{sin\ (8\psi)}{16\ sin(\psi/2)} \tag{2.13}$$

$$E_B = E_0 \frac{sin\ (4\psi)}{8\ sin(\psi/2)} \tag{2.14}$$

$$E_C = E_0 \frac{sin\ (8\psi)}{16\ sin(\psi/2)} \tag{2.15}$$

It is known that in adding interferometry the common signals from the antennas as well as additional signals of every antenna will be added up. In correlation or multiplying interferometry the signals between two antennas or groups will be correlated. In the process the latter responds primarily to the common signal between the two groups/antennas. The additional signals of any group/antenna will not be correlated. The cross-correlation of the group outputs A and B or B and C gives the interference fringes and their outputs

can be expressed as,

$$V(\psi) = E_0^2 \frac{sin\ (8\psi)}{16\ sin(\psi/2)} \frac{sin\ (4\psi)}{8\ sin(\psi/2)} cos\ (\beta L sin\ (\phi)) \tag{2.16}$$

where $V(\psi)$ is the corresponding fringe pattern, $\beta = 2\pi/\lambda$ and L is the distance between the two group centers. The correlated output between B and C gives the information of Stokes I and A and B corresponds to Stokes V respectively. Note that in the present configuration, the distance between the group centers of A, B and B, C is 120 meters. Therefore the resolution of the event in both Stokes I and V channels are same. Also it possible to correlate the channels A and C, which corresponds to Stokes V profile. But in this case the Sun will be resolved. The collecting area of the group B is $\approx 5 \times \lambda^2$ and group A or C is $\approx 10 \times \lambda^2$. The calculated minimum detectable flux (5σ level) of the array for both Stokes I and V is ≈ 0.05 sfu [1 sfu = 10^{-22} Watts m^{-2} Hz^{-1}]. Baselines of the phase centers of the group B and any major group is 120 meters so that angular resolution (1.8^o) and collecting area (12 λ^2) for both Stokes I and V are same. Few parameters related to the GRIP were shown in Table 2.2. Half power beam width (HPBW) of group A and C is 1.3^o and for group B is HPBW is 2.6^o. Since HPBW of the group A and C is within the HPBW of group B, correlated output of A and B or B and C will not produce any artifacts in the correlation interferometry. The Figure 2.9 shows the view of the GRIP. The first LPD in the image is the LPD which belongs to the major group-A. Note that arms of the antennas are oriented along the North-South direction. Second LPD onwards, next 8 antennas are called group-B and then next 16 antennas (group-4 and 5) are called major group-C. Note that other than the major group-A, LPD arms are aligned along the East-West direction. The white boxes shown in the Figure 2.9 are located at group centers in which all the power combiners, group amplifiers and DC power supply are kept.

Table 2.2: Specifications of the LPD antenna and GRIP at 80 MHz

Antenna parameter	Value
Antenna element used	Log periodic dipole (LPD)
Total length of the LPD	5.6 meters
Frequency of operation	$30 - 150$ MHz
HPBW of the E-plane	75^o
HPBW of the H-plane	105^o
Solid angle/beam area of LPD	2.34 sr
Directional gain of LPD	7 dBi
Collecting area of LPD	$0.6 \times \lambda^2$
GRIP parameter	**Value**
Angular resolution at 80 MHz	1.8^o
HPBW/FOV of major group A or C	1.3^o
HPBW/FOV of group B	2.7^o
I.F. Bandwidth	1 MHz
Correlator used	1 bit $(2 - \text{level})$
Sampling frequency	2 MHz and 4 MHz
Time resolution	256 milli sec
Sensitivity $(5\ \sigma)$	0.05 sfu (for 1s integration time)

2.6 Simulations of GRIP

Simulations of the group and array patterns, which are discussed in the section 2.4 and 2.5 was done and discussed in the following sections. Far-field pattern of the individual antenna elements is called primary beam pattern. Such individual antennas are arranged in specific way to get desired beam shape. Such arrays have 3 degrees of freedom which can modify the group pattern: (1) distance between the two groups, (2) relative gains of the antenna and (3) the relative phase difference between the individual antennas. Such linear arrays simulated at 40 and 80 MHz are shown in Figure 2.10 and 2.11 respectively. At 40 MHz the grating lobes are missing because, $d_\lambda \approx 1$. Since $d/\lambda \gg 1$ at 80 MHz grating lobes are present. Note that for larger d_λ values the grating lobes are formed and the spacing between the main lobe to grating lobe (ϕ_G) is,

$$\phi_G = sin^{-1}\frac{1}{d_\lambda} \text{ rad} \tag{2.17}$$

If $d_\lambda \gg 1$ the equation 2.18 reduces to,

$$\phi_G = \frac{1}{d_\lambda} \text{ rad} \tag{2.18}$$

In the absence of tracking system, grating lobes (separated by $\approx sin^{-1}(\lambda/\mathrm{d})$ can be effectively used to observe the Sun for longer duration. Intense emission from the Sun usually dominates the emission from the sidereal radio sources. But at times Sun may be located very close to a sidereal source. We take care if such observations need to be analyzed. The number of elements per group has to be selected carefully such that solar corona can be observed for a long duration. Using GRIP, everyday 5 lobe observations namely E_1, E_2, M_3, W_4, W_5 can be carried out, where E, M, W represents the East, Main and West lobes. The lobes formed in the East and West are called as East lobes

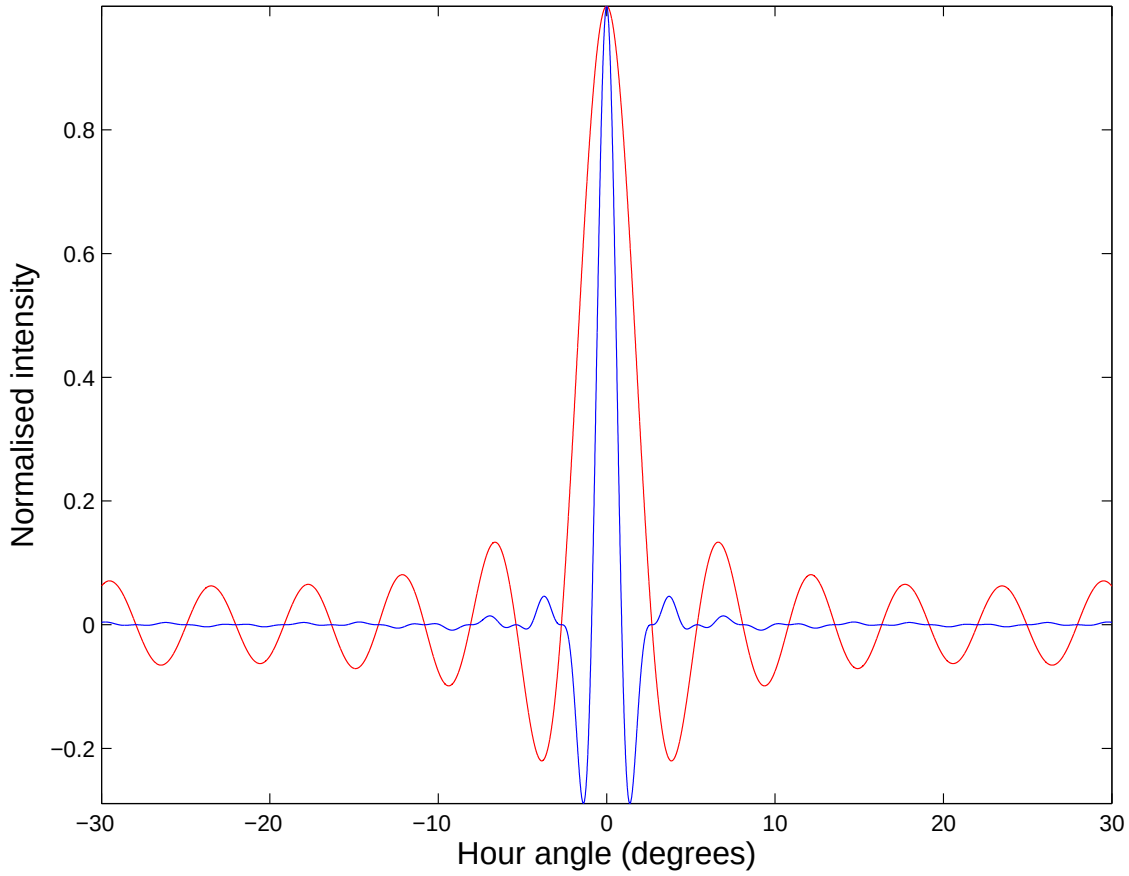

Fig. 2.10: The Figure shows the simulation of the group and interference pattern of the GRIP at 40 MHz. Grating lobes are not seen at 40 MHz ($\lambda = 7.5$ m), it is because the baseline length between any two antenna elements in a group is 10 meters, which is close to the observing wavelength. The red line shows the group pattern and the blue line is the interference pattern of the array.

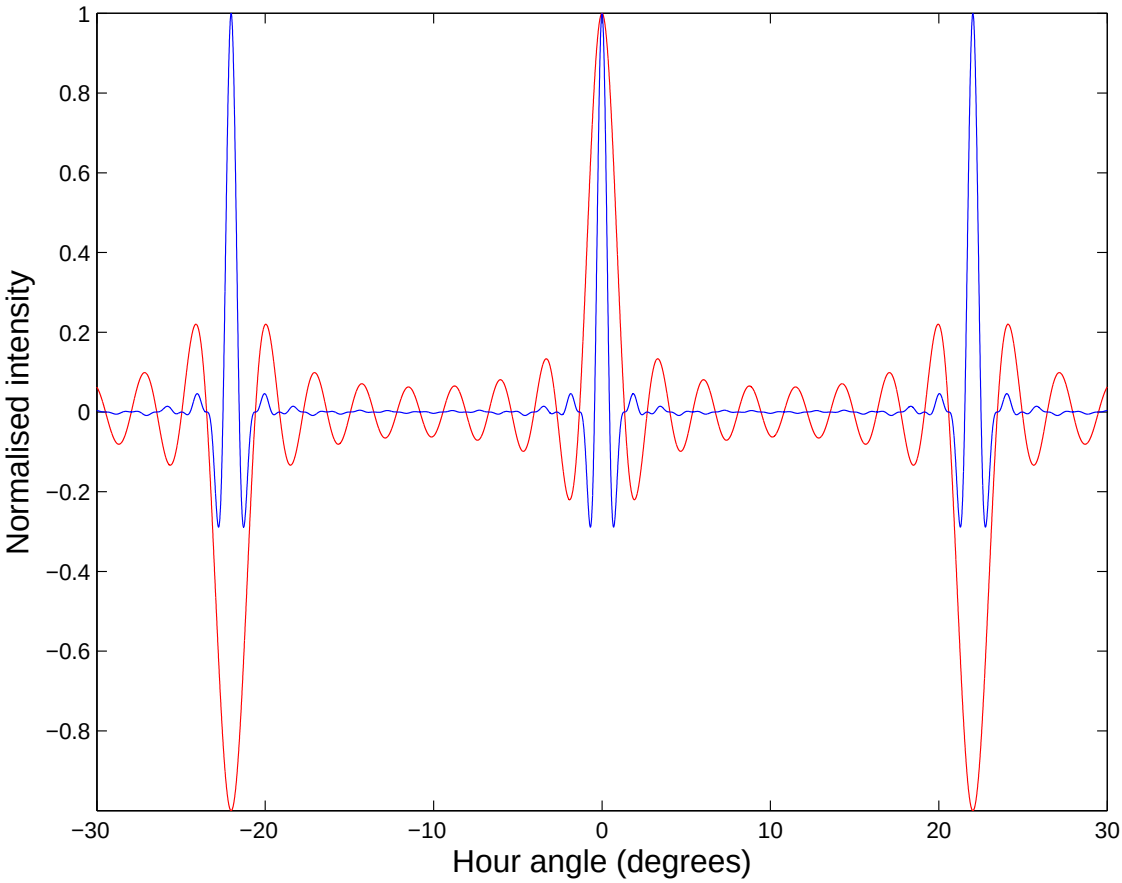

Fig. 2.11: Figure shows the simulation of the group and interference pattern of the GRIP at 80 MHz. Since $d/\lambda \gg 1$ the grating lobes are seen at 80 MHz. The red line shows the group pattern and the blue line is the interference pattern of the array.

and West lobes respectively. The lobe which is pointing towards to zenith is called a main lobe (M_3). Note that E_1 and W_5 are the lobes formed with large hour angle on East and West side respectively. The lobes E_2 and W_4 are formed adjacent to the main lobe (i.e. short hour angles). Note that the number of antennas in major group A, C are 16, where as 8 for the case of group B. Such setup is free from any artifacts, since the beam pattern of major group A, C is with in the group pattern of B. Such a system improves the sensitivity and resolution without introducing any artifacts in the observations and reduces the cost of the instrument. Since the distance between the two lobes are dependent on the wavelength by carefully choosing the observing frequency it is possible to carryout the multi frequency observations. Also during the null of one frequency grating lobes of other frequency is possible. Therefore by tuning the receiver system timely it is possible to carryout the multi frequency observations of the solar corona and observe the corona for longer duration everyday.

2.7 Analog receiver system

The signals from group A, B and C are brought to the receiver building using a low loss coaxial cables whose attenuation is 2 dB per 100 meters at 100 MHz, are processed separately in the receiver building. Firstly, the channel output passes through a Walsh switch which avoids the cross-talk between the different channels and DC offsets due to the A/D converters (see section 2.9.4). The modulated output, which was demodulated in correlator using Ex-OR gate (74LS86) is diverted to the front end analog receiver system. The schematic diagram of the analog receiver using the GRIP is shown in Figure 2.12. The analog receiver system used is similar to the one used in GRAPH [Ramesh et al., 1998]. The modulated output from Walsh switch of each group is filtered using a high pass filter whose cut off frequency is 50 MHz. Then, the output is low pass filtered using a filter whose cut off frequency is 150 MHz. In this way the spurious and interference

signals excluding 50-150 MHz bandwidth are suppressed. Using a power splitter the RF signal is splitted into 2 channels, one is connected to monitoring port, which is useful in checking whether signal from the group is as expected.

The second channel is connected to a mixer-1 which up/down converts the signals to RF+LO and RF-LO along with the corresponding harmonics, where RF is observing radio frequency and LO is the local oscillator frequency. In general, mixer has two inputs: (1) RF input (from antenna) and (2) the signal from local oscillator and a single output. Therefore the mixer-1 is connected with RF output and 1st local oscillator (LO-1) input. In the case of multi-frequency observations two local oscillators with two different frequencies are used named as LO-1a and LO-1b. These two local oscillator are connected to a RF switch which swaps between the two inputs and gives single output, which is considered as a LO-1. Note that in latter case time resolution goes down by a factor of 2 and every alternate sample corresponds to a single frequency. By changing the LO-1 from 210 to 320 MHz, GRIP can be tuned to operate in 40-140 MHz range. The down-converted signal is called intermediate frequency (henceforth IF-1) is further filtered using a band pass filter with center frequency (f_c) is 170 MHz and bandwidth (Δf) of 4 MHz. Therefore, the inter modular products are eliminated and only desired frequency is allowed. The filtered output is amplified with a amplifier of gain $\approx$ 28 dB. The amplified signal and the fixed frequency 2nd local oscillator (LO-2) are connected to mixer-2, which further down-converts the signal to intermediate frequency (IF-1) with a center frequency of 10.7 MHz. Note that at this stage LO-2 has fixed frequency of 180.7 MHz and the RF input was already tuned to 170 MHz. The IF-2 again produces the inter modular products which are filtered using a band pass filter with center frequency 10.7 MHz and bandwidth of 3.5 MHz. The filtered output is again amplified with a amplifier of gain 28 dB. The processed signal is further filtered using a low pass filter whose cut off frequency is (f_l) is 10.7 MHz and then further amplified the signal using amplifier of 28 dB. In this process inter modular products are completely filtered out. The amplified

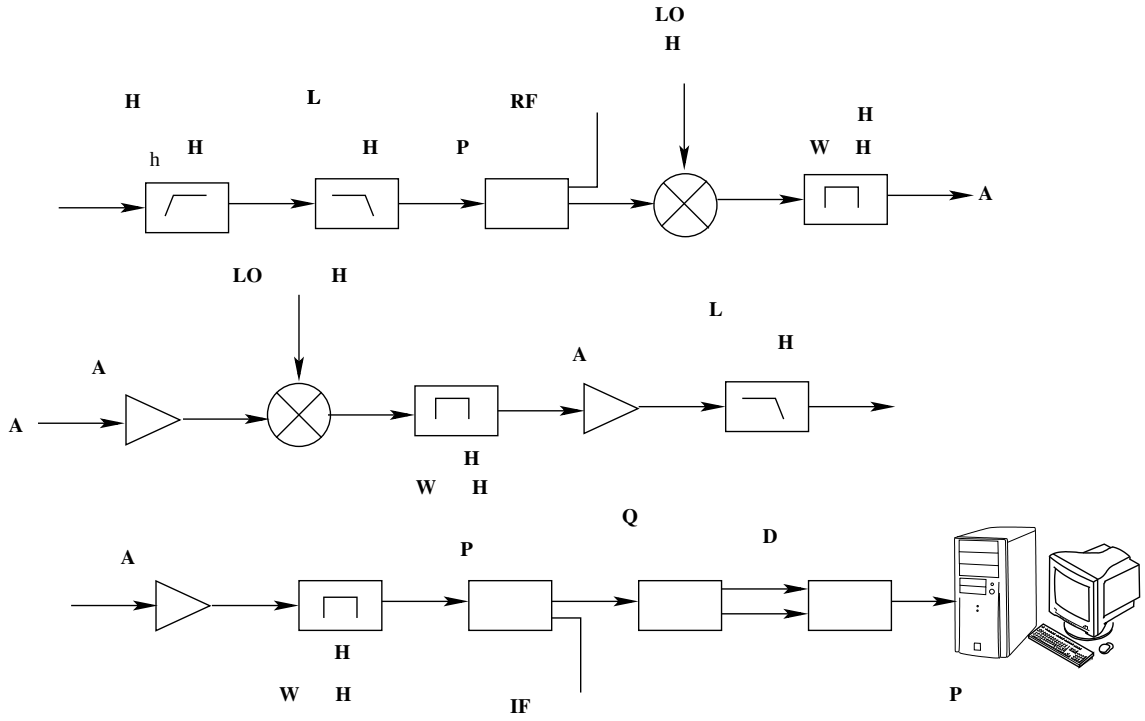

Fig. 2.12: Schematic diagram of the front end analog receiver system used in GRIP is shown in the Figure. This receiver system is similar to the one used in Gauribidanur Radio Heliograph expansion array.

signal is then passed though a narrow bandwidth of $\approx$ 1 MHz band pass filter whose center frequency is at 10.7 MHz. The final intermediate frequency output is split into two channels using a power splitter; one is feed to IF monitoring port and the second one is connected to quadrature power splitter. Quadrature power splitter gives the two outputs: (1) In phase cosine output and the (2) 90^o phase shifted sine output. The sine and cosine channels are given to the digital receiver. In the same fashion another two channels are processed and feed the sine and cosine channels to the digital correlator in a proper sequence. In this way using a double mixing analog receiver system by changing the LO-1, different frequency of observations are carried out without changing the RF components in the system unlike single mixing system. Also at a time multi frequency observations are carried out by changing the LO-1a and LO-1b.

2.8 Digital receiver system

In general, multiplying interferometers measure the mutual coherence function between the two antennas/groups of antennas which describes about the spatial coherence function between them. It is known that electric field due to the presence of the radio source in the sky induces the voltages in the antennas/group of antennas. Therefore by cross-correlating the output signal of the antennas mutual coherence function can be measured, which is also called visibility function. To measure the visibility the correlators are used in general. At present, there exists digital as well as analog correlators. The digital correlators are preferred because of their possibility of effective delay compensations where ever it is required, and high accuracy and easy handling compared with the analog correlators. In GRIP/GRAPH, one bit correlators are used in which the amplitude information is lost and has reduction in sensitivity takes place ($\approx 66\%$) compared with the analog case [Van Vleck and Middleton, 1966]. Although the one bit digital correlators are used because it can be implemented in simple digital logic and yields greater stability than the analog correlators.

The cosine and sine channels of the analog receivers of the 3 groups are connected to the digital correlator unit. This unit, samples, quantizes, correlates the signal and finally stores into a personal computer. Firstly, the cosine and sine IF outputs ($f_c \approx 10.7$ MHz and $\Delta f = 1$ MHz) from analog receiver are quantized to two levels (+1,0) using a zero crossing detector. The high speed comparator (AD790) is used for this purpose and its output is TTL either 'high' or 'low'. The reference voltage of the comparator sets the output to either 'high' or 'low', depending on whether the input voltage is higher or lower than the reference voltage respectively. In the present case 'ground' level is considered as reference voltage. The comparator output is sampled using a D-type flip-flop (74LS74) at a rate of 2.04 MHz which is higher than the required sampling rate 2 MHz (which is double of IF bandwidth, 1 MHz in the present case). It is known that to reconstruct any

signal it has to be sampled atleast two times of the bandwidth of the signal (sampling period $T_s = (2\Delta f)^{-1}$. If the sampling frequency is exactly equals to $2\Delta f$, then it is said that signal is Nyquist sampled. If any signal is sampled at less than the Nyquist rate, it is called 'under sampling'. Such under sampling causes the distortion while reconstructing the actual signal. The distortion due to the under sampling is called aliasing effect. Over sampling of the signals cannot create any distortions instead it decreases the quantization noise. In the present case the 5th harmonic of the sampling clock falls exactly at the outer edge of the IF band i.e. 11.2 MHz so that we get entire 1 MHz bandwidth. Walsh demodulation, which was modulated using a Walsh switching before the analog receiver is done using a Ex-OR gate (74LS86) [Ramesh et al., 1998]. The delay compensation between the two groups due to the low loss RF cable lengths brought to the receiver building from the field are compensated by using a combination of shift registers (74LS164) and multiplexers (74LS151). The maximum possible delay is 7.5 μ s which corresponds to the path length of 2250 meters. Correlators used in the GRAPH and GRIP are build using the chips primarily designed for the Nobeyama radioheliograph (NRH) which is described in Appendix-I. Schematic of the two element correlator is shown in the Figure A.2. The sampled and Walsh demodulated signal is fed to the correlator chip which provides the correlated output. The complex correlation of the cosine correlator and sine correlator is done using the equations-2.19 and 2.20.

$$C_1 \oplus C_2 + S_1 \oplus S_2 \tag{2.19}$$

$$C_1 \oplus S_2 + S_1 \bar{\oplus} C_2 \tag{2.20}$$

Where C_1, C_2, S_1, S_2 are the cosine and sine channel inputs, which are fed to the digital correlator and they corresponds to two different antenna groups. $\oplus$ and $\bar{\oplus}$ represents the Ex-OR and Ex-NOR operations respectively. The correlated outputs are integrated over a 256 ms which is called integration time. Integration is done using a digital

counter which counts over an integration time. Then the data is stored to a memory unit which is further read to the personal computer. In GRIP, correlation of group outputs A and B, B and C are done. For every baseline both cosine and sine channels are recorded in a particular fashion.

2.9 Instrumental errors

As mentioned in the section 2.6 baseline length between the antennas, relative amplitudes, phase variations of individual antenna elements create artifacts in the group pattern. Some of such artifacts are described in this section. Observations with interferometric arrays always suffer problems due to gain variations of the different RF components used in the front-end analog, back-end digital receiver systems and other spurious interferences like ground reflections, off-axial effects, atmospheric variations etc. The electric field of a linear array similar to the one shown in Figure 2.8 with n number of antennas can be written as,

$$E_g = A_1E_1 + A_2E_2\ e^{j\psi+\delta_1} + A_3E_3\ e^{j2\psi+\delta_2} + A_4E_4\ e^{j3\psi+\delta_3} + ... + A_{n+1}E_{n+1}e^{jn\psi+\delta_n} \quad (2.21)$$

where E_g is the total electric field of the all antennas after the addition, $E_1, E_2, E_3, E_4, ...E_n$ are the maximum electric fields of the individual antenna elements, $A_1, A_2, A_3, A_4, ...A_n$ are the amplitudes of individual outputs of the antennas after the RF components. $\delta_1, \delta_2, \delta_3, \delta_4, ...\delta_{n+1}$ are the phase fluctuations of the individual antenna outputs before combining them.

2.9.1 Amplitude variations

In interferometric arrays the amplitude variation of the individual elements of a group distort the group pattern or a 'beam' of the group. From simulations it was found that

when there are no other errors, the variation of the amplitude start affects the group pattern if the standard deviation of the amplitude variation is approximately half of its rms value. However along with the phase fluctuations, the amplitude variations distort the group pattern. Therefore while building the arrays, relative amplitude of the outputs of the individual elements have to be maintained constant. In GRIP such effects are nullified by using similar antenna elements, RF filters and pre-amplifiers. Also the length of RF cable of every antenna was maintained with equal length of 50 meters to avoid amplitude variations.

2.9.2 Phase fluctuations

The relative phase differences introduced by RF components used in the array like: RF cables, RF filters, RF amplifiers and power combiners etc., distort the group pattern. The distorted group pattern is simulated by assuming the amplitude rms variation ≈ 10 dBm and the rms phase fluctuations $\pm 180^o$ and is shown in Figure 2.13 at 80 MHz. In practical cases, even the physical cable length is maintained constant for all the channels of the interferometers the phase variations exist due to the manufacturing defects. The rms value of such phase variations are $\pm 180^o$. Therefore those errors has to be minimized. This can be achieved by applying a phase calibration technique (see section 2.10).

2.9.3 Errors involved in interference polarimeter arrays

In correlation interferometry, while multiplying two antenna groups/antennas other than the previously discussed errors (within the group), presence of other RF components in front and back end receiver systems also introduces the errors. The phase introduced due to such components is called instrumental phase ϕ_{ins}. While measuring the state of polarization the linearly polarized antennas have to be mounted in different orientations. The extra phase difference introduced due to the improperly aligned linearly polarized

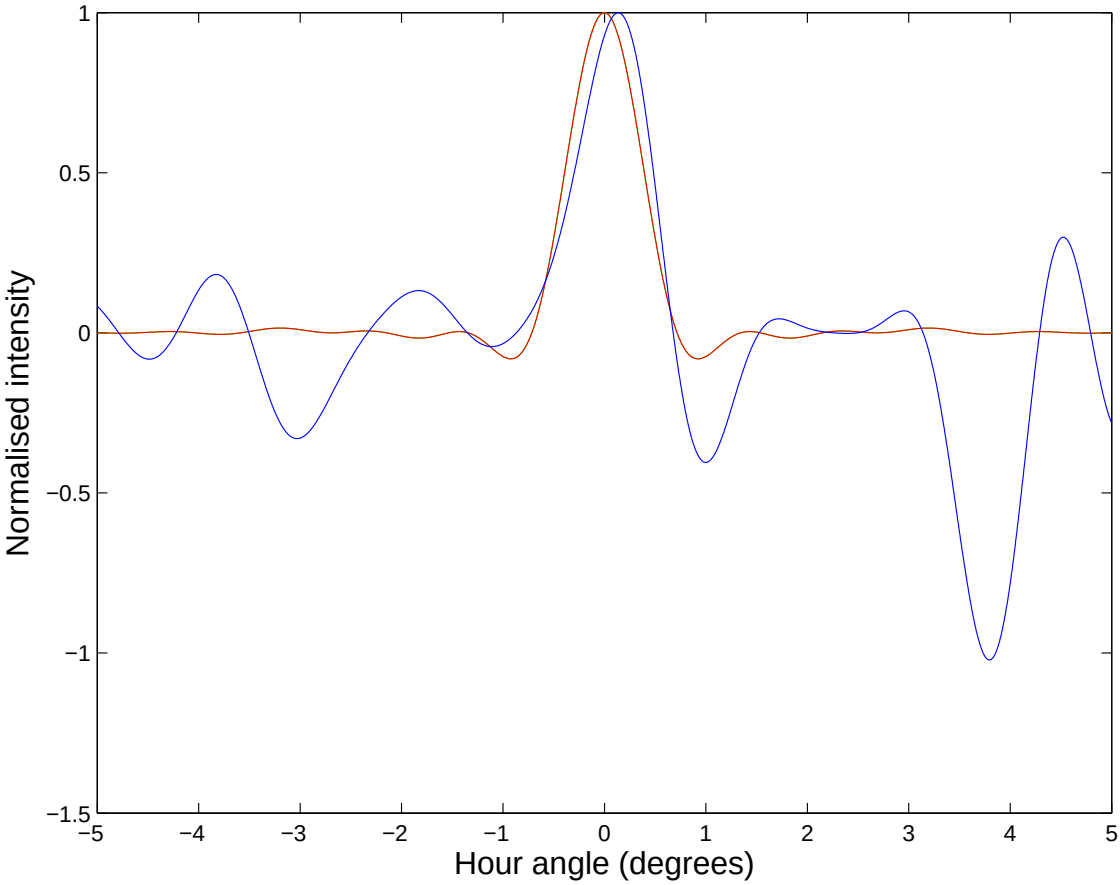

Fig. 2.13: Simulation of group pattern of the GRIP is shown in the Figure. Note that the pattern is distorted because the simulations are carried out by assuming the rms phase fluctuations $\pm 180^o$) and the rms variations of the amplitude is 10 dBm. The red color plot shows the group pattern when the amplitude and phase errors are zero and the blue plot is in the presence of the mentioned errors (see section 2.10).

antennas is ϕ_{ori} and the extra path difference traveled by the rays due to the baseline length between the antennas are called the geometrical phase ϕ_{geo}. The power pattern, $P(\phi)$ of the two element multiplying interferometer including the errors discussed above can be written as,

$$P(\phi) = E_1(\phi)E_2(\phi)cos(\psi + \phi_{geo} + \phi_{ins} + \phi_{ori}) \tag{2.22}$$

where $E_1(\phi)$ and $E_2(\phi)$ are electric fields of the group patterns. In GRIP, such errors are carefully removed by maintaining the relative phase difference (within $\pm 5^o$) across all the three channel outputs. The geometrical and orientation phase errors are minimized sufficiently to avoid the artifacts in GRIP.

2.9.4 Walsh switching

In the receiver system there will be a cross-talk between the different channels even after careful shielding of the IF and A/D converters. To eliminate such cross-talk, RF outputs from the 3 groups are switched using an electronic switch which is controlled by a Walsh function signal. Switching period of various groups are different and the fraction of the time period was integrated. Such a system average the cross-talks to zero since the latter is correlated to positively or negatively in either half of the integration time. The sequence of the switching is removed at the output of the sampler using the same Walsh function so that the possible DC offset errors in the A/D converters also will be eliminated. Since the integration time is smaller than the fringe frequency, the spurious signals whose amplitude is same over a Walsh cycle will be averaged to zero [Ramesh et al., 2006b, Thompson et al., 2007]. In GRIP, the integration time of the data obtained for Stokes I and V channels is 256 ms which is smaller than the time period of the interference fringe at 80 MHz is $\approx$ 7 minutes. So using the Walsh functioning the spurious signals due to the cross talks as well as DC offsets in the correlations are minimized in the case of GRIP. Use of Walsh

minimizes the cross-talks and DC-shifts in A/D converter in the receiver system [for more details see Ramesh et al., 2006b].

2.10 Calibration techniques

2.10.1 Instrumental calibration technique

Generally in order to get the actual flux of the observed source, one need to remove the artifacts introduced by the instrument like amplitude and phase variations as previously mentioned. These variations are eliminated by using the phase equalization technique for all the cables used in different channels of the polarimeter. The amplitude variations are eliminated by using identical RF elements in different channels and also by maintaining the cable lengths of different stages of different channels same. Other than amplitude variations, phase errors have to be eliminated. In general, phase equalization technique is, measurement of the relative phase difference between the RF cables and other RF components and bring out them to a constant relative phase difference among the cables at respective stages of the interferometer. All the co-axial cables used in GRIP array are maintained at constant length. Even after the physical length of the co-axial cable is maintained constant, there will be a change in electrical length because of the manufacturing defects. Such defects cause primarily the phase variations. The reflection coefficient (ρ) and the phase (Θ) of the coaxial cables (50 meters length) used in GRIP to feed the antenna signal (after pre-amplifier) to the group centers are measured using the experimental setup shown in Figure 2.14. In this experimental setup, the signal from the signal generator of frequency 110 MHz is feed to the input port 'A' of directional coupler. The coupling signals (port 'C' and 'D') from the directional couplers are connected to port 'a' and 'b' of the vector voltmeter respectively. The 'cable under test' (CUT) is connected to the port 'D' of the directional coupler and other end of the coaxial cable

is left open. Now by feeding the signal to port 'A', the reflection coefficient ρ_1 and the phase (Θ_1) values are noted which are shown in Table 2.3. It is noticeable that the Θ_1 is varying $\approx \pm 180^o$. In second step, without altering the system and by replacing other cable in place of 'CUT', the reflection coefficient and phase of the signal is measured. Next, the 'CUT' was chopped step by step till the reflection coefficient and phase arrives to a carefully chosen constant value. Similarly all the cables are bought to a constant reflection coefficient and phase. After applying this technique to all the cables, the Θ_2 and ρ_2 values remained constant (see Table 2.3). In third step, using the phase calibrated coaxial cables, after adding the RF connectors once again the experiment was repeated and measured the Θ_3 and ρ_3 which are shown in the Table 2.3. Note that ρ_1, ρ_2, ρ_3 are the reflection coefficients and Θ_1, Θ_2, Θ_3 are the phase of the signal measured in step 1, 2 and 3 respectively.

Table 2.3 reveals that for all the cables after the calibration, the phase error is $\lesssim 2^o$. Using the simulations it is found that rms phase errors introduced by the different components with $\lesssim 10^o$, will not affect the group pattern. Therefore in GRIP such errors due to the phase variations are minimized. Simulation shows that after the phase equalization and even in the presence of the rms phase errors of the order $\approx 2^o$, group pattern coincided with the pattern of ideal case (see Figure 2.15). Observations of the different calibrator sources in the transit mode (hour angle $\approx \pm 1.5^o$) match with the simulations shown in the Figure 2.15 at 80 MHz. Figure 2.16 show the observed time profile of Virgo-A at the same frequency. The declination of the above source is 12 N which is close to the local zenith at GRO (14 N). Figure 2.15 shows observations of other calibrator source, Cassiopeia-A, at 80 MHz. The declination of this source is 59^o N. A comparison of 2.16 and 2.17 with 2.15 indicates that the group pattern remains nearly the same at different declinations. Note that the comparatively larger width of the time profile of Cassiopeia-A is due its larger declination.

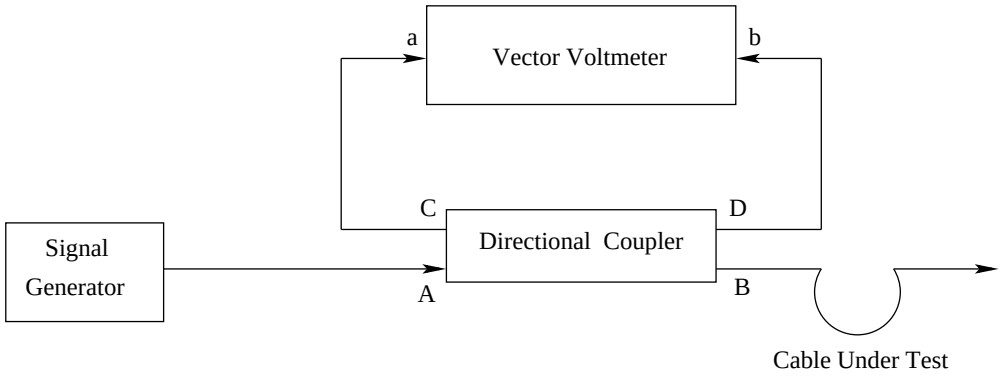

Fig. 2.14: The Figure shows the experimental setup used in phase equalization. Although the RF cables have the same physical length, there exists a phase difference among the cables. It is because of difference in electrical lengths due to various regions. Such phase difference is corrected by chopping the 'cable under test' step by step till it reaches to a constant phase and reflection coefficient. By repeating the same experiment, for all the coaxial cables used in GRIP, a constant phase difference among the cables was maintained.

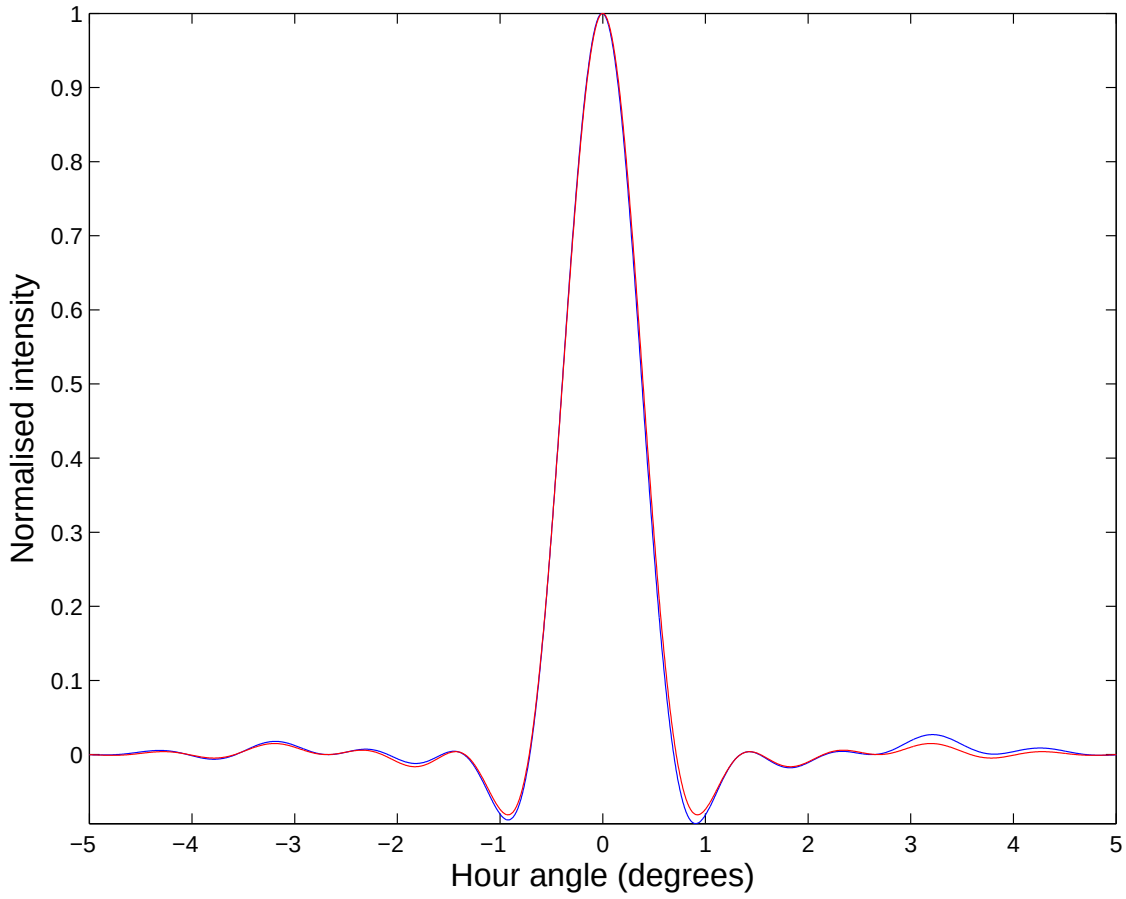

Fig. 2.15: The Figure shows that the simulation of the group pattern of the GRIP array. When the rms of the amplitude and phase fluctuations of the signal are about 2 dBm and 5^o respectively, the simulated plot approximately matches with the ideal group pattern. Note that in the Figure, the red and blue color plots correspond to the ideal group pattern and the group pattern after the phase equalization of individual elements in the GRIP respectively.

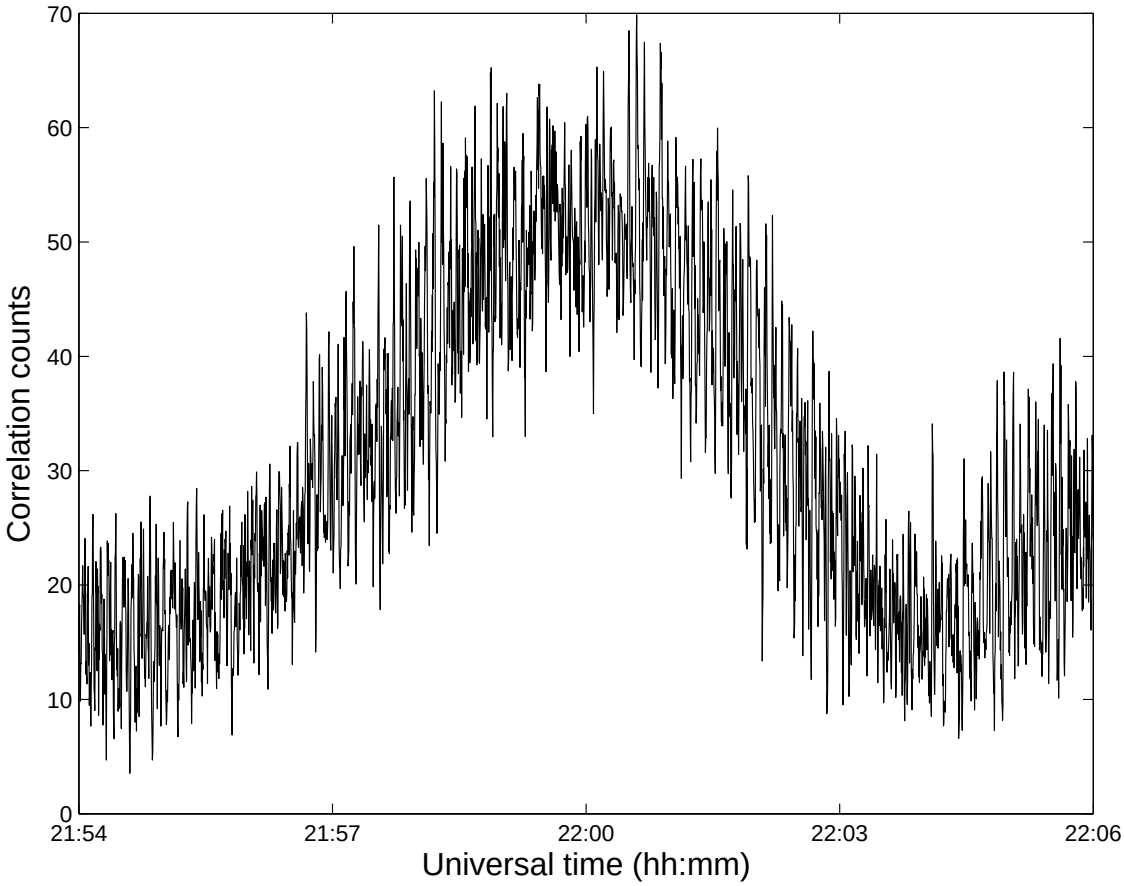

Fig. 2.16: Figure shows the observed time profile fo the Virgo-A at 80 MHz on 09 February 2013. RA and dec of the Virgo A is 12:31:18 (hh:mm:ss) and 12^o N (which is close to the zenith 14^o N at GRO) respectively. Note that the observations of the Virgo-A is similar to the simulations shown in the Figure 2.15.

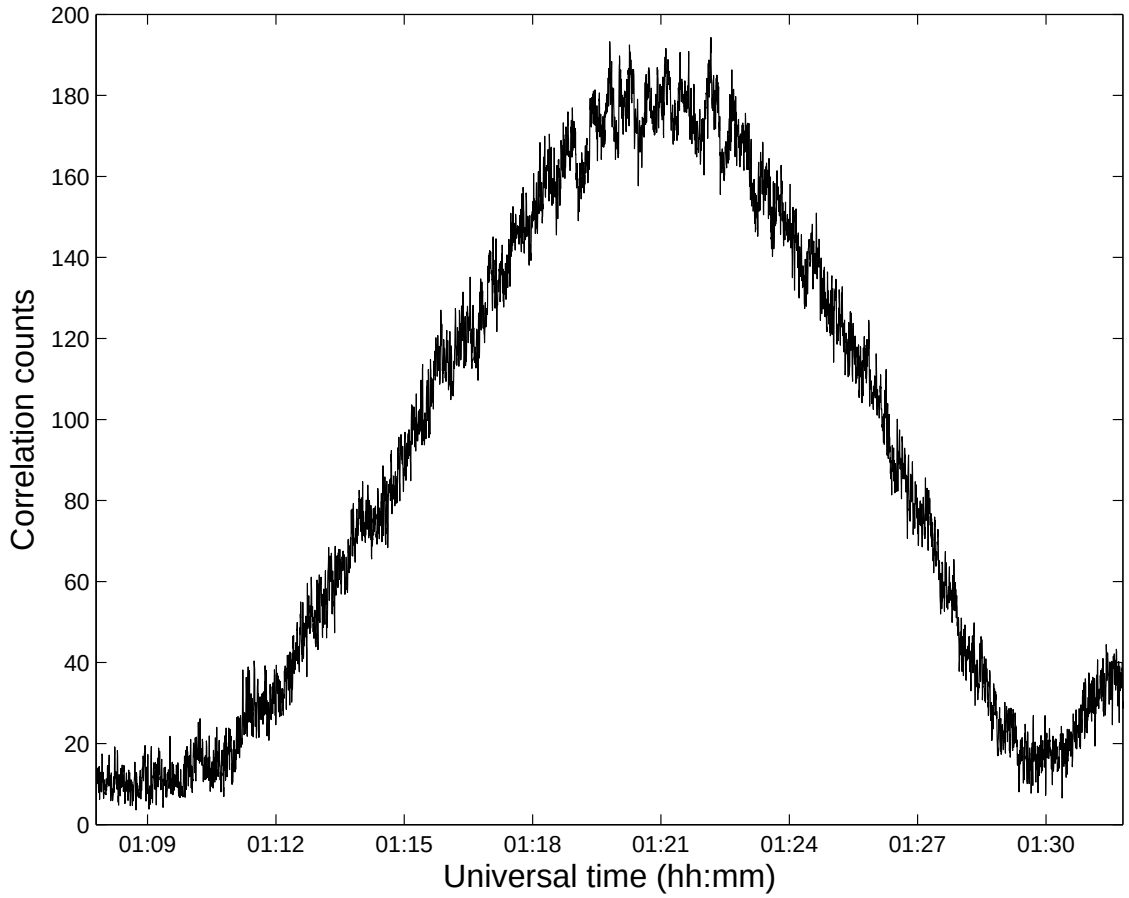

Fig. 2.17: Figure shows the observed time profile of the Cassiopeia-A at 80 MHz on 04 June 2013. RA and dec of the Cassiopeia-A is 23:23:51 (hh:mm:ss) and 59^o N (which is far away from the zenith 14^o N at GRO) respectively.

Table 2.3: The reflection coefficient and the relative phase difference among the co-axial cables used in the GRIP.

Cable No.	ρ_1	Θ_1	ρ_2	Θ_2	ρ_3	Θ_3	Cable No.	ρ_1	Θ_1	ρ_2	Θ_2	ρ_3	Θ_3
1	0.71	-126.3	0.61	155.9	0.99	-0.3	23	1.76	-9.3	0.61	156.1	0.99	-0.5
2	0.78	-96.5	0.6	157.3	1	0	24	0.72	-105.1	0.61	155.9	0.99	0
3	0.84	-4.8	0.61	156	0.99	-0.4	25	0.84	-27.5	0.68	156.2	0.99	-1
4	0.82	-75.2	0.6	155.3	0.99	0	26	0.65	175.6	0.65	156.7	0.99	0
5	0.99	-70.9	0.61	155.5	0.99	-0.9	27	0.64	-159.6	0.63	155.2	0.99	-0.7
6	0.7	-151.8	0.6	155.1	0.99	-0.5	28	0.84	-44.9	0.58	155.6	0.99	-0.3
7	0.84	19.3	0.63	155.9	0.99	-0.5	29	0.9	-54.1	0.6	155.2	1	-1.2
8	0.86	-55.5	0.61	155.3	0.99	-0.4	30	0.84	5.1	0.62	155.1	1	-1
9	0.84	-17.2	0.61	155.1	1	0	31	0.88	-35.1	0.77	154.5	0.99	0
10	0.82	-117.1	0.78	158	0.99	1	32	0.83	-52.2	0.61	155.1	1	0
11	0.86	-54.5	0.74	155.1	0.99	-0.9	33	0.78	-78.8	0.61	155.6	0.99	-0.5
12	0.85	-36.8	0.63	155.9	1	-0.3	34	0.79	-73.3	0.59	155.2	0.99	-0.4
13	0.93	-54.5	0.65	156.4	1	0.4	35	0.83	-1.3	0.63	155.7	1	-0.8
14	0.96	-103	0.79	156.2	0.99	-0.7	36	1.1	-83.3	0.59	155.5	0.99	-0.1
15	0.87	-41.2	0.77	155.1	1	0	37	0.87	-100.5	0.62	155.9	0.99	-0.1
16	1.39	22	0.68	156.3	0.99	-0.3	38	0.7	163.4	0.61	156	0.98	-0.2
17	0.89	-63.1	1.02	155.9	0.99	-0.1	39	0.92	-37.6	0.59	155.4	0.99	-0.7
18	1.02	-91.9	0.6	156	0.99	0.5	40	0.84	-0.9	0.6	155.2	0.99	-0.6
19	0.91	-81.9	0.61	156.1	0.99	0.2	41	0.83	54.1	0.77	156.2	1	-1
20	0.82	-112.4	0.64	155.1	0.99	-1.1	42	0.89	-14.8	0.61	155.5	1	-0.1
21	0.89	-112.3	0.87	155.3	0.99	-1.8	43	0.8	-64	0.61	155.7	0.99	-0.9
22	0.94	-135.9	0.61	155.1	0.99	-0.5	44	0.84	-65	0.61	155.1	1	-0.9

2.10.2 Flux calibration technique

In polarimetric observations one need to minimize the instrumental errors like cross talks between antennas, reflections from the ground and off-axial effects etc [Ramesh et al., 2008]. One way of removing the artifacts is the calibration technique in which actual flux of target source is estimated by observing the circularly polarized sidereal sources whose flux is constant over longer time. Since, there are no circularly polarized strong sources available at these frequencies atleast at GRO, the instrument has to be carefully designed by eliminating the errors discussed in section 2.9. Observations of the randomly polarized calibrator sources/weakly linearly polarized sources reveal that the instrumental errors found are negligible in both Stokes I and Stokes V channel. For example Cassiopeia-A, Cygnus-A, Taurus-A, Virgo-A are few strong radio sources whose flux is invariant through out the year. The flux densities of the these calibrator sources are revised using the well established equations mentioned in Kellermann et al. [1969], Braude et al. [1970], Baars et al. [1977], Borkowski et al. [1980], McLean and Labrum [1985]. The calibrator sources whose declination is close to the latitude of the GRO were chosen.

For example, observations of the Cygnus-A observed using GRIP on October 16, 2012 is shown in Figure 2.18. Two plots represent, the Stokes I and Stokes V observations of the same. It has a total flux density of $\approx$ 16668 Jy at 80 MHz. Significant degree of linear polarization of Cygnus (8 percent at 3 cm) supports that the emission mechanism of the source is a synchrotron emission which is responsible for the radio emission. It is also found that the degree of linear polarization decreases rapidly with increase in wavelength to about 1.5 percent at 5 cm. The degree of linear polarization is even less at longer wavelength compared to the mentioned wavelengths [Hollinger et al., 1964, Kraus, 1973]. So it is expected that the Cygnus-A is a randomly polarized source at 80 MHz (3.75 meters). From the observations of the GRIP which is shown in Figure 2.18, it is clear that there is no significant deflection of Cygnus-A in Stokes V, where as a good deflection in Stokes I. This is the case of Cygnus-A observations everyday and

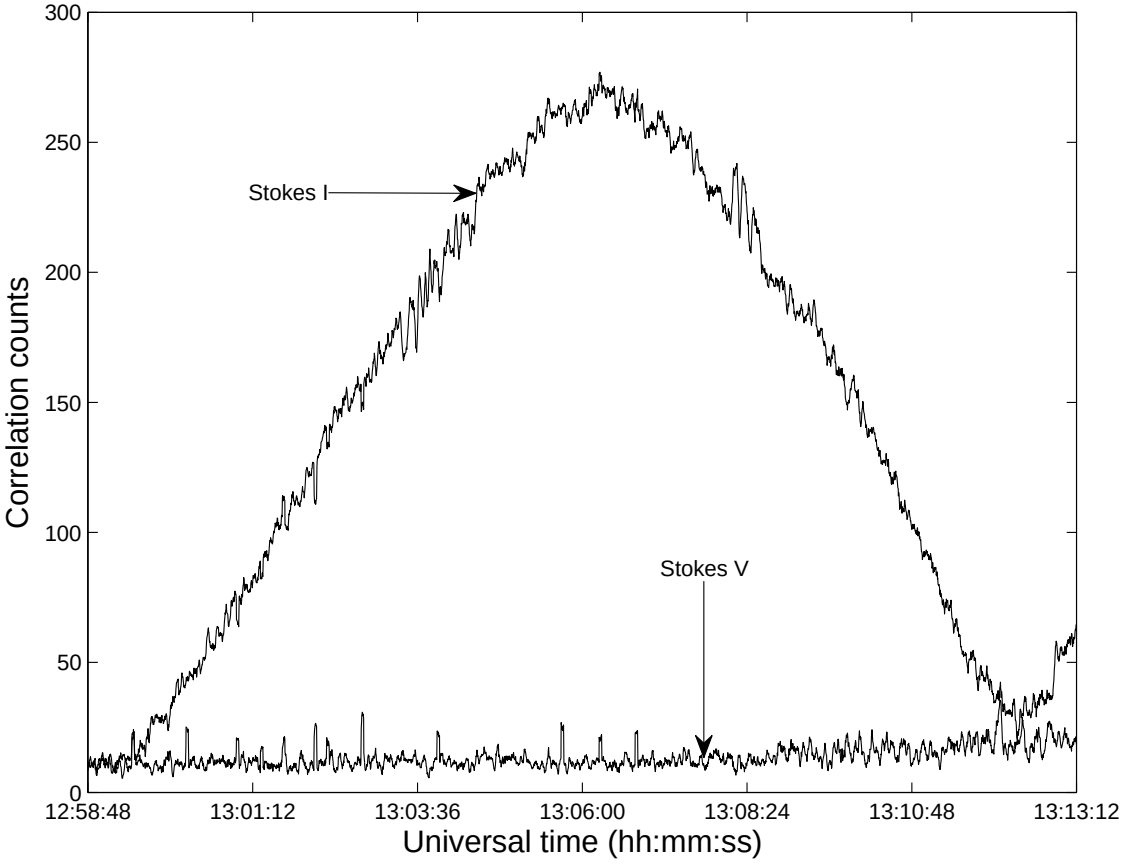

Fig. 2.18: The Figure shows the observations of randomly polarized calibrator source Cygnus-A in Stokes I and V modes. The observations are carried out using GRIP on 16 October 2012 at 80 MHz during its transit at GRO. The plot is generated by averaging the 4 samples. It is clearly seen that there is no deflection in Stokes V profile, which means that instrumental errors (like cross talk effects) are absolutely negligible.

is as expected and agreeing with the above mentioned past polarization measurements. Therefore based on these observations it is concluded that instrumental errors in Stokes V and Stokes I channels are negligible. Also absence of deflection in Stokes V confirms that the instrumental errors and other artifacts like circular polarization introduced by different components, cross-talks of antennas, ground reflection or off-axial effects are negligible.

2.11 Data analysis and estimation of true flux density

In a correlation interferometry the mutual coherence function was found which describes about the spatial coherence of the source. According to the Van Cittert Zernike theorem the Fourier transform of the visibility function gives the information of the brightness distribution of the source. In practical application cross-correlation of the two antenna outputs, called the visibility function (V_{ij}) is measured. The visibilities of in phase cosine V_{ij}^{c} and with 90^{o} phase shifted sine visibilities V_{ij}^{s} are measured for each baseline. Therefore the total amplitude corresponding to the respective baseline is measured using the equation 2.23

$$I_{ij} = \sqrt{(V_{ij}^{c})^2 + (V_{ij}^{s})^2} \tag{2.23}$$

The phase related to the fringes is obtained using the equation 2.24

$$\phi_{ij} = tan^{-1}\left(\frac{V_{ij}^{s}}{V_{ij}^{c}}\right) \tag{2.24}$$

The uncorrected instrumental errors can be removed by observing the calibrator sources. The calibrator sources are selected which are strong and close to the target source (Sun) and with known consistent flux density over a longer duration. If the known flux density of the calibrator source is $(S^{true})_{cal}$, observed correlation counts of the same calibrator source and the target source (Sun) are $(C_{ij}^{obs})_{cal}$, $(C_{ij}^{obs})_{Sun}$ respectively. Then the true flux density (S_{ij}^{true}) of the target source is estimated using the equation 2.25.

$$(S_{ij}^{true})_{Sun} = (C_{ij}^{obs})_{Sun} \times \frac{(S^{true})_{cal}}{(C_{ij}^{obs})_{cal}} \tag{2.25}$$

The estimated flux density has the units of Jansky (Jy) which is named after a scientist Karl Jansky and 1 Jy is defined as 10^{-26} Watt m^{-2} Hz^{-1} sr^{-1}.

Total visibility estimated for the baseline of group B and C is equal to half of the

total brightness of the observed source as the antennas accept only one polarization. Since the case is same for the calibrator source, by making use of the equation 2.25 the true flux density (Stokes I) of the target source is estimated. Since antennas in different groups (A, B and C) have been equalized for their gains, Stokes V flux density (observed correlation counts in the multiplication between group A and B) is estimated using correlation counts of the Stokes I (correlation counts between groups B and C).

2.12 Performance study of GRIP array

2.12.1 Noise contributions

At radio frequencies there are many noises that have to be considered. In general noise can be of two types (1) External noise and (2) Internal noise. External noise is due to the atmosphere (like lightening discharges, thunderstorms and other natural electrical disturbances), extra terrestrial noise (like solar noise due to the activity in the Sun, cosmic noise due to the radio sources) and industrial noise (automobiles, aircraft ignition, electrical motors, switching equipments, voltage leakages of electrical line, fluorescent lights, walkie-talkies etc). FM and TV broad casting also considered as interferences by the radio astronomers.

Internal noises are thermal noise which is due to the noise generated by the resistive components due to the rapid motions of the atoms or electrons inside the component. Such noise is called thermal noise/white noise/Jonson noise. Another kind of noise is Shot noise which is mainly in amplifying devices and virtually all active devices. It is due to the random variations in the arrival of electrons at the output electrodes [Kennedy et al., 2013]. However the dominant one is the thermal noise. In radio astronomy most of the cases noises are represented in terms of the temperature. A resistor at a temperature

(T) will have a power (P) due to the thermal electron motions in it. It is known that motion of thermal electrons create the currents and since the power is dependent on the square of the currents the absolute power is not zero [Jayaram et al., 2007]. So the power is defined in terms of temperature. The power measured at the terminals of the antenna is shown in equation 2.26, which is also called Nyquist formula.

$$T_a = \frac{P}{k} \tag{2.26}$$

where k is the Boltzmann constant and P is the power per unit frequency and T_a is antenna temperature. In the same way if the temperature is measured at the terminals of a radio telescope, it is defined as system temperature (T_{sys}). The power received at the output of a radio telescope is,

$$P_{total} = P_a + P_{sys} \tag{2.27}$$

Equations 2.26 and 2.27 gives the equation 2.28.

$$T_{total} = T_a + T_{sys} \tag{2.28}$$

Where P_{total} and T_{total} are the total power and corresponding temperature received at output of the radio telescope. The system temperature is contributed by many other forms of noise and they can be represented as a temperature. So the system temperature is given in equation 2.29

$$T_{sys} = T_{bg} + T_{sky} + T_{spill} + T_{rx} \tag{2.29}$$

where T_{bg} is due to the cosmic microwave background radiation (3 K) and also due to the galactic background, T_{sky} is noise contribution from the atmosphere, T_{spill} is noise contribution from the ground reflections and scatterings, T_{rx} is due to the receiver noise. However the noise figure of the pre-amplifier is $\approx$ 3 dB and total receiver noise temperature at 80 MHz is 600 K. At this frequency the sky noise is about 300 K. Therefore the system

temperature is around 900 K.

2.12.2 Minimum detectable flux of GRIP

Minimum detectable flux density (ΔS_{min}) is calculated using the equation 2.30 [Kraus, 1973]

$$\Delta S_{min} = \frac{2\ k\ K_s\ T_{sys}}{A_e\ \sqrt{\Delta\nu\ t\ n}} \tag{2.30}$$

Where, k is the Boltzmann constant ($= 1.38 \times 10^{-23}$ Joule K^{-1}), K_s is the sensitivity constant which depends on the receiver system used. For the correlation interferometer which includes one antenna and one receiver K_s is 0.71 [Kraus, 1973, p.258]. A_e is the effective collecting area of the antenna [$\approx 0.6 \times \lambda^2$ m^2], $\Delta\nu$ is the IF bandwidth [1×10^6 Hz], T_{sys} system temperature [K], t is the time resolution [256×10^{-3} s], n is the number of points averaged. At 80 MHz calculated minimum detectable flux density for the designed array is 500 Jy (5σ level) for 1 second integration time.

2.13 Summary and conclusions

GRIP is an instrument which is capable of observing the polarized radio signals from the solar corona and operated over the frequency range $\approx$ 150-30 MHz. The corresponding radio emission typically originate in the solar atmosphere over the radial distance range $\approx 1 - 2$ solar radii. At present observations in those heights are not there in other spectral window of electromagnetic spectrum. The GRIP, consists of 40 log-periodic dipole antennas and are arranged in 3 groups with different orientations. The three channels are processed separately using super heterodyne analog receivers. The cross-correlated output of the digital receiver is then read to the computer. Using the GRIP, observations of the different radio solar events/bursts and other calibrator sources are carried out in both Stokes I and V with improved sensitivity and time resolution.

Appendix A

Appendix

The IF input is sampled using a 1-bit digitizer circuit which is shown in the Figure A.1. As mentioned earlier the IF input is first quantized to two levels using a comparator which gives the TTL output of high or low depending on the reference voltage. In general ground is considered as the input reference voltage. Although in practical applications there will be some offset voltage which introduces the cross-talks in correlations. After the quantization, the signal is samples using a positive edge triggered dual D-type flip-flop (74LS74).

Then the output is passed through the delay circuits then to the correlator chip which is described subsequently in this section. The GRIP and GRAPH is specifically designed for observations of the solar corona in which solar radiation is strong enough so the loss in sensitivity due to usage of 1-bit correlators is not severe [Nakajima et al., 1993]. Also it is possible to regain the loss of amplitude information due to the usage of clipping of the input signal due to the zero crossing detector [Udaya Shankar and Ravi Shankar, 1990].

The correlator system was built using the correlator chip made by the Nobeyama radioheliograph, Japan. Each chip has 4 complex correlation units which can give 4

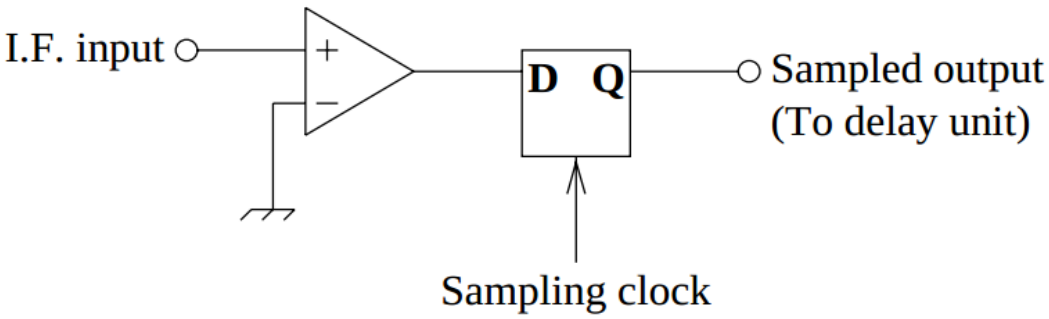

Fig. A.1: Schematic layout of the 1-bit digitizer is shown in the Figure. Image Credit: Ebenezer et al. [2001]

.

complex correlations from 4 groups of antennas. Each unit consists of three 4 bit parallel Ex-OR gates, one 4-bit parallel Ex-NOR circuit, two additional circuits, two integrator circuits, a latch and a multiplexer circuit. One unit of complex correlator chip is shown in Figure A.2. The complex correlations of the circuit are expressed in equations 2.19 and 2.20. Although 22 bit counter is used, during integration 6 LSBs are truncated and only 16 MSBs are used within the chip itself. Some more details of the complex correlators described in Ramesh et al. [2006a], Ebenezer et al. [2001].

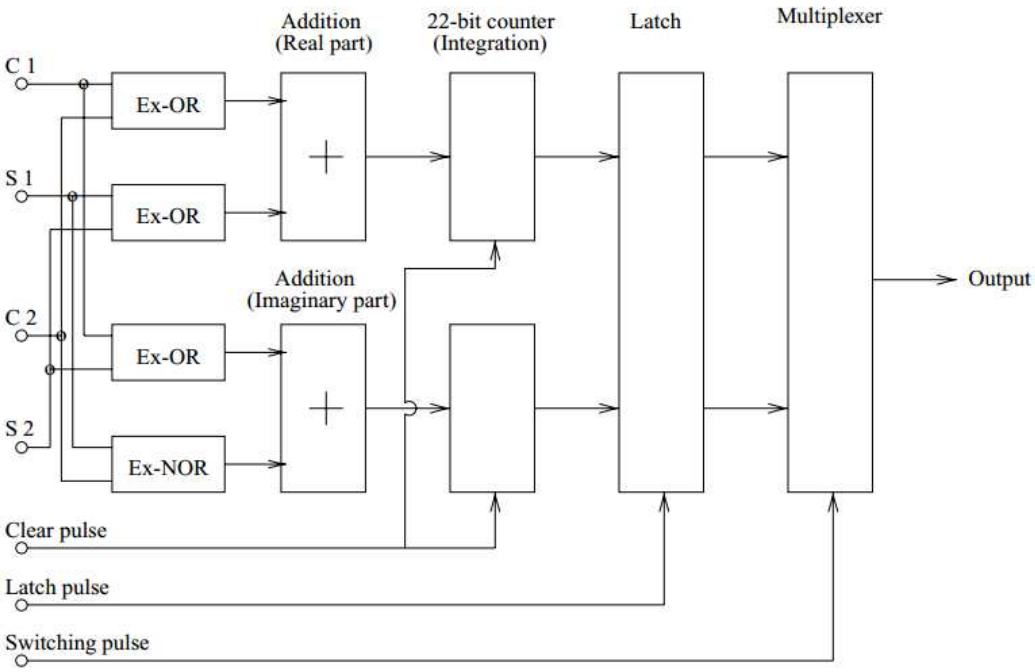

Fig. A.2: Schematic layout of the correlator chip is shown in the Figure. Image Credit: Ramesh et al. [2006a]

.

References

J. W. M. Baars, R. Genzel, I. I. K. Pauliny-Toth, and A. Witzel. The absolute spectrum of CAS A - an accurate flux density scale and a set of secondary calibrators. A&A, 61:99–106, October 1977.

C. A. Balanis. *Antenna theory : analysis and design*. 2005.

L. V. Blake and M. W. Long. *Antennas: Fundamentals, Design, Measurement*. SciTech Publishing, Inc, 2009.

K. M. Borkowski, P. Zlobec, and C. A. Zanelli. Problems of single-frequency meter-wavelength solar observations. Mem. Soc. Astron. Italiana, 51:247–261, June 1980.

S. Y. Braude, A. V. Megn, B. P. Ryabov, and I. N. Zhouck. The spectra of some discrete radio sources in 10 5000 MHz frequency range. Ap&SS, 8:275–322, August 1970. doi: 10.1007/BF00650891.

R. H. Duhamel and D. Isbell. Broadband logarithmically periodic antenna structures. In *IRE International Convention Record*, volume 5, pages 119–128, Mar 1957. doi: 10.1109/IRECON.1957.1150566.

E. Ebenezer, R. Ramesh, K. R. Subramanian, M. S. SundaraRajan, and C. V. Sastry. A new digital spectrograph for observations of radio burst emission from the Sun. A&A, 367:1112–1116, March 2001. doi: 10.1051/0004-6361:20000540.

R. J. M. Grognard and D. J. McLean. Non-Existence of Linear Polarization in Type III Solar Bursts at 80 MHz. Sol. Phys., 29:149–161, March 1973. doi: 10.1007/BF00153446.

T. Hatanaka. The Faraday Effect in the Earth's Ionosphere with Special Reference to Polarization Measurements of the Solar Radio Emission. PASJ, 8:73, 1956.

J. P. Hollinger, C. H. Mayer, and R. A. Mennella. Polarization of Cygnus a and Other Sources at 5 CM. ApJ, 140:656, August 1964. doi: 10.1086/147956.

Yi. Huang and Kevin Boyle. *Antennas: From Theory to Practice*. August 2008.

N. Chengalur. Jayaram, Gupta. Yashwant, and K. S. Dwarakanath. *Low frequency radio astronomy*. May 2007.

K. I. Kellermann, I. I. K. Pauliny-Toth, and P. J. S. Williams. The Spectra of Radio Sources in the Revised 3c Catalogue. ApJ, 157:1, July 1969. doi: 10.1086/150046.

George. Kennedy, Bernard. Davis, and S. R. M. Prasanna. *Electronic communication systems*. 2013.

J. D. Kraus. *Radio astronomy*. 1973.

J. D. Kraus. *Antennas*. 1950.

D. J. McLean and N. R. Labrum. *Solar radiophysics: Studies of emission from the sun at metre wavelengths*. 1985.

J. Nakajima, E. Otobe, K. Nishibori, H. Kobayashi, N. Tanaka, T. Saitoh, N. Watanabe, Y. Aramaki, T. Hoshikawa, K. Asuma, and T. Daishido. One-dimensional imaging with the Waseda FFT radio telescope. PASJ, 45:477–485, June 1993.

R Ramesh. Multi frequency observations of the outer solar corona with the gauribidanur radioheliograph. 1998b.

R. Ramesh, K. R. Subramanian, M. S. Sundararajan, and C. V. Sastry. The Gauribidanur Radioheliograph. Sol. Phys., 181:439–453, August 1998.

R. Ramesh, M. S. S. Rajan, and C. V. Sastry. The 1024 channel digital correlator receiver of the Gauribidanur radioheliograph. *Experimental Astronomy*, 21:31–40, February 2006a. doi: 10.1007/s10686-006-9065-y.

R. Ramesh, M. S. S. Rajan, and C. V. Sastry. The 1024 channel digital correlator receiver of the Gauribidanur radioheliograph. *Experimental Astronomy*, 21:31–40, February 2006b. doi: 10.1007/s10686-006-9065-y.

R. Ramesh, C. Kathiravan, M. S. Sundararajan, I. V. Barve, and C. V. Sastry. A Low-Frequency (30 - 110 MHz) Antenna System for Observations of Polarized Radio Emission from the Solar Corona. Sol. Phys., 253:319–327, December 2008. doi: 10.1007/s11207-008-9272-y.

K. Sasikumar Raja, C. Kathiravan, R. Ramesh, M. Rajalingam, and I. V. Barve. Design and Performance of a Low-frequency Cross-polarized Log-periodic Dipole Antenna. ApJS, 207:2, July 2013. doi: 10.1088/0067-0049/207/1/2.

R.K. Shevgaonkar. *Electromagnetic Waves*. Electrical & electronic engineering series. McGraw-Hill Education (India) Pvt Limited, 2005. ISBN 9780070591165.

A.R. Thompson, J. M. Moran, and G. W. Swenson. *Interferometry and Synthesis in Radio Astronomy*. 2007.

N. Udaya Shankar and T. S. Ravi Shankar. A digital correlation receiver for the GEETEE radio telescope. *Journal of Astrophysics and Astronomy*, 11:297–310, September 1990.

J.H. Van Vleck and D. Middleton. The spectrum of clipped noise. *Proceedings of the IEEE*, 54(1):2–19, Jan 1966. ISSN 0018-9219. doi: 10.1109/PROC.1966.4567.

Chapter 3

Pico flares and coronal heating

3.1 Introduction

Presence of Fe IX and Ca XIV spectral lines in the solar corona proves that coronal temperature is ≈ 1 MK. It is known that photospheric temperature is ≈ 5800 K. Second law of thermodynamics states that, heat cannot be transferred from cold body to hot body without an external agency. The mystery is that how the solar corona is heated to ≈ 1 MK by the ≈ 5800 K photosphere which is the so called coronal heating problem. Although there are many theories to explain the coronal heating problem, none is able to explain it efficiently. If the heating is because of the thermal conduction, coronal temperature has to drop down and cools off within few hours or days. But this is not the case. There were many models proposed to explain coronal heating. Few of the models are (1) DC stressing and reconnection model (2) AC wave heating model (3) Acoustic heating (4) Chromospheric reconnection (5) Velocity filtration. Briefly about these models are discussed in Aschwanden [2004, pp360] and references are given there. In this chapter, coronal heating problem is explained using the observations of noise storms which are frequently observed at low frequency radio observations.

3.2 Magnetic reconnection

The coronal magnetic field is constantly stressed and adjusted by restructuring the large scale magnetic field by topological changes and is called magnetic reconnection. The possible reasons for the magnetic stress is: (1) The solar dynamo in the solar interior, which constantly generates a new magnetic flux from the bottom of the convection zone which rises by buoyancy and emerges through the photosphere to outer atmosphere, (2) The differential rotation, convective motions at solar surface continuously wrap up the coronal field with rotation, and (3) Connectivity to the interplanetary field lines constant break up, which is due to avoid magnetic stress [Aschwanden, 2005]. If opposite polarity flux come together, a boundary layer will form to separate the two regimes of magnetic field in a form of pressure balance. Such high resistive system counteract the currents within allow the occurrence of non-ideal MHD processes and formation of structures having small spatial scales like current sheet. It leads to a low magnetic Reynolds number and allow diffusion to occur. The connectivity of the field lines cause ejection of plasma along the resulting, so that the reconnected field lines relax to a new equilibrium. Outflows cause a low pressure in the diffusion region and allow inflow of plasma. Figure 3.1 shows the geometry of the magnetic reconnection process in Sweet-Parker model and Petschek model. Magnetic reconnection is explained by Sweet [1958] and Parker [1963] by assuming a two-dimensional incompressible MHD approximation. If the reconnection layer length and thickness are Δ and δ respectively, then the outflow should balance the inflow. i.e.,

$$\rho_1 v_1 \Delta = \rho_2 v_2 \delta \tag{3.1}$$

where v_{in} and v_{out} is the velocities of the inflow and outflow respectively, ρ_1 and ρ_2 are the mass densities of inflow and outflow respectively. Note that in Sweet-Parker model length of diffusion region Δ is larger than its width δ. The rate of reconnection is then written interms of Lundquist number 'S_L', a dimension less quantity and defined as ratio

of an Alfvén wave crossing timescale to resistive diffusion timescale.

$$\frac{v_1}{v_2} = \frac{1}{\sqrt{S_L}} \tag{3.2}$$

where

$$S_L = \frac{\mu \Delta v_A}{\eta}$$

and v_A is the Alfvén speed, μ is the molecular weight, and η is the magnetic diffusivity. By substituting the respective values, it is found that the Sweet-Parker model is very slow to explain the magnetic dissipation in the solar flares. Note that using the Sweet-Parker model, the rate of dissipation is tens of days and is actually observed in minutes and hours of time [Byrne, 2010]. Faster reconnection model was proposed by Petschek [1964], which has reduced size of the diffusion region ($\Delta \approx \delta$). Since the length of the current sheet is shorter, the propagation time through the diffusion region is shorter and the reconnection process becomes faster. In latter model the inflowing plasma turns around outside the diffusion region and show mode shocks arise, so that the abrupt change of velocities from v_1 to v_2. The reconnection velocity in the Petschek model written as, [Aschwanden, 2005, Byrne, 2010]

$$v_1^2 = v_2^2 \left(\frac{\eta}{v_A \mu \Delta'} \right) \tag{3.3}$$

The equation-3.3 may be rewritten as follows

$$v_1 = \frac{v_2}{\sqrt{S_L}} \sqrt{\Delta / \Delta'} \tag{3.4}$$

where Δ' is length of diffusion region in Petschek model. Note that the factor $\sqrt{\Delta/\Delta'}$ is faster than the Sweet-Parker reconnection velocity.

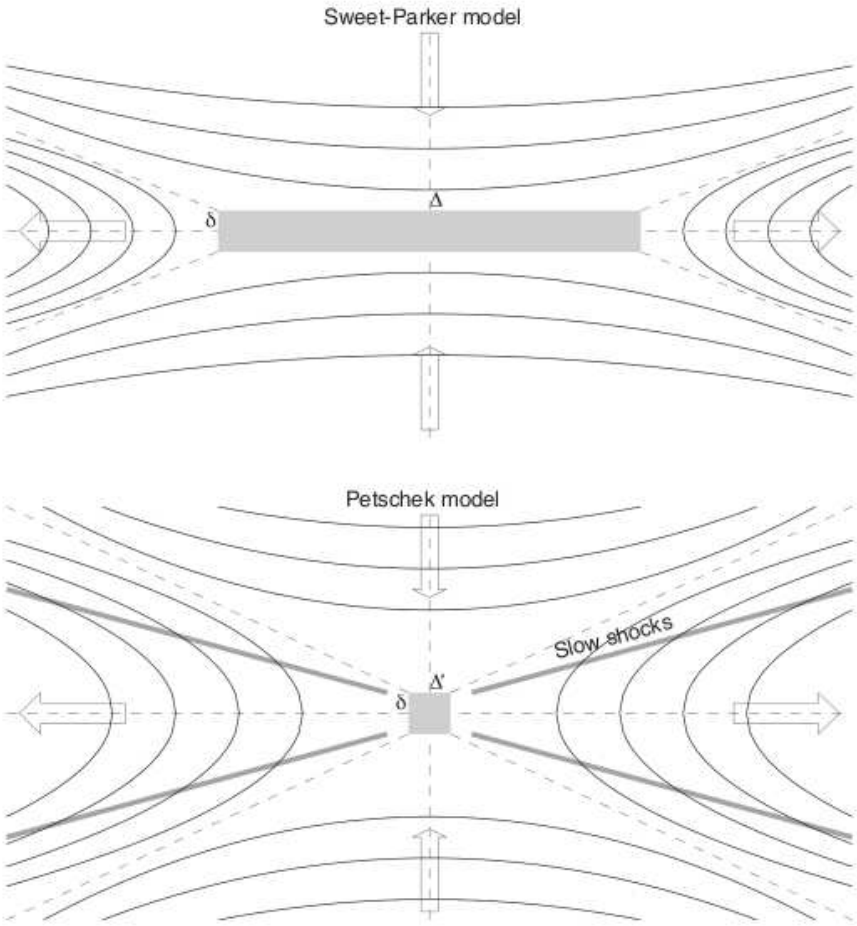

Fig. 3.1: Geometry of the reconnection models is shown in Figure. Top one is the Sweet Parker model and bottom one is the Petschek reconnection model. Image credit: Aschwanden [2005], Byrne [2010]

.

3.3 Solar flares and sub flares

Radio observations are the useful complementary tool in detecting the signatures of weak transient energy releases in the solar atmosphere, since the related non-thermal emission can be detected easily[Benz, 1995]. In recent years, systematic study and statistical analysis of small scale phenomena in solar corona and transition region has been carried out using the X-ray and EUV high resolution images. Such analysis is used to estimate the energy and other statistical parameters, so that the coronal heating problem can be addressed. These small scale features explored in solar atmosphere at different wavelengths are explained in Aschwanden [2004]. Some of the events observed in solar corona are: ephemeral regions, emerging flux events, canceling magnetic flux events, explosive events, blinkers, soft X-ray bright points, picoflare, nanoflares, microflares, soft X ray jets, active region transient brightenings etc.

3.3.1 Large flares

It is known that a typical large solar flare has the range of energy $\approx 10^{30} - 10^{33}$ erg. Based on the energy release, solar flares are categorized into few subclasses called subflares: microflares, nanoflares and picoflares. Depending on the temperature, the flares are seen at corresponding wavelengths. Large flares are observable in HXR, SXR and EUV regimes with temperature and density $\approx 8 - 40$ MK and $\approx 0.2 - 2 \times 10^{11}$ cm^{-3} respectively. Large solar flares are the superposition of microflares and microflares are superposition of nanoflares [Parker, 1988]. So the corona is heating, not only because of a single large flare but also number of microscopic events occurring due to the virtual magnetic reconnection processes. The magnetic reconnection processes are continuously restructuring by itself because of the generation of new magnetic flux from the solar interior which propagates to the corona, the differential rotation and the interplanetary fields. These microscopic magnetic reconnection process contribute to the coronal heating. But more often, sudden

energy releases from CMEs and flares, may alter the magnetic field structures in the corona.

3.3.2 Microflares

Microflares have energy in the range of $\approx 10^{27} - 10^{30}$ erg, which is $10^{-6} - 10^{-3}$ times of a large flare. These events are observable at SXR and EUV wavelength regimes. These events have the temperature and density in the range of $\approx 2-8$ MK and $0.2-2\times10^{10}$ cm^{-3} respectively. Active region transient brightenings (ARTB) are the group of events which appear in the active regions. X-ray bright points (XRBs) are seen in SXR, HXR and radio domains. Emission mechanism of them are gyroresonance, gyrosynchrotron and non-thermal microwave emission [Gopalswamy et al., 1994a, 1997, White et al., 1995, Gary, 1997]. Also energy of XRBs are in range of microflares, and they are seen even in quiet corona or coronal holes. But ARTBs are observed only in active regions. Microflares were detected by Lin et al. [1984] using high sensitive Balloon-borne instrumentation and their reported energy was $\approx 10^{26} - 10^{28}$ erg. Microflares are of interest because of their contribution to the coronal heating. Note that these bursts are impulsive and non-thermal in nature. Small amplitude radio bursts related to the microflares in solar atmosphere are first reported by Kundu et al. [1986]. Similar observations at 1.4 GHz were reported by Bastian [1991].

3.3.3 Nanoflares

The small scale features whose estimated energies are below 9 orders of a typical large flare are defined as nanoflares. Nanoflares energy $\approx 10^{24} - 10^{27}$ erg and these events are found in the temperature scales of $1 - 2$ MK. Density scales of the nanoflare regions are $\approx 0.2 - 2 \times 10^{9}$ cm^{-3}. Such nanoflares are first observed mainly in the EUV regions using SOHO/EIT data. EUV nanoflares cannot reach the temperature greater than 2 MK

so that they are not observable in SXR or HXR. Theoretical models of coronal heating postulate that nanoflares are seen throughout the solar corona [Levine, 1974, Parker, 1988]. Nanoflare loops are observed due to the DC interactions such as stress induced reconnection, current cascades and turbulence which produce the magnetic dissipative events. At radio low frequencies, Ramesh et al. [2010, 2013] estimated the energy of the type III bursts whose energy was $\approx 3.3 \times 10^{24}$ erg. Those events are belongs to the nanoflare category which were postulated by the Parker [1988]. The magnetic field estimated in those regions, where type III bursts originated was $\approx 2.5 \pm 0.2$ G at 77 MHz. Estimated brightness temperature of those events were $\approx 10^8$ K.

3.3.4 Picoflares

In addition to the above mentioned events, magnetic energy is released in several different forms that are necessarily related to the traditional definition of flares [Benz, 1995, Aschwanden, 2004]. For example, Katsukawa and Tsuneta [2001], Katsukawa [2003] proposed that the fluctuations in the soft X rays from active regions are due to the ubiquitous tiny bursts of energy releases. The estimated energy of the individual bursts was in the range of $10^{20} - 10^{22}$ erg. Since the mean value is $\approx 10^{21}$ erg which is 12 orders weaker than the larger flares in the solar atmosphere, they are called picoflares [Parnell and Jupp, 2000, Aschwanden, 2004, Tsuneta and Katsukawa, 2004]. In this chapter, such weak energies are explained using the observations of the type I radio bursts (also called radio noise storms), which constitute the most frequently observed type of solar activity.

Larger flares are seen in active regions and microflares, nanoflares and even picoflares are observable everywhere in the quiet Sun and coronal holes. It is believed that flares/microflares requires a significant amount of magnetic field strength $\approx 10 - 1000$ G. Such fields are found in active regions, but till now it is not known whether the microflares originate in the weak magnetic field region like $\approx 1 - 10$ G range. Note that these weak

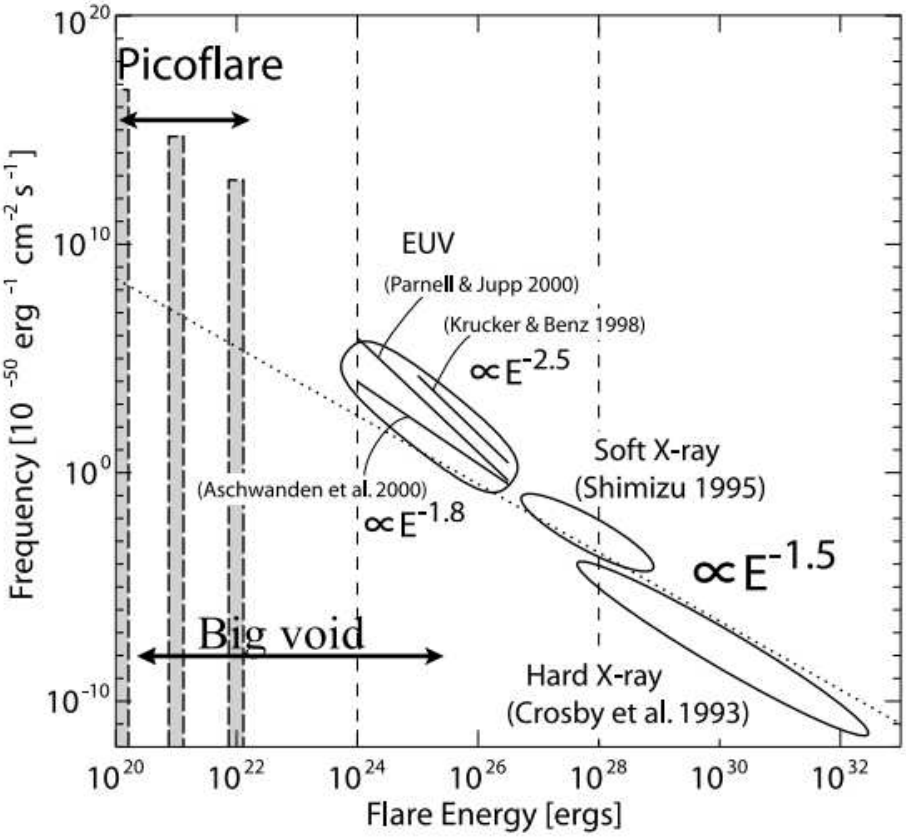

Fig. 3.2: The Figure shows the observation of flares at HXR, SXR, EUV wavelengths which are related to the microflare, nanoflare energy categories. Note that there are no observations reported in picoflare category range in the Figure. This void may be covered by the present observation of picoflares discussed in this chapter. It is clearly seen in the Figure that the power-law index decrease for weaker energy events. In the present case estimated power law indices of the picoflares varies from -2.2 to -2.7. Image credit: Tsuneta and Katsukawa [2004]

.

fields are seen in quiet corona and even in coronal hole regions. In recent days, it was found that the nanoflares and picoflares are observed in the weak magnetic field regions. For example, nanoflares were observed in region with magnetic field of $\approx 2.5 \pm 0.2$ G, whereas picoflares were seen in $\approx 183 - 950$ mG field regions [Ramesh et al., 2010, 2013]. Note that in the present chapter, it is concluded that weaker energies than microflares are also present in the solar corona and such events contribute to the coronal heating.

3.4 Noise storms

A long lasting solar radio emissions are first observed by McCready et al. [1947] in metric and decameter wavelengths. The noise storm emission consists of a series of short lived ($0.1 - 1$s) narrow-bandwidth radio bursts superimposed on continuous, slowly varying, long-lasting broadband background emission. Note that the background level with free of bursts is commonly referred to as background continuum, and the bursts superposed over it are called type I bursts [Wild et al., 1963, Ramesh and Shanmugha Sundaram, 2000]. These emissions last from a few hours to days so that they are called storms. These storms are analogous to the geomagnetic storms, hence the name noise storms [Allen, 1947]. More reviews on these noise storms are found in Elgarøy [1977], Kai et al. [1985]. It is considered that the bursts are an evidence of successive electron accelerations, which, unlike the transient acceleration associated with flares and continue for hours to days. It is now generally accepted that the radiation is fundamental (F) plasma emission mechanism [Sundaram and Subramanian, 2004] due to the coupling of Langmuir and low-frequency waves (either lower-hybrid or ion-acoustic). Observations of strong circular polarization result from the propagation effects in the presence of a magnetic field. Type I bursts are primarily related to non-flaring sunspot active regions and also observed in an exceedingly restless corona even during non flaring situations. These bursts are considered to be the signatures of many small steps in coronal evolution, whose cumulative effect is the 'gradual' evolution of the solar corona. The emerging magnetic flux and the changes in the existing active region magnetic fields with time inevitably lead to field reconnection and type I bursts, which are associated with these small sites of reconnection [Benz and Wentzel, 1981, Spicer et al., 1982].

Noise storms are usually observed from 50 to 500 MHz bandwidth. The background as well as the type I bursts are highly circularly polarized nonthermal emissions. The degree of circular polarization reaches to $\approx 100\%$. Some times, noise storm may accom-

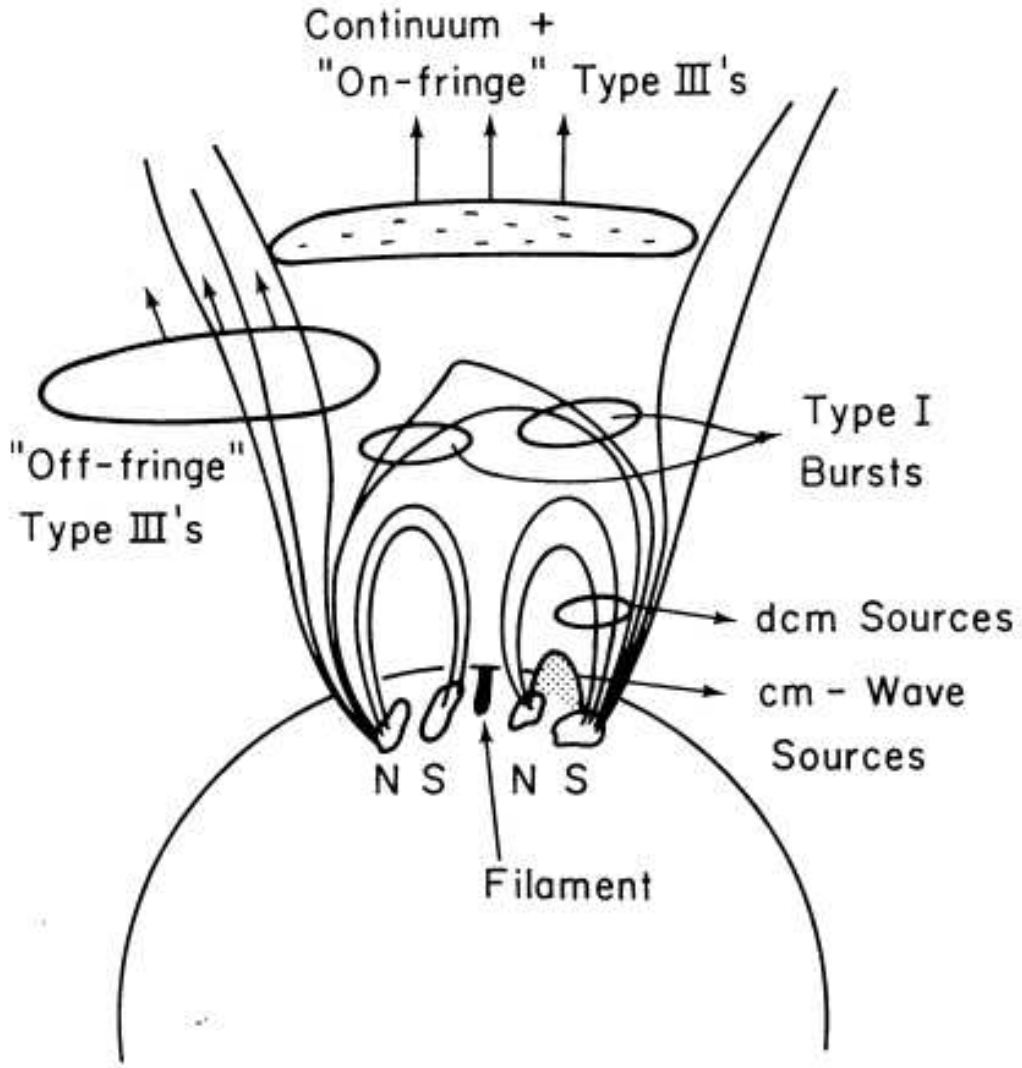

Fig. 3.3: The Figure describes a model of storm region indicating the position of storm type (on-fringe) and impulsive (off-fringe) type III bursts along with type I burst regions and sources of intense continuum emission at high frequencies which are close to the disk. Also the location of decimeter (dcm sources) and microwave (cm wave sources) bursts are shown in the Figure. The 'on-fringe' type III's coincide within position with the continuum and 'off-fringe' one are slightly displaced in position with the continuum. These two types differ in other properties also. Image credit: Gergely and Kundu [1975]

.

panied by type III bursts. Observations show that type I bursts occur in strong magnetic bipolar regions, where as type III bursts occur in weak magnetic unipolar regions [Kai, 1970]. The type I and type III bursts are closely connected at decameter and hectometer wavelengths. There may be a continuous conversion of pure type I to type III, when the accelerated electrons propagate in the corona outward. Frequently, type I bursts occur, where as some of the supra-thermal electrons which accelerates further to the speeds of $> 0.1c$ and those electrons may cause the type III bursts. Boischot et al. [1970], Stewart and Labrum [1972] proposed few models and explained the different possibilities of association of type I and type III bursts. In this chapter only noise storms are discussed and in chapter-4 type III bursts are discussed. The Figure 3.3 show the location and information about physical conditions to originate the bursts at different wavelengths including type I and type III bursts.

3.5 Observations and data analysis

The radio data discussed in this chapter was observed during five different observing periods at 80 MHz. The selected noise storms are analyzed which are observed in the absence of temporally associated coronal mass ejections (CMEs), Hα/X-ray flares with the heliograph [Ramesh et al., 1998] and the East-West one dimensional polarimeter [Ramesh et al., 2008] at GRO. The noise storms are observed in polarimetric mode using the GRIP. The heliograph (Gauribidanur Radio Heliograph, GRH and after the expansion of the GRH, it is called GRAPH) is a T-shaped radio interferometer array which produces two-dimensional images of the solar corona. The angular resolution of the array is $\approx 10' \times 15'$ (R.A. $\times$ decl.) at the above frequency. The antenna elements used in both the arrays are log periodic dipoles which operate from 30 to 150 MHz. The antenna elements are pointed towards the zenith and are non-trackable. However, different lobes of observations is carried out by tilting/steering of the antenna response 'beam' to the

required direction is achieved electronically by making use of the diode switches. The signals of the diodes are controlled from the lab through suitable cable network and automated software. Beam steering in different declinations is also done using the same mechanism in the GRH.

The polarimeter responds to the total intensity and polarized flux density from the 'whole' Sun. The response function or the 'beam' of the polarimeter array is broader compared to the Sun at that frequency in both right ascension (East-West direction) as well in declination (North-South direction). The beam in right ascension and declination at 80 MHz is $\approx 4^o$ and $\approx 90^o$ respectively. Therefore, the time profiles observed with the polarimeter correspond to the East-West beam. The amplitude of the signal is proportional to the strength of the radio emission from the 'whole' Sun at that observing frequency and polarization mode. The time profiles are weighted by the antenna gains in the direction of the observations. The antennas in the polarimeter array are non steerable unlike the GRH. The positional information of the radio sources is observed using the GRH and circularly polarized emissions are observed using polarimeter. Note that the two-dimensional radio heliograms and the polarization observations are carried out at the same time.

Because of the good time resolution and sensitivity, noise storms are observed frequently with both polarimeter and GRH. Since the instrument operates in transit mode, the statistical analysis carried out in this chapter is restricted only to main lobe observations. The observations of noise storms were cross checked with Culgoora spectrograph database[1]. The noise storms data was calibrated using the calibrator sources whose flux density is known and invariant for long durations. Calibration procedure is discussed in the section-2.10. The quiet Sun component from the noise storm observations was removed by subtracting a fitted polynomial from the actual data.

The minimum detectable flux density of the GRH and the polarimeter was $\approx$

[1]http://www.ips.gov.au/World_Data_Centre/1/9

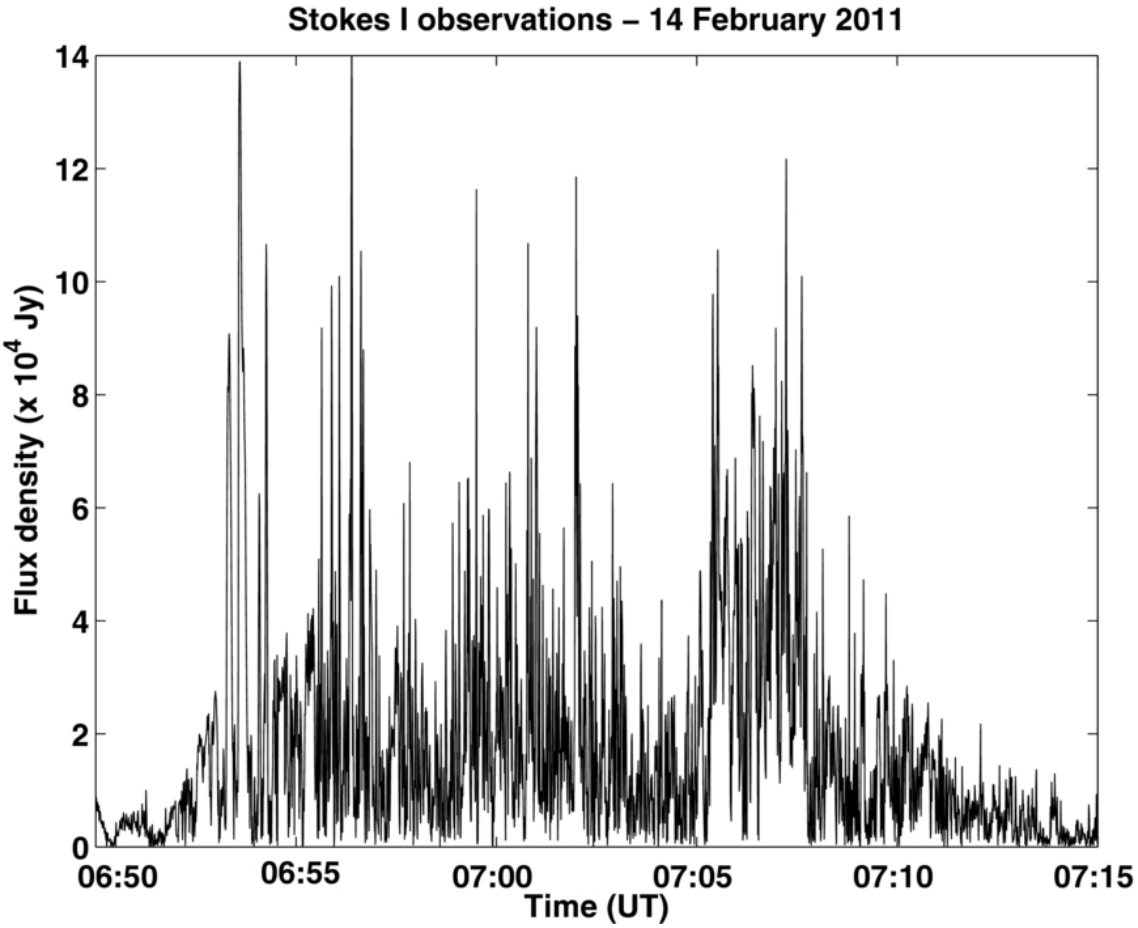

Fig. 3.4: Gauribidanur polarimeter observations of type I solar radio bursts in Stokes I at 80 MHz on 14 April 2011. The integration time was ≈ 256 ms

.

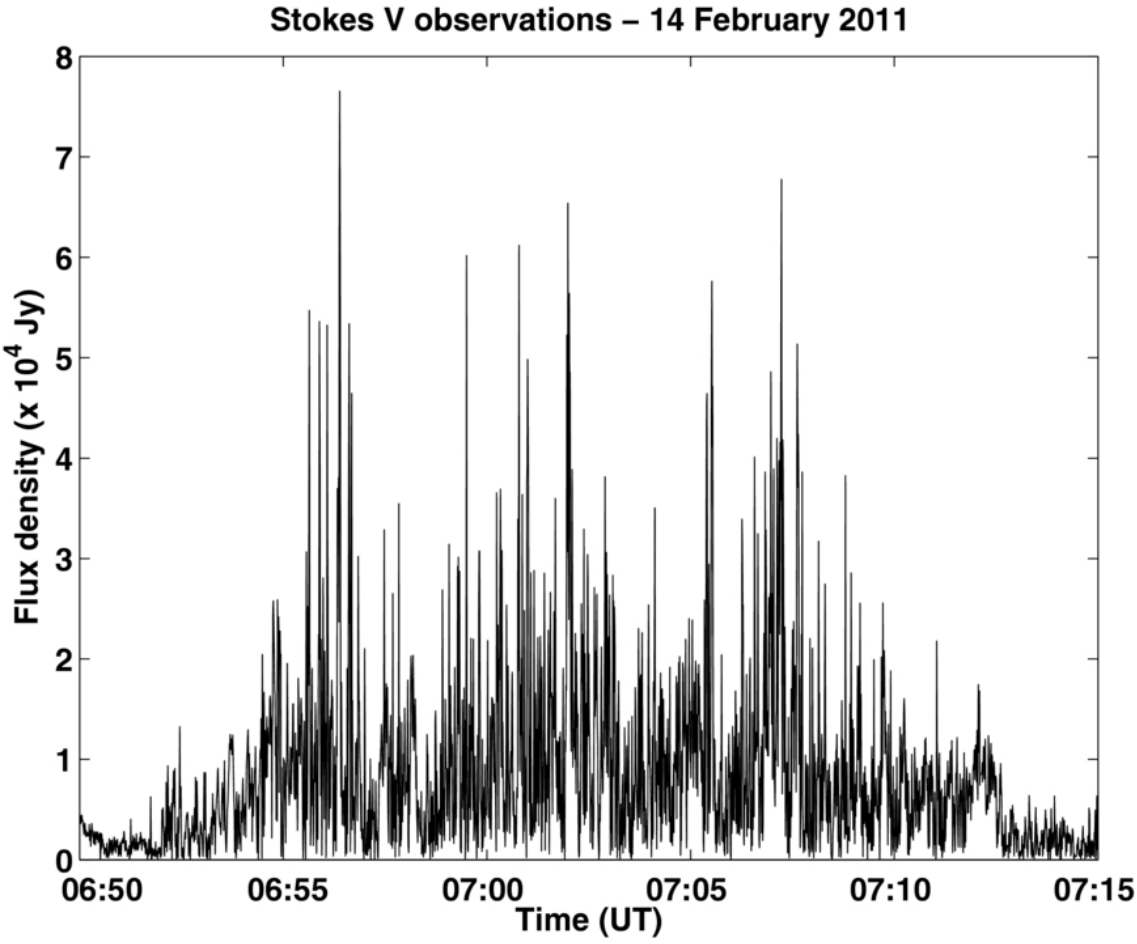

Fig. 3.5: Gauribidanur polarimeter observations of type I solar radio bursts in Stokes V at 80 MHz on 14 April 2011. The integration time was ≈ 256 ms

.

200 and 1000 Jy, respectively during the observing period, for an integration time of $\approx$ 256 ms, and a bandwidth of $\approx$ 2 MHz. Figures 3.4 and 3.5 show the time profiles obtained with the polarimeter in both Stokes I and V on 14 February 2011 during the interval $06:50-07:15$ UT, i.e., around the transit of the Sun over GRO. The limited observing period is mainly due to the non steerability of the antenna response, and its width (4^o) as mentioned earlier. One can note the presence of numerous short-lived peaks in both the Stokes I and V time profiles. These are characteristic signatures of the type I radio bursts from the solar corona which were discussed in detailed by Elgarøy [1977], Kai et al. [1985]. It is Independently ascertained that the spectral nature of the observed emission as type I radio bursts are verified from online reports[2].

3.5.1 Calculation of the total energy radiated from the noise storm

Its known from the observations that typical type I bursts reach the flux density at most 10^{-21} $\mathrm{Wm^{-2}Hz^{-1}}$ in the $150-200$ MHz region and at 100 MHz, the flux density may exceed 10^{-19} $\mathrm{Wm^{-2}Hz^{-1}}$ at maximum for the large flares. The total energy (W) emitted by the burst is calculated using the relation shown in equation 3.5 [Elgarøy, 1977],

$$W = S\Delta t\Delta\nu R^2\Omega e^{\tau} \tag{3.5}$$

where S is the flux density at the observed frequency ν, Δt is the duration of the burst, $\Delta\nu$ is the bandwidth of the burst, R is the Sun-Earth distance [$\approx 150\times10^9$] meters, Ω is the solid angle into which the radio waves are emitted. Note that the solid angle of the noise storms are measured using the stereo observations. To obtain the total flux emitted by the noise storm it is essential to know the total solid angle where the whole energy is beamed into. Once the noise storm is emitted, depending on the physical conditions of

[2]ftp://ftp.ngdc.noaa.gov/STP/SOLAR_DATA/SOLAR_RADIO/BURSTS_Tables/Spectral

that source region, it may not be radially towards the Earth, but may be tilt by some angle (θ). Therefore observation of the two-dimensional images cannot give the correct estimate of the solid angle. Therefore, solid angle is estimated using the stereo observations which is similar to the one shown in Figure 3.6. First time, the beam pattern of type I is estimated from the simultaneously obtained observations using stereo spacecraft Soviet probe Mars-3, and a Earth's observer Nançay radioheliograph (France) at 169 MHz. The solid angle is estimated by assuming all bursts are having the same emission polar diagram $f(\theta)$ which is symmetric around the axis making an angle θ. From the polar emission diagram, half power beam width of type I found was $\approx 25^o$, which corresponds to a solid angle of 0.15 sr [Steinberg et al., 1974] and τ is the optical depth near the source position of corresponding observing frequency (ν).

In the present case, $S = 14 \times 10^4$ Jy, $t \approx 256$ ms, and $\nu = 80$ MHz. Assuming $\Delta\nu = 0.02\nu \approx 2 \times 10^6$ Hz [Benz and Wentzel, 1981], which, as mentioned earlier is the same as the bandwidth of the observations in the present case, ≈ 0.15 sr [Steinberg et al., 1974], and $\tau \approx 3$ at 80 MHz [Ramesh, 2005]. Substituting these parameters in the equation 3.5, gives $W \approx 0.5 \pm 0.1 \times 10^{21}$ erg for the 14 February 2011 event and is shown in 3.4. Similarly the total energy emitted by different noise storms are listed in column 7 of Table 3.1. Note that Klein [1995] and Subramanian and Becker [2004] had estimated the energy contained in the electron population (âĹij10 keV) associated with the noise storm emission to be 10^{26} erg. Therefore, the energy emitted by the burst source mentioned above is probably the lower limit that the acceleration process provides to the radiating electrons [Klein, 1995].

Comparison of the estimated energies using the type I bursts are shown in Table 3.1. On comparison of the estimated energies with those compiled by Crosby et al. [1993] and Aschwanden [2004] from observations at other regions of the electromagnetic spectrum indicates that the present values are the weakest energy releases in the solar atmosphere reported to date. These weakest energy events probably fall into the category of picoflares

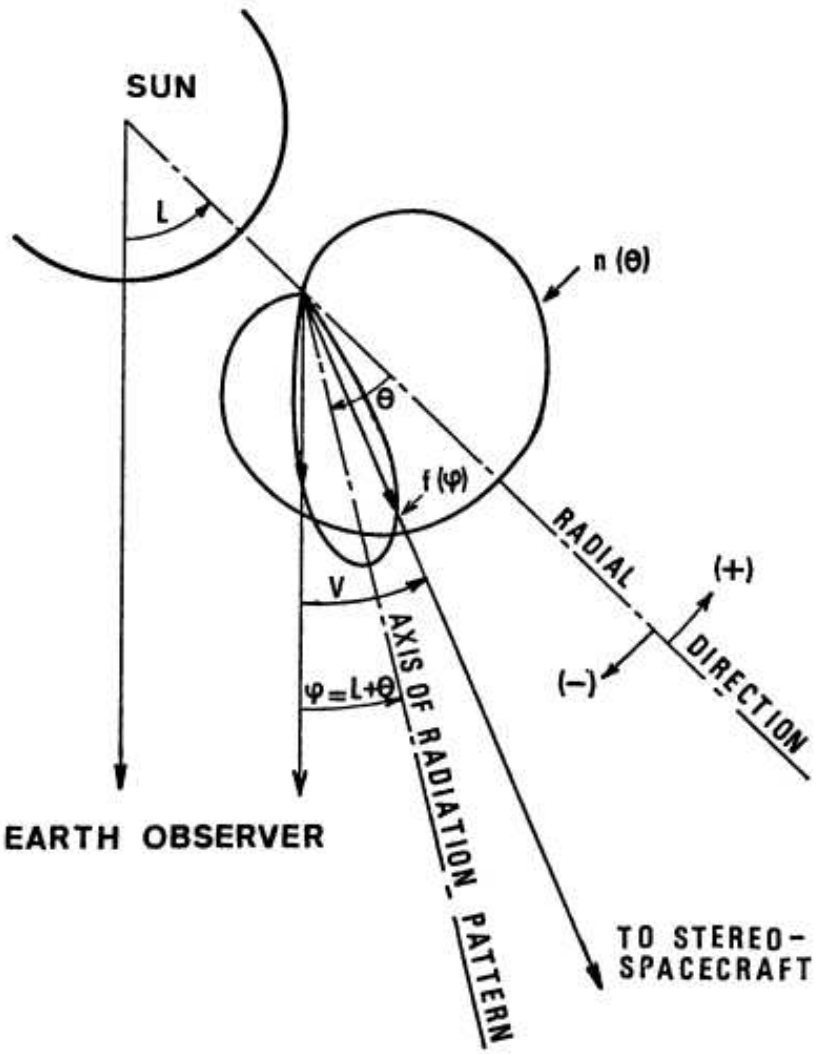

Fig. 3.6: Geometry of the stereo observations from which solid angle of the radio burst is estimated. Note that stereo observations are carried out using the Soviet probe Mars-3 (Stereo spacecraft) and the second one is Nançay radio heliograph (Earth's observer) which is at France. In the Figure, L is the heliographic longitude of the source, $\phi = L+\theta$, where θ is the angle between the bursts emission $f(\theta)$ and the radial direction through the source, $n(\theta)$ is the probability density function of θ. Image courtesy: Steinberg and Caroubalos [1970].

as mentioned. The possibility of fluctuations in the amplitude of the type I bursts which are shown in Figures 3.4 and 3.5 as well as the other events in Table 3.1 are due to either a screening of the radio source region by a hot and dense evaporated chromospheric material in the aftermath of flare onset as pointed out by Boehme and Krueger [1982], Aurass et al. [1990, 1993], Zaitsev et al. [1994]. Formation/deformation of reconnection regions, from where the type I emission is generated after/before CMEs as shown by Chertok et al. [2001] and Iwai et al. [2012], can be ruled out. Note that since the events reported in the present work were not accompanied by either CMEs or $H\alpha$/X-ray flares as mentioned earlier in this chapter and is verified using online resources[3] and the SGD reports. Also note the following points: (1) It is mentioned in the literature that onset of a flare during an on going radio noise storm causes reduction in the overall flux to the $> 35\%$ of the latter within a short interval of $\approx 2-3$ minutes followed by a slow recovery. Such recovery takes approximately an hour of time. However in the present case, it is contrary to the above statement and first of all, there is no reduction in the flux as mentioned above. (2) CME related variations in the radio flux of the noise storms mentioned in the literature occur over comparatively larger timescales (of order of few hrs) unlike the present case, where the changes are over much shorter timescales ($\lesssim 1$ s). Therefore, it is clear that the observed radio emission is likely due to variations in the heating conditions near the source region as described by Li et al. [2009].

3.6 Estimation of Brightness temperature

Often the brightness of the radio sources is measured in temperature units which is called brightness temperature. It is the Rayleigh-Jeans temperature of an equivalent black body, which provides the same power as the source. Using the Rayleigh-Jeans law, brightness

[3] www.lmsal.com/solarsoft/latest_events/

temperature (T_b) of the source is given in equation 3.6.

$$T_b = \frac{S\lambda^2}{2k\Omega} \tag{3.6}$$

where S is the flux density of the observed source [Jy], λ is the observed wavelength [m], $\Omega = \theta_{EW}\theta_{NS}$ is the solid angle of the source, k is the Boltzmann constant [$= 1.38 \times 10^{-16}$ erg K^{-1}], and θ_{EW} and θ_{NS} are the source sizes (half-power diameters) in East-West and North-South directions [arc min] respectively. By substituting the above parameters in equation 3.6, it can be rewritten as equation 3.7.

$$T_b = \frac{4283\ S\ \lambda^2}{\theta_{EW}\theta_{NW}}\ \text{K} \tag{3.7}$$

Using the equation 3.7 and assuming that the source sizes of a typical noise storms θ_{EW} and θ_{NS} are $\approx 1'$ at 80 MHz [Ramesh et al., 2012], the brightness temperature (T_b) was estimated. Note that the flux density of the observed source was found by calibrating with an observed suitable calibrator source. The estimated T_b values are shown in Table 3.1. Peak brightness temperature (T_b) of the bursts in Figure 3.4 are calculated. The value is $\approx 0.8 \pm 0.1 \times 10^9$ K for the event which is shown in Figure 3.4. The T_b values are consistent with the theoretical predictions for type I radio bursts [Melrose, 1980]. Note that the assumption on the source size is justified because (1) Lang and Willson [1987] and Kerdraon [1979] had earlier reported observations of type I bursts of size of $\approx 0'.7$ and $\approx 0'.8$ at 328 and 169 MHz, respectively and (2) the source size increases with a decrease in frequency [Elgarøy, 1977]. In other words, since the open magnetic field lines diverges radially outwards, the source size increases with increasing height in the solar corona.

3.7 Measurement of degree of circular polarization

Degree of circular polarization (dcp) is measured using equation 3.8

$$dcp = S_V / S_I \tag{3.8}$$

where S_V and S_I are the flux densities of Stokes V and I respectively. Time profile of the dcp for few individual bursts which are observed on 14 April 2011 are shown in Figure 3.7 and the width of each profile is ≈ 1 s and the peak dcp of the bursts is in the range of $\approx 0.3 - 0.4$.

The information on the location of the radio bursts was inferred from the radio heliogram obtained with the GRH around the same time. Due to the limited angular resolution, only the background noise storm continuum is seen in Figure 3.8. However, note that the position of the type I bursts usually scatter over the associated continuum source, and their centroid is within the observed source region of the continuum [Malik and Mercier, 1996]. The nearly constant peak dcp of the different bursts mentioned above is probably because of this. Therefore, the bursts originate from almost the same region of the corona.

3.8 Estimation of magnetic fields

Following Ramesh et al. [2011], the coronal magnetic field (B) near the location of type I bursts were estimated. The method of estimation of magnetic field is described as follows. Briefly about the magneto-ionic theory is described in the section 1.11 and the characteristic parameters of the magneto-ionic medium like solar coronal plasma are,

$$X = \frac{f_p^2}{f^2} \tag{3.9}$$

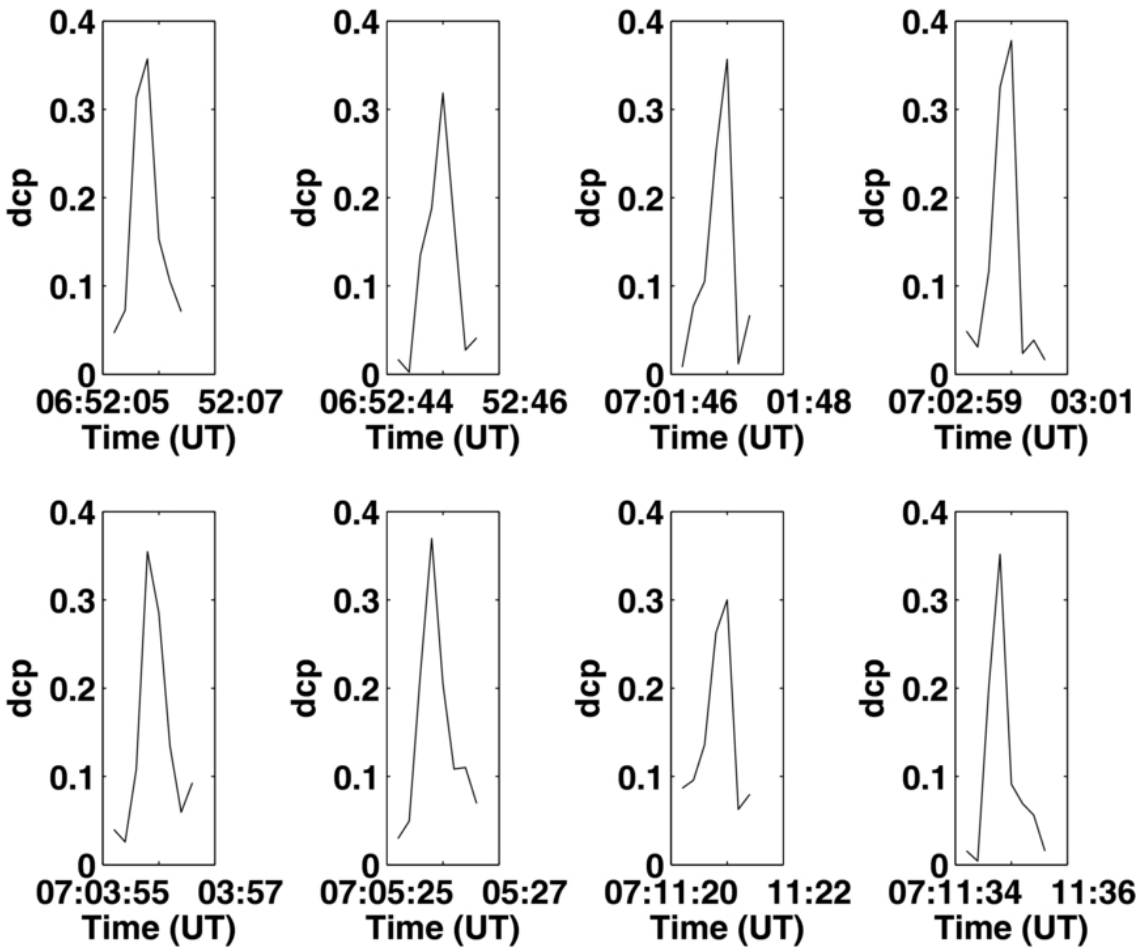

Fig. 3.7: Time profile of the dcp for a few individual type I bursts in Figure 3.4 and 3.5.The time span in each plot is 2s.

$$Y = \frac{f_B}{f} \tag{3.10}$$

$$f_p = 9 \times 10^3 \sqrt{N_e} \tag{3.11}$$

$$f_B = 2.8 \times B \tag{3.12}$$

It is known that in magneto-ionic medium, the radio waves propagate in two modes: o-mode and e-mode. These modes are due to the differential absorption of the corona. These two modes have different optical depths. It is also known that 'zero' refractive index occurs when $f_p = f$ and f_p decreases radially outward in the solar atmosphere. In this case X=1 and X=1-Y [Aschwanden, 2005]. Generally, o-mode is defined as the mode that is not affected by the magnetic field and reaches the observer where as the e-mode cannot penetrate the X=1-Y level. This is because, the o-mode has a high optical depth than the e-mode. Note that, the case may be different at high frequencies, since gyrofrequency is dominant. Therefore, it is defined, dcp in terms of the differential absorption of the o and e-modes.

$$dcp = \frac{T_b^o - T_b^e}{T_b^o + T_b^e} \tag{3.13}$$

Where T_b^o and T_b^e are brightness temperatures of the o mode and e-mode respectively. Noise storm emissions are strongly circularly polarized i.e. dcp ≈ 1 in the o-mode which is one of the distinguishing properties, when the associated active region is close to the central meridian on the Sun [Elgarøy, 1977]. Partial polarization of the noise storms are rare [Zlobec et al., 1982]. Note that dcp of the noise storms are weak when they are not close to the central meridian of Sun. Another possible scenario is that the depolarization of the strongly circularly polarized noise storms, since the source may be located in between the X=1 and X=1-Y levels [Wentzel et al., 1986, Gopalswamy et al., 1994b, Bastian, 1995, Melrose, 2006]. Therefore, this leads to the condition near the emission region which is shown in equation 3.14.

$$Y > 1 - X \tag{3.14}$$

Substituting the equations 3.9 and 3.10 in 3.14,

$$B > \frac{f^2 - f_p^2}{2.8f} \tag{3.15}$$

where B is the magnetic field estimated [Gauss] and f, f_p are the observing and plasma frequencies [MHz] respectively. Plasma waves generated by electrons with typical velocity v_b have a frequency given by White et al. [1992] is,

$$f \approx f_p + \frac{3v_t^2}{2v_b^2} f_p \tag{3.16}$$

where v_t is the most probable thermal speed of electrons in the ambient plasma. The expression to estimate the thermal speed is given in equation 3.17

$$v_t = \sqrt{\frac{2kT_e}{m}} \tag{3.17}$$

Here T_e is average temperature of the electrons [$\approx 1.5 \times 10^6$ K] (see Aschwanden [2004]), k is the Boltzmann constant [$= 1.38 \times 10^{-16}$ erg K^{-1}] and m is the mass of the electron[$\approx 9.1 \times 10^{-31}$ kg]. Substituting these values in the equation 3.17, the estimated v_t was $\approx$ 6741 km s^{-1}. Assuming that the T_b of the escaping noise storms radiation cannot exceed that of the Langmuir waves, T^L which is limited by the energy of the fast moving electrons, the latter can be found using equation 3.18 [Melrose and McLean, 1985, Habbal et al., 1989]

$$T^L \leq \frac{m_e v_b^2}{2k} \tag{3.18}$$

By substituting the respective parameter which corresponds to the observed peak brightness temperature of the noise storms around the central meridian passage, in equation 3.18 v_b is estimated. Substituting the observing frequency $f = 80$ MHz and the calculated v_t and v_b values in equation 3.16, the plasma frequency was estimated for the all the noise storm events. By knowing the f_p and substituting the same in equation 3.15, the lower

limit of the magnetic field was estimated and listed in Table 3.1. Note that greater the T_b, lower the magnetic field values. For the 14 February 2011 event, estimated magnetic field (B) is $\approx$ 319 mG. Similar values for other events are listed in column 9 of Table 3.1. It is known that contribution to the Stokes V emission from the background corona is expected to be small at 80 MHz [Sastry, 2009]. Therefore, the tabulated values of B correspond primarily to that of the bursts only but not from the background.

3.9 Results and Discussions

Very Large Array (VLA) observations at higher frequency (333 MHz) indicate that the bursts and the continuum are separated by $\approx 1'$ [Krucker et al., 1995]. It has to be pointed out here that the noise storm continuum in Figure 3.8 is not radially above the associated active region but displaced by $\approx 3'$. This is because the noise storm sources are usually located in the large scale coronal loop system connected with an active region, and low frequency emission comes from the vicinity of the summit of the higher loops in the corona [Sheridan et al., 1983, Klein, 1998]. The average displacement at 80 MHz mentioned in the literature is $\approx 2'$ [Dulk and Nelson, 1973]. The displacement can be related to the height of the radio emission region in cases where the latter is located near the solar limb [Elgarøy, 1977]. The details of the location, peak flux density (S), dcp, and T_b for the events reported in the present work are listed in columns 3 to 6 of Table 3.1.

3.9.1 Whether picoflares contribute for coronal heating?

It is well known that the distribution of the number of solar flares (dN) in the energy range of W to W + dW follows a power-law pattern,

$$dN \propto W^{\gamma} dW \tag{3.19}$$

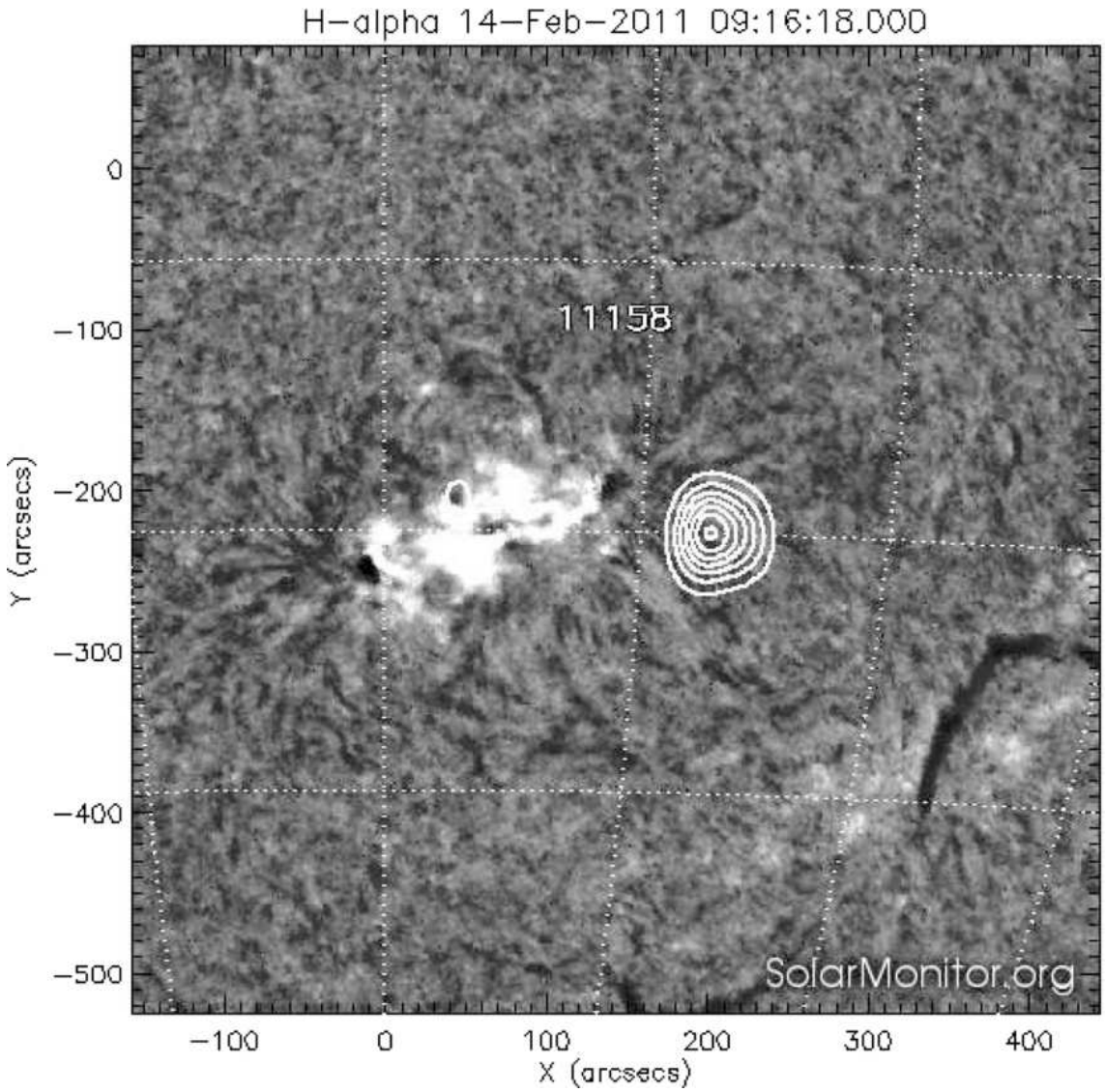

Fig. 3.8: Composite of the H_α image observed at the Big Bear solar Observatory on 14 February 2011 at $\approx 09:16$ UT and the GRH radio heliogram (white contours) obtained on the same day at $\approx 07:00$ UT. The bright H_α emission adjacent to the radio contours in from AR 11158 active region.

$$\frac{dN}{dW} = AW^{\gamma} \tag{3.20}$$

where γ is the power law index and A is the normalization factor which will vary with degree of activity. Many authors found that the γ should be in the range of ≈ -1.5 to -1.8 [Drake, 1971, Datlowe et al., 1974, Dennis, 1985, Crosby et al., 1993]. It was pointed out by Hudson [1991] that for weak energy releases ($W \lesssim 10^{27}$ erg) in the solar atmosphere, γ should be smaller and it should be < -2. Theoretical calculations showing two different power-law indices, $\gamma \approx -1.8$ and -3.5 respectively, for regular and weak flares in the solar atmosphere were presented by Vlahos et al. [1995] and Georgoulis and Vlahos [1996]. From EUV, UV, and X-ray observations, it was found that $\gamma \approx -2.3$ for events with energies in the range of $\approx 10^{24} - 10^{26}$ erg [Porter et al., 1995, Krucker and Benz, 1998, Parnell and Jupp, 2000]. Litvinenko [1994] showed that the weak events with $\gamma < -2$ can be explained if the reconnecting current sheet model is assumed for energy accumulation and release. Type I radio bursts are due to small-scale reconnections in the solar atmosphere, and the energy emitted by them is also low which is shown in column 7 in Table 3.1. Crosby et al. [1996] proposed that flare-like energy released in the active region is a necessary condition for the onset of type I radio bursts. This prompted us to verify whether the distribution of the number of type I radio bursts (dN) in the flux density range S to S + dS in the present case exhibits a pattern similar to that mentioned previously. In Figure 3.9, it is plotted number of type I radio bursts observed on 14 February 2011 which is shown in Figure 3.4 against their peak flux densities in the range S to S + dS. It is noticeable that the two quantities vary in a power-law fashion with an index of $\gamma \approx -2.3$. All the other events followed a similar trend which is shown in column 8 of Table 3.1. The type I burst observations reported by Mercier and Trottet [1997] has the $\gamma \approx -3$. They studied these events at slightly higher frequencies i.e. 164, 237, and 327 MHz. Note that the flux density of the type I bursts observed by the above authors were $> 10^7$ Jy. Compared to this, flux density of the events reported in the current chapter are of the order of 10^4 Jy.

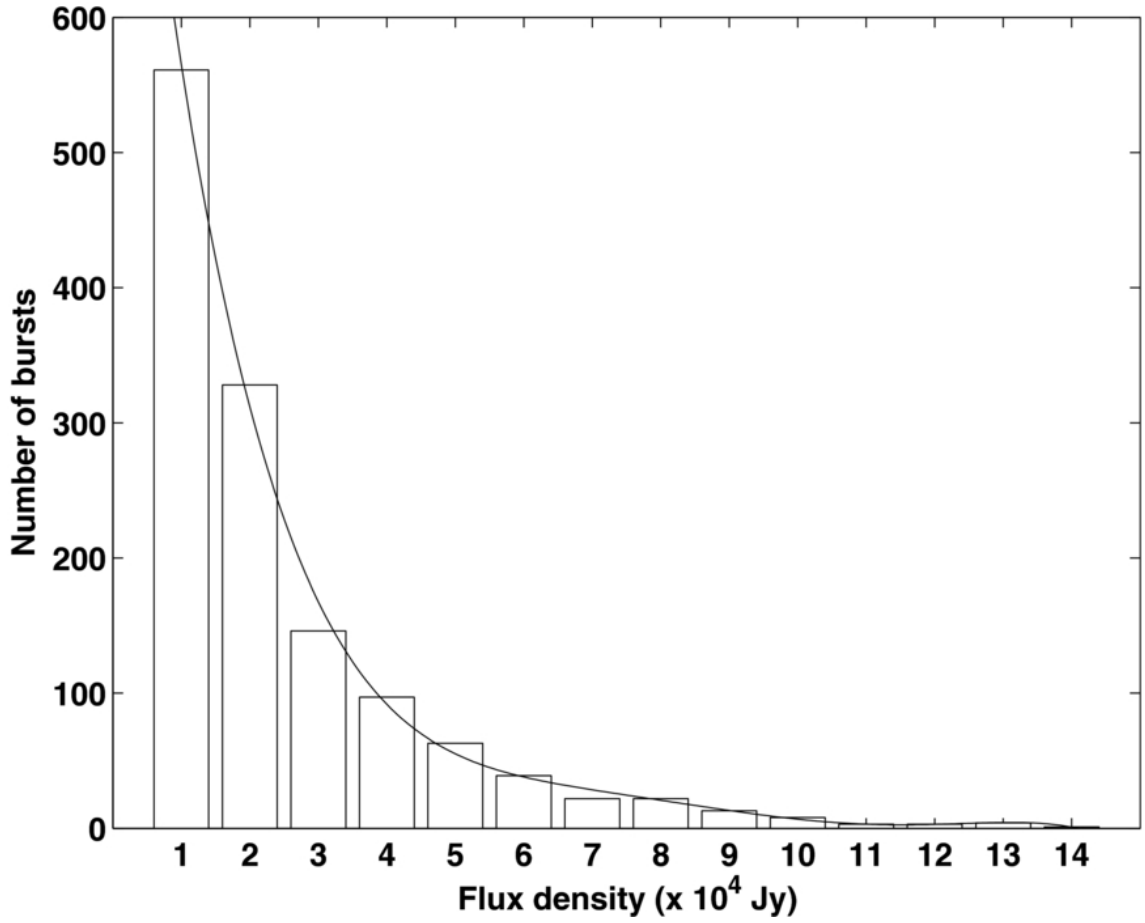

Fig. 3.9: Distribution of the number of type I radio bursts observed on 14 February 2011 which is shown in Figure 3.4 vs. their corresponding peak flux densities. The index of the power-law fit to the distribution is ≈ -2.3

.

Table 3.1: Details of the type I radio bursts observed with the polarimeter and heliograph

S.No	Date	Location	S ($\times 10^4$ Jy)	dcp	T_b ($\times 10^9$ K)	W ($\times 10^{21}$ erg)	index (γ)	B (mG)
(1)	(2)	(3)	(4)	(5)	(6)	(7)	(8)	(9)
1	2011 Feb 14	S17W24	14	50	0.8	0.5	-2.3	319
2	2011 Mar 12	N07W90	15	40	0.9	0.5	-2.2	354
3	2011 Apr 1	N37E34	7	43	0.4	0.3	-2.2	733
4	2011 Apr 4	N37W10	24	50	1.4	0.9	-2.2	183
5	2011 Jul 30	N16W18	6	33	0.4	0.2	-2.7	950

Assuming the smallest and the largest flare energies estimated from observations so far to be $W \approx 10^{26}$ erg and $W \approx 10^{33}$ erg, respectively [Lin et al., 1984, Aschwanden, 2004], we calculated the expected power-law index as described in Gary [1999] for weak transient events at the low-energy limit, i.e., $W \approx 10^{21}$ erg. The value of power-law index $\gamma \approx -2.6$. The present case observational estimates of γ for different type I bursts is in the range of ≈ -2.2 to -2.7 which is listed in column 8 in Table 3.1 and these values are consistent with the earlier results. An inspection of Figure 3.4 indicates that ≈ 1000 bursts are present in the total observing period of ≈ 20 minutes. This gives an occurrence rate of ≈ 1 burst per second, which is consistent with the values mentioned in the literature [Benz, 1995]. Therefore, the power emitted by the type I bursts in the present case is 10^{21} erg s^{-1}.

3.10 Summary and conclusions

In this chapter, it is reported that observations of weak, circularly polarized, type I radio bursts from the solar atmosphere whose estimated energy (W) $\sim 10^{21}$ erg. These are the weakest energy release events in the solar atmosphere reported till date. The distribution of the number of bursts (dN) in the flux density range of S to S + dS varies as a power-law fashion with the index $\gamma \approx -2.2$ to -2.7. Mean magnetic field strength near the burst source for the events was estimated. The estimated magnetic fields are in the range of $\approx 200 - 900$ mG. The present observations reinforce the usefulness of low-frequency radio observations for observing weak-energy releases in the solar atmosphere. Note that the void at weak energy range which is shown in Figure 3.2 can be filled with the present results.

Regarding the question of whether or not these weak-energy releases belong to the picoflare category can contribute to the coronal heating, as pointed out by several authors [Parnell and Jupp, 2000, Tsuneta and Katsukawa, 2004], Note that Book [1981] explained

the high temperature of the corona in terms of heating which results from the effect of the emerging magnetic flux on the plasma. Summary of his conclusions are as follows. (1) The associated energy is deposited within vertical distances of âĹij$10^4 - 10^5$ km from the solar surface. For comparison, the typical height at which type I radio emission is observed at frequencies around 80 MHz is $\approx 2 \times 10^5$ km [Ramesh et al., 2011]. (2) The characteristic Alfv́en speed (v_A) related to the flux emergence is $\lesssim$ 500km $-$ s^{-1} [Book, 1981, Spicer et al., 1982]. Substituting the V_A in the expression 3.21,

$$v_A = \frac{B}{\sqrt{4MN_e}} \tag{3.21}$$

where N_e is the electron density at 80 MHz [$N_e = 7.9 \times 10^7$ cm^{-3}], M is the mass ascribed to each electron in the plasma which includes 10% He [1.9×10^{-24} g]. Substituting these parameter, the estimated magnetic field (B) at 80 MHz is $\lesssim$ 2 G. The estimated magnetic fields discussed in the section 3.8 agree reasonably with this. Evidence has been presented showing that the emerging magnetic flux may provide enough energy to heat the corona by the release of magnetic energy [Schrijver et al., 1997]. These results suggest a possible connection with the type I noise storms since newly emerging flux has been reported to be one of the causes for the onset of the former. The following reports strengthen the above possibility: (1) Spicer et al. [1982] predicted coronal heating prior to the onset of the type I storms, (2) Melrose [1980] pointed out that the required level of low-frequency turbulence for the generation of type I emission is likely to be present in the region where corona is heated, (3) Raulin and Klein [1994] noted that the common features in the time profile of soft X-ray brightenings and noise storms point to a physical link between the heating of the plasma in the active region and the noise storm emission. However, from the present observations, it was found that the power emitted by the type I bursts ($\approx 10^{21}$ erg s^{-1}) is small compared to the energy input for the heating of the corona, which is, $10^{27} - 10^{28}$ erg s^{-1} [Benz, 1995, Shimizu, 1995]. Since type I solar radio bursts/picoflares are one of the various weak-energy releases as mentioned in earlier sections and also in

the literature [Aschwanden, 2004], it is possible that all these weak events (including picoflares) together contribute to the coronal heating.

References

C. W. Allen. Solar Radio-Noise of 200 Mc. /s. and its relation to Solar Observations. MNRAS, 107:386, 1947.

M. J. Aschwanden. *Physics of the Solar Corona. An Introduction*. Praxis Publishing Ltd, August 2004.

M. J. Aschwanden. *Physics of the Solar Corona. An Introduction with Problems and Solutions (2nd edition)*. December 2005.

H. Aurass, A. Boehme, and M. Karlicky. Particle beams as a source of noise storm depression? Sol. Phys., 130:19–29, December 1990. doi: 10.1007/BF00156776.

H. Aurass, A. Hofmann, A. Magun, I. Soru-Escaut, and P. Zlobec. Evaporation causes flare-related radio burst continuum depressions. Sol. Phys., 145:151–168, May 1993. doi: 10.1007/BF00627991.

T. S. Bastian. Solar radio microbursts at 1.4 GHz. ApJ, 370:L49–L52, March 1991. doi: 10.1086/185974.

T. S. Bastian. Angular scattering of radio waves: Implications for mode coupling in the solar corona. ApJ, 439:494–498, January 1995. doi: 10.1086/175190.

A. O. Benz. Flares and Coronal Heating in the Sun and Stars. In A. O. Benz and A. Krüger, editors, *Coronal Magnetic Energy Releases*, volume 444 of *Lecture Notes in Physics, Berlin Springer Verlag*, page 1, 1995. doi: 10.1007/3-540-59109-5_39.

A. O. Benz and D. G. Wentzel. Coronal evolution and solar type I radio bursts - an ion-acoustic wave model. A&A, 94:100–108, January 1981.

A. Boehme and A. Krueger. The flare-related depression of the noise storm on May 5, 1978. Sol. Phys., 76:63–75, February 1982. doi: 10.1007/BF00214130.

A. Boischot, J. de La Noe, and B. Moller-Pedersen. Relation between Metric and Decametric Noise Storm Activity. A&A, 4:159, February 1970.

D. L. Book. A mechanism for heating the solar corona. *Comments Plasma Phys. Controlled Fusion, Vol. 6, p. 193 - 198*, 6:193–198, 1981.

J. P. Byrne. *The Kinematics and Morphology of Solar Coronal Mass Ejections*. PhD dissertation, University of Dublin, School of Physics, September 2010. This is a full PHDTHESIS entry.

I. M. Chertok, S. Kahler, H. Aurass, and A. A. Gnezdilov. Sharp Decreases of Solar Metric Radio Storm Emission. Sol. Phys., 202:337–354, September 2001. doi: 10.1023/A:1012211412695.

N. Crosby, N. Vilmer, N. Lund, K.-L. Klein, and R. Sunyaev. Deka-KeV X-Ray Emission Associated with the Onset of Radio Noise Storms. Sol. Phys., 167:333–348, August 1996. doi: 10.1007/BF00146343.

N. B. Crosby, M. J. Aschwanden, and B. R. Dennis. Frequency distributions and correlations of solar X-ray flare parameters. Sol. Phys., 143:275–299, February 1993. doi: 10.1007/BF00646488.

D. W. Datlowe, M. J. Elcan, and H. S. Hudson. OSO-7 observations of solar X-rays in the energy range 10-100 keV. Sol. Phys., 39:155–174, November 1974. doi: 10.1007/BF00154978.

B. R. Dennis. Solar hard X-ray bursts. Sol. Phys., 100:465–490, October 1985. doi: 10.1007/BF00158441.

J. F. Drake. Characteristics of Soft Solar X-Ray Bursts. Sol. Phys., 16:152–185, January 1971. doi: 10.1007/BF00154510.

G. A. Dulk and G. J. Nelson. The Position of a Type I Storm Source in the Magnetic Field of an Active Region. *Proceedings of the Astronomical Society of Australia*, 2: 211, October 1973.

E. Ø. Elgarøy. *Solar noise storms.* 1977.

D. E. Gary. Radio Counterparts to SXR Transients. In T. S. Bastian, N. Gopalswamy, and K. Shibasaki, editors, *Proceedings of the Nobeyama Symposium*, pages 129–134, December 1999.

G. A. Gary. Rendering Three-Dimensional Solar Coronal Structures. Sol. Phys., 174: 241–263, August 1997. doi: 10.1023/A:1004978630098.

M. K. Georgoulis and L. Vlahos. Coronal Heating by Nanoflares and the Variability of the Occurence Frequency in Solar Flares. ApJ, 469:L135, October 1996. doi: 10.1086/310283.

T. E. Gergely and M. R. Kundu. Decameter storm radiation. II. Sol. Phys., 41:163–188, March 1975. doi: 10.1007/BF00152966.

N. Gopalswamy, T. E. W. Payne, E. J. Schmahl, M. R. Kundu, J. R. Lemen, K. T. Strong, R. C. Canfield, and J. de La Beaujardiere. Transient microwave brightenings in solar active regions: Comparison between VLA and YOHKOH observations. ApJ, 437:522–528, December 1994a. doi: 10.1086/175015.

N. Gopalswamy, V. V. Zheleznyakov, S. M. White, and M. R. Kundu. Polarization

features of solar radio emission and possible existence of current sheets in active regions. Sol. Phys., 155:339–350, December 1994b. doi: 10.1007/BF00680599.

N. Gopalswamy, J. Zhang, M. R. Kundu, E. J. Schmahl, and J. R. Lemen. Fast Time Structure during Transient Microwave Brightenings: Evidence for Nonthermal Processes. ApJ, 491:L115, December 1997. doi: 10.1086/311063.

S. R. Habbal, N. E. Ellman, and R. Gonzalez. Synthesis mapping of a solar type I storm simultaneously at 90 and 20 centimeters with the VLA. ApJ, 342:594–603, July 1989. doi: 10.1086/167619.

H. S. Hudson. Solar flares, microflares, nanoflares, and coronal heating. Sol. Phys., 133: 357–369, June 1991. doi: 10.1007/BF00149894.

K. Iwai, Y. Miyoshi, S. Masuda, M. Shimojo, D. Shiota, S. Inoue, F. Tsuchiya, A. Morioka, and H. Misawa. Solar Radio Type-I Noise Storm Modulated by Coronal Mass Ejections. ApJ, 744:167, January 2012. doi: 10.1088/0004-637X/744/2/167.

K. Kai. The Structure, Polarization, and Spatial Relationship of Solar Radio Sources of Spectral Types I and III. Sol. Phys., 11:456–466, March 1970. doi: 10.1007/BF00153079.

K. Kai, D. B. Melrose, and S. Suzuki. *Storms*, pages 415–441. 1985.

Y. Katsukawa. Spatial and Temporal Extent of Solar Nanoflares and Their Energy Range. PASJ, 55:1025–1031, October 2003.

Y. Katsukawa and S. Tsuneta. Small Fluctuation of Coronal X-Ray Intensity and a Signature of Nanoflares. ApJ, 557:343–350, August 2001. doi: 10.1086/321636.

A. Kerdraon. Observation of small size solar radio bursts at metric wavelengths. A&A, 71:266–268, January 1979.

K.-L. Klein. Long-Duration Non-Thermal Energy Release in Flares and Outside Flares. In A. O. Benz and A. Krüger, editors, *Coronal Magnetic Energy Releases*, volume 444 of *Lecture Notes in Physics, Berlin Springer Verlag*, page 55, 1995. doi: 10.1007/3-540-59109-5_42.

K.-L. Klein. Suprathermal Electrons in Non-flaring Active Regions (Invited review). In C. E. Alissandrakis and B. Schmieder, editors, *Three-Dimensional Structure of Solar Active Regions*, volume 155 of *Astronomical Society of the Pacific Conference Series*, page 182, 1998.

S. Krucker and A. O. Benz. Energy Distribution of Heating Processes in the Quiet Solar Corona. ApJ, 501:L213, July 1998. doi: 10.1086/311474.

S. Krucker, A. O. Benz, M. J. Aschwanden, and T. S. Bastian. Location of Type I Radio Continuum and Bursts on YOHKOH Soft X-Ray Maps. Sol. Phys., 160:151–169, August 1995. doi: 10.1007/BF00679102.

M. R. Kundu, T. E. Gergely, A. Szabo, R. Loiacono, and S. M. White. Solar microbursts at meter-dekameter wavelengths. ApJ, 308:436–442, September 1986. doi: 10.1086/164513.

K. R. Lang and R. F. Willson. VLA observations of a solar noise storm. ApJ, 319:514–519, August 1987. doi: 10.1086/165474.

R. H. Levine. A New Theory of Coronal Heating. ApJ, 190:457–466, June 1974. doi: 10.1086/152898.

B. Li, I. H. Cairns, and P. A. Robinson. Simulations of coronal type III solar radio bursts: 3. Effects of beam and coronal parameters. *Journal of Geophysical Research (Space Physics)*, 114:A02104, February 2009. doi: 10.1029/2008JA013687.

R. P. Lin, R. A. Schwartz, S. R. Kane, R. M. Pelling, and K. C. Hurley. Solar hard X-ray microflares. ApJ, 283:421–425, August 1984. doi: 10.1086/162321.

Y. E. Litvinenko. An explanation for the flare frequency-energy dependence. Sol. Phys., 151:195–198, April 1994. doi: 10.1007/BF00654092.

R. K. Malik and C. Mercier. Motions, Relative Positions, and Sizes of Continua and Bursts in Solar Noise Storms. Sol. Phys., 165:347–375, May 1996. doi: 10.1007/BF00149719.

L. L. McCready, J. L. Pawsey, and R. Payne-Scott. Solar Radiation at Radio Frequencies and Its Relation to Sunspots. *Royal Society of London Proceedings Series A*, 190: 357–375, August 1947. doi: 10.1098/rspa.1947.0081.

D. B. Melrose. A plasma-emission mechanism for type I solar radio emission. Sol. Phys., 67:357–375, September 1980. doi: 10.1007/BF00149813.

D. B. Melrose. Depolarization of Radio Bursts Due to Reflection off Sharp Boundaries in the Solar Corona. ApJ, 637:1113–1121, February 2006. doi: 10.1086/498499.

D. B. Melrose and D. J. McLean. *Future prospects (in solar radiophysics).*, pages 469–471. 1985.

C. Mercier and G. Trottet. Coronal Radio Bursts: A Signature of Nanoflares? ApJ, 474: L65, January 1997. doi: 10.1086/310422.

E. N. Parker. Nanoflares and the solar X-ray corona. ApJ, 330:474–479, July 1988. doi: 10.1086/166485.

E. N. Parker. The Solar-Flare Phenomenon and the Theory of Reconnection and Annihiliation of Magnetic Fields. ApJS, 8:177, July 1963. doi: 10.1086/190087.

C. E. Parnell and P. E. Jupp. Statistical Analysis of the Energy Distribution of Nanoflares in the Quiet Sun. ApJ, 529:554–569, January 2000. doi: 10.1086/308271.

H. E. Petschek. Magnetic Field Annihilation. *NASA Special Publication*, 50:425, 1964.

J. G. Porter, J. M. Fontenla, and G. M. Simnett. Simultaneous ultraviolet and X-ray observations of solar microflares. ApJ, 438:472–479, January 1995. doi: 10.1086/175091.

R. Ramesh. Low Frequency (30-110 MHz) Radio Imaging Observations Of Solar Coronal Mass Ejections. In K. Dere, J. Wang, and Y. Yan, editors, *Coronal and Stellar Mass Ejections*, volume 226 of *IAU Symposium*, pages 83–94, 2005. doi: 10.1017/S1743921305000190.

R. Ramesh and G. A. Shanmugha Sundaram. Type I radio bursts and the minimum between sunspot cycles 22 and 23. A&A, 364:873–875, December 2000.

R. Ramesh, K. R. Subramanian, M. S. Sundararajan, and C. V. Sastry. The Gauribidanur Radioheliograph. Sol. Phys., 181:439–453, August 1998. doi: 10.1023/A:1005075003370.

R. Ramesh, C. Kathiravan, M. S. Sundararajan, I. V. Barve, and C. V. Sastry. A Low-Frequency (30 - 110 MHz) Antenna System for Observations of Polarized Radio Emission from the Solar Corona. Sol. Phys., 253:319–327, December 2008. doi: 10.1007/s11207-008-9272-y.

R. Ramesh, C. Kathiravan, I. V. Barve, G. K. Beeharry, and G. N. Rajasekara. Radio Observations of Weak Energy Releases in the Solar Corona. ApJ, 719:L41–L44, August 2010. doi: 10.1088/2041-8205/719/1/L41.

R. Ramesh, C. Kathiravan, and A. S. Narayanan. Low-frequency Observations of Polarized Emission from Long-lived Non-thermal Radio Sources in the Solar Corona. ApJ, 734:39, June 2011. doi: 10.1088/0004-637X/734/1/39.

R. Ramesh, C. Kathiravan, I. V. Barve, and M. Rajalingam. High Angular Resolution Radio Observations of a Coronal Mass Ejection Source Region at Low Frequencies

during a Solar Eclipse. ApJ, 744:165, January 2012. doi: 10.1088/0004-637X/744/2/165.

R. Ramesh, K. Sasikumar Raja, C. Kathiravan, and A. S. Narayanan. Low-frequency Radio Observations of Picoflare Category Energy Releases in the Solar Atmosphere. ApJ, 762:89, January 2013. doi: 10.1088/0004-637X/762/2/89.

J. P. Raulin and K.-L. Klein. Acceleration of electrons outside flares: Evidence for coronal evolution and height-extended energy release during noise storms. A&A, 281:536–550, January 1994.

C. V. Sastry. Polarization of the Thermal Radio Emission from Outer Solar Corona. ApJ, 697:1934–1939, June 2009. doi: 10.1088/0004-637X/697/2/1934.

C. J. Schrijver, A. M. Title, A. A. van Ballegooijen, H. J. Hagenaar, and R. A. Shine. Sustaining the Quiet Photospheric Network: The Balance of Flux Emergence, Fragmentation, Merging, and Cancellation. ApJ, 487:424, September 1997. doi: 10.1086/304581.

K. V. Sheridan, N. R. Labrum, W. J. Payten, G. J. Nelson, and E. R. Hill. Preliminary observations of solar radio sources with the Culgoora radioheliograph operating at four frequencies. Sol. Phys., 83:167–177, February 1983. doi: 10.1007/BF00148251.

T. Shimizu. Energetics and Occurrence Rate of Active-Region Transient Brightenings and Implications for the Heating of the Active-Region Corona. PASJ, 47:251–263, April 1995.

D. S. Spicer, A. O. Benz, and J. D. Huba. Solar type I noise storms and newly emerging magnetic flux. A&A, 105:221–228, January 1982.

J.-L. Steinberg and C. Caroubalos. Space Radioastronomy of Solar Bursts at all Frequencies. A&A, 9:329, December 1970.

J. L. Steinberg, C. Caroubalos, and J. L. Bougeret. STEREO-1 measurements of the beam pattern of 169 MHz type I bursts on November 18, 1971. A&A, 37:109–115, December 1974.

R. T. Stewart and N. R. Labrum. Meter-wavelength observations of the solar radio burst storm of August 17 22, 1968. Sol. Phys., 27:192–202, November 1972. doi: 10.1007/BF00151783.

P. Subramanian and P. A. Becker. Noise-Storm Continua: Power Estimates for Electron Acceleration. Sol. Phys., 225:91–103, November 2004. doi: 10.1007/s11207-004-3256-3.

G. A. S. Sundaram and K. R. Subramanian. Spectrum of Solar Type I Continuum Noise Storm in the 50-80 MHz Band and Plasma Characteristics in the Associated Source Region. ApJ, 605:948–959, April 2004. doi: 10.1086/382582.

P. A. Sweet. The Neutral Point Theory of Solar Flares. In B. Lehnert, editor, *Electromagnetic Phenomena in Cosmical Physics*, volume 6 of *IAU Symposium*, page 123, 1958.

S. Tsuneta and Y. Katsukawa. Coronal Heating with Sweet-Parker Picoflares. In T. Sakurai and T. Sekii, editors, *The Solar-B Mission and the Forefront of Solar Physics*, volume 325 of *Astronomical Society of the Pacific Conference Series*, page 289, December 2004.

L. Vlahos, M. Georgoulis, R. Kluiving, and P. Paschos. The statistical flare. A&A, 299: 897, July 1995.

D. G. Wentzel, P. Zlobec, and M. Messerotti. A test for large-angle radio scattering in the solar corona. A&A, 159:40–48, April 1986.

S. M. White, G. Thejappa, and M. R. Kundu. Observations of mode coupling in the

solar corona and bipolar noise storms. Sol. Phys., 138:163–187, March 1992. doi: 10.1007/BF00146202.

S. M. White, M. R. Kundu, T. Shimizu, K. Shibasaki, and S. Enome. The Radio Properties of Solar Active Region Soft X-Ray Transient Brightenings. ApJ, 450:435, September 1995. doi: 10.1086/176153.

J. P. Wild, S. F. Smerd, and A. A. Weiss. Solar Bursts. ARA&A, 1:291, 1963. doi: 10.1146/annurev.aa.01.090163.001451.

V. V. Zaitsev, H. Aurass, A. Kruger, and G. Mann. On the origin of noise storm continuum depressions. A&A, 291:990–1000, November 1994.

P. Zlobec, U. Koren, and M. Messerotti. Propagation effects in noise storm emission from polarization behavior. In A. O. Benz and P. Zlobec, editors, *Solar Radio Storms, CESRA Workshop #4*, page 89, 1982.

Chapter 4

Magnetic field measurements in solar corona

4.1 Introduction

The magnetic field (B) dominates the solar corona and plays a crucial role in the formation, evolution and dynamics of the structures in it. Magnetism is an external agency, due to which the coronal temperature remains in the order of > 1 MK. Magnetic field is the only source of huge energy release during the flares. Magnetism only channelizes the particles in the chromosphere/corona and responsible for coronal mass ejections. Magnetism of the Sun is responsible for the origin of the different events in the solar atmosphere. Magnetic field of the Earth is of the order of $\lesssim 1$ G which protects the planet from the charged particles by producing a shielding effect. However, magnetic field strength of the Sun and corona is so high. For example, in sunspots the magnetic field ≈ 1000 G. The magnetic field of the tachocline at the bottom of the convection zone is $\approx 10^5$ G. When the thermal pressure of the interior of the Sun exceeds the magnetic pressure, it creates a huge impact in the chromosphere and heliosphere. Such a phenomenon fills the corona with magnetic flux tubes of different densities and temperatures and therefore results in different events

in the solar atmosphere. It is clear that in order to understand the Sun, it is essential to understand the magnetic topology and also have to quantify it.

In this scenario, estimation of the magnetic field is a real challenge in front of solar physicists. As mentioned in chapter-1, radiation from different heights originates at different frequencies. In order to estimate the total magnetic field strength, it has to be observed in different wavelengths of the electromagnetic spectrum. At photospheric level, magnetic field of the sunspots are estimated using the Zeeman splitting method. It is some what possible to estimate the same at chromospheric level using the Hanle effect. But direct magnetic field measurements using Zeeman splitting and Hanle effects are not possible in low density coronal plasma. Direct measurement of the magnetic field in the corona is difficult, and some of the estimated magnetic fields have large uncertainties [Lin et al., 2000]. Brief review of the estimated magnetic fields are given by Lin et al. [2000] and some of them are discussed here. Magnetic fields estimated using Zeeman effect based on the 'green', Fe XIV ($\lambda = 530.3$ nm) observations was 13 ± 20 [Harvey, 1969]. Using spectro-polarimetric observations at near infrared line Fe XIII ($\lambda = 1074.7$ nm) the estimated magnetic field was 40 G [Kuhn, 1995]. Linear polarization measurements of the Hanle effect in coronal emission line were successful in making maps of the direction of coronal magnetic fields [Mickey, 1973, Querfeld and Smartt, 1984, Arnaud and Newkirk, 1987]. But, measurement using the Hanle effect is not sensitive to quantify the magnetic field [Casini and Judge, 1999, Lin et al., 2000]. In the outer corona, it is possible to estimate the magnetic field strength using the Faraday rotation of linearly polarized radio signals emitted by either natural sources, interplanetary space probes and spacecraft radio beacons etc [Stelzried et al., 1970] during the occultation by the solar corona.

But, in the middle corona, estimation of the magnetic field strength is difficult using direct measurements due to its low density. At these heights, Faraday effect and occultation observations were ruled out. However, there are some indirect methods to estimate the magnetic fields at these heights at radio wavelengths. One of them is the

polarization studies. Since most of the radio events are circularly polarized, it is possible to estimate the degree of circular polarization (dcp) which is mentioned in chapter-3. Adopting different techniques and by making use of dcp, magnetic field strength of the solar corona can be estimated. Since it is known that origin of the radio emissions in the solar corona can be due to different emission mechanisms like thermal bremsstrahlung, cyclotron emission, gyrosynchrotron, plasma emissions etc, brief discussion of emission mechanism were given in chapter-1. In the present chapter, by making use of the group of type III bursts coronal magnetic field strength at 1.3 $R_{\odot}$ was estimated. In the chapter 5, using the observations of moving type IV bursts in polarization mode, the magnetic field strength was estimated. Note that there are no direct methods to estimate the magnetic field in middle corona at any other frequencies. Estimation of magnetic field strengths in middle corona is possible using the low frequency spectroscopic or polarization measurements.

4.2 Magnetic field estimates

4.2.1 Magnetic field extrapolation technique

It is known that the photosphere, chromosphere and corona are coupled by the magnetic fields, the strength of the magnetic field is estimated using the mathematical extrapolation of the observed line of sight component of the photospheric magnetic field. Such measurements are made by assuming a potential or force free model [Schatten et al., 1969, Schrijver and Title, 2003]. By knowing the magnetic field strength of the photosphere, using the non-linear force-free extrapolation techniques, magnetic fields of the chromosphere and corona can be estimated. Such estimates are possible only by (1) building instruments capable of measuring the full vector magnetic field in the photosphere, and (2) development of algorithms for solving the magnetic boundary value problem in the

solar atmosphere under the constraint of nonlinear force free conditions which may be applicable to the 'quasi-static' (slowly varying) corona. Determination of the full magnetic vector at the photosphere requires spectro-polarimetric measurements with sophisticated modeling of the lower atmosphere which is challenging. Also, once the suitable magnetic data is available, the system of MaxwellâĂŹs equations plus a boundary measurement set then constitutes a mixed elliptic-hyperbolic boundary value problem which is remarkably difficult to solve [Gary, 1989, McClymont and Mikic, 1994, Amari et al., 1999]. Lee et al. [1999] used radio observations of an active region to estimate the coronal magnetic fields using a nonlinear force free field extrapolation of photosphere vector magnetogram.

4.2.2 Zeeman effect

Splitting of the spectral lines in the presence of the magnetic field is called Zeeman effect. In the absence of the magnetic field there is non splitting of the spectral lines takes place. But, if the magnetic field is non zero, then splitting of spectral lines takes place. If the wavelength of the line is λ, and displacement of the line from its original position is λ_0 then magnetic field strength can be estimated using the following equation 4.1

$$\lambda - \lambda_0 = \frac{e}{4\pi c m_e} g^* \lambda^2 B \tag{4.1}$$

where B is the magnetic field in Gauss, e is the charge of the electron, c is the speed of light, m_e is the mass of the electron, $g^* = gM - g'M'$ and g, g' and M, M' are the Lande factors and magnetic quantum numbers for lower and upper states of transitions, since the Zeeman splitting increases with the wavelength. Hence, separation of the Zeeman components can be seen clearly at infrared than visible. More details on this can be found in Stix [2002, pp 120]. Zeeman effect is insensitive to weak turbulent magnetic fields. Solar corona has a low density plasma with weak magnetic fields. Therefore, Zeeman splitting is not effective there.

4.2.3 Hanle effect

Magnetic field is not always required to generate polarized light. Scattering phenomenon also produces a polarized radiation. It is known that the main reason for the scattering polarization is the anisotropic illumination of the scattering particles. Therefore, even in the absence of a magnetic field, scattering of the anisotropic radiation on atoms and molecules produces linear polarization. Hanle effect modifies the linear polarization (either increase or decrease) and causes change in position angle of the resonance line scattering polarization in the presence of the magnetic field [Ignace, 2003]. Such a modification is a clue in diagnostic of magnetic fields in chromospheric range. Hanle effect is suitable for weak turbulent magnetic fields of the order of few Guass to 300 G. Estimates of the magnetic fields using Hanle effect in the solar corona is not well established.

4.2.4 Faraday rotation

Solar coronal magnetic field in the solar wind at distances of $2 - 15 R_{\odot}$ were possible using remote sensing observations. Using a Faraday effect acting on linearly polarized signal, while passing through the solar corona, magnetic fields can be measured. Also it is possible to estimate the magnetic fields by observing a suitable natural radio source or by using the spacecraft beacons during the solar occultation [Bird, 1981, 1982]. Such observations were made first time using Pioneer-6 spacecraft [Stelzried et al., 1970]. By measuring the orientation vector of the electric field of transmitted and received signals, the Faraday rotation is estimated. In other words, the angle of plane of polarization rotated by the medium, Θ is estimated from which one can estimate the magnetic field strength of the solar corona using the equation 4.2.

$$\Delta\psi = 2.6 \times 10^{-13} N_e B \lambda^2 L cos\Theta \tag{4.2}$$

where $\Delta\psi$ is in radians, N_e is the electron density in meters^{-3}, B is the magnetic field in tesla, positive when the field towards the observer, λ is the wavelength in meters, and L is the path length in meters [Kraus, 1973, Thompson et al., 2007]. In the outer corona ($> 3\ R_\odot$), it is possible to estimate the magnetic field using Faraday rotation technique [Patzold et al., 1987, Spangler, 2005, Ingleby et al., 2007]. Based on the observations from the HELIOS spacecraft and using the Faraday rotation technique at a heliocentric distance $3\ R_\odot \leq R \leq 10\ R_\odot$ magnetic field was estimated by Patzold et al. [1987]. It was about 57 mG at 6.2 $R_\odot$. Using the Faraday rotation technique on extragalactic radio sources in the heliocentric distance range $6\ R_\odot \leq R \leq 10\ R_\odot$, the estimated average magnetic field strength was 40 mG at a distance of 2 $R_\odot$ [Spangler, 2005].

4.2.5 Radio thermal and nonthermal emissions

The discussed direct methods of estimation of the magnetic fields in optical or infrared and radio emissions are limited to $< 1.2\ R_\odot$ which includes the photosphere and chromosphere. Estimation of the magnetic field in the outer corona is possible using Faraday rotation techniques as mentioned. There are no direct methods to estimate the magnetic field in the middle corona which begins from 1.2 $R_\odot$ to $< 3\ R_\odot$). Although, using the radio observations (from spectrograms and mainly based on polarization observations), estimates of the magnetic fields in this region are possible.

4.2.5.1 Thermal emissions

Presence of a magnetic field makes the solar corona anisotropic. Propagation of the unpolarized thermal radiation in an anisotropic medium the radiation splits into two opposite circularly polarized modes: ordinary and extraordinary modes. The differences in the total optical depth of the two modes depends on the prevailing magnetic field strength. Such phenomenon is a clue in estimation of the magnetic field. Using the observations

of the circularly polarized thermal radio emissions from the solar coronal streamers, estimated magnetic fields was 6 ± 2 G and 5 ± 1 G at 1.5 and 1.7 $R_{\odot}$ respectively [Ramesh et al., 2010b]. It was also shown recently that it is possible to extend radio methods in, inner corona at microwave frequencies through bremsstrahlung emission [Gelfreikh, 2004] to larger distances in the 'undisturbed' middle corona [Sastry, 2009, Ramesh et al., 2010b].

4.2.5.2 Non thermal emissions

Magnetic field estimates of the solar corona based on the observations of the non-thermal sources is possible by observing them in both Stokes I and V. As mentioned in chapter-1 type I, type III, type IV bursts originate due to the non-thermal emission mechanism. Their high brightness temperature is due to emission mechanism such as plasma oscillations, gyrosynchrotron etc. In this chapter, magnetic fields are estimated using the non-thermal quasi-periodic groups of type III bursts. Estimation of the magnetic field using dcp as well as quasi-periodicity are clearly discussed in the following sections of this chapter. Magnetic field estimates using the non-thermal noise storm/type I bursts were discussed in chapter-3 [Ramesh et al., 2010a, 2013, Sasikumar Raja and Ramesh, 2013]. Magnetic field strength was estimated using the polarization measurements of the moving type IV bursts which originates due to the gyrosynchrotron emission. The more detailed on the estimates of magnetic field using moving type IV bursts are described in chapter-5.

4.3 Radio solar type III bursts

Type III solar radio bursts are the signatures of accelerated electrons streaming outward through the corona and the interplanetary medium in the aftermath of flares and weak chromospheric brightenings. The electrons stream at speeds $\approx c/3$ along the open field magnetic field lines. Passage of such streams setups a plasma oscillations in the corona which are called 'Langmuir waves'. The plasma oscillations produces the radiation at

characteristic frequency. In the spectrograms, the drift speed ($\Delta f/\Delta t$) of type III bursts is 100 MHz s^{-1} in meter wave range. The above frequency drift results from the decrease of electron density and hence the plasma frequency, with distance in the solar atmosphere. Therefore bursts are seen first at higher frequencies (which is close to the solar disk) and then appears at low-frequencies in the solar atmosphere. The bursts occur over the frequency range from $\approx$ 1 GHz-10 kHz, corresponding to a distance range extending from the low corona to beyond the orbit of the Earth. The streams of electrons which are accelerated in inner corona retain their identity at a distance of 1 AU and even beyond. Recently, spacecraft observations like URAP-Ulysses, WAVES-WIND, WAVES-STEREO etc are used to study the interplanetary bursts including type III bursts. Type III bursts are further classified into different categories depending on their life time. An individual type III bursts are called 'isolated' type III bursts. Type III bursts occurring as a groups with certain a quasi-periodicity in the time scales < 5 minutes are called 'group' of type III bursts (also called type VI events). If they lasts for few minutes to hours, then they are said to be type III 'storms'.

4.3.1 Theory and origin of type III bursts

The origin and location of the type III bursts are shown in a Figure 3.3. The radio emission is widely accepted to be because of the following two-step process: (1) the excitation of high levels of plasma oscillations (Langmuir waves) by the propagating electron streams/beams and (2) subsequent conversion of these Langmuir waves into electromagnetic waves at the fundamental (F) and second harmonic (H) of the local plasma frequency. The H emission results from the coalescence of two Langmuir waves.

As mentioned previously, plasma oscillations can be excited by a variety of mechanisms. In the solar corona propagating electron beams and shocks can excite the plasma waves. The excited plasma waves are longitudinal oscillations and they are converted to

transverse oscillations through a nonlinear wave-wave interactions. The resultant transverse waves have the frequency approximately at f_p or $2f_p$ which are called fundamental or harmonic emissions respectively. Interaction/coalescence of a Langmuir wave with the low frequency wave like ion-acoustic wave gives the transverse wave. The resonance conditions of origin of fundamental emission is represented mathematically as follows,

$$f_L + f_S = f_T \tag{4.3}$$

$$k_L + k_S = k_T \tag{4.4}$$

Here, f_L, f_S and f_T are the frequencies of Langmuir wave, ion-acoustic wave and transverse wave respectively. Similarly k_L, k_S and k_T are the wave numbers of Langmuir wave, ion-acoustic wave and transverse wave respectively. Harmonic emission mechanism is due to the head on collision of two Langmuir waves. The resonance condition of harmonic emission mechanism is as follows,

$$f_L^1 + f_L^2 = f_T \tag{4.5}$$

$$k_L^1 + k_L^2 = k_T << k_L \tag{4.6}$$

Equations-4.5 and 4.6 can be rewritten as,

$$f_T \approx 2f_L \tag{4.7}$$

$$k_L^1 \approx -k_L^2 \tag{4.8}$$

4.3.2 Identification of F and H emissions

A distinguishing property of the type III bursts is their harmonic emissions. Theoretical explanation of emission mechanism of fundamental (F) emissions and harmonic (H) emissions are described in section-4.3.1. Wild et al. [1959] pointed out that both the F and the H type III solar radio emissions should generally be observable only for events which are close the center of the solar disk. Elsewhere, it should be a purely harmonic emission. This is because, F emission is more directive compared to the H emission. According to Caroubalos and Steinberg [1974], the ground based observations of type III radio bursts associated with sunspot regions located at a heliographic longitude $\gtrsim 70^o$ either side of East or West of the central meridian on the Sun, are primarily due to H emissions. Therefore, F component has a limiting directivity of $\pm 65^o$ from the central meridian on the Sun at 80 MHz [Suzuki and Sheridan, 1982]. One more important parameter to distinguish the F and H emissions is polarization property which is discussed in section-4.3.3. A similar result was recently reported by Thejappa et al. [2012] for the very low frequency solar type III radio bursts observed in the interplanetary medium.

4.3.3 Polarization properties

Most of the type III bursts are weak, circularly polarized with dcp < 0.15. However, some bursts, which are identified as due to fundamental plasma emission, have dcp ≈ 0.5 [Suzuki and Sheridan, 1978, Dulk and Suzuki, 1980]. Harmonic emission is observed mainly at low frequencies. Presence of the background magnetic field at the source region of type III radio bursts can give rise to a net dcp in the 'o' mode for the escaping radiation [Melrose and Sy, 1972, Melrose et al., 1978, 1980, Zlotnik, 1981]. The polarization observations of the H component of type III radio bursts are a better diagnostic tool to estimate the solar coronal magnetic field. This is because, the polarization of the F component is affected by propagation effects [Dulk and McLean, 1978]. Present chapter describes about the

observations of quasi-periodic harmonic type III bursts [Wild et al., 1963, Janssens et al., 1973, Mangeney and Pick, 1989, Zhao et al., 1991, Aschwanden et al., 1994, Ramesh et al., 2003, 2005]. From those observations coronal magnetic field was estimated using the empirical relationship between the magnetic field and the dcp for the harmonic plasma emission [Melrose et al., 1978]. Also the results are verified the results by independent estimations of the magnetic field using the quasi-periodic nature of the observed type III radio bursts [Ramesh et al., 2005]. Interestingly, both the methods give consistent results indicating the usefulness of solar radio observations to measure the coronal magnetic field at low frequencies.

4.4 Instrumental details

The radio data reported in the present work was obtained at 80 MHz on 20 September 2012, 18 January 2013 and 11 March 2013 with the heliograph [Ramesh et al., 1998, 1999b, 2006], the polarimeter [Ramesh et al., 2008], and the spectrograph [Ebenezer et al., 2001, 2007] at the GRO, India. Recently the heliograph array at GRO was expanded and it has the longest baseline length of $\approx$ 2560 meters in East-West and 882 meters in North-South direction. After the expansion, the heliograph (GRH) was renamed as Gauribidanur RAdioheliograPH (GRAPH) which is a T-shaped radio interferometer array which produces two dimensional images of the solar corona with an angular resolution of $\approx 5^{'} \times 7^{'}$ (R.A. $\times$ decl.) at 80 MHz. The integration time is $\approx$ 250 ms and the observing bandwidth is $\approx$ 2 MHz. The polarimeter (GRIP) is an East-West one-dimensional array operating in the interferometer mode and it responds to the integrated and polarized flux densities from the 'whole' Sun (see chapter-2 for more details). The half-power width of the response function (beam) of the GRIP is broad (compared to the Sun) in both right ascension/East-West direction which is $\approx 2^{o}$ at 80 MHz and declination/North-South direction ($\approx 90^{o}$). Therefore, a plot of the GRIP data is a time profile and observations are carried out in

transit mode. Therefore, time profile is essentially the 'East-West beam' of the array with an amplitude/correlation counts proportional to the strength of the emission from the 'whole' Sun at the observing frequency, weighted by the antenna gain in that direction. The advantage is that the radio sources responsible for the circularly polarized emission observed with the GRIP are identified using the two-dimensional radio heliograms obtained with the GRAPH around the same time. Note that linear polarization, if present at the coronal source region, tends to be obliterated at low radio frequencies because of the differential Faraday rotation of the plane of polarization within the observing bandwidth [Grognard and McLean, 1973]. The spectrograph antenna system which is called Gauribidanur LOw frequency solar Spectrograph (GLOSS) which produces the spectrograms of the solar corona. GLOSS is a total power instrument and the half-power width of its antenna response is $\approx 90^o \times 6^o$ (R.A. $\times$ decl.) at 80 MHz. The integration time is $\approx$ 100 ms and the observing bandwidth is $\approx$ 300 KHz at each frequency. The width of the response of GLOSS in hour angle is nearly independent of frequency. The Sun is a point source for both the GRIP and the GLOSS. All the above three instruments observe the Sun everyday during the interval 4 - 9 UT. Note that minimum detectable flux density of the GRAPH, GRIP and GLOSS are $\approx$ 20 Jy, 200 Jy, 3000 Jy, respectively.

4.5 Observations

Figure 4.1 describes about the temporal evolution of the Stokes I & V radio emission from the solar corona at 80 MHz as observed with the GRIP on 20 September 2012 during the interval 06:36-06:39 UT, i.e. around the transit of the Sun over GRO. It is noticeable that the presence of intense quasi-periodic emission in both the Stokes I and V time profiles and it has one to one correspondence. These are the characteristic signature of groups of type III solar radio bursts from the Sun [Suzuki and Dulk, 1985]. The observed individual type III bursts matches with the dynamic spectra in the frequency range of 85-35 MHz

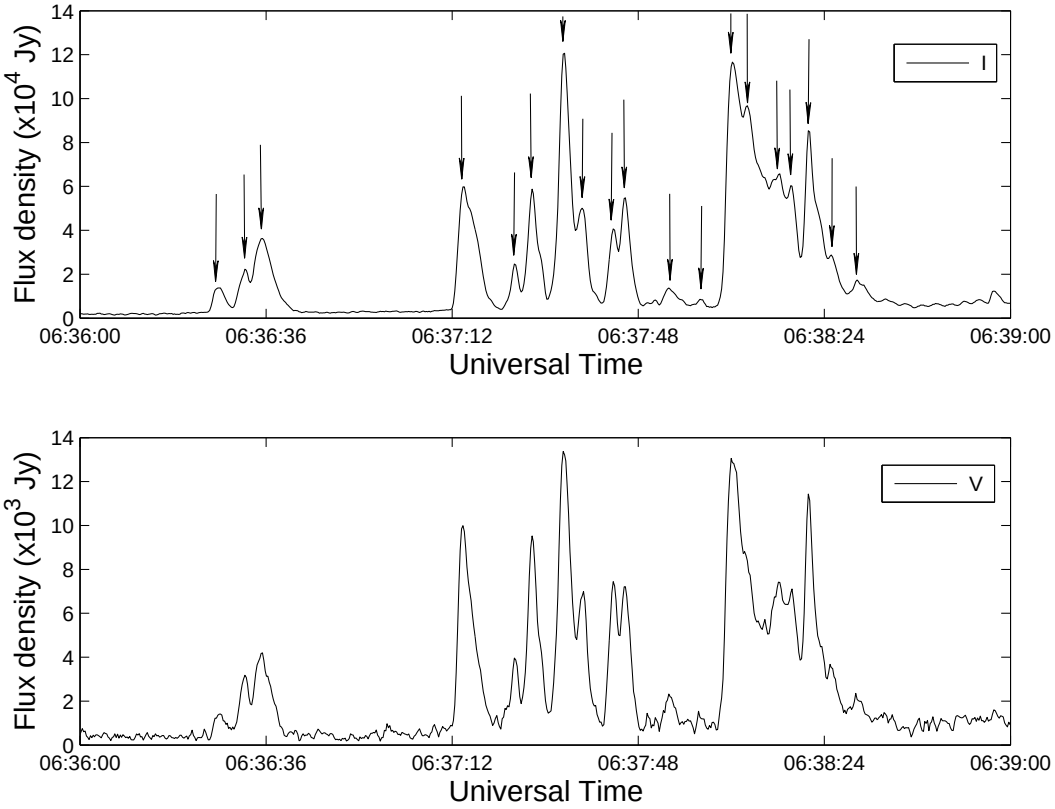

Fig. 4.1: GRIP observations of group of type III solar radio bursts on 20 September 2012 at 80 MHz in Stokes I (upper panel) and Stokes V (lower panel). The arrow marks indicate the individual bursts.

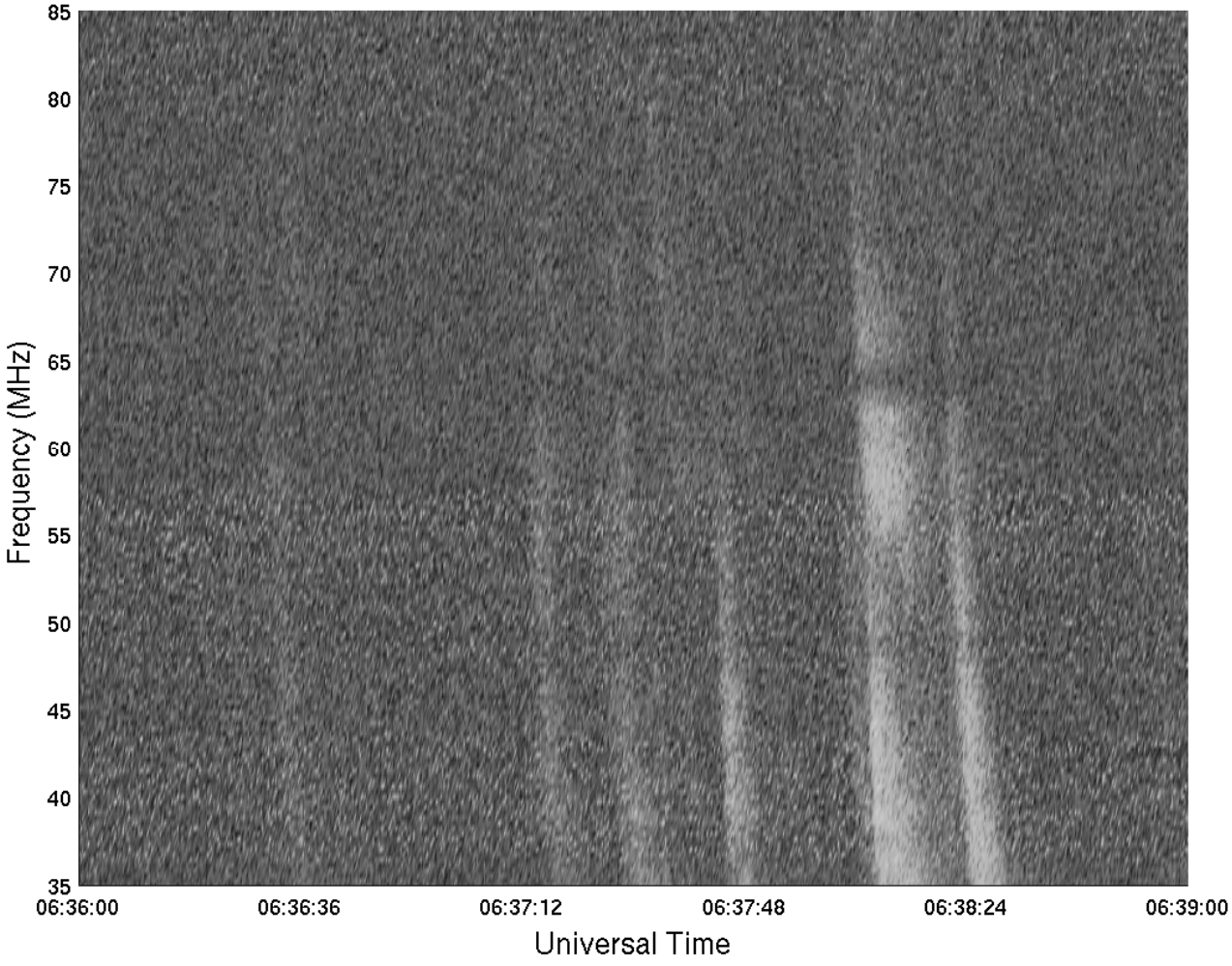

Fig. 4.2: GLOSS dynamic spectra (85-35 MHz) of the group of type III solar radio bursts in Figure 4.1.

obtained with GLOSS during the above interval. The spectrogram obtained with the GLOSS is shown in Figure 4.2. The peak Stokes I and V flux densities in Figure 4.1 are $\approx 1.2 \times 10^5$ Jy and 1.6×10^4 Jy respectively. The corresponding dcp was obtained using the following formula,

$$dcp = |\mathrm{V_{flux}}|/I_{flux} \tag{4.9}$$

The dcp of the event obtained is ≈ 0.11. Note the average flux density of the type III solar radio bursts reported in the literature is typically $\approx 10^7$ Jy [Suzuki and Dulk, 1985]. In the present case, the average flux density is two orders of magnitude higher than the peak flux density of the type III burst of 20 September 2012, indicating that the latter is a weak event. The estimated average periodicity of the radio emission in Figure 4.1 is ≈ 4.5 sec, in both Stokes I & V. The location of the source of the bursts was identified from the radio heliogram obtained with the GRAPH around the same time. The heliograms obtained with the GRAPH was shown in Figures 4.3 and 4.4. The Figure 4.3 is the heliogram generated before peaking of the event. Peak of the event in shown in Figure 4.4. One can notice the bursts originated close to the solar limb. They were associated with a SF class Hα flare from AR 11574[1] located at S25W69[2]. A shift in the solar radio source position due to ionospheric effects is expected to be $\lesssim 0.1\ R_\odot$ at 80 MHz in the hour angle range is $\pm$ 2 hr [Stewart and McLean, 1982]. The present observations were carried out close to the transit of the Sun over the local meridian at GRO. Similarly, the effects of scattering, (irregular refraction due to density inhomogeneities in the solar corona) on the observed source position are also considered to be small at 80 MHz compared to lower frequencies [Aubier et al., 1971, Bastian, 2004]. The shift in position of discrete solar radio sources due to scattering is expected to be $\lesssim 0.2\ R_\odot$ at 80 MHz [Riddle, 1974, Robinson, 1983, Thejappa et al., 2007]. Ray tracing calculations employing realistic coronal electron density models and density fluctuations

[1] http://www.swpc.noaa.gov/
[2] http://www.lmsal.com/solarsoft/latest_events/

show that the turning points of the rays that undergo irregular refraction almost coincide with the location of the plasma ('critical') layer in the non-scattering case even at 73.8 MHz [Thejappa and MacDowall, 2008]. Obviously, the situation should be better at 80 MHz. Note that high angular resolution observations of the solar corona indicate that discrete radio sources of angular size $\approx 1'$ are present in the solar atmosphere from where low frequency radio radiation originates [Kerdraon, 1979, Lang and Willson, 1987, Willson et al., 1998, Ramesh et al., 1999a, Ramesh and Sastry, 2000, Ramesh and Ebenezer, 2001, Mercier et al., 2006, Kathiravan et al., 2011, Ramesh et al., 2012]. The projection effects are also expected to be minimal since in the present case only the limb events are used (see for eg. Figure 4.4). The details related to the type III radio burst observed on 20 September 2012 are described above and the other two events are listed in Table 4.1.

4.6 Estimation of magnetic field (B)

4.6.1 From the relationship between dcp and B for type III solar radio bursts

In the present case, the heliographic longitude of the sunspot regions associated with the type III radio bursts are all $\gtrsim 70^o$ (see Table 4.1). The estimated averaged dcp of type III bursts are for the three events close ≈ 0.11 which correspond to the circularly polarized H component of the type III bursts. Note that for the F component, the reported average dcp ≈ 0.35 [Dulk and Suzuki, 1980]. The above arguments on the directivity and the dcp indicate that the type III bursts observed in the present case are due to H emissions. Under such circumstances, the magnetic field (B) near the source region of the bursts can be calculated using the following relationship [Suzuki and Sheridan, 1978, Dulk and Suzuki, 1980, Mercier, 1990, Reiner et al., 2007, Melrose et al., 1978, Zlotnik, 1981, Ramesh et al.,

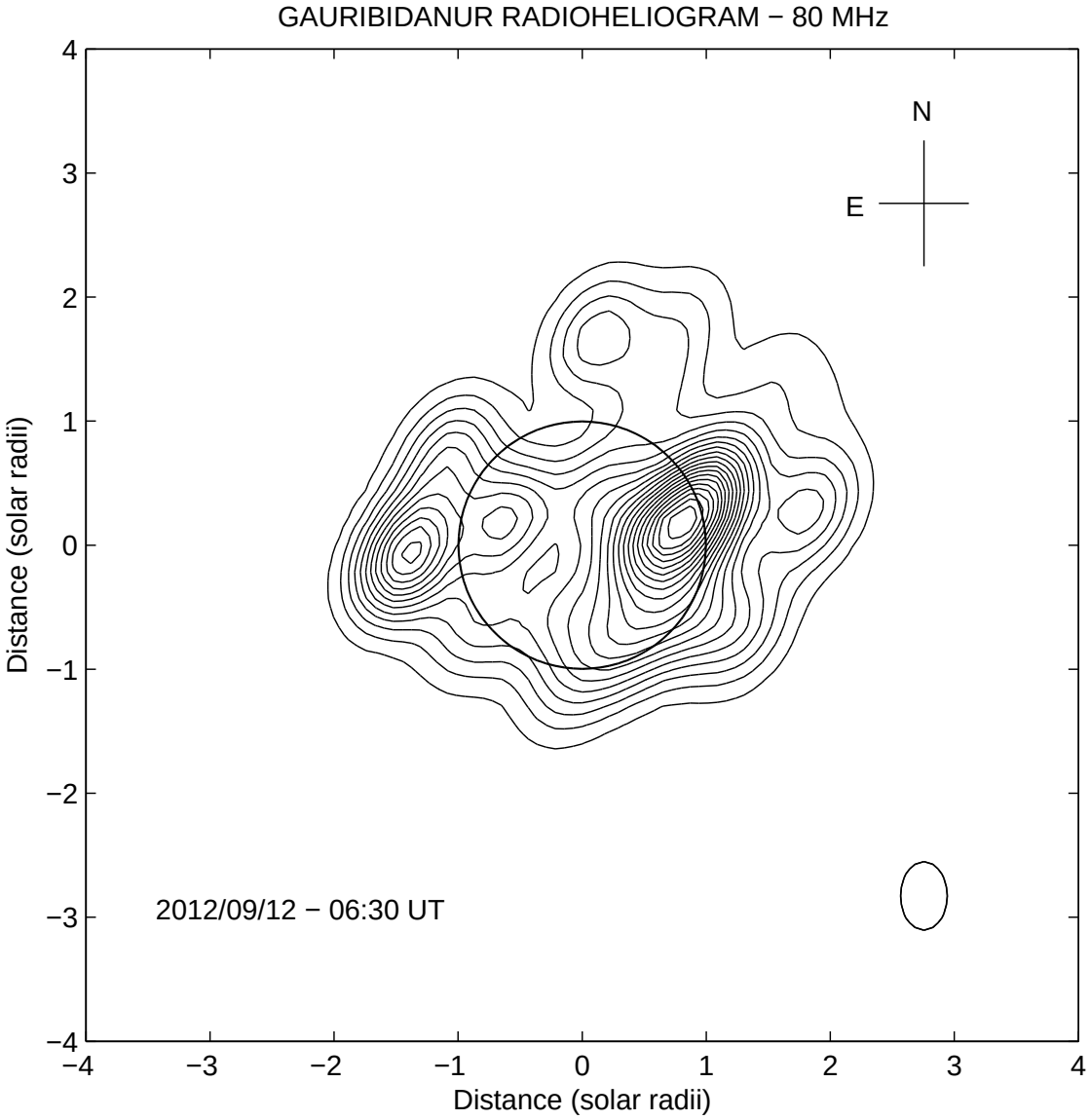

Fig. 4.3: GRAPH radio heliogram obtained on 20 September 2012 around 06:30 UT, prior to the quasi-periodic type III burst emission in Figure 4.1. The open circle at the center represents the solar limb. The size of the GRAPH beam at 80 MHz is shown near the lower right. The intense discrete source close to the West limb is the source region of the type III bursts in Figures 4.1 and 4.2.

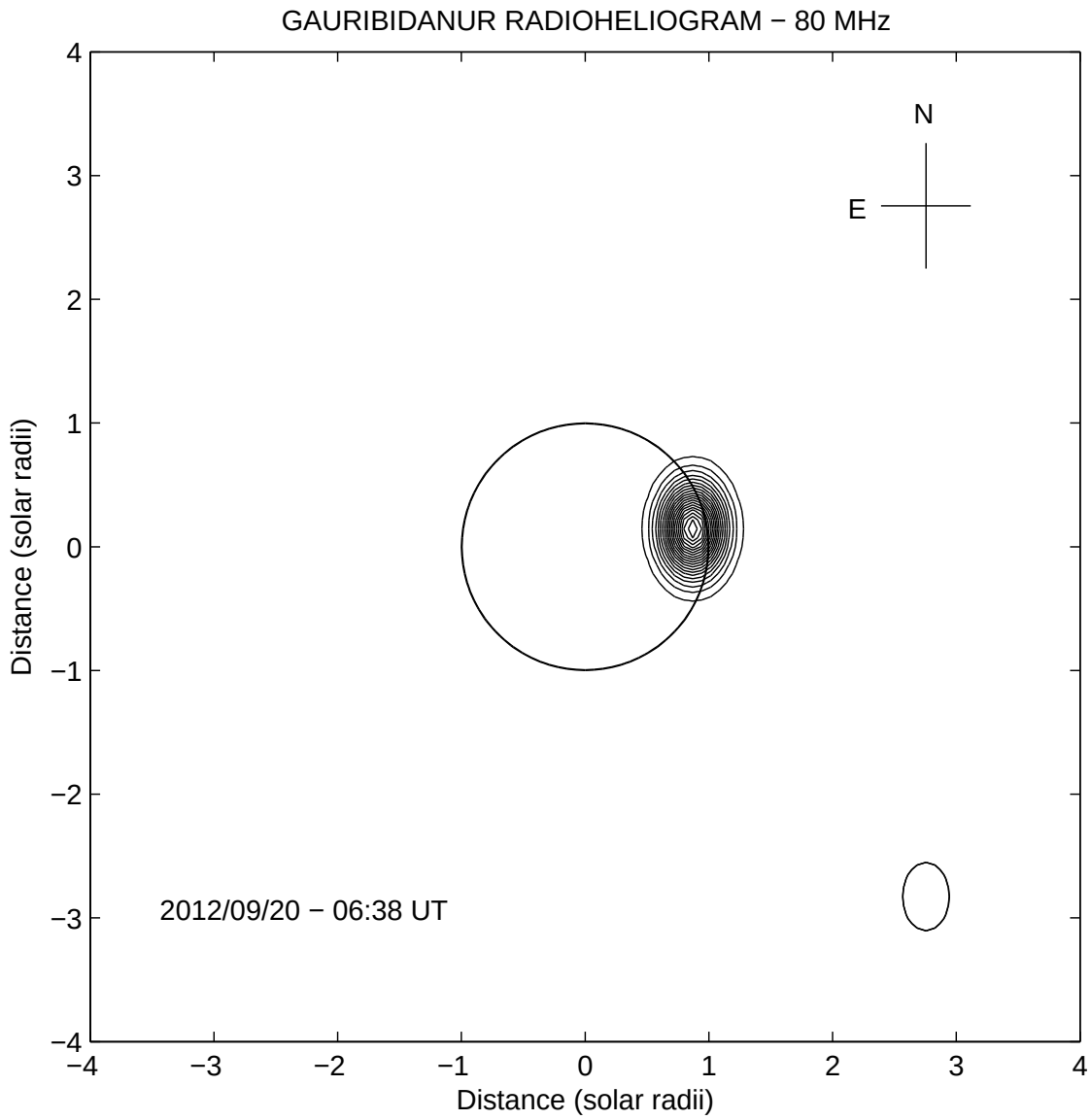

Fig. 4.4: Same as Figure 4.3 but obtained during the peak phase of the burst in Figure 4.1 at ≈ 06:38 UT.

2010b].

$$B = \frac{f_p \times dcp}{2.8\ a(\theta, \theta_0)} \tag{4.10}$$

where f_p is the plasma frequency in MHz and B is in Gauss. $a(\theta, \theta_0)$ is a slowly varying function that depends on viewing angle θ between the magnetic field component and the line of sight direction, and θ_0 is the angular distribution of the Langmuir waves. The viewing angle and angular distribution of Langmuir waves are shown schematically in Figure 4.5

In the present case, θ is varying from $70^o - 90^o$ which is shown in Table 4.1. It is assumed that $f_p = 40$ MHz, since the observed emission is at 80 MHz which is most likely the H component. Langmuir waves are considered to be confined to a small range of angles, i.e., a cone of opening angle $\theta_0 \approx 10^o - 30^o$ in the magnetic field direction for harmonic type III emission in the 'o' mode [Melrose et al., 1978, Dulk and Suzuki, 1980, Willes and Melrose, 1997, Benz, 2002]. Assuming the average value i.e., $\theta_0 \approx 20^o$, the estimated $a(\theta, \theta_0) \approx 0.4$ in the aforementioned range of θ [Melrose et al., 1980, Gary, 1982, Suzuki and Dulk, 1985]. Note that the Figure 4.5 shows the variation of $a(\theta, \theta_0)$ for different values of θ and θ_0 for both forward and loss cones. The full and dashed lines correspond to 'o' and 'e' modes radiation respectively.

The magnetic field was estimated using equation 4.10 for the type III events reported in the present work and are listed in Table 4.1. Note that the error of ± 1 G in the B values is because of the above uncertainty in $a(\theta, \theta_0)$. Figure 4.7 shows the magnetic field values corresponding to the individual bursts in the quasi-periodic type III burst emission observed on 20 September 2012 which is shown in Figure 4.1. They remain approximately constant, within the error limits, during the duration of the quasi-periodic emission. It is found that magnetic field values corresponding to the bursts observed on 18 January 2013 and 11 March 2013 also exhibited a similar trend.

–

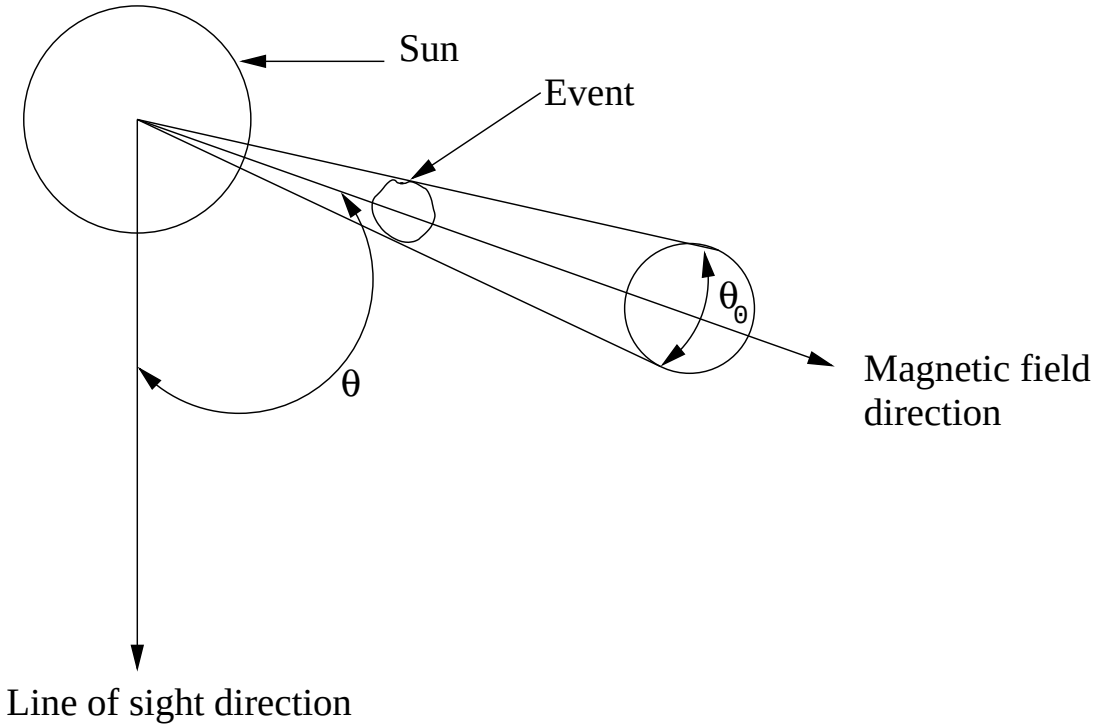

Fig. 4.5: The Figure shows the viewing angle θ which is the angle between the magnetic field direction and the line of sight direction. The angular distribution of Langmuir waves (θ_0) is also shown schematically.

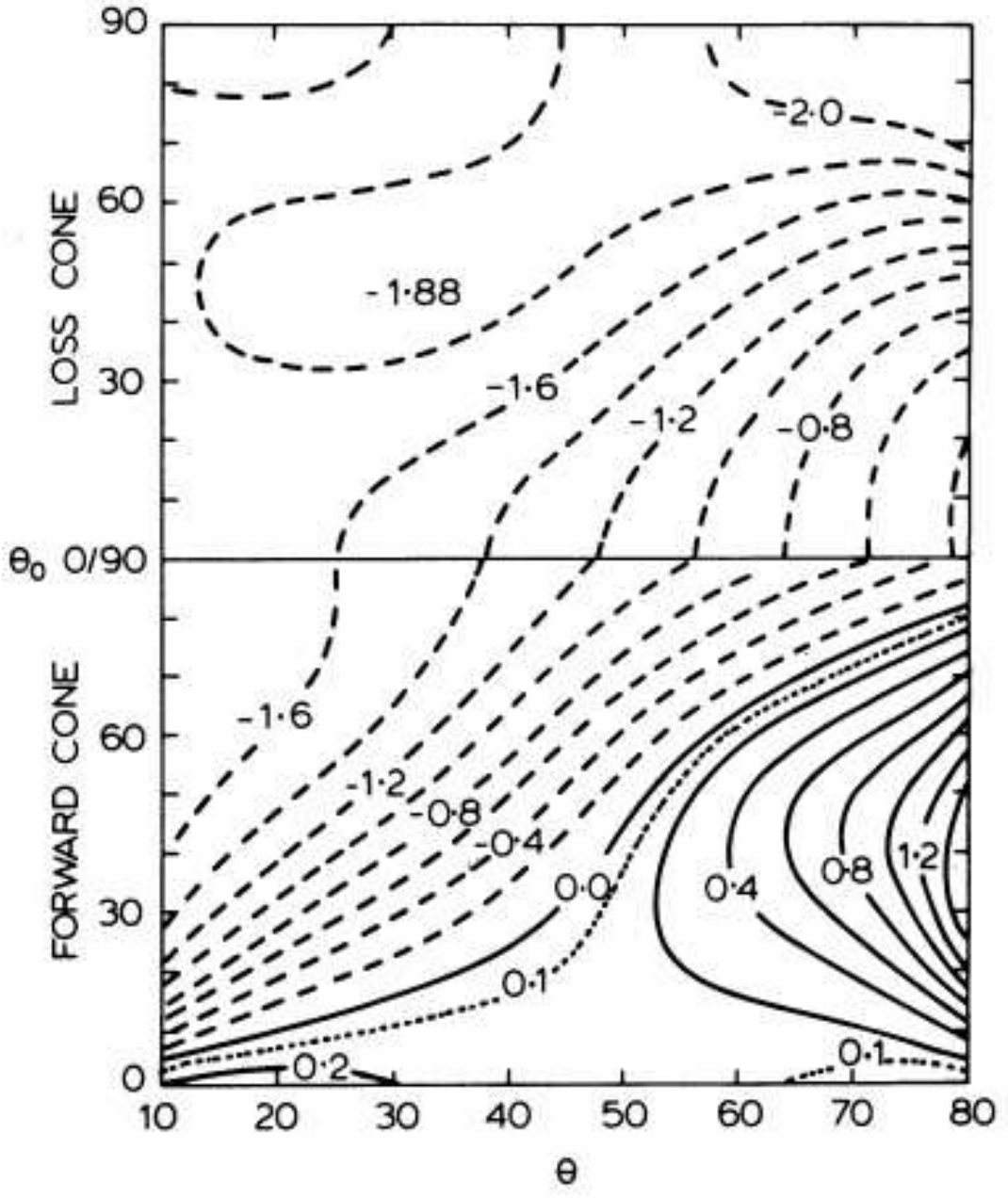

Fig. 4.6: The contours shows the variation of $a(\theta, \theta_0)$ for different values of θ and θ_0 for both the forward and loss cones. The full and dashed lines represents 'o' mode and 'e' mode radiation respectively. Image Credit: [Melrose et al., 1980]

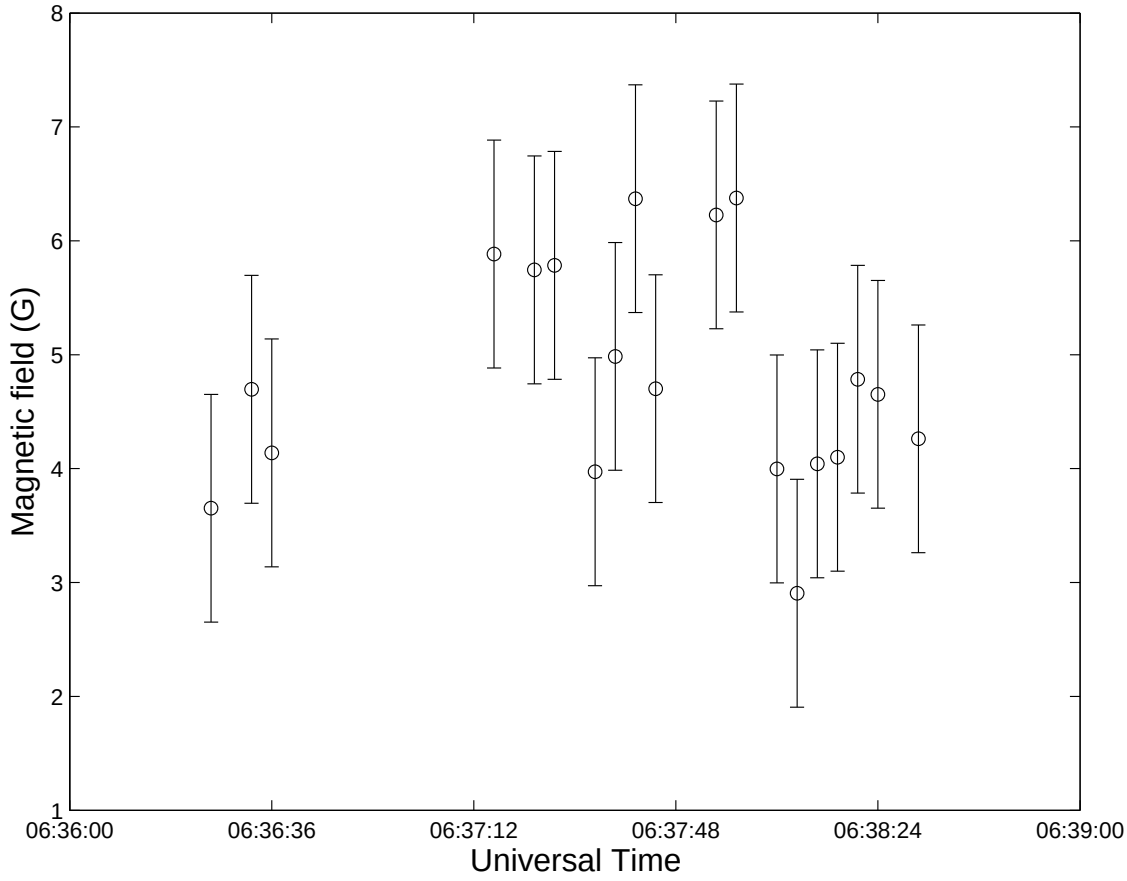

Fig. 4.7: B values corresponding to the individual type III bursts in the quasi-periodic emission in Figure 4.1, based on the relationship between B and dcp.

4.6.2 From the quasi-periodicity of the observed type III radio bursts

Type III bursts are regularly seen in spectrograms as either isolated or in groups and some times as storms. While the isolated bursts have a life-time of about few seconds at any given frequency as mentioned earlier and the groups of bursts last for ≈ 5 minutes [Suzuki and Dulk, 1985]. Groups of type III bursts are generally associated with flares which are observed in X-rays and/or Hα. Type III bursts are the classic signatures of the impulsive phase of flares in which the radiation is primarily non-thermal. It is believed that each individual burst is due to the radiation associated with electron streams moving outwards through the corona along large scale diverging magnetic field lines connected to a common acceleration/injection site [Mercier, 1975, Pick and Ji, 1986]. The presence of non-thermal bursts is a clear indication of particle acceleration during an event. Since the emission mechanism is coherent in nature, the generation of radio emission by non-thermal electron beams is very efficient. In this case, observed events are the group of type III bursts which lasted in 5 minutes. Figure 4.1 shows the time profiles of type III bursts in both Stokes I and V. One can clearly notice that the bursts are quasi-periodic in nature. One of the suggested reasons for the quasi-periodicity in the type III solar radio burst emission is the modulation of the electron beam acceleration/injection process responsible for the type III emission by quasi-periodic oscillations setup by propagating MHD waves in the corona [Aschwanden et al., 1994, Ramesh et al., 2005, Nindos and Aurass, 2007].

The term quasi-periodicity or pulsations in solar radio physics refers to the quasi-periodic amplitude variations in the time profile of the observed radio flux at any particular observing frequency. The associated physical mechanisms have been classified into three categories as on date: (1) modulation of the emission by coronal loop oscillations, (2) intrinsic oscillations of the emission created by oscillatory wave-wave interactions and wave-particle interactions, and (3) modulation of electron acceleration/injection process

responsible for the emission [Aschwanden, 1987, Nindos and Aurass, 2007]. Among all three categories, category (2) can be ruled out in the present case, since they apply primarily to fundamental 'o' mode and harmonic extra-ordinary mode ('e' mode) whereas the type III bursts reported in the present work correspond to harmonic 'o' mode as mentioned in Aschwanden and Benz [1988]. In view of this, it has been carried out the calculations for categories (1) and (3) in the reminder of this section. Laboratory experiments and numerical simulations reveal that the release of magnetic energy by reconnection must be considered as a highly time dependent process (see for eg. Pick and van den Oord [1990]). According to Kliem et al. [2000], the temporal variations in the radio burst flux are caused by modulations of the particle acceleration in a highly dynamic reconnection process. Also a similar model, i.e. quasi-periodic reconnection and particle injection was reported by Zlotnik et al. [2003]. Note that even a very small ($\approx 2\%$) quasi-periodic modulation of the magnetic field is sufficient for periodic electron acceleration. Both these models belong to the category (3) as mentioned above and were successful in explaining the associated observations. The modulation is likely to be communicated on a magnetohydrodynamic (MHD) time scale in the acceleration region as mentioned [Tajima et al., 1987, Aschwanden et al., 1994, Kliem et al., 2000, Asai et al., 2001]. In such a case, the corresponding Alfvén speed (v_A) can be estimated as follows

$$v_A \approx \frac{l}{p} \tag{4.11}$$

where p is the period of the quasi-periodic emission in seconds (s) and $l \approx 10000$ km is the typical dimension of the region over which the type III radio burst producing electrons are injected [Lantos et al., 1984, Aschwanden, 2002]. It is possible that the individual bursts that are temporally separated in a type III group are also spatially fragmented within the same acceleration region [Pick and van den Oord, 1990, Vlahos and Raoult, 1995, Isliker et al., 1998]. Considering category (1) where the observed quasi-periodicities are caused by the MHD oscillations of the associated coronal loops, the corresponding relationship

for the Alfvén speed is given Roberts et al. [1984],

$$v_A = 2.6\frac{a}{p} \tag{4.12}$$

where, $a \approx 3500$ km is the width of the coronal loop. According to Aschwanden [1987], the quasi-periodic emission observed in the upper part of the corona from where the radio emission originates at meter-decameter wavelengths, particularly those due to plasma processes as in the present case, are best described by the above model. Asai et al. [2001] showed that the quasi-periodic pulsation observed by them in the microwave range are due to the modulation of the acceleration/injection rate of the non thermal electrons by the oscillations in the associated coronal loops. Once v_A is known in either category (1) or (3), the associated magnetic field (B) can be calculated from the equation which is mentioned in equation 3.21. By substituting the values given in that section, equation 4.13 can be derived.

$$v_A = 2.05 \times 10^6 \; B \; N_e^{-1/2} \tag{4.13}$$

Where, N_e is the electron density in units of cm^{-3} and can be estimated using the relationship,

$$f_p = 9 \times 10^{-3} N_e^{1/2} \tag{4.14}$$

Note that the estimated values of v_A in equation 4.12 are in units of km s^{-1}. The v_A and B values estimated using equations 4.12 and 4.13 for the type III events reported in the present work are listed in Table 4.1. Equations 4.12 and 4.13 result in nearly the same values for both v_A and B for all the events.

Table 4.1. Parameters related to the group of type III radio bursts observed with the Gauribidanur facilities

S.No .	Date	Time (UT)	Period p (s)	Alfvén speed v_A (km/s)	Sunspot heliographic co-ordinates	Viewing angle θ (deg)	dcp	Magnetic field B (G)	
								Harmonic emission[a]	Quasi-periodic emission[b]
1	20 Sep 2012	06:35-06:38	4.5	2022	S25W69	71	0.13	3.7 ± 1	4.4 ± 0.3
2	18 Jan 2013	06:51-06:57	6.4	1422	N18W88	88	0.08	2.3 ± 1	3.1 ± 0.3
3	11 Mar 2013	07:00-07:03	4.8	1896	N10E88	88	0.14	4.0 ± 1	4.1 ± 0.3

[a]See Section-4.6.1 for details.

[b]See Section4.6.2 for details.

4.7 Summary and Conclusions

In this chapter, estimates of the coronal magnetic field using low frequency (80 MHz) radio observations of quasi-periodic harmonic type III burst emission associated with sunspot regions close to the solar limb was discussed. The data were obtained with the heliograph, the polarimeter and the spectrograph at the Gauribidanur radio observatory. Though several type III bursts are observed everyday with the aforementioned suite of instruments, the events with $dcp \lesssim 0.15$ was selected for the study and whose associated source region is close to the limb of the Sun. The above are the criteria to identify a harmonic type III burst as mentioned previously. Also it is limited the data which obtained close to the transit of the Sun over the local meridian at Gauribidanur in order to minimize errors in the source position due to propagation effects. Independent approaches to estimate the magnetic field was adopted: (1) based on the relationship between the dcp and the B for harmonic type III radio burst emission, and (2) using the quasi-periodicity in the observed type III radio burst emission. Interestingly, both the methods give the approximately same result i.e., the average $B \approx 4.2$ G. Note that the often referred empirical relationship for the coronal magnetic field [Dulk and McLean, 1978] predicts $B \approx 3$ G at 80 MHz. It is assumed that the 80 MHz plasma level to be located at radial distance $r \approx 1.3$ $R_\odot$ in the solar atmosphere for the above calculation [Ramesh et al., 2011]. Note that Lin et al. [2004] had measured $B \approx 4$ G at $r \approx 1.1$ $R_\odot$ using Zeeman splitting observations of the Fe XIII λ1075 nm coronal emission line from an active region close to the solar limb. Using the equation 4.15 which was mentioned in Dulk and McLean [1978], the estimated magnetic field was $B \approx 3.1$ G at $r \approx 1.3$ $R_\odot$. Note that the equation 4.15 is valid in the height range of $1.02 - 10$ $R_\odot$.

$$B = 0.5 \left(\frac{r}{R_\odot} - 1 \right)^{-1.5} \text{ G} \tag{4.15}$$

The present estimates are also in reasonable agreement with the magnetic field associated with the coronal streamers which is $\approx 5 \pm 1$ G at 77 MHz at $r \approx 1.5$ $R_\odot$. Note the type III radio bursts are considered to be closely associated with the coronal streamers [Kundu et al., 1983]. Also the estimated v_A in the present case (see Table 4.1) are consistent with the corresponding values reported by Gopalswamy et al. [2001], Vršnak et al. [2002] for the active region solar corona.

References

T. Amari, T. Z. Boulmezaoud, and Z. Mikic. An iterative method for the reconstruction-break of the solar coronal magnetic field. I. Method for regular solutions. A&A, 350: 1051–1059, October 1999.

J. Arnaud and G. Newkirk, Jr. Mean properties of the polarization of the Fe XIII 10747 A coronal emission line. A&A, 178:263–268, May 1987.

A. Asai, M. Shimojo, H. Isobe, T. Morimoto, T. Yokoyama, K. Shibasaki, and H. Nakajima. Periodic Acceleration of Electrons in the 1998 November 10 Solar Flare. ApJ, 562:L103–L106, November 2001. doi: 10.1086/338052.

M. J. Aschwanden. Theory of radio pulsations in coronal loops. Sol. Phys., 111:113–136, March 1987. doi: 10.1007/BF00145445.

M. J. Aschwanden. Particle acceleration and kinematics in solar flares - A Synthesis of Recent Observations and Theoretical Concepts (Invited Review). Space Sci. Rev., 101:1–227, January 2002. doi: 10.1023/A:1019712124366.

M. J. Aschwanden. *Physics of the Solar Corona. An Introduction*. Praxis Publishing Ltd, August 2004.

M. J. Aschwanden and A. O. Benz. On the Electron-Cyclotron Maser Instability. II. Pulsations in the Quasi-stationary State. ApJ, 332:466, September 1988. doi: 10.1086/166670.

M. J. Aschwanden, A. O. Benz, and M. L. Montello. Coherent-phase or random-phase acceleration of electron beams in solar flares. ApJ, 431:432–449, August 1994. doi: 10.1086/174497.

M. Aubier, Y. Leblanc, and A. Boischot. Observations of the Quiet Sun at Decameter Wavelengths - Effects of Scattering on the Brightness Distribution. A&A, 12:435, June 1971.

T. S. Bastian. Low-frequency solar radiophysics with LOFAR and FASR. Planet. Space Sci., 52:1381–1389, December 2004. doi: 10.1016/j.pss.2004.09.015.

A. Benz, editor. *Plasma Astrophysics, second edition*, volume 279 of *Astrophysics and Space Science Library*, June 2002.

M. K. Bird. Coronal Sounding with Pulsars. In H. Rosenbauer, editor, *Solar Wind 4*, page 78, 1981.

M. K. Bird. Coronal investigations with occulted spacecraft signals. Space Sci. Rev., 33: 99–126, March 1982. doi: 10.1007/BF00213250.

C. Caroubalos and J. L. Steinberg. Direct Measurements of the Directivity of Type i and Type III Radiation at 169 MHZ (presented by C. Caroubalos). In G. A. Newkirk, editor, *Coronal Disturbances*, volume 57 of *IAU Symposium*, page 239, 1974.

R. Casini and P. G. Judge. Spectral Lines for Polarization Measurements of the Coronal Magnetic Field. II. Consistent Treatment of the Stokes Vector forMagnetic-Dipole Transitions. ApJ, 522:524–539, September 1999. doi: 10.1086/307629.

G. A. Dulk and D. J. McLean. Coronal magnetic fields. Sol. Phys., 57:279–295, April 1978. doi: 10.1007/BF00160102.

G. A. Dulk and S. Suzuki. The position and polarization of Type III solar bursts. A&A, 88:203–217, August 1980.

E. Ebenezer, R. Ramesh, K. R. Subramanian, M. S. SundaraRajan, and C. V. Sastry. A new digital spectrograph for observations of radio burst emission from the Sun. A&A, 367:1112–1116, March 2001. doi: 10.1051/0004-6361:20000540.

E. Ebenezer, K. R. Subramanian, R. Ramesh, M. S. Sundararajan, and C. Kathiravan. Gauribidanur radio array solar spectrograph (GRASS). *Bulletin of the Astronomical Society of India*, 35:111–119, June 2007.

D. E. Gary. *Radio emission from solar and stellar coronae*. PhD thesis, Colorado Univ., Boulder., March 1982.

G. A. Gary. Linear force-free magnetic fields for solar extrapolation and interpretation. ApJS, 69:323–348, February 1989. doi: 10.1086/191316.

G. B. Gelfreikh. Coronal Magnetic Field Measurements Through Bremsstrahlung Emission. In D. E. Gary and C. U. Keller, editors, *Astrophysics and Space Science Library*, volume 314 of *Astrophysics and Space Science Library*, page 115, September 2004. doi: 10.1007/1-4020-2814-8_6.

N. Gopalswamy, A. Lara, M. L. Kaiser, and J.-L. Bougeret. Near-Sun and near-Earth manifestations of solar eruptions. J. Geophys. Res., 106:25261–25278, November 2001. doi: 10.1029/2000JA004025.

R. J. M. Grognard and D. J. McLean. Non-Existence of Linear Polarization in Type III Solar Bursts at 80 MHz. Sol. Phys., 29:149–161, March 1973. doi: 10.1007/BF00153446.

J. W. Harvey. *Magnetic Fields Associated with Solar Active-Region Prominences.* PhD thesis, Colorado Univ., Boulder., 1969.

R. Ignace. The Hanle Effect as a Magnetic Diagnostic. In L. A. Balona, H. F. Henrichs, and R. Medupe, editors, *Magnetic Fields in O, B and A Stars: Origin and Connection*

to Pulsation, Rotation and Mass Loss, volume 305 of *Astronomical Society of the Pacific Conference Series*, page 28, 2003.

L. D. Ingleby, S. R. Spangler, and C. A. Whiting. Probing the Large-Scale Plasma Structure of the Solar Corona with Faraday Rotation Measurements. ApJ, 668:520–532, October 2007. doi: 10.1086/521140.

H. Isliker, L. Vlahos, A. O. Benz, and A. Raoult. A stochastic model for solar type III bursts. A&A, 336:371–380, August 1998.

T. J. Janssens, K. P. White, and R. M. Broussard, III. Quasi-Periodic Structure in Solar Microwave Bursts. Sol. Phys., 31:207–217, July 1973. doi: 10.1007/BF00156083.

C. Kathiravan, R. Ramesh, I. V. Barve, and M. Rajalingam. Radio Observations of the Solar Corona During an Eclipse. ApJ, 730:91, April 2011. doi: 10.1088/0004-637X/730/2/91.

A. Kerdraon. Observation of small size solar radio bursts at metric wavelengths. A&A, 71:266–268, January 1979.

B. Kliem, M. Karlický, and A. O. Benz. Solar flare radio pulsations as a signature of dynamic magnetic reconnection. A&A, 360:715–728, August 2000.

J. D. Kraus. *Radio astronomy.* 1973.

J. R. Kuhn. Infrared Coronal Magnetic Field Measurements. In J. R. Kuhn and M. J. Penn, editors, *Infrared tools for solar astrophysics: What's next?*, page 89, 1995.

M. R. Kundu, T. E. Gergely, P. J. Turner, and R. A. Howard. Direct evidence of type III electron streams propagating in coronal streamers. ApJ, 269:L67–L71, June 1983. doi: 10.1086/184057.

K. R. Lang and R. F. Willson. VLA observations of a solar noise storm. ApJ, 319:514–519, August 1987. doi: 10.1086/165474.

P. Lantos, M. Pick, and M. R. Kundu. Coronal extension of flaring region magnetic fields inferred from high-resolution microwave and type III burst observations. ApJ, 283: L71–L74, August 1984. doi: 10.1086/184336.

J. Lee, S. M. White, M. R. Kundu, Z. Mikić , and A. N. McClymont. A Test for Coronal Magnetic Field Extrapolations. ApJ, 510:413–421, January 1999. doi: 10.1086/306556.

H. Lin, M. J. Penn, and S. Tomczyk. A New Precise Measurement of the Coronal Magnetic Field Strength. ApJ, 541:L83–L86, October 2000. doi: 10.1086/312900.

H. Lin, J. R. Kuhn, and R. Coulter. Coronal Magnetic Field Measurements. ApJ, 613: L177–L180, October 2004. doi: 10.1086/425217.

A. Mangeney and M. Pick. Quasi-periodicities in solar type II burst groups. A&A, 224: 242–244, October 1989.

A. N. McClymont and Z. Mikic. Thickness variations along coronal loops inferred from vector magnetograph data. ApJ, 422:899–905, February 1994. doi: 10.1086/173781.

D. B. Melrose and W. N. Sy. Plasma emission processes in a magnetoactive plasma. *Australian Journal of Physics*, 25:387, August 1972.

D. B. Melrose, G. A. Dulk, and S. F. Smerd. The polarization of second harmonic plasma emission. A&A, 66:315–324, June 1978.

D. B. Melrose, G. A. Dulk, and D. E. Gary. Corrected formula for the polarization of second harmonic plasma emission. *Proceedings of the Astronomical Society of Australia*, 4:50–53, 1980.

C. Mercier. Evidence of large scale diverging paths in the solar corona for type III bursts exciters. Sol. Phys., 45:169–179, November 1975. doi: 10.1007/BF00152229.

C. Mercier. Polarisation of type III bursts between 164 and 435 MHz - Structure and variation with frequency. Sol. Phys., 130:119–129, December 1990. doi: 10.1007/BF00156783.

C. Mercier, P. Subramanian, A. Kerdraon, M. Pick, S. Ananthakrishnan, and P. Janardhan. Combining visibilities from the giant meterwave radio telescope and the Nancay radio heliograph. High dynamic range snapshot images of the solar corona at 327 MHz. A&A, 447:1189–1201, March 2006. doi: 10.1051/0004-6361:20053621.

D. L. Mickey. Polarization Measurements in the Green Coronal Line. ApJ, 181:L19, April 1973. doi: 10.1086/181175.

A. Nindos and H. Aurass. Pulsating Solar Radio Emission. In K.-L. Klein and A. L. MacKinnon, editors, *Lecture Notes in Physics, Berlin Springer Verlag*, volume 725 of *Lecture Notes in Physics, Berlin Springer Verlag*, page 251, 2007.

M. Patzold, M. K. Bird, H. Volland, G. S. Levy, B. L. Seidel, and C. T. Stelzried. The mean coronal magnetic field determined from HELIOS Faraday rotation measurements. Sol. Phys., 109:91–105, September 1987. doi: 10.1007/BF00167401.

M. Pick and S. C. Ji. Type III burst sources and electron beam injection. Sol. Phys., 107: 159–165, March 1986. doi: 10.1007/BF00155349.

M. Pick and G. H. J. van den Oord. Observations of beam propagation. Sol. Phys., 130: 83–99, December 1990. doi: 10.1007/BF00156781.

C. W. Querfeld and R. N. Smartt. Comparison of coronal emission-line structure and polarization. Sol. Phys., 91:299–310, April 1984. doi: 10.1007/BF00146301.

R. Ramesh and E. Ebenezer. Decameter Wavelength Observations of an Absorption Burst from the Sun and Its Association with an X2.0/3B Flare and the Onset of a "Halo" Coronal Mass Ejection. ApJ, 558:L141–L143, September 2001. doi: 10.1086/323498.

R. Ramesh and C. V. Sastry. Radio observations of a coronal mass ejection induced depletion in the outer solar corona. A&A, 358:749–752, June 2000.

R. Ramesh, K. R. Subramanian, M. S. Sundararajan, and C. V. Sastry. The Gauribidanur Radioheliograph. Sol. Phys., 181:439–453, August 1998. doi: 10.1023/A:1005075003370.

R. Ramesh, K. R. Subramanian, and C. V. Sastry. Eclipse Observations of Compact Sources in the Outer Solar Corona. Sol. Phys., 185:77–85, March 1999a. doi: 10.1023/A:1005149830652.

R. Ramesh, K. R. Subramanian, and C. V. Sastry. Phase calibration scheme for a "T" array. A&AS, 139:179–181, October 1999b. doi: 10.1051/aas:1999387.

R. Ramesh, C. Kathiravan, A. S. Narayanan, and E. Ebenezer. Metric observations of transient, quasi-periodic radio emission from the solar corona in association with a "halo" CME and an "EIT wave" event. A&A, 400:753–758, March 2003. doi: 10.1051/0004-6361:20030019.

R. Ramesh, A. S. Narayanan, C. Kathiravan, C. V. Sastry, and N. U. Shankar. An estimation of the plasma parameters in the solar corona using quasi-periodic metric type III radio burst emission. A&A, 431:353–357, February 2005. doi: 10.1051/0004-6361:20041130.

R. Ramesh, M. S. S. Rajan, and C. V. Sastry. The 1024 channel digital correlator receiver of the Gauribidanur radioheliograph. *Experimental Astronomy*, 21:31–40, February 2006. doi: 10.1007/s10686-006-9065-y.

R. Ramesh, C. Kathiravan, M. S. Sundararajan, I. V. Barve, and C. V. Sastry. A Low-Frequency (30 - 110 MHz) Antenna System for Observations of Polarized Radio Emission from the Solar Corona. Sol. Phys., 253:319–327, December 2008. doi: 10.1007/s11207-008-9272-y.

R. Ramesh, C. Kathiravan, I. V. Barve, G. K. Beeharry, and G. N. Rajasekara. Radio Observations of Weak Energy Releases in the Solar Corona. ApJ, 719:L41–L44, August 2010a. doi: 10.1088/2041-8205/719/1/L41.

R. Ramesh, C. Kathiravan, and C. V. Sastry. Estimation of Magnetic Field in the Solar Coronal Streamers Through Low Frequency Radio Observations. ApJ, 711:1029–1032, March 2010b. doi: 10.1088/0004-637X/711/2/1029.

R. Ramesh, C. Kathiravan, and A. S. Narayanan. Low-frequency Observations of Polarized Emission from Long-lived Non-thermal Radio Sources in the Solar Corona. ApJ, 734: 39, June 2011. doi: 10.1088/0004-637X/734/1/39.

R. Ramesh, C. Kathiravan, I. V. Barve, and M. Rajalingam. High Angular Resolution Radio Observations of a Coronal Mass Ejection Source Region at Low Frequencies during a Solar Eclipse. ApJ, 744:165, January 2012. doi: 10.1088/0004-637X/744/2/165.

R. Ramesh, K. Sasikumar Raja, C. Kathiravan, and A. S. Narayanan. Low-frequency Radio Observations of Picoflare Category Energy Releases in the Solar Atmosphere. ApJ, 762:89, January 2013. doi: 10.1088/0004-637X/762/2/89.

M. J. Reiner, J. Fainberg, M. L. Kaiser, and J.-L. Bougeret. Circular Polarization Observed in Interplanetary Type III Radio Storms. Sol. Phys., 241:351–370, April 2007. doi: 10.1007/s11207-007-0277-8.

A. C. Riddle. On the Observation of Scattered Radio Emission from Sources in the Solar Corona. Sol. Phys., 35:153–169, March 1974. doi: 10.1007/BF00156964.

B. Roberts, P. M. Edwin, and A. O. Benz. On coronal oscillations. ApJ, 279:857–865, April 1984. doi: 10.1086/161956.

R. D. Robinson. Scattering of radio waves in the solar corona. *Proceedings of the Astronomical Society of Australia*, 5:208–211, 1983.

K. Sasikumar Raja and R. Ramesh. Low-frequency Observations of Transient Quasi-periodic Radio Emission from the Solar Atmosphere. ApJ, 775:38, September 2013. doi: 10.1088/0004-637X/775/1/38.

C. V. Sastry. Polarization of the Thermal Radio Emission from Outer Solar Corona. ApJ, 697:1934–1939, June 2009. doi: 10.1088/0004-637X/697/2/1934.

K. H. Schatten, J. M. Wilcox, and N. F. Ness. A model of interplanetary and coronal magnetic fields. Sol. Phys., 6:442–455, March 1969. doi: 10.1007/BF00146478.

C. J. Schrijver and A. M. Title. The Magnetic Connection between the Solar Photosphere and the Corona. ApJ, 597:L165–L168, November 2003. doi: 10.1086/379870.

S. R. Spangler. The Strength and Structure of the Coronal Magnetic Field. Space Sci. Rev., 121:189–200, November 2005. doi: 10.1007/s11214-006-4719-7.

C. T. Stelzried, G. S. Levy, T. Sato, W. V. T. Rusch, J. E. Ohlson, K. H. Schatten, and J. M. Wilcox. The Quasi-Stationary Coronal Magnetic Field and Electron Density as Determined from a Faraday Rotation Experiment. Sol. Phys., 14:440–456, October 1970. doi: 10.1007/BF00221330.

R. T. Stewart and D. J. McLean. Correcting low-frequency solar radio source positions for ionospheric refraction. *Proceedings of the Astronomical Society of Australia*, 4: 386–389, 1982.

M. Stix. *The sun: an introduction*. 2002.

S. Suzuki and G. A. Dulk. *Bursts of Type III and Type V*, pages 289–332. 1985.

S. Suzuki and K. V. Sheridan. Observations of the circular polarization of fundamental and harmonic type III bursts throughout the frequency range 24 to 220 MHz. *Radiophysics and Quantum Electronics*, 20:989–996, March 1978. doi: 10.1007/BF01356769.

S. Suzuki and K. V. Sheridan. On the fundamental and harmonic components of low-frequency Type III solar radio bursts. *Proceedings of the Astronomical Society of Australia*, 4:382–386, 1982.

T. Tajima, J. Sakai, H. Nakajima, T. Kosugi, F. Brunel, and M. R. Kundu. Current loop coalescence model of solar flares. ApJ, 321:1031–1048, October 1987. doi: 10.1086/165694.

G. Thejappa and R. J. MacDowall. Effects of Scattering on Radio Emission from the Quiet Sun at Low Frequencies. ApJ, 676:1338–1345, April 2008. doi: 10.1086/528835.

G. Thejappa, R. J. MacDowall, and M. L. Kaiser. Monte Carlo Simulation of Directivity of Interplanetary Radio Bursts. ApJ, 671:894–906, December 2007. doi: 10.1086/522664.

G. Thejappa, R. J. MacDowall, and M. Bergamo. Emission Patterns of Solar Type III Radio Bursts: Stereoscopic Observations. ApJ, 745:187, February 2012. doi: 10.1088/0004-637X/745/2/187.

A.R. Thompson, J. M. Moran, and G. W. Swenson. *Interferometry and Synthesis in Radio Astronomy*. 2007.

L. Vlahos and A. Raoult. Beam fragmentation and type III bursts. A&A, 296:844, April 1995.

B. Vršnak, J. Magdalenić, H. Aurass, and G. Mann. Band-splitting of coronal and interplanetary type II bursts. II. Coronal magnetic field and Alfvén velocity. A&A, 396:673–682, December 2002. doi: 10.1051/0004-6361:20021413.

J. P. Wild, K. V. Sheridan, and A. A. Neylan. An Investigation of the Speed of the Solar Disturbances responsible for Type III Radio Bursts. *Australian Journal of Physics*, 12:369, December 1959. doi: 10.1071/PH590369.

J. P. Wild, S. F. Smerd, and A. A. Weiss. Solar Bursts. ARA&A, 1:291, 1963. doi: 10.1146/annurev.aa.01.090163.001451.

A. J. Willes and D. B. Melrose. The Polarisation of Second Harmonic Coronal Type III Bursts. Sol. Phys., 171:393–418, April 1997. doi: 10.1023/A:1004993601351.

R. F. Willson, S. L. Redfield, K. R. Lang, B. J. Thompson, and O. C. St. Cyr. First VLA Observations of Nonthermal Metric Bursts Associated with Coronal Mass Ejections Detected by the Solar and Heliospheric Observatory. ApJ, 504:L117, September 1998. doi: 10.1086/311585.

R.-Y. Zhao, A. Mangeney, and M. Pick. Periodicities in solar type III burst groups and source characteristics. A&A, 241:183–186, January 1991.

E. I. Zlotnik. The polarization of second harmonic radio emission in Type III bursts. A&A, 101:250–258, August 1981.

E. Y. Zlotnik, V. V. Zaitsev, H. Aurass, G. Mann, and A. Hofmann. Solar type IV burst spectral fine structures. II. Source model. A&A, 410:1011–1022, November 2003. doi: 10.1051/0004-6361:20031250.

Chapter 5

Coronal mass ejections and associated magnetic fields

5.1 Introduction

Among the other types of solar radio bursts, type IV bursts are interesting to astronomers because of their influence on space weather and Earth's climate. It is believed that type IV bursts cause Forbush decreases (i.e. decrease in intensity of cosmic rays on Earth) and geomagnetic storms. It is possible that the observations of type IV bursts enable forecasters to predict the above mentioned. It is known that intense, long-lasting (tens of minutes to hours) non-thermal radio continuum are observed sometimes in association with the flares and CMEs in the solar atmosphere. Boischot [1957] had designated these events as type IV bursts. Further studies showed that there are two classes of type IV bursts: The first variety occurs after the impulsive phase of the flares and drifts in the spectrum to lower frequencies. Interferometer observations indicate that the radio source exhibits outward movement through the solar atmosphere with speeds in the range $\approx 200 - 1500$ km s^{-1}. Emission can be observed even when the source is located at

large radial distances ($r \approx 5\ R_\odot$) above the plasma level corresponding to the frequency of observation. The sources have low directivity and are partially circularly polarized. The sense of polarization correspond usually to the extraordinary mode (e-mode) of the magneto-ionic theory. These are called the moving type IV (type IVm) bursts. The second variety, called the stationary type IV bursts (type IVs), appear near the flare site during the impulsive phase at frequencies $\gtrsim 300$ MHz and in the post-flare phase at lower frequencies. The type IVs burst is characterized by a source whose position does not change and which is located close to or slightly above the plasma level corresponding to the frequency of observation. The emission is circularly polarized usually in the ordinary mode (o-mode) of the magneto-ionic theory. The cone of emission is narrow since type IVs bursts are rarely observed when the associated flare is near the limb of the Sun. The high directivity, location close to the plasma level, and the presence of fine structures suggest that the emission mechanism is related to the plasma frequency. The type IVs bursts at low frequencies may occur with or without a type IVm burst [Pick-Gutmann, 1961, Boischot and Pick, 1962, Weiss, 1963, Wild et al., 1963, Stewart, 1985, Aurass et al., 2005, Pick and Vilmer, 2008].

Between the type IVm and typs IVs bursts, the former are considered useful to understand the CMEs because of their close spatio-temporal association with the latter and the possibility to estimate the strength of the CME magnetic field using them. Gergely [1986] had noted that 5% of all CMEs are associated with type IVm bursts and $33-50\%$ of type IVm bursts are associated with CMEs. But only a few estimates of the field strength have been reported in the literature due to the lack of concurrent white light and radio observations, particularly over $r \lesssim 2\ R_\odot$, and the rarity of type IVm bursts which are pre-dominantly a low frequency phenomenon, occurring at frequencies < 100 MHz White [2007]. Second harmonic plasma emission from non-thermal electrons trapped in the plasmoids associated with the CMEs [Duncan, 1981, Stewart et al., 1982, Gopalswamy and Kundu, 1989b, Kundu et al., 1989, Ramesh et al., 2013] and optically thin non-thermal

gyro-synchrotron emission from mildly relativistic electrons spiralling in the CME loops [Gopalswamy and Kundu, 1989a, Bastian and Gary, 1997, Bastian et al., 2001, Maia et al., 2007, Tun and Vourlidas, 2013] are the mechanisms invoked to explain the type IVm bursts. Using simultaneous white light, radio heliograph, radio polarimeter and radio spectral observations we have presented arguments to show that the type IVm burst associated with the 'halo' CME event of 15 March 2013 can be explained on the basis of non-thermal gyro-synchrotron emission and estimated the magnetic field strength near the source region of the burst.

5.2 Classification of Type IV bursts

Solar type IV bursts are studied by many authors at different frequencies [Kundu, 1961, Kundu and Firor, 1961, Takakura and Kai, 1961, Takakura, 1961, Kundu, 1965]. Especially at meter wavelengths, these bursts are classified into two types based on their drifting speeds or morphology of the spectrum of the radiation: (1) Stationary type IV bursts (IVs), and (2) Moving type IV bursts (IVm).

5.2.1 Stationary type IV bursts (IVs)

Wild [1970] first used the term 'flare continuum' (FCM), which is also called stationary type IV bursts at meter wavelengths. These bursts appear in early phase of flare events. Stationary type IV bursts, also called flare continuum emissions do not travel in the solar corona. Therefore, the radiation is observed over a larger bandwidth of observations. FCM is different from the 'storm continuum' (SC) which occurs late in some flare events. Note that SC is strongly circularly polarized and may end up as a 'storm'. Typical source size of the type IVs bursts $\lesssim 4'$. These bursts originate close to the flaring region. Brightness temperatures of the bursts will be of the order of $\approx 10^{10}$ K. No systematic movement of

the source is seen and the source is situated near the corona at the corresponding plasma layer. The flux density of type IV bursts varies smoothly and type I bursts may appear gradually over the continuum with time.

5.2.2 Moving type IV bursts (IVm)

Robinson and Smerd [1975], Robinson [1978b] noticed that many type IVm bursts are preceded by type IVs bursts. Meter wavelength continuum emitted by a source region which travels outward in the solar corona after a flare or an eruptive prominence mass ejecta is called moving type IV radio bursts. Most of the type IVm bursts last for 30 minutes at 80 MHz, but sometimes, continue up to 2 hours. The dcp of these events gradually increases to $\gtrsim 90\%$. Brightness temperatures of the type IVm bursts are in the range $\approx 10^7 - 10^{10}$ K. These bursts also have a smoothly varying continuum and may have some structure in the beginning of the bursts. The brightness temperatures of the sources is $\gtrsim 10^{10}$ K and $\gtrsim 10^9$ K at 80 and 169 MHz [Stewart et al., 1978, Trottet et al., 1981]. The source speeds were in between $\approx 200 - 1600$ km s^{-1}. For any specific event, the source speed is approximately constant [Robinson, 1978c] and the distribution of speeds is similar to that of coronal mass ejections [Hildner, 1977]. These bursts reach $10^5 - 10^6$ km above the photosphere. Typical source sizes of these bursts are $\approx 10'$ or larger.

5.3 Difference between type IV bursts and noise storms

Type IV and noise storms look alike but different in few characteristics. Firstly, if the emission is steady, smooth varying continuum and free of type I and type III bursts superposed over the continuum, then they are identified as type IV bursts. Also, 'duration' of the former is few minutes to hours, whereas the latter continue for few hours to days of time. Type IV bursts are observable at all frequencies present, i.e., they are broad

band continuum emissions, where as type I emission is not broad band emission. Another important characteristic of type IV bursts is their association with microwave outbursts. This is never the case with noise storms, since they are limited mainly to meter wavelengths. Noise storms are highly circularly polarized radio events, whereas dcp of the type IV bursts gradually increases from low to high values. Source sizes of type IV bursts obtained with imaging instruments $\approx 4' - 10'$, where as the source sizes of noise storms are $\lesssim 1'$. Some times, type IV bursts are associated with the type II bursts where as type I storms are not. Another significant difference between type IV from type I is their correlations with geomagnetic activity. Note that there will be a high correlation between geomagnetic storms and type IV radiation. Correlation of type I storms with geomagnetic storms is much weaker.

5.4 Observations

The radio data were obtained on 15 March 2013 at 80 MHz with the Gauribidanur RAdioheliograPH [Ramesh et al., 1998, 1999a,b, 2006a] in the imaging mode, the Gauribidanur Radio Interference Polarimeter [Ramesh et al., 2008] at 80 MHz and 40 MHz in the transit mode, and over the 85 - 35 MHz band with the Gauribidanur LOw frequency Solar Spectrograph [Ebenezer et al., 2001, 2007, Kishore et al., 2014] in the spectral mode. The GRAPH is a T-shaped radio interferometer array and produces two dimensional images of the solar corona with an angular resolution of $\approx 5^{'} \times 7^{'}$ (Right Ascension, R.A. $\times$ Declination, decl.) at the above frequency. The integration time is $\approx$ 250 ms and the observing bandwidth is $\approx$ 2 MHz. GRIP is an East-West one-dimensional array operating in the interferometer mode at 80 MHz and 40 MHz simultaneously. It responds to the polarized flux density from the 'whole' Sun. The observations correspond primarily to the circularly polarized emission since linear polarization, if it is there at the coronal source region, tends to be obliterated at low radio frequencies because of the differential Faraday

rotation of the plane of polarization within the typical observing bandwidths [Grognard and McLean, 1973]. The half-power width of the response pattern ('beam') of the GRIP is broad (compared to the Sun) in both R.A./East-West direction ($\approx 1.5^o$ at 80 MHz) and decl./North-South direction ($\approx 90^o$). The width of the response pattern of the GRIP in declination is nearly independent of frequency. This implies that a plot of the GRIP data (i.e. the time profile) for observations in the transit mode is essentially the 'East-West beam' of the array with an amplitude proportional to the strength of the emission from the 'whole' Sun, weighted by the antenna gain in that direction. The integration time is ≈ 250 ms and the observing bandwidth is ≈ 2 MHz, same as GRAPH. The radio source(s) responsible for the circularly polarized emission observed with the GRIP are identified using the two-dimensional radioheliograms obtained with the GRAPH around the same time. GLOSS has a very broad response $\approx 90^o \times 5^o$ (R.A. $\times$ decl.) and the Sun is a point source for the latter. The integration time is ≈ 100 ms and the observing bandwidth is ≈ 300 kHz at each frequency. The width of the response pattern of the GLOSS in R.A. (i.e. hour angle) is nearly independent of frequency. The Sun is a point source for both the GRIP and the GLOSS. All the above instruments observe the Sun everyday during the interval $\approx 4 - 9$ UT. The minimum detectable flux density of the GRAPH, GRIP and GLOSS are ≈ 20 Jy, 200 Jy, 3000 Jy, respectively. The optical data were obtained with the Large Angle and Spectrometric Coronagraph [Brueckner et al., 1995] onboard the Solar and Heliospheric Observatory (SOHO), COR1 coronagraph and 195 Å Extreme-UltraViolet Imager (EUVI) of the Sun-Earth Connection Coronal and Heliospheric Investigation [Howard et al., 2008] onboard the Solar TErrestrial RElations Observatory (STEREO), and in 193 Å with the Atmospheric Imaging Assembly [Lemen et al., 2012] onboard the Solar Dynamics Observatory (SDO).

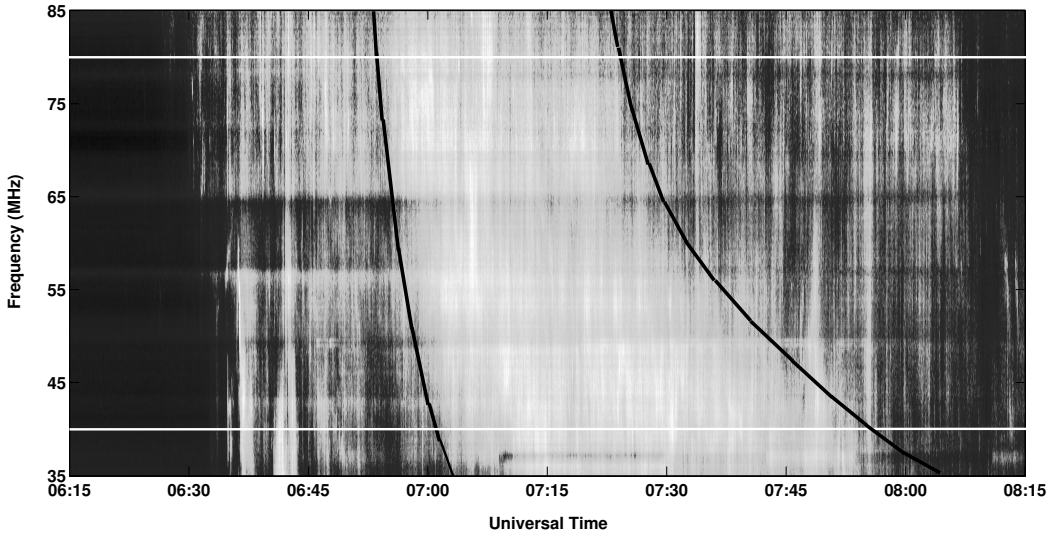

Fig. 5.1: Dynamic spectrum of the solar radio emission observed with the GLOSS on 15 March 2013 during 06:15 - 08:15 UT in the frequency range $85 - 35$ MHz. The stationary emission during the interval $\approx$ 06:30 - 08:10 UT and the drifting emission during $\approx$ 06:55 - 07:50 UT correspond respectively to the type IVs and type IVm bursts mentioned in the text. The two 'white' horizontal lines indicate 40 MHz and 80 MHz portion of the spectrum. The other horizontal line like features noticeable in the spectrum, for eg. near $\approx$ 55 MHz, $\approx$ 65 MHz, etc. are due to local radio frequency interference (RFI). The two slanted 'black' lines indicate the approximate interval over which the type IVm burst was observed at different frequencies.

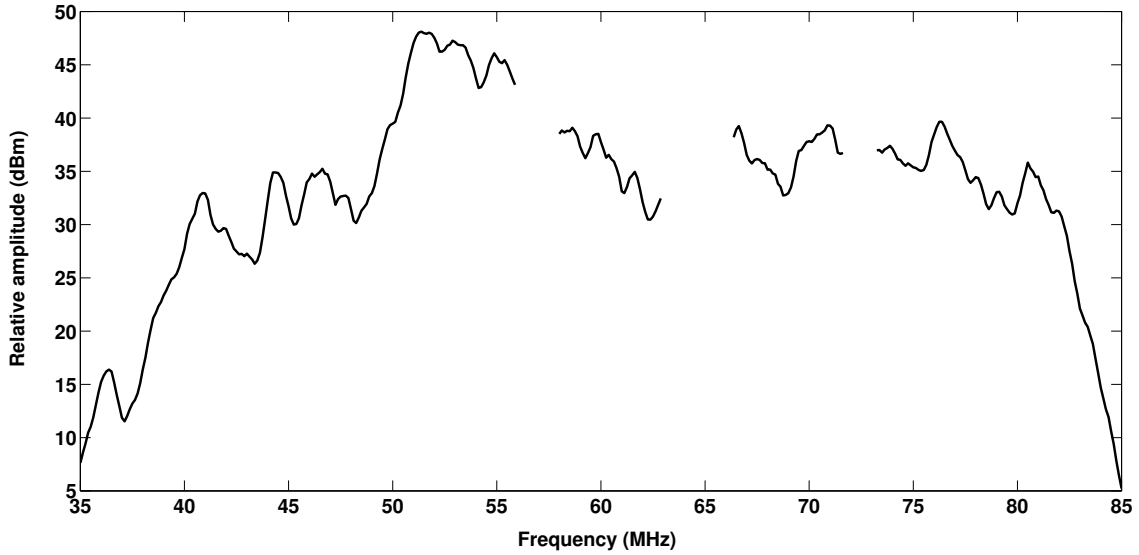

Fig. 5.2: Spectral profile of the type IVm burst in Figure 5.1 at ≈ 06:55 UT. The gaps in the profile near ≈ 55 MHz, ≈ 65 MHz, etc. correspond to the frequency channels affected by RFI.

Figure 5.1 shows the dynamic spectrum obtained with the GLOSS on 15 March 2013 during the interval 06:15 - 08:15 UT in the frequency range 85 – 35 MHz. Two types of enhanced radio emission with differing spectral characteristics are simultaneously noticeable in the spectrum: 1) a weak stationary continuum during the period ≈ 06:30 - 08:10 UT with fine structures, and 2) a comparatively intense patch of continuum drifting from 85 MHz to 35 MHz during the period ≈ 06:55 - 07:50 UT. The fine structures in the background of the latter are most likely part of the ongoing stationary continuum during the same interval. The stationary and the drifting continuum described above are the typical spectral signatures of the type IVs and type IVm bursts in the solar atmosphere, respectively [Stewart, 1985]. The average duration (τ) of the type IVm burst in Figure 5.1 increases with decreasing frequency. The increase in the temporal width with decrease in frequency of the region enclosed between the 'black' lines from 85 MHz to 35 MHz in the spectrum indicates this. The typical widths (i.e. duration) are $\tau \approx 25$ min and $\tau \approx$ 45 min at 85 MHz and 35 MHz, respectively. These are consistent with the statistical results on the duration of type IVm bursts reported by Robinson [1978a]. The onset of the burst at 85 MHz is ≈ 06:55 UT and at 35 MHz is ≈ 07:05 UT.

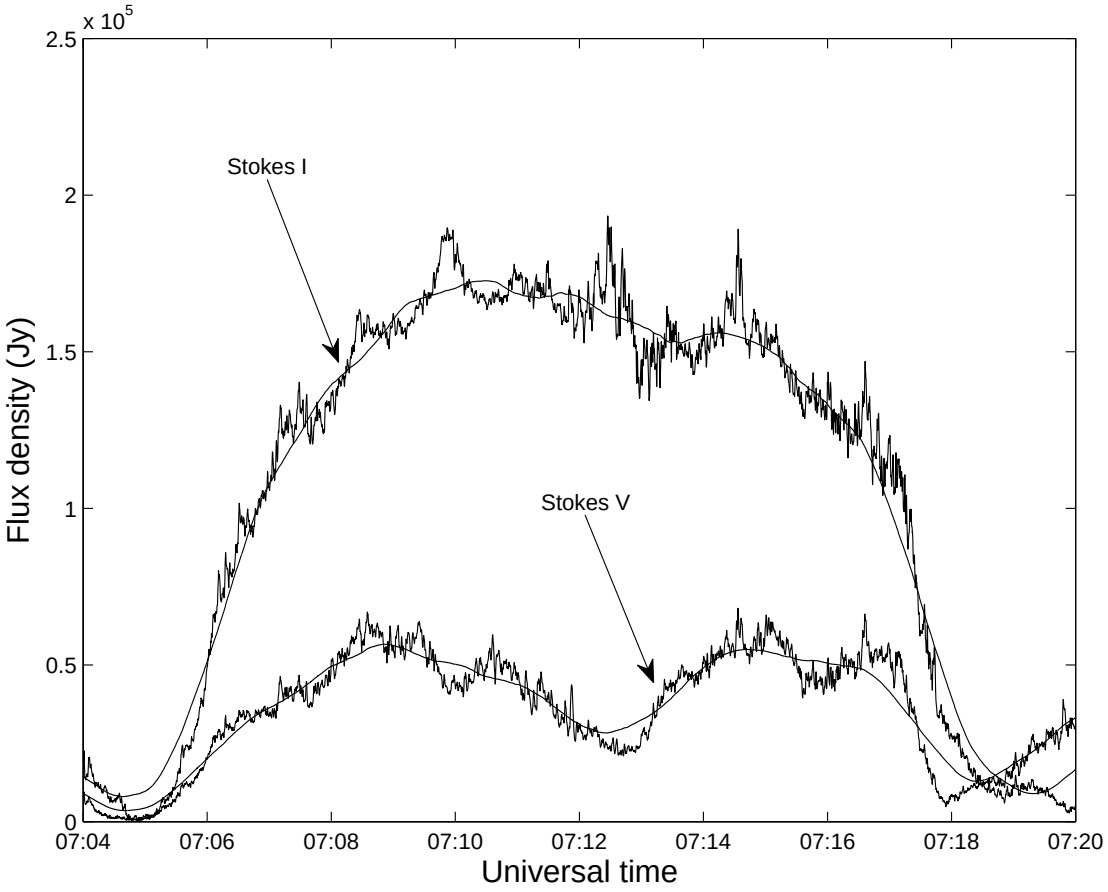

Fig. 5.3: Time profile of the Stokes I and Stokes V emission observed with the GRIP at 80 MHz on 15 March 2013 in the transit mode. The duration of the observations correspond approximately to the width of the response pattern of the GRIP at 80 MHz in the East-West direction. The overplotted smooth line is the polynomial fit to the observations.

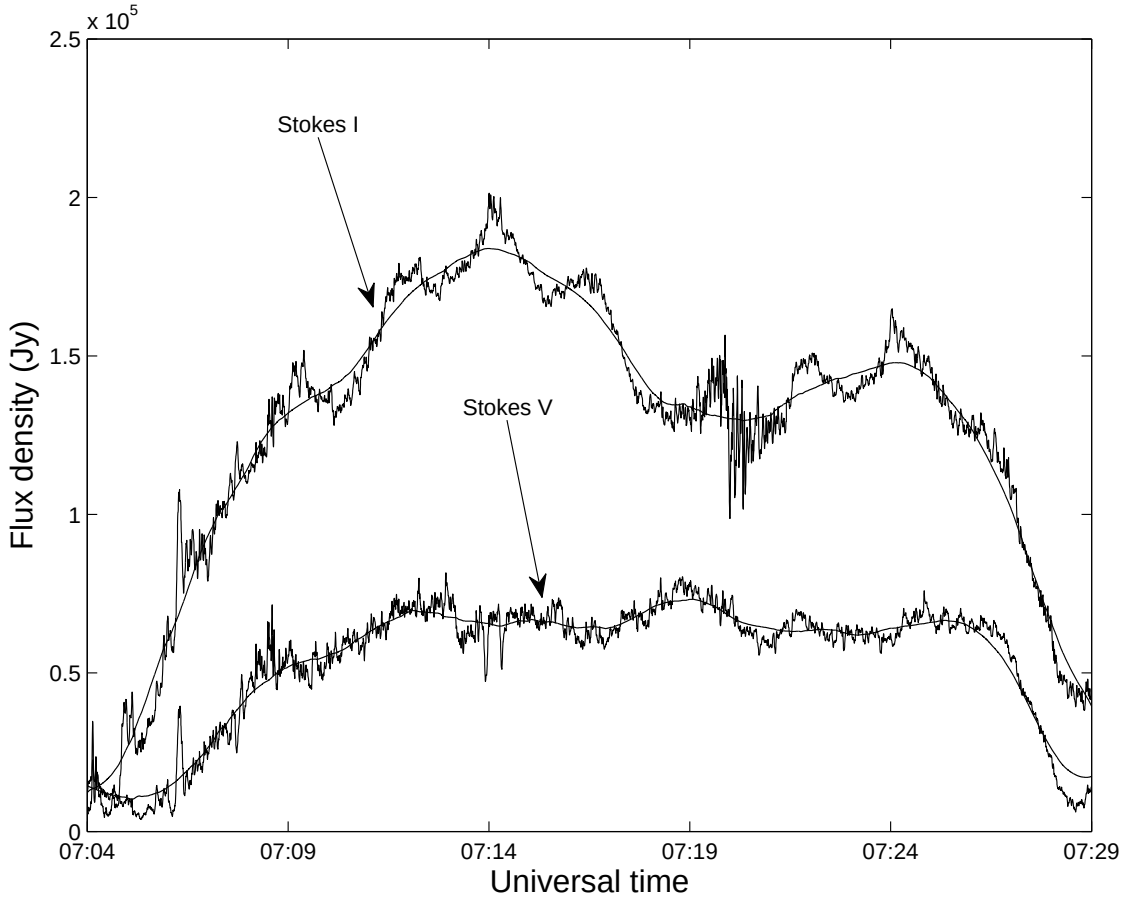

Fig. 5.4: Time profile of the Stokes I and Stokes V emission observed with the GRIP at 40 MHz on 15 March 2013 in the transit mode. The duration of the observations correspond approximately to the width of the response pattern of the GRIP at 40 MHz in the East-West direction. The overplotted smooth line is the polynomial fit to the observations.

Figure 5.3 shows the time profile of the Stokes I & V radio emission from the solar corona at 80 MHz as observed with the GRIP on 15 March 2013. Similar observations at 40 MHz are shown in Figure 5.4. The observations were carried out in the transit mode and hence the observed time profile and their duration essentially corresponds to the East-West response pattern of the GRIP. The peak flux densities, estimated using the polynomial fit to the observations (see the overplotted smooth line in Figures 5.3 and 5.4), are $\approx$ 170,000 Jy (Stokes I) and $\approx$ 50,000 Jy (Stokes V) at 80 MHz, and $\approx$ 181,000 Jy (Stokes I) and 62,000 Jy (Stokes V) at 40 MHz. These values correspond mostly to that of the type IVm burst alone since we had subtracted the corresponding mean flux densities of the background type IVs burst fine structures using GRIP observations of the same outside the type IVm burst period. The respective values for the type IVs bursts are $\approx$ 110,000 Jy (Stokes I) and $\approx$ 53,000 Jy (Stokes V) at 80 MHz, and $\approx$ 117,000 Jy (Stokes I) and $\approx$ 61,000 Jy (Stokes V) at 40 MHz. That the flux density of particularly the Stokes I emission for the type IVs burst is a significant fraction of that of the type IVm burst in the present case is noticeable from their contrast with respect to the background in Figure 5.1 also. The 80 MHz flux densities are consistent with that reported earlier for type IVm bursts at similar frequency [Kai, 1969]. The spectral index (α) between 40 MHz and 80 MHz using the above Stokes I flux densities is $\alpha \approx -0.1$. Since the non-thermal spectral index is generally < 0 [Kraus et al., 1986, Subramanian and Sastry, 1988], the above value $\alpha \approx -0.1$ indicates that the observed emission in the present case is of non-thermal origin. The estimated degree of circular polarization (dcp) of the type IVm burst in Figures 5.3 and 5.4 are $\approx 0.29 \pm 0.1$ at 80 MHz and $\approx 0.34 \pm 0.1$ at 40 MHz. Note that due to instrumental limitations, we observed only |V| with the GRIP and hence dcp = |V|/I in the present case.

The above radio events were associated with a M1.1 class GOES soft X-ray flare during the interval $\approx$ 05:46 - 08:35 UT with peak at $\approx$ 06:58 UT, a 1F class Hα flare during the interval $\approx$ 06:13 - 08:33 UT with peak at $\approx$ 06:37 UT from the active region

AR 11692 located at N11E12 on the solar disk[1], and a 'halo' CME[2]. Figure 5.5 shows the composite of the GRAPH radioheliogram at 80 MHz, the SOHO-LASCO C2 image and the SDO-AIA 193 Å image, all obtained around ≈ 08:00 UT. Since the observations were during the type IVs burst period in Figure 5.1, the discrete radio source near the disk center is most likely the source region of the type IVs burst. Its peak brightness temperature (T_b) is $\approx 3 \times 10^8$ K. In the present chapter, the discussion is limited only to the type IVm burst. Unfortunately, there was no GRAPH observation during the type IVm burst in Figure 5.1. The discrete source close to the limb in the North East quadrant in Figure 5.5 is presumably weak non-thermal radio noise storm activity often observed near the location of a CME in its aftermath [Kerdraon et al., 1983, Kathiravan et al., 2007]. The peak T_b of the source is $\approx 10^7$ K.

From the movies of the 'halo' CME, we find that the its LE was first observed in the STEREO-COR1B field of view (FOV) around ≈ 06:15 UT at $r \approx 1.6\ R_\odot$. Later, at the onset time of the type IVm burst at 85 MHz around ≈ 06:55 UT (Figure 5.1), the LE was at $r \approx 3.5\ R_\odot$. This gives a projected linear speed of ≈ 551 km s^{-1} for the CME LE. The SOHO-LASCO height-time (h-t) measurements indicate that the CME LE was located at $r \approx 4.1\ R_\odot$ around ≈ 07:12 UT[3]. These values are consistent with those extrapolated using the STEREO-COR1B measurements. The projected linear speed of the ejecta that moved outwards behind the CME LE observed in the STEREO-COR1B FOV (see Figure 5.6) was estimated. The centroid of the ejecta was at $r \approx 1.6\ R_\odot$ during its first appearance at ≈ 06:45 UT. Ten minutes later, i.e. at 06:55 UT close to the onset time of the type IVm burst at 85 MHz, the ejecta was at $r \approx 1.9\ R_\odot$ (see Figure 5.6). The above h-t measurements give a speed of ≈ 348 km s^{-1} for the ejecta. This is nearly the same as the speed estimated using SOHO-LASCO C2 observations of the same ejecta during ≈ 07:24 - 08:24 UT (see Figure 5.5). It appears from Figures 5.5 and 5.6 that the

[1] swpc.noaa.gov/warehouse/2013.html
[2] umbra.nascom.nasa.gov/lasco/observations/halo/2013/130315
[3] cdaw.gsfc.nasa.gov

ejecta is close to the plane of the sky for both STEREO-COR1B and SOHO-LASCO C2.

The close agreement between the measured projection speeds of the CME LE and the ejecta with the above two instruments indicate that the ejecta moved at the same angle to the Sun-Earth and Sun-STEREO-B lines. As STEREO-B and Earth were separated by an angle of about 140° at the time of the event, we estimate this angle to be ≈ 70°. So the angle between the ejecta and the plane of the sky for STEREO-COR1B or SOHO-LASCO C2 is about 20°. Note that any error in the position/size of the type IVs burst in Figure 5.5 due to ionospheric effects and/or scattering (irregular refraction due to density inhomegeneities in the solar corona) is expected to be minimal ($\approx \pm 0.2\ R_\odot$) because: 1) positional shifts due to ionospheric effects is expected to be $\lesssim 0.2\ R_\odot$ at 80 MHz in the hour angle range ± 2h [Stewart and McLean, 1982]. The local noon at Gauribidanur on 15 March 2013 was around ≈ 07:00 UT and the GRAPH observations described above are within the above hour angle range; 2) the effects of scattering are considered to be small at 80 MHz compared to lower frequencies [Aubier et al., 1971, Bastian, 2004, Ramesh et al., 2006b]. The results from high angular resolution observations of the solar corona that discrete radio sources of angular size $\approx 1' - 3'$ are likely to be there in the solar atmosphere from where low frequency radio radiation originates [Kerdraon, 1979, Lang and Willson, 1987, Willson et al., 1998, Ramesh et al., 1999b, Ramesh and Sastry, 2000, Ramesh and Ebenezer, 2001, Mercier et al., 2006, Kathiravan et al., 2011, Ramesh et al., 2012] also constrain scattering; 3) the positional shift of discrete solar radio sources due to scattering is expected to be $\lesssim 0.2\ R_\odot$ at 80 MHz [Riddle, 1974, Robinson, 1983]. Ray tracing calculations employing realistic coronal electron density models and density fluctuations show that the turning points of the rays that undergo irregular refraction almost coincide with the location of the plasma ('critical') layer in the non-scattering case even at 73.8 MHz [Thejappa and MacDowall, 2008]. Obviously the situation should be better at 80 MHz.

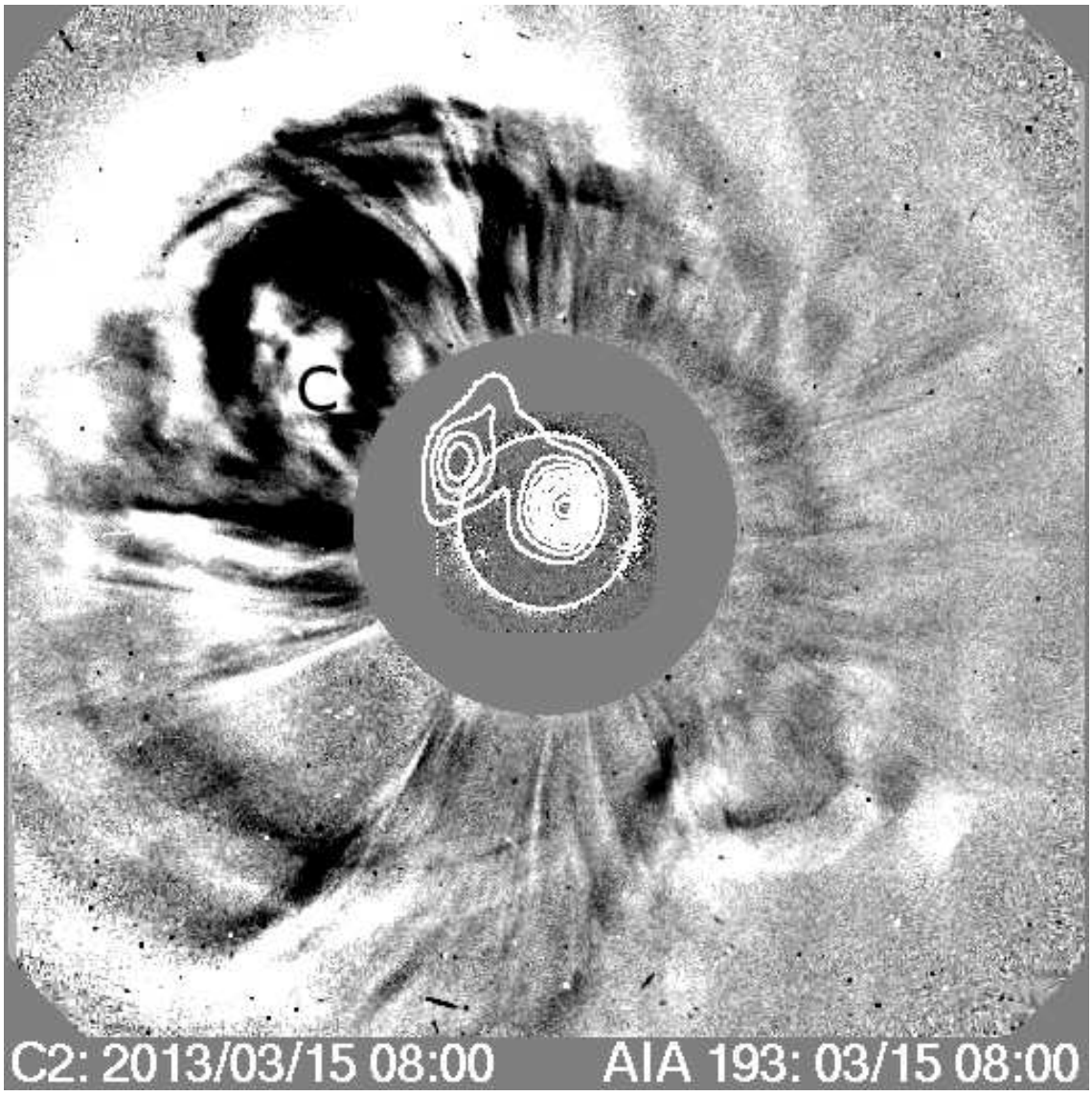

Fig. 5.5: A composite of the 80 MHz GRAPH radioheliogram of the type IVs burst observed on 15 March 2013 around ≈ 08:00 UT (contours in white colour) and the SOHO-LASCO C2, SDO-AIA (193 Å) images obtained close to the same time that day. The discrete source of radio emission near the disk center is the type IVs burst mentioned in the text. The 'white' circle (radius = 1 $R_{\odot}$) at the center indicates the solar limb. The bigger, concentric 'grey' circle (radius ≈ 2.2 $R_{\odot}$) represents the occulting disk of the SOHO-LASCO C2 coronagraph. Solar North is straight up and solar East is to the left in the image. The white light feature marked 'C' is the CME core like ejecta mentioned in the text.

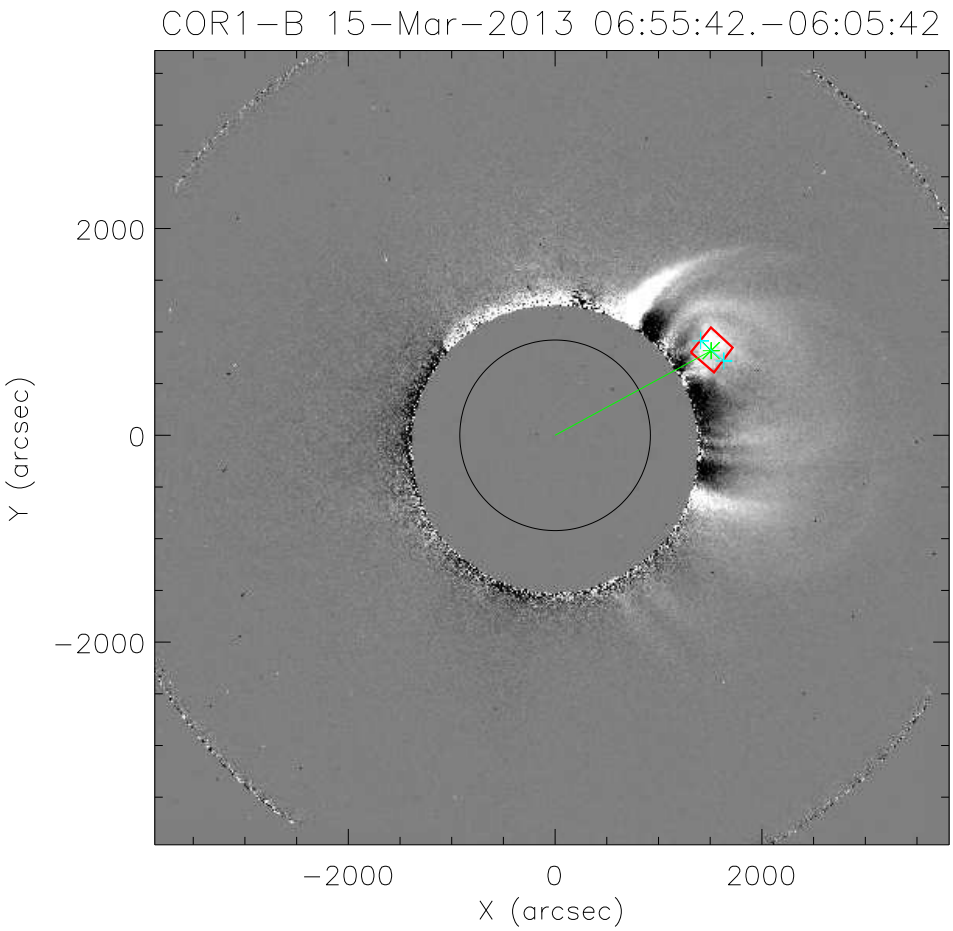

Fig. 5.6: STEREO-COR1B pB difference image obtained on 2013 March 15 around 06:55 UT. The subtracted reference image was observed at 06:05 UT prior to the CME onset. The region marked with a rectangular box is used for measuring the density of the CME ejecta. The 'grey' circle (radius $\approx 1.4\ R_{\odot}$) represents the occulting disk of the coronagraph. The asterisk within the rectangular box marks the same feature (ejecta) marked 'C' in Figure 5.5.

5.5 Results and analysis

5.5.1 Emission mechanism

The type IVm burst in the present case is most likely associated with the CME core like ejecta behind the CME LE because: 1) the CME LE was located at a large radial distance ($r \approx 3.5\ R_{\odot}$) at the onset time of the type IVm burst at 85 MHz. The above value is close to the outer limit of the radial distance up to which the type IVm bursts have been observed [Smerd and Dulk, 1971, Robinson, 1978a]; 2) the location of the ejecta ($r \approx 1.9\ R_{\odot}$) close to the onset of the type IVm burst at 85 MHz around ≈ 06:55 UT (see Figure 5.1) is consistent with the statistical estimate of the radial distance of the type IVm bursts during their onset at 80 MHz [Smerd and Dulk, 1971]; 3) no other bright moving structures were noticeable in the STEREO-COR1B FOV during ≈ 06:55 - 07:50 UT over $r < 2\ R_{\odot}$, the interval over which the radio emission was observed in Figure 5.1; 4) based on a statistical study of the type IVm bursts at 80 MHz, Gergely [1986] had earlier concluded that majority of the type IVm bursts move out with the ejecta behind the CME LE.

Though optically thin gyro-synchrotron emission from mildly relativistic electrons and second harmonic plasma emission have been suggested as possible mechanisms for the type IVm bursts, It is found that the former is the most likely process in the present case because: 1) in the presence of a medium, the gyro-synchrotron emission is strongly suppressed at frequencies $< 2f_p$, where f_p is the plasma frequency [Wild and Smerd, 1972, Dulk, 1973, Melrose, 1985]. To verify this, we used the pB measurements obtained with STEREO-COR1B to estimate the total coronal electron density (i.e the density of the background corona and the CME together) at the location of the ejecta at ≈ 06:55 UT [Wang and Davila, 2014]. The value is $\approx 7 \times 10^6$ cm^{-3}. This corresponds to $f_p \approx 24$ MHz. This implies that if the type IVm burst of 15 March 2013 had been due to gyro-synchrotron emission, it should have been suppressed at frequencies $\lesssim 48$ MHz at ≈ 06:55

UT. The present observations are consistent with this. The spectral profile of the type IVm burst in Figure 5.2 clearly shows a reduction in the observed intensity at frequencies $\lesssim$ 52 MHz. However at later times the burst is observable at lower frequencies (see Figure 5.1). This is because the ejecta had moved outward in the solar atmosphere as well as expanded in size with time (see Figures 5.5 and 5.6). As a consequence there is a gradual decrease in the total density at the location of the ejecta and hence the cut-off frequency for gyro-synchrotron emission. Probably this shift in the cut-off towards lower frequencies with time is also responsible for the observed drift of the type IVm burst in Figure 5.1. Note that the total density when the ejecta was first observed in the STEREO-COR1B FOV around $\approx$ 06:45 UT at $r \approx 1.6\ R_{\odot}$ was $\approx 15 \times 10^6$ cm^{-3}. Comparing this with the corresponding measurements at $\approx$ 06:55 UT, we find that the ejecta had moved a radial distance of $\approx 0.3\ R_{\odot}$ in $\approx$ 10 min and the total density during that period had decreased by about a factor of two. Note that the densities of the other rising structures (above the occulter of the coronagraph) of the CME like the 'legs' and the frontal loop which are comparitively fainter (see Figure 5.6) are $< 7 \times 10^6$ cm^{-3}. This indicates that the corresponding $f_p < 24$ MHz. Therefore if the type IVm burst had been due to any of the aforementioned structures of the CME, the reduction in the intensity of the burst at $\approx$ 06:55 UT should have been at lower frequencies than $\approx$ 52 MHz. But this is not the case; 2) the estimated *dcp* is larger compared to that for reported for type IVm bursts due to second harmonic plasma emission [Gary et al., 1985]; 3) the spectral index of the type IVm burst between 40 MHz and 80 MHz as estimated from the GRIP observations is $\alpha \approx$ -0.1 (see Section-5.5.2). This is nearly the same as the expected spectral index for gyrosynchrotron emission over the frequency range $38.5 - 73.8$ MHz [Gopalswamy and Kundu, 1990].

5.5.2 Estimation of spectral index and energy spectral index

It is known that flux density $S(f)$ of a source is related to the frequency f and spectral index α as follows [Kraus, 1973]

$$S(f) \propto f^{\alpha} \tag{5.1}$$

Using the equation 5.1, the following equation can be obtained,

$$\frac{S(f_1)}{S(f_2)} = \left(\frac{f_1}{f_2}\right)^{\alpha} \tag{5.2}$$

Where, $S(f_1)$ and $S(f_2)$ are the observed flux densities at two different frequencies f_1 and f_2 respectively. Rewritting the equation 5.2 gives,

$$\alpha = \frac{\ln S(f_1) - \ln S(f_2)}{\ln f_1 - \ln f_2} \tag{5.3}$$

By using the spectral index, the electron energy spectral index / power law index δ is estimated using the equation 5.5 [Dulk, 1985, White et al., 2011].

$$\alpha = 1.20 - 0.90\delta \tag{5.4}$$

Re-writing the equation 5.4,

$$\delta = \frac{1.20 - \alpha}{0.90} \tag{5.5}$$

In the present case, the power-law index δ can be estimated from the radio flux spectral index (α) through equation 5.5. The estimated spectral index was $\alpha \approx -0.1$ and this implies $\delta \approx 1.4$.

5.5.3 Estimate of the magnetic field

In the case of optically thin non-thermal gyro-synchrotron emission, the *dcp* and B are related as follows [Dulk, 1985]:

$$dcp \approx 1.26 \times 10^{0.035\delta} 10^{-0.071 cos\theta} \left(\frac{f}{f_B}\right)^{-0.782+0.545 cos\theta} \tag{5.6}$$

where, *dcp* is the degree of circular polarization, δ is electron energy spectral index, θ is the viewing angle (i.e angle between the direction of magnetic field and line of sight), f is the frequency of observation [MHz], f_B is gyro frequency [$\approx 2.8 \times B$], B is the magnetic field [Gauss], τ_ν is the optical depth. By knowing the dcp and other parameters, magnetic fields are estimated. Rewriting the Equation 5.6 for B.

$$B = \frac{f}{2.8} \times 10^{x} \tag{5.7}$$

where,

$$x = \frac{log_{10}(dcp) - 0.035\delta + 0.071\ cos\theta - 0.1004}{0.782 - 0.545\ cos\theta} \tag{5.8}$$

The angle between the ejecta and the plane of the sky in the present case is $\approx 20°$ (see section 5.4). This indicates that the ejecta is nearly normal to the LOS and the associated field lines are likely to be radial. So we assumed the viewing angle between the LOS and the magnetic field in the type IVm burst source region to be the same as the positional angle from the LOS to the ejecta. Hence $\theta \approx 70°$ (see section 5.4). Substituting for the different parameters in equation 5.7 and 5.8, the magnetic field strengths are calculated. The magnetic field strength (B) at 80 and 40 MHz was $\approx 2.2 \pm 0.4$ G $\approx 1.4 \pm 0.2$ G respectively. The corresponding radial distances are most likely $r \approx 1.9\ R_\odot$ (80 MHz) and $r \approx 2.2\ R_\odot$ (40 MHz). The magnetic fields are estimated from the location of the ejecta ($r \approx 1.9\ R_\odot$) during the onset of the type IVm burst at 85 MHz ($\approx$ 06:55 UT), the projected speed of the ejecta ($\approx 348\ km\ s^{-1}$), and the onset of the type IVm burst

at 35 MHz ($\approx$ 07:05 UT). The *dcp* and the B values are consistent with the results of the model calculations reported by Robinson [1974] for $\theta \approx 70°$. The sense of polarization is in the e-mode. Gary et al. [1985] had remarked that gyro-synchrotron emission is a possible mechanism at 80 MHz if conditions like $B \approx 2.8$ G at $r \approx 2.5\ R_\odot$ are satisfied. The above estimates of B at 80 MHz in the present case agree reasonably with this.

5.6 Conclusions

Low frequency ($<$ 100 MHz) radio imaging, spectral and polarimeter observations of the type IVm burst and type IVs burst that occurred simulatenously on 15 March 2013 in association with a 'halo' CME and a M1.1/1F class soft X-ray/Hα flare are reported. Our results indicate that the type IVm burst is likely due to optically thin gyro-synchrotron emission from the non-thermal electrons in the CME core like ejecta behind the CME LE. The estimated magnetic field strength near the type IVm burst source region is $B \approx 2.2 \pm 0.4$ G and $\approx 1.4 \pm 0.2$ G at 80 MHz and 40 MHz respectively. The corresponding radial distances are $r \approx 1.9\ R_\odot$ (80 MHz) and $r \approx 2.2\ R_\odot$ (40 MHz). The following results mentioned in the literature indicate that the above values of B are plausible: 1) Dulk et al. [1976] estimated the average field strength to be in the range $\approx 3.1 - 0.7$ G over $r \approx 1.8 - 3.1\ R_\odot$ by assuming gyro-synchrotron mechanism for similar CME associated non-thermal radio continuum; 2) Stewart et al. [1982] reported $B > 0.6$ G at $r \approx 2.5\ R_\odot$ for the type IVm burst observed by them at 80 MHz in association with the CME core. The authors had attributed the radio emission to be either at the fundamental or the second harmonic of the plasma frequency. Note that if the density requirements for particularly the second harmonic plasma emission are nearly the same as that for the gyro-synchrotron emission, then it is possible that the corresponding B values could be similar [Dulk et al., 1976]; 3) Gopalswamy and Kundu [1989a], Bastian et al. [2001] evaluated $B \approx 1.5$ G at $r \approx 1.5\ R_\odot$ based on similar non-thermal radio continuum due to

gyro-synchrotron emission from the associated CMEs; 4) Ramesh et al. [2010] computed the magnetic field in a coronal streamer at $r \approx 1.7\ R_\odot$ to be ≈ 5 G, through observations of polarized radio emission from the associated radio source at 77 MHz. This is nearly the same as the estimated B in the present case. The fact that the CMEs are density enhancements similar to the streamers could probably be a reason for this; 5) Tun and Vourlidas [2013] showed that $B \approx 5 - 15$ G for the type IVm bursts observed by them at $r \approx 1.7\ R_\odot$. The authors had shown that the bursts are likely due to optically thin gyro-synchrotron emission from the mildly relativistic non-thermal electrons in the magnetic field of the associated CME core; 6) Ramesh et al. [2013] estimated $B \approx 4$ G at $r \approx 1.6\ R_\odot$ for the type IVm radio bursts due to second harmonic plasma emission from the enhanced electron density associated with the 'leg' of the corresponding CMEs. Considering that the coronal magnetic field associated with the active regions have a range of values [Dulk and McLean, 1978, Ramesh et al., 2003, 2011b, Sasikumar Raja and Ramesh, 2013], the different estimates mentioned above can be regarded as reasonable. Given the paucity of the coronal magnetic field measurements, particularly in close association with a CME, the results indicate the usefulness of the contemporaneous observations of the solar corona in white light and radio frequencies particularly over $r \lesssim 2\ R_\odot$.

References

M. Aubier, Y. Leblanc, and A. Boischot. Observations of the Quiet Sun at Decameter Wavelengths - Effects of Scattering on the Brightness Distribution. A&A, 12:435, June 1971.

H. Aurass, G. Rausche, G. Mann, and A. Hofmann. Fiber bursts as 3D coronal magnetic field probe in postflare loops. A&A, 435:1137–1148, June 2005. doi: 10.1051/0004-6361:20042199.

T. S. Bastian. Low-frequency solar radiophysics with LOFAR and FASR. Planet. Space Sci., 52:1381–1389, December 2004. doi: 10.1016/j.pss.2004.09.015.

T. S. Bastian and D. E. Gary. On the feasibility of imaging coronal mass ejections at radio wavelengths. J. Geophys. Res., 102:14031–14040, July 1997. doi: 10.1029/97JA00483.

T. S. Bastian, M. Pick, A. Kerdraon, D. Maia, and A. Vourlidas. The Coronal Mass Ejection of 1998 April 20: Direct Imaging at Radio Wavelengths. ApJ, 558:L65–L69, September 2001. doi: 10.1086/323421.

A. Boischot. Caractères d'un type d'émission hertzienne associé à certaines éruptions chromosphériques. *Academie des Sciences Paris Comptes Rendus*, 244:1326–1329, 1957.

A. Boischot and M. Pick. Structure of the Type IV Radio Burst and Its Relation with

Solar Cosmic Rays. *Journal of the Physical Society of Japan Supplement*, 17:B203, 1962.

G. E. Brueckner, R. A. Howard, M. J. Koomen, C. M. Korendyke, D. J. Michels, J. D. Moses, D. G. Socker, K. P. Dere, P. L. Lamy, A. Llebaria, M. V. Bout, R. Schwenn, G. M. Simnett, D. K. Bedford, and C. J. Eyles. The Large Angle Spectroscopic Coronagraph (LASCO). Sol. Phys., 162:357–402, December 1995. doi: 10.1007/BF00733434.

G. A. Dulk. The Gyro-Synchrotron Radiation from Moving Type IV Sources in the Solar Corona. Sol. Phys., 32:491–503, October 1973. doi: 10.1007/BF00154962.

G. A. Dulk. Radio emission from the sun and stars. ARA&A, 23:169–224, 1985. doi: 10.1146/annurev.aa.23.090185.001125.

G. A. Dulk and D. J. McLean. Coronal magnetic fields. Sol. Phys., 57:279–295, April 1978. doi: 10.1007/BF00160102.

G. A. Dulk, S. Jacques, S. F. Smerd, R. M. MacQueen, J. T. Gosling, R. T. Steward, K. V. Sheridan, R. D. Robinson, and A. Magun. White light and radio studies of the coronal transient of 14-15 September 1973. I - Material motions and magnetic field. Sol. Phys., 49:369–394, August 1976.

R. A. Duncan. Langmuir-wave conversion as the explanation of moving type IV solar meter-wave radio outbursts. Sol. Phys., 73:191–204, September 1981. doi: 10.1007/BF00153154.

E. Ebenezer, R. Ramesh, K. R. Subramanian, M. S. SundaraRajan, and C. V. Sastry. A new digital spectrograph for observations of radio burst emission from the Sun. A&A, 367:1112–1116, March 2001. doi: 10.1051/0004-6361:20000540.

E. Ebenezer, K. R. Subramanian, R. Ramesh, M. S. Sundararajan, and C. Kathiravan.

Gauribidanur radio array solar spectrograph (GRASS). *Bulletin of the Astronomical Society of India*, 35:111–119, June 2007.

D. E. Gary, G. A. Dulk, L. L. House, R. Illing, and W. J. Wagner. The Type IV burst of 1980 June 29, 0233 UT - Harmonic plasma emission? A&A, 152:42–50, November 1985.

T. E. Gergely. Type IV bursts and coronal mass ejections. Sol. Phys., 104:175–178, March 1986. doi: 10.1007/BF00159959.

N. Gopalswamy and M. R. Kundu. A slowly moving plasmoid associated with a filament eruption. Sol. Phys., 122:91–110, March 1989a. doi: 10.1007/BF00162829.

N. Gopalswamy and M. R. Kundu. Radioheliograph and white-light coronagraph studies of a coronal mass ejection event. Sol. Phys., 122:145–173, March 1989b. doi: 10.1007/BF00162832.

N. Gopalswamy and M. R. Kundu. Multiple moving magnetic structures in the solar corona. Sol. Phys., 128:377–397, August 1990. doi: 10.1007/BF00838474.

R. J. M. Grognard and D. J. McLean. Non-Existence of Linear Polarization in Type III Solar Bursts at 80 MHz. Sol. Phys., 29:149–161, March 1973. doi: 10.1007/BF00153446.

E. Hildner. Mass ejections from the solar corona into interplanetary space. In M. A. Shea, D. F. Smart, and S. T. Wu, editors, *Study of Travelling Interplanetary Phenomena*, volume 71 of *Astrophysics and Space Science Library*, pages 3–20, 1977.

R. A. Howard, J. D. Moses, A. Vourlidas, J. S. Newmark, D. G. Socker, S. P. Plunkett, C. M. Korendyke, J. W. Cook, A. Hurley, J. M. Davila, W. T. Thompson, O. C. St Cyr, E. Mentzell, K. Mehalick, J. R. Lemen, J. P. Wuelser, D. W. Duncan, T. D. Tarbell, C. J. Wolfson, A. Moore, R. A. Harrison, N. R. Waltham, J. Lang, C. J.

Davis, C. J. Eyles, H. Mapson-Menard, G. M. Simnett, J. P. Halain, J. M. Defise, E. Mazy, P. Rochus, R. Mercier, M. F. Ravet, F. Delmotte, F. Auchere, J. P. Delaboudiniere, V. Bothmer, W. Deutsch, D. Wang, N. Rich, S. Cooper, V. Stephens, G. Maahs, R. Baugh, D. McMullin, and T. Carter. Sun Earth Connection Coronal and Heliospheric Investigation (SECCHI). Space Sci. Rev., 136:67–115, April 2008. doi: 10.1007/s11214-008-9341-4.

K. Kai. Observations of strong circular polarization in a moving type IV burst. *Proceedings of the Astronomical Society of Australia*, 1:189, March 1969.

C. Kathiravan, R. Ramesh, and H. S. Nataraj. The Post-Coronal Mass Ejection Solar Atmosphere and Radio Noise Storm Activity. ApJ, 656:L37–L40, February 2007. doi: 10.1086/512013.

C. Kathiravan, R. Ramesh, I. V. Barve, and M. Rajalingam. Radio Observations of the Solar Corona During an Eclipse. ApJ, 730:91, April 2011. doi: 10.1088/0004-637X/730/2/91.

A. Kerdraon. Observation of small size solar radio bursts at metric wavelengths. A&A, 71:266–268, January 1979.

A. Kerdraon, M. Pick, G. Trottet, C. Sawyer, R. Illing, W. Wagner, and L. House. The association of radio noise storm enhancements with the appearance of additional material in the corona. ApJ, 265:L19–L21, February 1983. doi: 10.1086/183950.

P. Kishore, C. Kathiravan, R. Ramesh, M. Rajalingam, and I. V. Barve. Gauribidanur Low-Frequency Solar Spectrograph. Sol. Phys., April 2014. doi: 10.1007/s11207-014-0539-1.

J. D. Kraus. *Radio astronomy.* 1973.

J. D. Kraus, M. Tiuri, A. V. Raisanen, and T. D. Carr. *Radio astronomy receivers.* 1986.

M. R. Kundu. Some Studies on the Occurrence of Type IV Solar Bursts of Continuum Radiation. ApJ, 134:96, July 1961. doi: 10.1086/147132.

M. R. Kundu. Some Aspects of the Type-IV Continuum Radiation on Decimeter Wavelengths. In C. de Jager, editor, *The Solar Spectrum*, volume 1 of *Astrophysics and Space Science Library*, page 408, 1965.

M. R. Kundu and J. W. Firor. Interferometric Studies of Type IV Solar Bursts of Continuum Radiation on 340 and 87 Mc/s. ApJ, 134:389, September 1961. doi: 10.1086/147166.

M. R. Kundu, E. J. Schmahl, N. Gopalswamy, and S. M. White. Three dimensional structures of coronal streamers, holes and CME plasmoids from multifrequency imaging observations. *Advances in Space Research*, 9:41–45, 1989. doi: 10.1016/0273-1177(89)90092-6.

K. R. Lang and R. F. Willson. VLA observations of a solar noise storm. ApJ, 319:514–519, August 1987. doi: 10.1086/165474.

J. R. Lemen, A. M. Title, D. J. Akin, P. F. Boerner, C. Chou, J. F. Drake, D. W. Duncan, C. G. Edwards, F. M. Friedlaender, G. F. Heyman, N. E. Hurlburt, N. L. Katz, G. D. Kushner, M. Levay, R. W. Lindgren, D. P. Mathur, E. L. McFeaters, S. Mitchell, R. A. Rehse, C. J. Schrijver, L. A. Springer, R. A. Stern, T. D. Tarbell, J.-P. Wuelser, C. J. Wolfson, C. Yanari, J. A. Bookbinder, P. N. Cheimets, D. Caldwell, E. E. Deluca, R. Gates, L. Golub, S. Park, W. A. Podgorski, R. I. Bush, P. H. Scherrer, M. A. Gummin, P. Smith, G. Auker, P. Jerram, P. Pool, R. Soufli, D. L. Windt, S. Beardsley, M. Clapp, J. Lang, and N. Waltham. The Atmospheric Imaging Assembly (AIA) on the Solar Dynamics Observatory (SDO). Sol. Phys., 275:17–40, January 2012. doi: 10.1007/s11207-011-9776-8.

D. J. F. Maia, R. Gama, C. Mercier, M. Pick, A. Kerdraon, and M. Karlický. The Radio-

Coronal Mass Ejection Event on 2001 April 15. ApJ, 660:874–881, May 2007. doi: 10.1086/508011.

D. B. Melrose. *Gyromagnetic emission and Bremsstrahlung*, pages 211–236. 1985.

C. Mercier, P. Subramanian, A. Kerdraon, M. Pick, S. Ananthakrishnan, and P. Janardhan. Combining visibilities from the giant meterwave radio telescope and the Nancay radio heliograph. High dynamic range snapshot images of the solar corona at 327 MHz. A&A, 447:1189–1201, March 2006. doi: 10.1051/0004-6361:20053621.

M. Pick and N. Vilmer. Sixty-five years of solar radioastronomy: flares, coronal mass ejections and Sun Earth connection. A&A Rev., 16:1–153, October 2008. doi: 10.1007/s00159-008-0013-x.

M. Pick-Gutmann. Évolution des émissions radioélectriques solaires de type IV et leur relation avec d'autres phénomènes solaires et géophysiques. *Annales d'Astrophysique*, 24:183, February 1961.

R. Ramesh and E. Ebenezer. Decameter Wavelength Observations of an Absorption Burst from the Sun and Its Association with an X2.0/3B Flare and the Onset of a "Halo" Coronal Mass Ejection. ApJ, 558:L141–L143, September 2001. doi: 10.1086/323498.

R. Ramesh and C. V. Sastry. Radio observations of a coronal mass ejection induced depletion in the outer solar corona. A&A, 358:749–752, June 2000.

R. Ramesh, K. R. Subramanian, M. S. Sundararajan, and C. V. Sastry. The Gauribidanur Radioheliograph. Sol. Phys., 181:439–453, August 1998. doi: 10.1023/A:1005075003370.

R. Ramesh, K. R. Subramanian, and C. V. Sastry. Phase calibration scheme for a "T" array. A&AS, 139:179–181, October 1999a. doi: 10.1051/aas:1999387.

R. Ramesh, K. R. Subramanian, and C. V. Sastry. Eclipse Observations of Compact Sources in the Outer Solar Corona. Sol. Phys., 185:77–85, March 1999b. doi: 10.1023/A:1005149830652.

R. Ramesh, C. Kathiravan, A. S. Narayanan, and E. Ebenezer. Metric observations of transient, quasi-periodic radio emission from the solar corona in association with a "halo" CME and an "EIT wave" event. A&A, 400:753–758, March 2003. doi: 10.1051/0004-6361:20030019.

R. Ramesh, M. S. S. Rajan, and C. V. Sastry. The 1024 channel digital correlator receiver of the Gauribidanur radioheliograph. *Experimental Astronomy*, 21:31–40, February 2006a. doi: 10.1007/s10686-006-9065-y.

R. Ramesh, H. S. Nataraj, C. Kathiravan, and C. V. Sastry. The Equatorial Background Solar Corona during Solar Minimum. ApJ, 648:707–711, September 2006b. doi: 10.1086/505677.

R. Ramesh, C. Kathiravan, M. S. Sundararajan, I. V. Barve, and C. V. Sastry. A Low-Frequency (30 - 110 MHz) Antenna System for Observations of Polarized Radio Emission from the Solar Corona. Sol. Phys., 253:319–327, December 2008. doi: 10.1007/s11207-008-9272-y.

R. Ramesh, C. Kathiravan, and C. V. Sastry. Estimation of Magnetic Field in the Solar Coronal Streamers Through Low Frequency Radio Observations. ApJ, 711:1029–1032, March 2010. doi: 10.1088/0004-637X/711/2/1029.

R. Ramesh, C. Kathiravan, and A. S. Narayanan. Low-frequency Observations of Polarized Emission from Long-lived Non-thermal Radio Sources in the Solar Corona. ApJ, 734: 39, June 2011b. doi: 10.1088/0004-637X/734/1/39.

R. Ramesh, C. Kathiravan, I. V. Barve, and M. Rajalingam. High Angular Resolution Radio Observations of a Coronal Mass Ejection Source Region at Low Frequencies

during a Solar Eclipse. ApJ, 744:165, January 2012. doi: 10.1088/0004-637X/744/2/165.

R. Ramesh, P. Kishore, S. M. Mulay, I. V. Barve, C. Kathiravan, and T. J. Wang. Low-frequency Observations of Drifting, Non-thermal Continuum Radio Emission Associated with the Solar Coronal Mass Ejections. ApJ, 778:30, November 2013. doi: 10.1088/0004-637X/778/1/30.

A. C. Riddle. On the Observation of Scattered Radio Emission from Sources in the Solar Corona. Sol. Phys., 35:153–169, March 1974. doi: 10.1007/BF00156964.

R. D. Robinson. On the polarization characteristics of moving type IV solar radio bursts. *Proceedings of the Astronomical Society of Australia*, 2:258–261, September 1974.

R. D. Robinson. Observations and Interpretation of Moving Type IV Solar Radio Bursts. Sol. Phys., 60:383–398, December 1978a. doi: 10.1007/BF00156538.

R. D. Robinson. A study of solar flare continuum events observed at metre wavelengths. *Australian Journal of Physics*, 31:533–545, December 1978b.

R. D. Robinson. Observations and Interpretation of Moving Type IV Solar Radio Bursts. Sol. Phys., 60:383–398, December 1978c. doi: 10.1007/BF00156538.

R. D. Robinson. Scattering of radio waves in the solar corona. *Proceedings of the Astronomical Society of Australia*, 5:208–211, 1983.

R. D. Robinson and S. F. Smerd. Solar flare continua at the metre wavelengths. *Proceedings of the Astronomical Society of Australia*, 2:374–378, October 1975.

K. Sasikumar Raja and R. Ramesh. Low-frequency Observations of Transient Quasi-periodic Radio Emission from the Solar Atmosphere. ApJ, 775:38, September 2013. doi: 10.1088/0004-637X/775/1/38.

S. F. Smerd and G. A. Dulk. In R. Howard, editor, *Solar Magnetic Fields*, volume 43 of *IAU Symposium*, page 616, 1971.

R. T. Stewart. *Moving Type IV bursts*, pages 361–383. 1985.

R. T. Stewart and D. J. McLean. Correcting low-frequency solar radio source positions for ionospheric refraction. *Proceedings of the Astronomical Society of Australia*, 4: 386–389, 1982.

R. T. Stewart, R. A. Duncan, S. Suzuki, and G. J. Nelson. Observations of high brightness temperatures in moving type IV solar radio bursts. *Proceedings of the Astronomical Society of Australia*, 3:247–249, 1978.

R. T. Stewart, G. A. Dulk, K. V. Sheridan, L. L. House, W. J. Wagner, R. Illing, and C. Sawyer. Visible light observations of a dense plasmoid associated with a moving Type IV solar radio burst. A&A, 116:217–223, December 1982.

K. R. Subramanian and C. V. Sastry. The low-frequency radio spectrum of the continuum emission from the undisturbed sun. *Journal of Astrophysics and Astronomy*, 9:225–229, December 1988. doi: 10.1007/BF02715067.

T. Takakura. Acceleration of Electrons in the Solar Atmosphere and Type IV Radio Outbursts. PASJ, 13:166, 1961.

T. Takakura and K. Kai. Spectra of Solar Radio Type IV Bursts. PASJ, 13:94, 1961.

G. Thejappa and R. J. MacDowall. Effects of Scattering on Radio Emission from the Quiet Sun at Low Frequencies. ApJ, 676:1338–1345, April 2008. doi: 10.1086/528835.

G. Trottet, A. Kerdraon, A. O. Benz, and R. Treumann. Quasi-periodic short-term modulations during a moving type IV burst. A&A, 93:129–135, January 1981.

S. D. Tun and A. Vourlidas. Derivation of the Magnetic Field in a Coronal Mass Ejection Core via Multi-frequency Radio Imaging. ApJ, 766:130, April 2013. doi: 10.1088/0004-637X/766/2/130.

T. Wang and J. M. Davila. Sol. Phys., 289:3723, 2014.

A. A. Weiss. The Type IV Solar Radio Burst at Metre Wavelengths. *Australian Journal of Physics*, 16:526, December 1963. doi: 10.1071/PH630526.

S. M. White, A. O. Benz, S. Christe, F. Fárník, M. R. Kundu, G. Mann, Z. Ning, J.-P. Raulin, A. V. R. Silva-Válio, P. Saint-Hilaire, N. Vilmer, and A. Warmuth. The Relationship Between Solar Radio and Hard X-ray Emission. Space Sci. Rev., 159: 225–261, September 2011. doi: 10.1007/s11214-010-9708-1.

S.M. White. *Asian J. Phys*, 16:189, 2007.

J. P. Wild. Some investigations of the solar corona: the first two years of observation with the Culgoora radioheliograph. *Proceedings of the Astronomical Society of Australia*, 1:365, September 1970.

J. P. Wild and S. F. Smerd. Radio Bursts from the Solar Corona. ARA&A, 10:159, 1972. doi: 10.1146/annurev.aa.10.090172.001111.

J. P. Wild, S. F. Smerd, and A. A. Weiss. Solar Bursts. ARA&A, 1:291, 1963. doi: 10.1146/annurev.aa.01.090163.001451.

R. F. Willson, S. L. Redfield, K. R. Lang, B. J. Thompson, and O. C. St. Cyr. First VLA Observations of Nonthermal Metric Bursts Associated with Coronal Mass Ejections Detected by the Solar and Heliospheric Observatory. ApJ, 504:L117–L121, September 1998. doi: 10.1086/311585.

Chapter 6

Scattering studies of the solar corona

6.1 Introduction

One of the observational evidences of scattering in radio astronomy is an apparent increase in the angular diameter of a distant radio source when its radiation passes through a scattering medium present along the observer's line of sight (LOS). Random fluctuations in the spatial distribution of the electron density in the medium introduce irregular variations in the refractive index which lead to scattering of radio waves. Spacecraft observations prove that solar wind is a turbulent plasma which results in fluctuations in all plasma parameters such as electron density, plasma flow velocity and magnetic fields. Turbulent characteristics vary systematically with heliocentric distances [Spangler and Sakurai, 1995]. Propagating radio waves in the solar corona undergoes refraction, reflection, scattering due to the the nonuniform distributions of the electron densities from point to point. During the propagation of radio waves in such a medium, the above mentioned phenomenon modulates the structure of the actual distant cosmic source or spacecraft beacons. Such a modulation gives the important information of the solar corona/solar wind. There were many attempts to estimate the modulated structure function in solar

wind. Coles and Harmon [1989a] described about such techniques briefly. It is known that the density variation from point to point in the solar corona causes variations in refractive index of the medium and those fluctuations are represented using the wave structure function, $D(s)$. Wave structure function of the solar corona is estimated using different techniques. Few of them are: spectral broadening, angular broadening, spacecraft beacon phase scintillation, interferometer phase scintillation, and intensity scintillation. Wave structure function is related to the density fluctuation spectrum in the form of a linear transformation and estimation of the former is the more precise than the latter. Some of the different techniques used to estimate the mutual coherence function, and the structure function are discussed briefly in the subsequent sections.

The mutual coherence function, which a radio interferometer measures, is directly related to the wave structure function of the scattering medium which, in turn, is related to the spatial spectrum of the electron density inhomogeneities there [Coles and Harmon, 1989a, Armstrong et al., 1990, Anantharamaiah et al., 1994]. Note that radio interferometer measurements (on a baseline of length s) of a celestial source viewed through a turbulent medium is affected by density inhomogeneities of scale size s. The other radio astronomy observational techniques using which the spatial spectrum of the electron density inhomogeneities can be studied are spectral broadening, phase scintillations, and intensity scintillations [Armstrong et al., 1990, Bastian, 1994].

The angular scattering of radio waves caused by inhomogeneities in the electron density distribution over the heliocentric distance range $r \approx 10 - 60\ R_\odot$ has been studied since 1952 at frequencies $\lesssim 100$ MHz using occultation observations of the Crab nebula over interferometer baselines $\lesssim 3$ km [Machin and Smith, 1952, Hewish, 1955, Bolton et al., 1958, Vitkevich, 1958, Slee, 1959, Högbom, 1960, Gorgolewski et al., 1962, Erickson, 1964, Bazelyan et al., 1970, Harries et al., 1970, Sastry and Subramanian, 1974]. Crab nebula lies close to the plane of the ecliptic and its line of sight passes as near as $r \approx 5\ R_\odot$ around $15 - 16$ June every year. The variation of the scattering with r and increase in the angle

of scattering with wavelength were some of the main results which emerged out of these observations. It was also noted that the anisotropy in scattering on spatial scales $\lesssim 3$ km, estimated from the axial ratio of the angular broadened images, was 50% more during solar maximum as compared to the solar minimum [Ward, 1975].

Two dimensional images of the angular broadened Crab nebula were first produced using aperture synthesis techniques using Culgoora radio heliograph by Blesing and Dennison [1972] at < 200 MHz. Other than the Crab nebula, using Very Large Array (VLA) study of angular broadening of the radio sources 3C279 was carried out by Armstrong et al. [1986, 1990]. Also Cornwell et al. [1989] reported observations of the 3C279 with high time resolution when the line of sight passed close to the Sun and established coherence properties of the corona. Brief review of the angular broadening and other methods to measure the structure function of the turbulent medium was reviewed in Coles and Harmon [1989a], Anantharamaiah et al. [1994]. Similar observations of other radio sources with the VLA at comparatively higher frequencies and over the range $r \approx 2 - 13\ R_\odot$ were reported by Armstrong et al. [1990], Anantharamaiah et al. [1994]. The observations were sensitive to spatial scales in the range $\approx 1 - 35$ km. VLBI observations of angular broadening, sensitive to spatial scales $\approx 200 - 2000$ km over the range $r \approx 18 - 243\ R_\odot$ were reported by Sakurai et al. [1992].

The spatial scales of the corresRecently Subramanian and Cairns [2011] used the above model to address the angular sizes of the radio sources embedded in the solar corona at a typical frequency of 327 MHz. They had extrapolated the model in the sunward direction to $r < 2\ R_\odot$ in a straightforward manner. The results indicate that discrete sources of size $\lesssim 10''$ can be observed in the solar corona at the above frequency. But observations reported by Lang and Willson [1987], Zlobec et al. [1992], Mercier et al. [2006] indicate that the smallest observable angular size of the coronal radio sources at frequencies ≈ 327 MHz is $\approx 40''$. Note that the angular resolution in the observations reported by the above authors was $\approx 4''$. Source sizes estimated from majority of the

high angular resolution observations at low frequencies ($\approx$ 30-100 MHz) also seem to be limited to $\gtrsim 60''$ [Willson et al., 1998, Ramesh et al., 1999, Ramesh and Sastry, 2000, Ramesh and Ebenezer, 2001, Ramesh et al., 2012]. This is consistent with the reports on the minimum observable source sizes in the above frequency range [Riddle, 1974, Bastian, 2004, Cairns, 2004]. In view of the non-availability of estimates of $C_N^2(r)$ over smaller spatial scales at present, and presuming that relevant spatial scales to understand the angular broadening of discrete sources embedded in the solar corona are $\lesssim$ 10 km [Bastian, 1994], an independent estimates of $C_N^2(r)$ on smaller spatial scales were obtained.

6.2 Motivation

As mentioned previously, direct measurements of magnetic field strength in the corona $\gtrsim 0.2\ R_\odot$ are not available. The magnetic field strength in the corona is found from the extrapolation of optical measurements of photospheric fields. Coronal magnetic field measurements reported by Lin et al. [2000] from observations of the Stokes V profiles of the coronal emission line Fe XIII ($\lambda = 1074.7$ nm) resulting from the longitudinal Zeeman effect was $\approx$ 10 and 33 G above active regions at heights of 0.12 and 0.154 $R_\odot$ respectively. High resolution circularly polarized observations in the frequency range $1 - 20$ GHz are routinely used to measure the magnetic field strength above active regions at $\approx 0.05\ R_\odot$ [Kakinuma and Swarup, 1962, Gelfreikh, 2004, Ryabov, 2004, White, 2004]. The radio emission from the 'undisturbed' Sun, coronal streamers, and coronal holes at heights $\gtrsim 0.2\ R_\odot$ lies at frequencies $\lesssim$ 100 MHz. Thermal nature of the radiation was recognized by Smerd [1950]. Also it was never pointed out that the direct measurements of the strength of the magnetic fields exist in the outer corona. The polarization characteristics of the continuum radiation from the 'undisturbed' Sun never been attempted [Sastry, 2009]. Magnetic field strengths estimated using the circularly polarized thermal radio emission from solar coronal streamers were 5 ± 1 G and 6 ± 2 G at 1.7 and 1.5 $R_\odot$

respectively [Ramesh et al., 2010]. Sastry [2009], using the Haselgrove equations from the radio ray propagation technique in an anisotropic medium, the dcp of the thermal radio emissions at low frequencies in the corona was estimated. Given methodology can be used to determine the weak magnetic field strengths directly by knowing the dcp at low frequencies and it is briefly reviewed here.

The anisotropy in the corona is due to the presence of the magnetic fields in it. When an unpolarized radio radiation propagates through such a medium, the radiation splits into two modes as mentioned previously: o-mode and e-mode due to the difference in the optical depths which arises due to the prevailing magnetic fields. The ray paths of these two modes are found using the magneto-ionic theory assuming the cold plasma approximation. It is known that in an inhomogeneous anisotropic medium, the energy associated with electromagnetic waves does not travel in the direction of the wave normal even in the case of plane waves but in a different direction called the ray path. The ray refractive index of the solar corona at a low frequency varies from zero (at the level where the plasma and observing frequencies are equal) to unity (at a large distance away from the Sun). Therefore the ray paths are curved instead of straight lines. By knowing the propagated energy along the ray path and the integrated absorption coefficient along the path, the total optical depth of either of the modes can be estimated. Note that the ray refractive index is not known a priori but information on the phase refractive index, which is a function of the position and direction of the wave normal can be derived from the Appleton-Hartree equation. A set of differential equations to determine the rate of change of the wave normal direction along the ray path in terms of the phase refractive index and its derivatives were derived by Haselgrove [1955], Haselgrove and Haselgrove [1960], Haselgrove [1963]. The Haselgrove equations in two dimensions were used to derive the one-dimensional brightness distribution of the outer corona at a frequency of 30 MHz for the two circular modes [Golap and Sastry, 1994]. Different modelings and observations confirm that the structure of the magnetic field consists of open field line connections

between the solar surface and the heliosphere.

The expected magnetic field strengths in the 'undisturbed' corona at heliocentric distances ($1.5\ R_\odot \lesssim R \lesssim 3\ R_\odot$) are estimated from average of the field strengths [Spangler, 2005]. He also used the Faraday rotation technique on extragalactic radio sources at various times in the heliocentric distance range $6\ R_\odot \lesssim R \lesssim 10\ R_\odot$. The average field strength at a distance $\approx 6.2\ R_\odot$ measured by him was 40 mG. Pätzold et al. [1987], used the Faraday rotation measurements using the Helios spacecraft in the heliocentric distance range $3\ R_\odot \lesssim R \lesssim 10\ R_\odot$. The estimated field strength at $6.2\ R_\odot$ was 57 mG. By using the Newkirk density model and assuming the reference magnetic field given by Spangler [2005] the magnetic fields were estimated using the expression 6.1 which was given by Dulk and McLean [1978].

$$\vec{B}(R) = \frac{B_o}{[R-1]^{1.5}}\hat{r} \tag{6.1}$$

Using the methodology described by Sastry [2009], brightness temperatures of the o-mode (T_b^o) and e-mode (T_b^e) were estimated. The corresponding dcp was also estimated using the equation 6.2.

$$dcp[\%] = \frac{T_b^e - T_b^o}{T_b^e + T_b^o} \times 100 \tag{6.2}$$

In the heliocentric distance range of $1.5\ R_\odot \lesssim R \lesssim 3\ R_\odot$, the plasma frequencies in the corona vary from 30 to 10 MHz according to the Newkirk [1961] model with $D = 1$ (see section 1.12). The distribution of the degree of polarization is calculated at each of the three frequencies 10, 20 and 30 MHz from the center to the limb in the equatorial plane of the 'radio' Sun. The field strength at each frequency is varied from 100 mG up to 1600 mG. Note that in this methodology, the model of Spangler [2005] was used to determine the reference field alone whereas in the dcp calculations, the equation 6.2 was used. The maximum value of dcp at all the three frequencies occurs in the central regions of the 'radio' Sun. The dcp increases with field strength at all the frequencies and for the same field strength the dcp increases with decreasing frequency. It is possible

that field strengths of ≈ 200 mG can be detected from low frequency circular polarization observations of the 'undisturbed' Sun.

The magnetic field strength in the corona above active regions, estimated from radio burst observations, decreases from $1-8$ G at 1.6 $R_\odot$ to $0.3-0.9$ G at 2.5 $R_\odot$ [Vršnak et al., 2002]. The enhanced radio radiation emitted by coronal streamers with density larger by a factor ≈ 5 compared to the 'undisturbed' Sun at heliocentric distances of $1.5-2.5$ $R_\odot$ which lies in the frequency range $80-20$ MHz. A computation of the distribution of the dcp across the 'radio' Sun by uniformly increasing the density ($D > 1$ in the Newkirk model) over the entire corona revealed that the dcp variations will be significant only at distances away from the center at frequencies around 80 MHz, for any magnetic field strength. The distribution of the dcp at 80 MHz across the 'radio' Sun with a streamer incorporated at the limb was computed. For the Newkirk electron density model the distribution of dcp across the radio Sun is found to depend on the factor by which the density increases in the region of the streamer, orientation of the axis of the streamer, the strengths of the fields in the ambient and streamer regions, and the size of the streamer. The axis of the streamer is placed in the equatorial plane and the dcp was calculated at various distances from the center to the limb. The field strength is varied from 1 to 4 G at the 80 MHz plasma level in the streamer and a small ambient field strength ≈ 300 mG. The assumed azimuth and width of the streamer were 65^o (almost the solar limb) and $10'$ respectively. It was noticed that comparison of the brightness distributions with and without streamer shows that the width of the 'radio' Sun increases considerably in the presence of the streamer. The dcp attains the maximum value close to the half-power point, i.e., where the brightness temperature of the o and e-mode (T_b^o and T_b^e) radiations become equal to half of their peak values, and increases with the field strength. Finally it is found that the dcp of the streamer increases with decreasing frequency for any magnetic field strength. From these results, it follows that when the location of the coronal streamer is near the limb of the 'radio' Sun the effect of the magnetic field is

maximum at frequencies around 80 MHz and its strength can be estimated by measuring the dcp of the emitted radio frequency thermal radiation.

Magnetic field lines in coronal holes are believed to be open from the base of the corona. But there are no estimates of the magnetic field strength in the outer coronal holes. Since there is no limit to the size of the coronal holes and a coronal hole can occupy a large fraction of the disk, by assuming the size of the coronal hole $10'$ and the axis is placed in the equatorial plane of the Sun with an azimuth of 65^o (i.e. close to the solar limb similar to the streamer case) the magnetic field strength was estimated. The field strength in the ambient corona is set to a small value of $\approx$ 300 mG. But in the case of coronal hole magnetic field was varied in the range $\approx 1 - 2$ G. The distribution of the dcp at 80 MHz was also computed by assuming the Newkirk density model. From the computations it was found that the values of the dcp in the case of the coronal hole are relatively larger than those of the coronal streamer for the same field strengths. It was noticed that, in the case of the coronal streamer the dcp increases with decreasing frequency of observation. Therefore it is clear that the strength of the magnetic field can be estimated by measuring the dcp of the thermal radiation from the coronal holes.

The dcp of the thermal radiation due to the presence of the magnetic field in the direction of any point on the Sun and at any frequency depends on the magnitude of absorption coefficient/total optical depth at various points in the path of the radiation, in the absence of the magnetic field, in that direction. The presence of the magnetic field modifies in such a way that the absorption coefficients/total optical depths of the ordinary and extraordinary radiations may differ resulting in difference of the o and e brightness temperatures. Therefore the emergent radiation will be circularly polarized. At frequencies greater than 80 MHz, the central thermal optical depth of the corona, in the absence of the magnetic field, is already large [Smerd, 1950, Sheridan and McLean, 1985]. Therefore any change in the optical depths due to the presence of the magnetic field has little or no effect on the brightness temperature of the o and e-mode radiations,

resulting in negligible dcp values. However, in the direction away from the center of the Sun, the thermal optical depth in the absence of the magnetic field reduces considerably. Therefore, in the presence of the magnetic field, the difference in the optical depths of o and e radiations can become large causing the emerging radiation to be circularly polarized. At frequencies less than 30 MHz, the central thermal optical depth of the corona, in the absence of the magnetic field, is small [Bracewell and Preston, 1956, Sheridan and McLean, 1985]. Hence the circular polarization effect due to the presence of the magnetic fields can be seen even in that direction. These are the reasons for the occurrence of maximum dcp in the central directions at low frequencies and also for the increase of dcp with decreasing frequency.

Therefore, direct magnetic field measurement in the middle corona using the low frequency radio observations are possible. Initial motivation behind Crab nebula observations in the present case is to infer the magnetic field associated with density enhancements/irregularities in LOS to the Crab nebula at various distances from the Sun [Ramesh et al., 2001b, Ramesh and Sastry, 2005, Sastry, 2009]. These enhancements/irregularities may be streamers or CMEs or irregular density distribution in the solar atmosphere. When Crab nebula radiation passes through such clumps/irregularities, there may be a possible circular polarization either due to the splitting of randomly polarized or linearly polarized radiation into oppositely polarized magneto-ionic modes (o-mode and e-mode) as mentioned. In the above discussion it is explicitly mentioned that by knowing the dcp in the corona, magnetic field strength can be estimated directly. Hence, the Crab nebula occultation observations were carried out in polarimetric mode. But we did not detect any deflection in Stokes V channel (see Figure 6.7). It is possible that the strength of the associated circular polarization is too weak to detect. However, the observations lead to the scattering studies of the solar corona which is discussed in the following sections.

6.3 Estimation of the structure function

Occultation of natural radio sources like pulsars, supernovae remnants and extra galactic radio sources by the solar corona, is considered as a situation of a plane wave interaction with the scattering medium (solar corona/solar wind). In some cases if the radio source is within the corona then spherical diverging radiation is assumed. In the present case Crab nebula occultation technique is used to estimate the structure function so the plane wave approximation is assumed. Figure 6.1 shows the thin screen scintillation model. Initially, a plane wave which travels from a distance source (star) passes through a turbulent solar wind and due to the inhomogeneous density fluctuation in it the plane wave gets crumpled.

Large scale variations shown in the Figure 6.1 correspond to the refractive scintillations and the small scale fluctuations correspond to the diffractive scintillations. Diffractive scintillations cause the angular broadening of the radio sources and the spectral corrugation of the radiation from the pulsars [Spangler, 2009]. Large scale gradients which correspond to the refractive scintillations cause the source position wandering in the sky. Note that diffractive scintillations are strong function of irregularities of the power law index (γ) and the measurements of γ are consistent with spacecraft observations. The density inhomogeneities in a turbulent medium can be characterized by their spatial power spectrum

$$P_{\delta n}(k) = C_N^2(r) k^{-\beta} \tag{6.3}$$

where δn is the fluctuating part of the electron density and k is the wave number. The latter is in the range $k_o < k < k_i$, where k_o and k_i are the reciprocals of the outer (largest) and inner (smallest) spatial scales of the density inhomogeneities [Rickett, 1990]. The spectrum is characterized by two parameters, the power-law exponent β ($2 < \beta < 4$) and the normalization constant $C_N^2(r)$. The latter is an indicator of the level of the density fluctuations (turbulence). Using VLBI observations of phase scintillations, Spangler et al. [1996] found that $C_N^2(r) = 1.8 \times 10^{10}(r/10)^{-3.66}$ over the range 10 $R_\odot \lesssim r \lesssim 60$ $R_\odot$. The

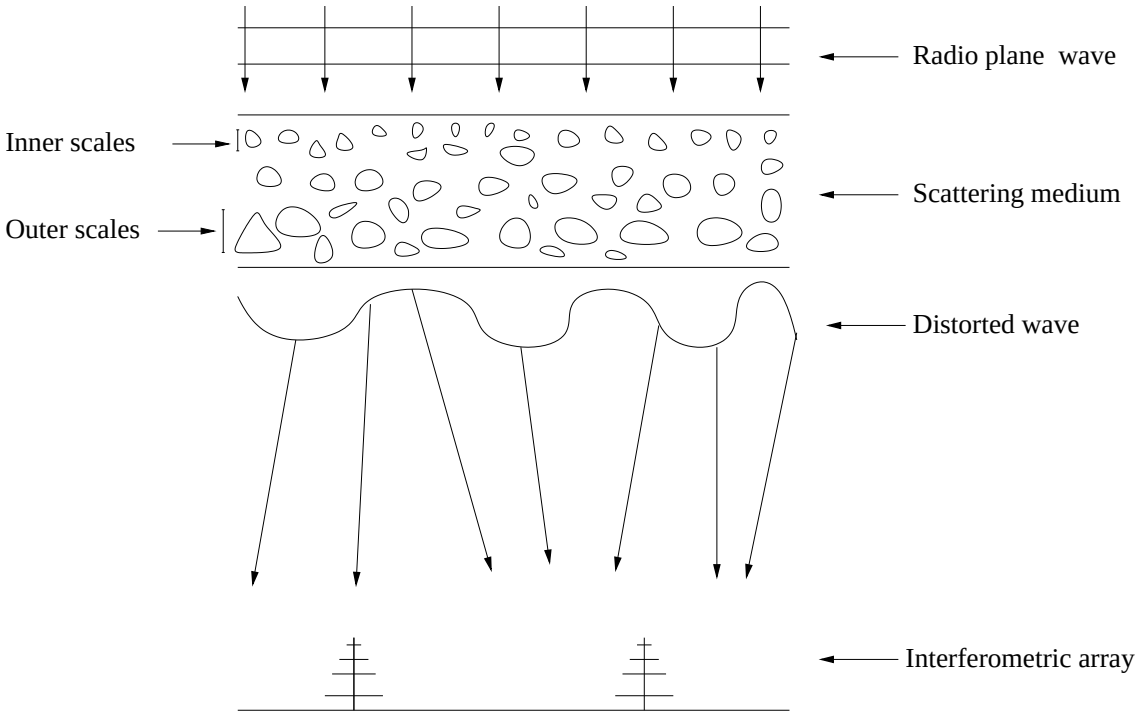

Fig. 6.1: The Figure shows the geometry of the thin-screen scintillation model. A plane wave from the distance celestial sources incident on a scattering medium (like solar wind/interplanetary medium, interstellar medium or Earth's ionosphere), the plane wave gets distorted due to the small scale irregularities (inner scales) and large scale irregularities (outer scales) are also shown.

above equation is valid for the Kolmogorov spectrum ($\beta = 11/3$) and its units are $m^{-20/3}$. In order to determine the quantity C_N^2 in the solar corona, different techniques are used so far and some of which are discussed briefly in the following sections.

6.3.1 Intensity scintillations

Earlier days, by observing the intensity scintillations of the natural radio sources, the turbulent spectrum was measured [Hewish et al., 1964, Cohen and Gundermann, 1969, Ekers and Little, 1971, Scott, 1978, Scott et al., 1983, Tyler et al., 1981, Coles and Harmon, 1989b]. The radiation from a compact radio sources is scattered in passage through a solar

wind and produces a diffraction pattern on Earth which causes the intensity scintillations.

6.3.2 Angular broadening

The angular and spectral broadening techniques measure the loss in the spatial or temporal coherence suffered by a coherent plane wave propagating through a scattering medium. By knowing correlation flux density when the radiation pass through a scattering medium and true correlation flux density, the mutual coherence function is measured which is Fourier transformation of the angular spectrum. Using the mutual coherence function the structure function of the scattering medium is measured. Angular broadening measurements have been made on extra galactic radio sources, sources of molecular masers and pulsars. The mutual coherence function, $\Gamma(s)$ is defined as $\langle E(p)E^*(p+s)\rangle/\langle|E|^2\rangle$, Where p is the position of the antenna and s is the baseline length between the two antennas (see section-6.8). Angular broadening measurements due to the solar wind is carried out by Hewish [1955].

6.3.3 Spectral broadening

Spectral broadening is an alternate technique to angular broadening to estimate the structure function. When the medium is moving with respect the observer the received signal will be broadened into a spectrum which is a Fourier transformation of temporal autocorrelation function. Using the function the structure function is estimated. Such observations have to be done using a single dish antenna to study the effect of scattering medium over a temporal coherence wave [Scott et al., 1983]. If the medium is moving with velocity V with respect to the observer the received signal will be broadened into a spectrum $P(f)$ whose Fourier transformation is the temporal autocorrelation function $\Gamma(\tau)$.

$$\Gamma(\tau) = \langle E(p)E^*(p+s)\rangle/\langle|E|^2\rangle \tag{6.4}$$

Since $s = V\tau$, $\Gamma(\tau)$ is related with the $\Gamma(s)$ the structure function is estimated using the formula 6.5,

$$D(s = V\tau) = -2\ ln[F[P(f)]] \tag{6.5}$$

where, 'F' indicates the Fourier transformation and

$$F[P(f)] = \Gamma(\tau) \tag{6.6}$$

6.3.4 Phase scintillations

For the scales greater than $\approx$ 100 km the correlation number becomes comparable to the estimated errors. Therefore, angular and spectral broadening techniques fail to estimate the mutual coherence function precisely. However, the mutual coherence function is measured by estimating the phase fluctuations using single dish coherent beacons. By comparing the phases of the dual frequency signals transmitted through a scattered medium using a spacecraft coherent beacons, the D(s) is estimated [Woo and Armstrong, 1979].

6.3.5 Very long baseline interferometry (VLBI)

The structure function, D(s) measurements are possible using a very long baseline interferometer (VLBI) observations of a point source. In VLBI measurements differential phase ($\Delta\phi_o(s)$) of interferometer approaches a geometrical phase ($\phi(p) - \phi(p + s)$) due to the large baseline length. By knowing the phase fluctuations, the structure function $D_o(s) \equiv [\langle[\Delta\phi_o(s)]^2\rangle]$ is estimated. The estimated $D_o(s)$ is approximately equal to the structure function $D(s)$. Diffractive scintillation phenomenon is observable in the case of pulsars because of finite angular size of the sources quenches the scintillations [Spangler, 2009, p.35].

Also the structure function is estimated using echoes of the radar observations.

Such estimates were made by observing the Venus using the Arecibo radar observations [Harmon and Coles, 1983]. Note that spectral broadening technique is limited to the scales $\approx 0.1 - 100$ km. Phase scintillation measurements useful for the scales which are greater than 100 km. Using the VLBI it is possible to estimate the scale lengths in the range $100 - 1000$ km. To estimate the structure functions of the medium, pulsars are preferable because of their compact sizes. Although the disadvantage of using pulsars is their poorly known distances in the ISM and also the galactic ionized hydrogen which is interposed on the line of sight and causes the drastic changes of the strength and properties of the angular broadening. Also intrinsic variability of pulsar makes analysis of the interferometer data complex. Therefore, sources of invariable flux density (like Crab nebula) are preferable for angular broadening measurements.

6.4 Leblanc density model

Density models in the middle corona are discussed in section-1.12 and note that those models are not suitable in the outer corona. In interplanetory space in-situ measurements of electron density were made by Bougeret et al. [1984] from 0.3 to 1 AU. They used the observations from the Helios 1 and 2 spacecraft and derived the density model. This model is reliable since it is derived directly from the observations. Leblanc et al. [1998b] derived an electron density model in the ecliptic plane from corona to 1 AU. The density model is based on the observations from 13.8 MHz to few kHz using the WAVES aboard the spacecraft of WIND. From the observations of type III bursts at each frequency the electron densities are estimated along the trajectory of the burst. In this model, it is assumed that the electron density from low corona to 1 AU is

$$N_e = ar^{-2} + br^{-4} + cr^{-6} \tag{6.7}$$

In the above equation the density fall off is steeper close to the Sun than the outer corona, which is in agreement with density measurements in the corona. The term r^{-2} is dominant from few tens of $R_\odot$ to and beyond 1 AU distance. The coefficient a is fixed by the density measurements obtained using WIND i.e N_e at 1 AU. In the corona $\approx 1.3 - 3\ R_\odot$ observations shows the variation of $N_e \approx r^{-6}$ [Newkirk, 1967, Saito et al., 1977]. In the first approximation, the coefficient c is determined by N_e which corresponds to the highest observing frequency (i.e usually 13.8 MHz). The other term also added which is proportional to r^{-4} to improve the transition between the corona and solar wind. The coefficient b is derived from the best least square fit of all the data points and simultaneously c is also improved. The density is calculated at every height in the solar corona using the equation-6.8. Figure 6.2 shows the variation of the electron density in the $1.8 - 215\ R_\odot$.

$$N_e = 3.3 \times 10^5\ R^{-2} + 4.1 \times 10^6\ R^{-4} + 8.0 \times 10^7\ R^{-6}\ \mathrm{cm}^{-3} \tag{6.8}$$

where R is the radial distance from the Sun in units of $R_\odot$.

$$N_e = 7.2\ R^{-2} + 1.95 \times 10^{-3}\ R^{-4} + 8.1 \times 10^{-7}\ R^{-6}\ \mathrm{cm}^{-3} \tag{6.9}$$

Note that in equation 6.9, R is in units of AU (1 AU = 215 $R_\odot$). The estimated electron density model using these equations are very well agreement with the model of Bougeret et al. [1984] and Issautier et al. [1997].

6.5 Crab nebula occultation

Crab nebula (radio source IAU No. 05N2A or 3c144 or Taurus-A) is a supernovae remnant and a strong radio source at lower frequencies. It has a constant flux density over a long time. Crab nebula is occulted by the solar corona in mid of the June, every year. First

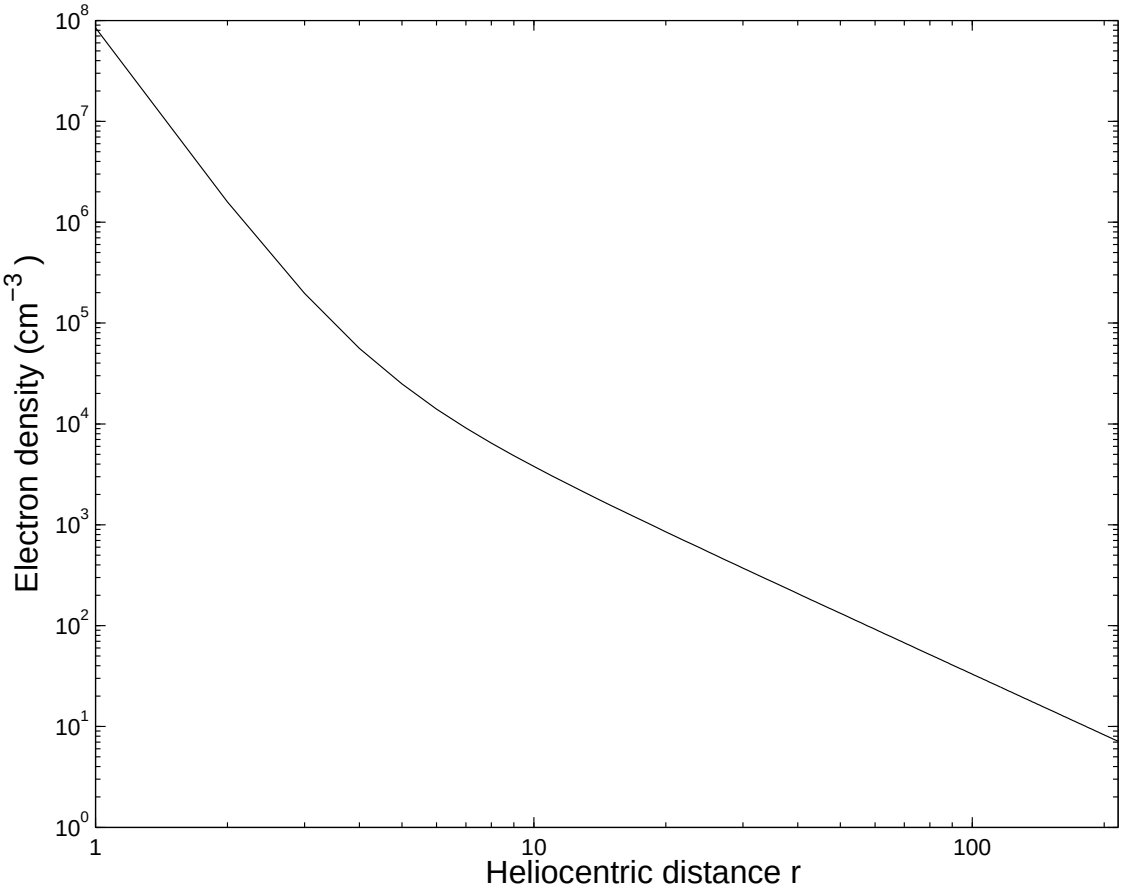

Fig. 6.2: The Figure shows the Leblanc density model which gives the electron density from $1.8 - 215\ R_\odot$ range.

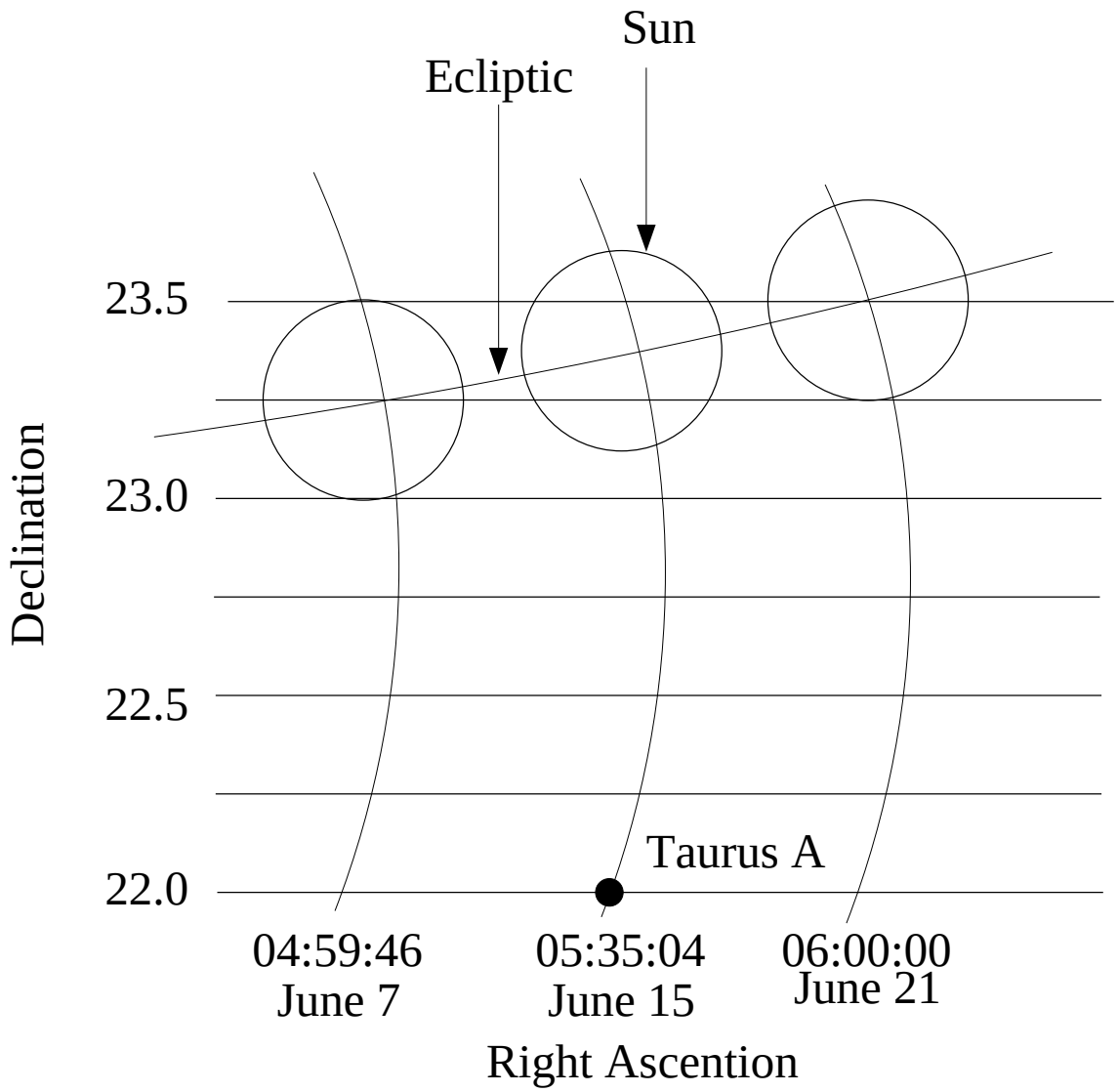

Fig. 6.3: Figure shows the geometry of the Crab nebula occultation by the solar corona/solar wind occurs in mid June of the every year. On 15 and 16 June 2011, Crab nebula has the elongation of $\approx 5\ R_{\odot}$ which is the closest to the solar disk.

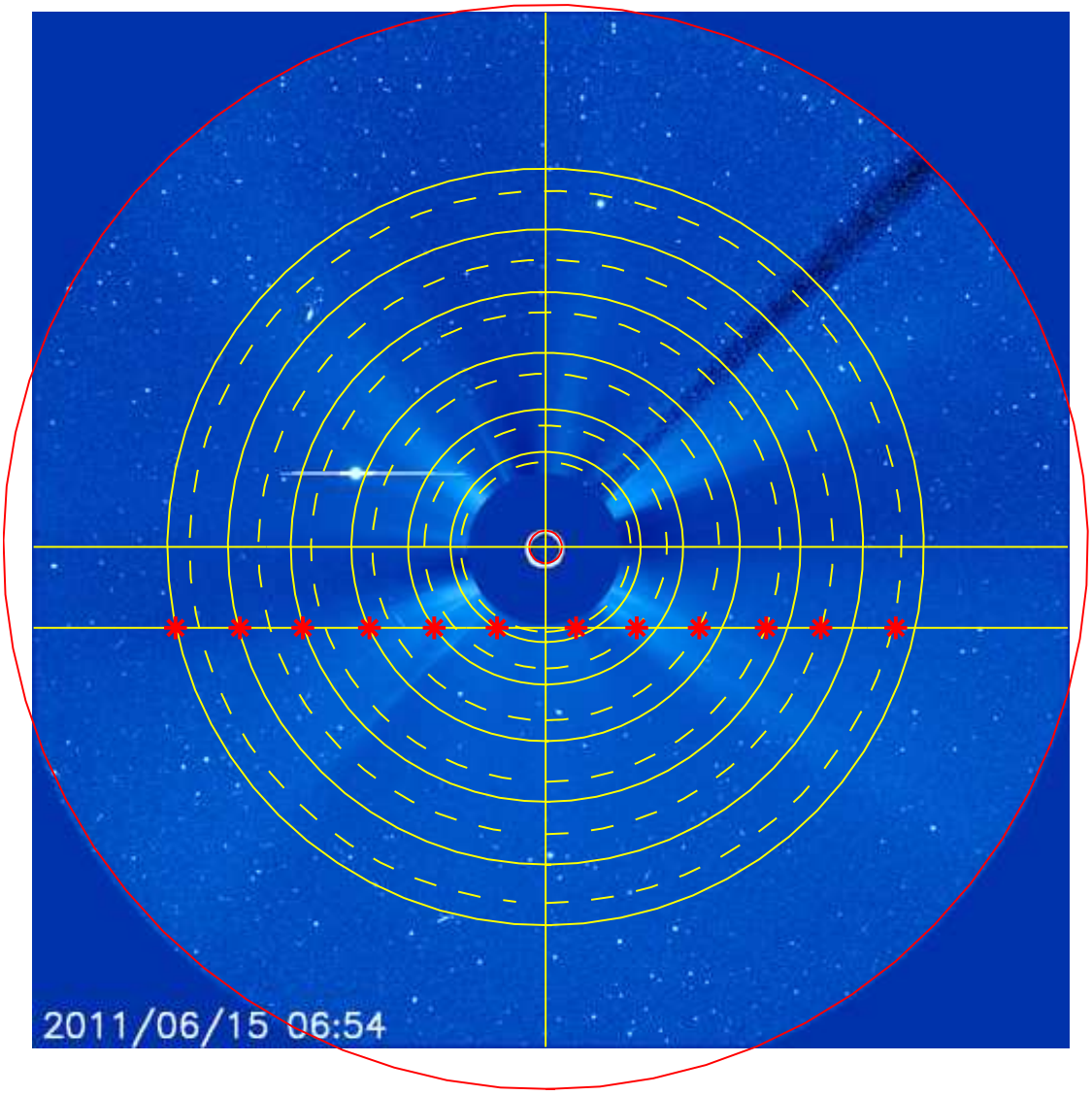

Fig. 6.4: The position of the Crab nebula in different days of June 2011 which was over plotted on the LASCO C3 image observed on 15 June 2011 at 06:54 UT is shown in the Figure. The 'red stars' in the Figure shows the location of the Crab nebula in different days of June. The left and right most 'red stars' were the locations of Crab nebula on 10 and 21 June 2011 respectively.

time this was observed by Machin and Smith [1951]. Many others studied the Crab nebula occultation phenomenon for several years [Hewish, 1955, Bolton et al., 1958, Slee, 1959, Högbom, 1960, Erickson, 1964, Sastry and Subramanian, 1974, Ramesh et al., 2001b]. Right ascension (RA) of the Crab nebula is 05 : 35 : 04 and Declination (Dec) is 22^o. Since the RA and Dec of the Crab nebula is close to ecliptic and therefore the solar corona occults the Crab nebula at 5 $R_\odot$ distance. The angle between the Sun and Crab nebula (solar elongation) decreases and reaches to 5 $R_\odot$ and then increases. The Figure 6.3 shows the geometry of the Crab nebula occultation in different days of June/at various distances in corona. The Figure 6.4 shows the location of the Crab nebula in different days of the June with respect to the solar disk. Note that the red stars superposed on the LASCO C3 image was the location of Crab nebula in different days of June. The expression given by Baars et al. [1977] for Crab nebula to estimate the flux density was not accurate at meter wavelengths. However Braude et al. [1970] has given the equation, which is efficient in finding the actual flux of it. The actual flux of the Crab nebula using the equation 6.10 found is 2015 Jy at 80 MHz.

$$log\ S_{TauA} = -0.182 - 0.27\ log\ f,\ \ f > 30 \text{ MHz} \tag{6.10}$$

$$log\ S_{TauA} = -0.650 - 0.83\ log\ f,\ \ f < 30 \text{ MHz} \tag{6.11}$$

In Gauribidanur Radio Observatory (GRO), Gauribidanur, India, observations of the Crab nebula occultation was carried out at 80 MHz. The Crab nebula occultation was observed in the years 2011, 2012 and 2013. Crab nebula was not seen during 2012 due to the 'disturbed' Sun. The fortuitous lull of Sun enabled us to observe the occultation in the year 2011 and 2013. Scattering effects of the solar corona by using the observations of the Crab nebula occultation in 2011 and 2013 were studied. From the obtained correlation counts with the array described in the following sections, the source sizes were estimated in the turbulent plasma. The turbulent plasma broadens the distant cosmic sources which

is useful in understanding the inner heliosphere. Angular broadening of the radio sources causes the decrease/vanish of the fringes obtained with the suitable interferometric arrays.

6.6 Instrumentation

The observations reported were carried out in the meridian transit mode at 80 MHz during June 2011 and 2013 at the GRO [Ramesh, 2011]. The schematic diagram of the array used to observe Crab nebula occultation is shown in the Figure 6.5. Note that the array consists of three groups (A, B and C) of antennas. Each group consists of eight log periodic dipole antennas (LPDs) and within a group each antenna was separated by a 10 m distance [Ramesh et al., 1998]. In group A, antennas were mounted in 0^o (i.e. arms of the LPDs were mounted along North-South direction) whereas antenna arms in group B and C are mounted in 90^o (arms of the LPDs were mounted along East-West direction). Such array gives a half-power beam width of $\approx 3^\circ \times 90^\circ$ (R.A. $\times$ Dec.) for the response pattern of each group. The effective collecting area (A_e) of each LPD is $\approx 0.6 \times \lambda^2$, where λ is the wavelength of observation. The minimum detectable sensitivity is $\approx$ 200 Jy. The signal transmission network, analog receiver chain and the digital back end receiver used were all similar to that described in Ramesh et al. [2006b, 2008]. The outputs of group A, B and C are brought to the lab and down-converted to 10.7 MHz called intermediate frequency (IF) using the analog receiver. Since IF bandwidth is 1 MHz, the signal was sampled at 2 MHz rate and correlated using the digital correlator, which is similar to the one used in GRIP/GRAPH [Ramesh et al., 1998]. Integration time of the observations were 1s. Note that the correlation between group B and C corresponds to the total intensity/Stokes I observation and the correlation between group A and C gives information on circularly polarized intensity/Stokes V. From the Figure 6.5 it is clear that polarimetric observations (Stokes I and V) are carried out over long baseline length, which is $\approx$ 1600 m. Therefore interference fringe separation is $\approx 8^{'}$ for both Stokes I and V observations at 80 MHz.

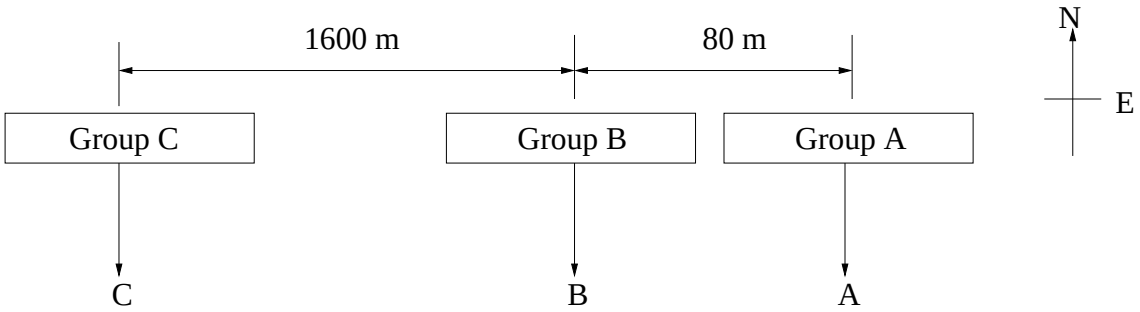

Fig. 6.5: Schematic diagram of antenna array used for Crab nebula occultation is shown in the figure. There are three groups: In group A the arms of the antennas are aligned in 0^o orientation (i.e. North-South direction) and in group B and group C the arms of the antenna are oriented in 90^o (i.e. in East-West direction)

The above angular resolution indicates that contribution from the 'background' corona during observations of the Crab nebula when the latter is close to the Sun will be very minimal since the average half-power diameter of the 'radio Sun' at 80 MHz is large, $\approx 40'$ [Sheridan and McLean, 1985, Thejappa and Kundu, 1992, Ramesh et al., 2006a]. Hence the 'background' corona gets resolved out.

6.7 Observations

Using the described array, polarimetric observations (Stokes I and V) of the Crab nebula were carried out in June, 2011, 2012 and 2013. Note that the observations were carried out at 80 MHz without disturbing the observational system during the occultation. However because of the solar activity Crab nebula was not seen in the observations of year 2012 as mentioned. Note that Crab nebula can be considered as a point source for the present observations since its angular size ($\lesssim 4'$) is smaller than the interferometer fringe separation [Kraus, 1966]. The interferometer record of 2 June 2013 in Figure 6.6 is typical of the pattern obtained with our setup on days when Crab nebula is well separated from the Sun. The absence of fringes on 14 June 2013 is due to the large angular broadening (as a result of pronounced scattering) suffered by the radio radiation from the Crab nebula as it comes close to the Sun. The Figure 6.7 shows the total amplitude of the Crab

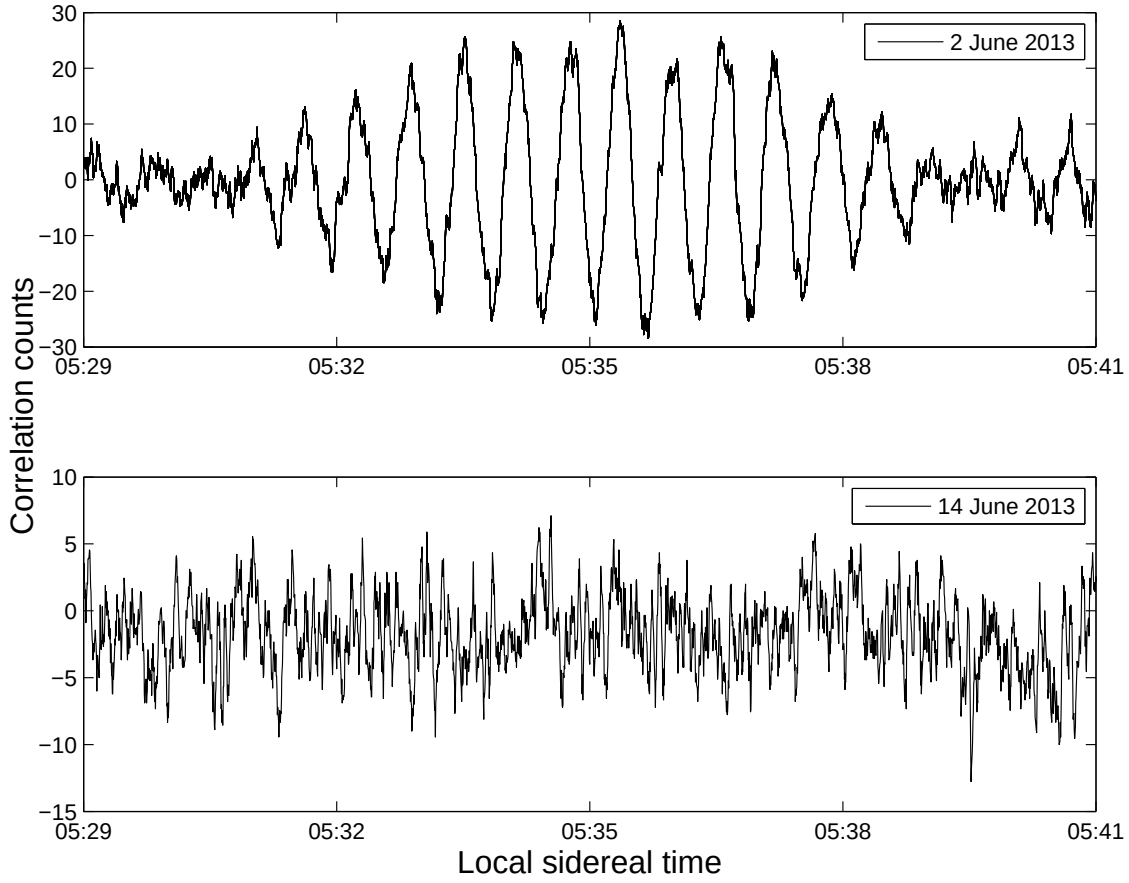

Fig. 6.6: Radio interferometer observations of the Crab nebula at 80 MHz during its transit over the local meridian in Gauribidanur on 2 June 2013 and 14 June 2013 is shown in the Figure. The interferometer baseline length was $\approx$ 1600 meters and oriented in the East-West direction.

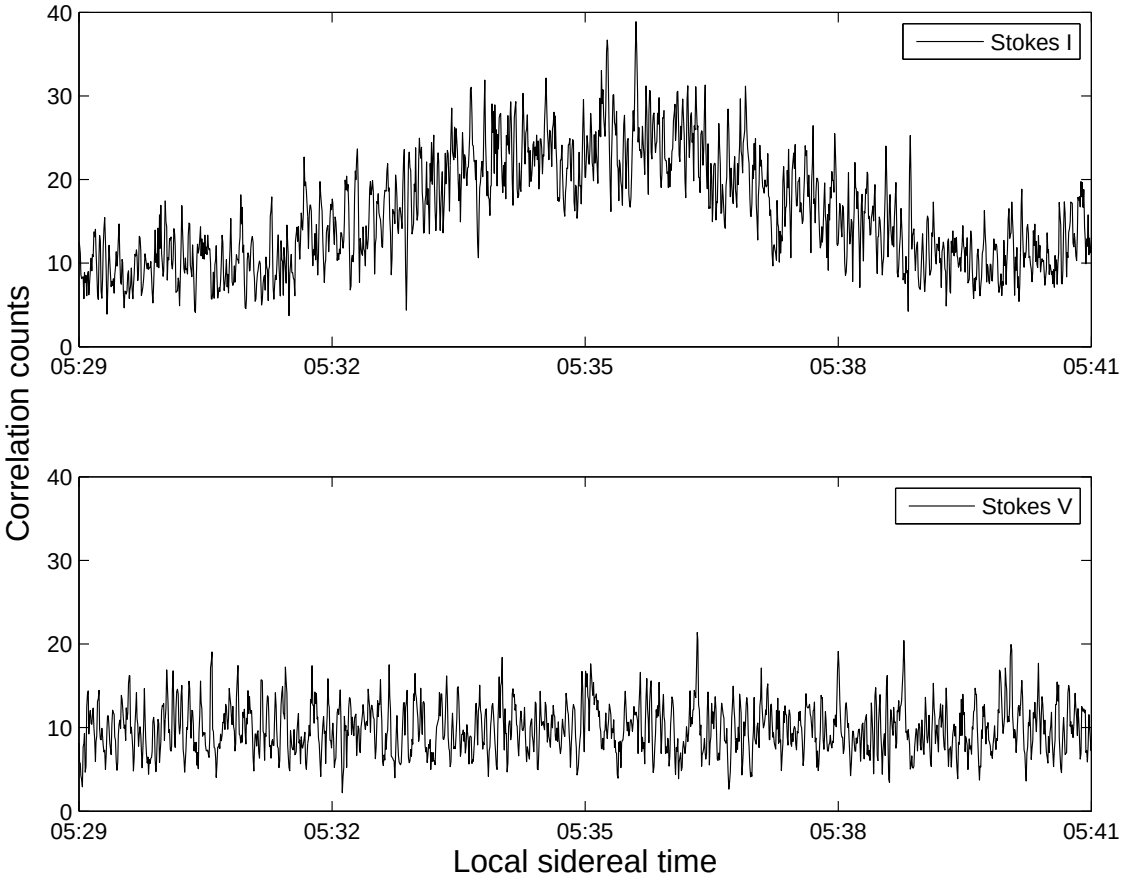

Fig. 6.7: Radio interferometer observations of the Crab nebula at 80 MHz during its transit over the local meridian in Gauribidanur on 10 June 2013 is shown in the Figure. The top and bottom panels correspond to the observations of Stokes I and V respectively. Note that the interferometer baseline length was $\approx$ 1600 meters.

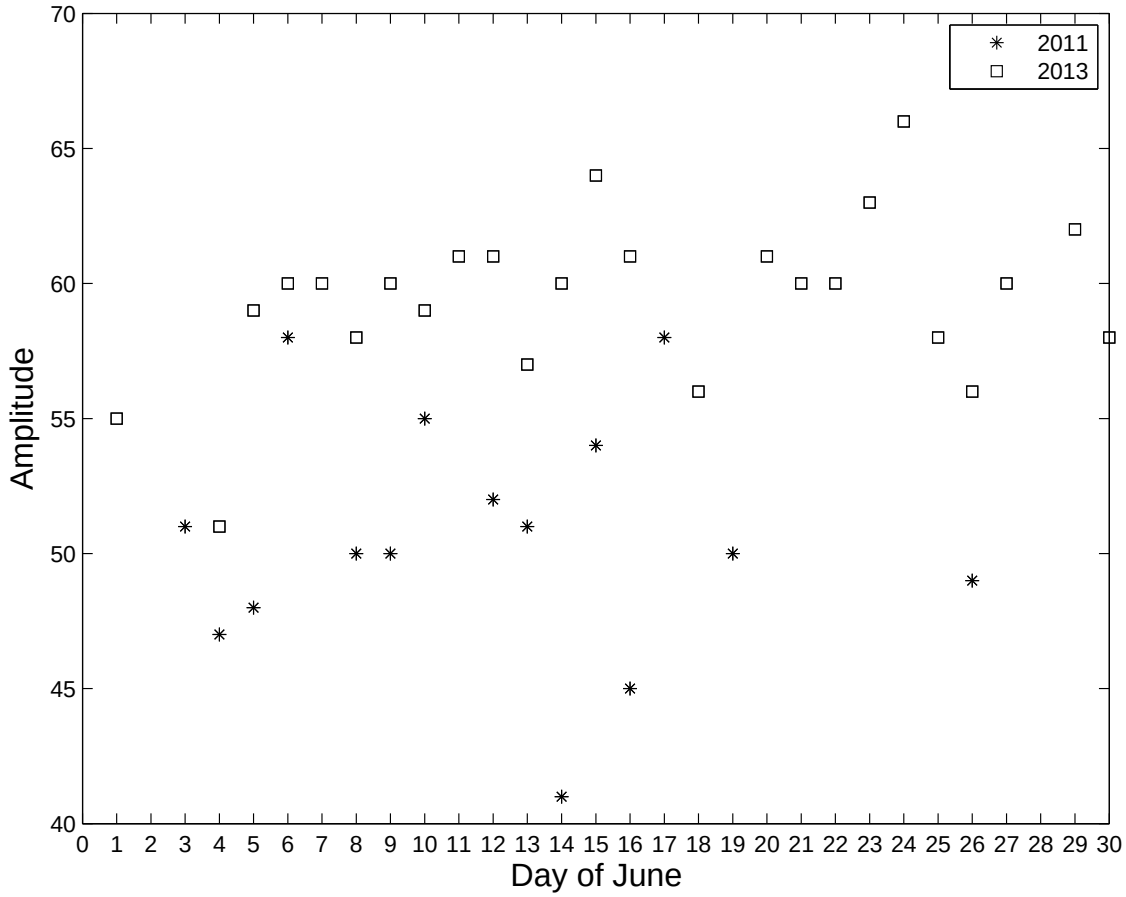

Fig. 6.8: Variation of peak-peak amplitude of the interference fringes of a calibrator source (Virgo A) during different days of June in 2011 and 2013 is shown in the Figure. This plot shows the instrumental stability and consistence of the correlation counts in both years during the period of occultation observations. Note that the '*' and 'squares' indicated the observation of Virgo A on 2011 and 2013 respectively.

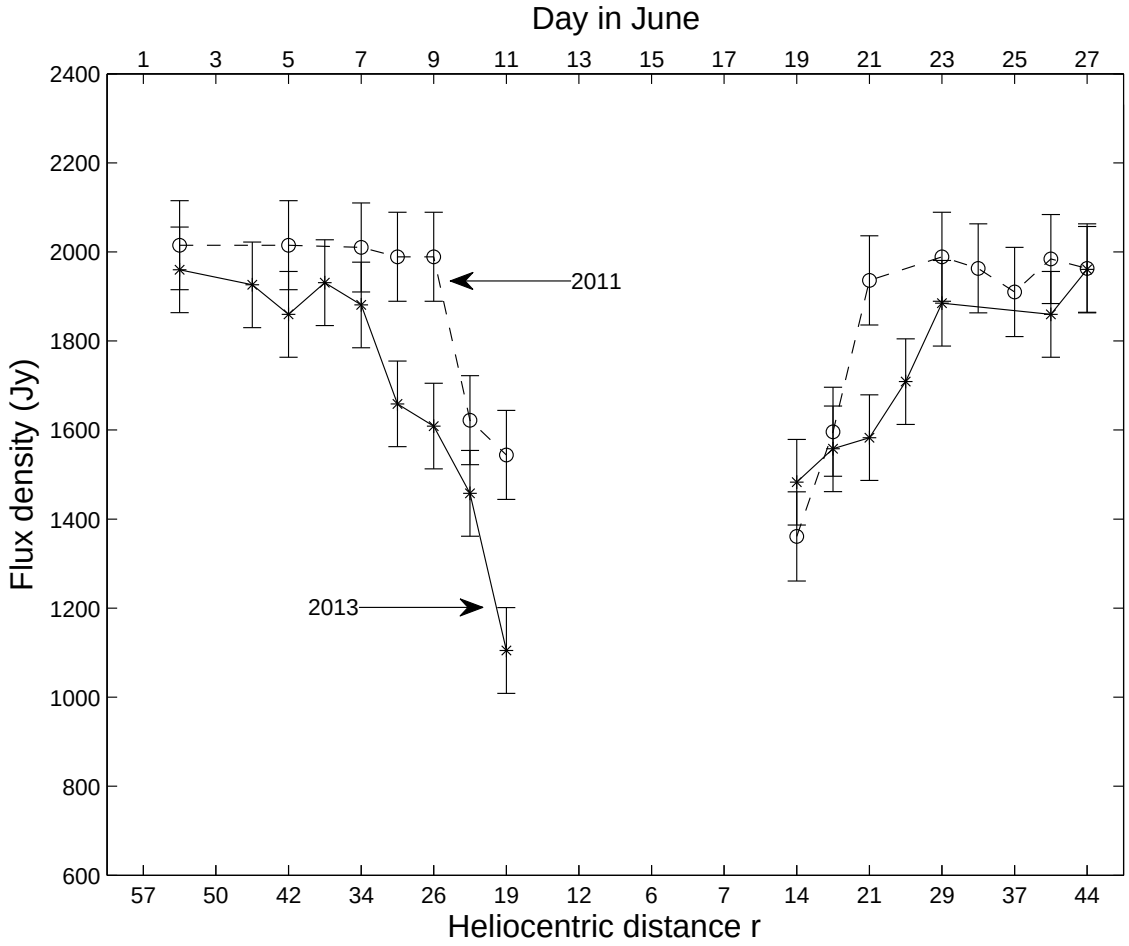

Fig. 6.9: Observed flux densities of the Crab nebula on different days during its occultation by the solar corona. The period before and after June 15th corresponds to the ingress and egress, respectively. The plots marked 'o' and '*' correspond to measurements during June 2011 and June 2013, respectively.

nebula observations carried out on 10 June 2013 in both Stokes I and V modes. The total amplitude of Stokes I and V channels are estimated using the method described in section 2.11. Note that the top and bottom panels corresponds the total intensity/Stokes I and circularly polarized intensity/Stokes V time profiles respectively. None of the day, deflection in Stokes V channel was noticed during the two years of observations. Probable reason could be the intensity of circular polarization may be too weak to detect.

The data obtained were corrected for gain and phase errors using observations on Virgo A (M87, 3c274; R.A. $\approx 12^h31^m$, Dec. $\approx 12^o$), another point source. The observed correlation counts of the Virgo A is shown in the Figure 6.8 which shows the instrumental stability and consistency of the observational setup during the occultation. Figure 6.9 shows the flux density of Crab nebula on different days during June 2011 and 2013. The corresponding separation from the Sun, and the flux density values are listed in columns 2, 3a and 3b in Table 6.1, respectively. It is obvious that the radio radiation from Crab nebula undergoes increased scattering as it approaches the Sun. While there is a steady decrease in the flux (from the pre-occultation value of $\approx 2015 \pm 100$ Jy) from 10th June ($r \approx 23\ R_\odot$) during the ingress in 2011, the decrease is noticeable from 8th June onwards ($r \approx 30\ R_\odot$) in 2013. A similar situation can be noticed during the egress also. While the pre-occultation value is reached around 21st June ($r \approx 21\ R_\odot$) in 2011, it is only around 23rd June ($r \approx 29\ R_\odot$) in 2013. No fringes were observed during $12 - 18$ June in both 2011 and 2013. In terms of distance of the Crab nebula from the Sun, it is $r \approx 15\ R_\odot$ on 12th June (ingress) and $r \approx 10\ R_\odot$ on 18th June (egress). This is consistent with the theoretical predictions of Bastian [2004] for the interferometer baselines and the heliocentric distances over which a background radio source will be resolved at 80 MHz due to angular broadening by the solar wind turbulence. The Sun was 'undisturbed' and no strong radio bursts were reported during our observing period[1]. Also there are no other strong radio sources at other declinations in the same R.A. range as the Crab

[1] www.swpc.noaa.gov

nebula, which otherwise might contribute through the wide response pattern ($\approx 90^o$) of our antenna system in declination.

6.8 Scattering measurements of the solar corona

A two-element correlation radio interferometer of baseline length 's' measures the time averaged spatial covariance of the electric field corresponding to the electromagnetic wave incident on the two antennas. It is defined as the visibility $V(s)$. For a spatially coherent source of radio waves (point source), the normalized visibility is referred to as the mutual coherence function, i.e. $\Gamma(s) = V(s)/V(o)$. In the present case, $V(o)$ was taken to be the observed flux density of the Crab nebula when it was far ($r \gtrsim 40\ R_\odot$) from the Sun, i.e. the pre-occultation value. An inspection of Figure 6.9 indicates that the flux density of Crab nebula remained nearly constant close to the above heliocentric distance range in both June 2011 and June 2013 implying that angular broadening due to scattering by electron density inhomogeneities there was negligible. In the presence of an intervening scattering medium, we have $\Gamma(s) = e^{-D(s)/2}$, where $D(s)$ is the structure function of the phase perturbations caused by the density inhomogeneities in the medium, i.e. the solar wind in the present case [Prokhorov et al., 1975, Ishimaru, 1978, Coles and Harmon, 1989a, Armstrong et al., 1990]. From the above set of expressions we can write,

$$D(s) = -2log\Gamma(s) = -2log\,[V(s)/V(o)] \tag{6.12}$$

Our interest is to estimate the values of $C_N^2(r)$ at different heliocentric distances. Note that scattering depends quantitatively on whether the wavefront is planar (1-D) or spherical (3-D). While the latter formalism (3-D) is adopted for a source embedded in the scattering medium, the former (1-D) applies to the case of a plane wave from a distant source trans-illuminating the scattering medium. The present set of observations belong

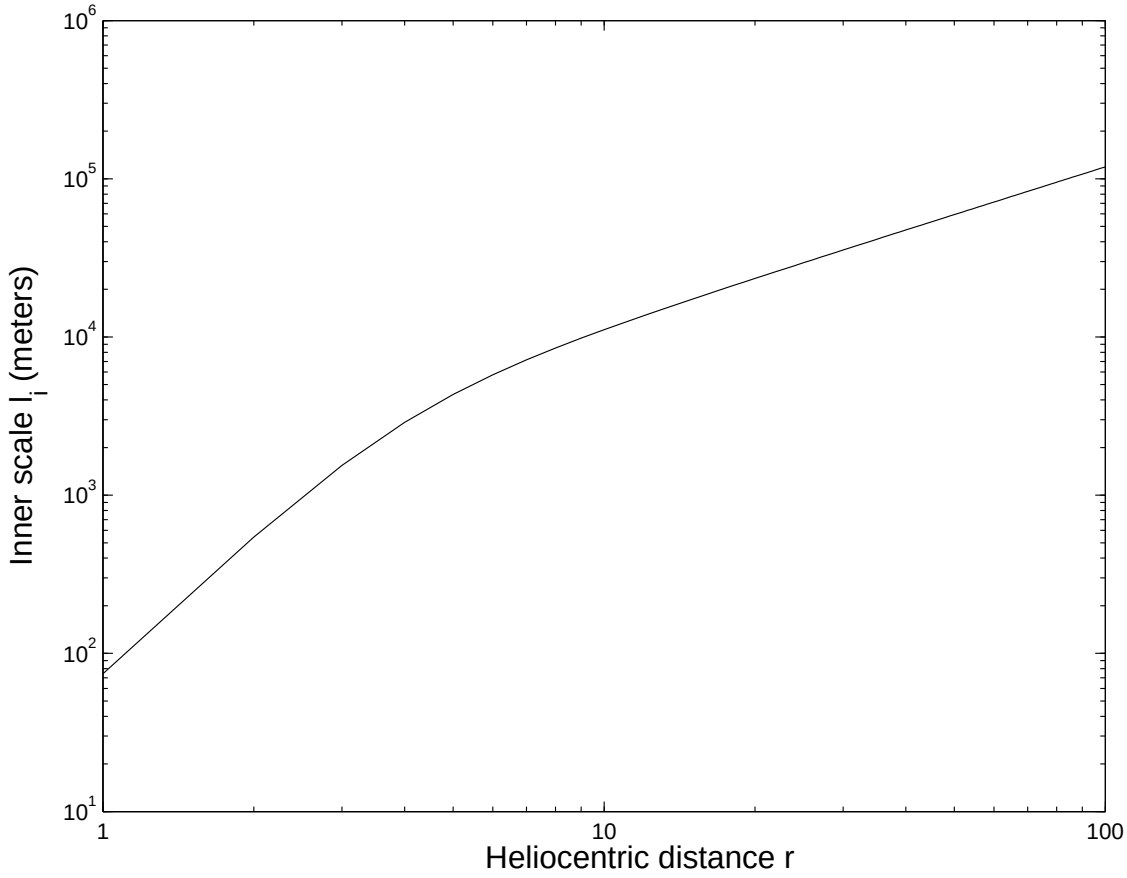

Fig. 6.10: The Figure shows the variation of inner scale length in the solar atmosphere. These values are calculated using the equation 6.14.

to the second category. Following Coles et al. [1987], Bastian [1994], Subramanian and Cairns [2011], we write:

$$\frac{\partial}{\partial R}D(s,r) = \frac{4\pi^2}{2^\alpha}\Gamma(1-\alpha/2)C_N^2(r)r_e^2\lambda^2 l_i(r)^{\alpha-2}s^2 \tag{6.13}$$

$$l_i = \frac{684}{\sqrt{N_e(R)\ cm^{-3}}}\ \text{km} \tag{6.14}$$

where l_i is the inner spatial scale of the electron density inhomogeneities in meters [Coles et al., 1987, Thejappa and MacDowall, 2008], $n(r)$ is the background electron density in the solar atmosphere in units of cm^{-3}, $r_e \approx 2.8\times10^{-15}$ m is the classical electron

radius, λ is the wavelength of observation (= 3.75 m in the present case), $\Gamma(1-\alpha/2)$ is the Gamma function of argument $1-\alpha/2$, and $\alpha = \beta - 2$ $(0 < \alpha < 2)$. Assuming the model of Leblanc et al. [1998a] for $n(r)$, the inner scales length $(l_i(r))$ was found and the values are $\approx 10-100$ km in the range $r \approx 10-100\ R_\odot$ from the Sun. The Leblanc density model was assumed because it is valid in the range $r \approx 2-215\ R_\odot$ from the Sun and the present observations correspond to the range $r \approx 10-60\ R_\odot$ (see Figure 6.9). Note that equation 6.13 is applicable only in the limit $s << l_i(r)$ as in the present case. Integrating equation 6.13 over the thickness of the scattering medium as mentioned in Sakurai et al. [1992],

$$D(s,r) = \frac{4\pi^2}{2^\alpha}\Gamma(1-\alpha/2)r_e^2\lambda^2 l_i(r)^{\alpha-2}s^2 \int C_N^2(r')dr' \tag{6.15}$$

Since the electron density decreases radially outward in the solar corona, the principal contribution to $\int C_N^2(r')dr'$ in equation 6.15 comes from the region around $r = R_o$, the heliocentric distance of the point of closest approach of the line of sight to the Crab nebula (the impact parameter), on any given day [Spangler and Sakurai, 1995]. There were no transient changes in the angular broadening, related to the possible presence of either a corotating interaction region [Ananthakrishnan et al., 1980] or an interplanetary shock wave [Woo and Schwenn, 1991] or a coronal mass ejection [Woo, 1997, Ramesh et al., 2001a], during our observing period. Also the Sun was 'undisturbed'. So we made the simplifying assumption that the turbulence is spherically symmetric. Following Spangler and Sakurai [1995] and substituting $\int C_N^2(r')dr' = \frac{\pi}{2}C_N^2(r)R_o$ in equation 6.15 gives,

$$C_N^2(r) = \frac{D(s,r)2^\alpha}{2\pi^3 R_o r_e^2 \lambda^2 l_i(r)^{\alpha-2}s^2\Gamma(1-\alpha/2)} \tag{6.16}$$

An inspection of Figure 6.9 indicates that the reduction in the flux density of Crab nebula occurs primarily when the latter is within $r \approx 25\ R_\odot$ from the Sun. Assuming

$\beta \approx 3$ based on earlier interferometer observations on baseline lengths nearly the same as that used in the present work [Coles and Harmon, 1989a, Anantharamaiah et al., 1994, Bastian, 1994, Anantharamaiah et al., 1995, Subramanian, 2000] and substituting r_e, $l_i(r)$ and λ in meters, we get

$$C_N^2(r) = 1.65 \times 10^{26} D(s,r) R_o^{-1} l_i(r) s^{-2} \quad \mathrm{m}^{-6} \tag{6.17}$$

Estimated $C_N^2(r)$ for different days in the month of June 2011 and June 2013 from the values of $D(s,r)$ obtained using equation 6.12, and the corresponding values of $l_i(r)$ and R_0. The same, after converting to units of $\mathrm{m}^{-20/3}$, are listed in Columns 4a (June 2011) and 4c (June 2013) in Table 6.1. The $C_N^2(r)$ assuming $\beta = 11/3$ (i.e. Kolmogorov spectrum) was also estimated. The corresponding equation in this case is,

$$C_N^2(r) = 8.34 \times 10^{25} D(s,r) R_o^{-1} l_i(r)^{1/3} s^{-2} \quad \mathrm{m}^{-20/3} \tag{6.18}$$

The estimated values, which are straightaway in units of $\mathrm{m}^{-20/3}$, are listed in Columns 4b (June 2011) and 4d (June 2013) in Table 6.1.

Figure 6.11 shows the variation $C_N^2(r)$ on different days in the month of June 2011 and June 2013. The values in June 2013 are higher than those in June 2011 by about an order of magnitude. Combining this with the larger reduction in the flux density of the Crab nebula in June 2013 compared to June 2011 for the same heliocentric distance in the range $r \lesssim 25\ R_\odot$ (Figure 6.9), and the enhanced 10.7 cm flux in June 2013 compared to June 2011, it was noted that the scattering is probably more pronounced during periods of increased solar activity. This is consistent with the results reported earlier based on similar observations by Slee [1966], Ward [1975] that scattering varies with the phase of solar cycle. In Figure 6.11 it was also shown $C_N^2(r)$ values obtained using the model of Spangler et al. [1996] over the same distance range obtained using the equation 6.19.

$$C_N^2(R) = 1.8 \times 10^{10} (R/10R_\odot)^{-3.66} \tag{6.19}$$

Note that due to the solar wind variability the power law index varies with R from -3.66 to -4. However, it is noticeable that the estimates are higher by $\approx 5-6$ orders of magnitude. On the other hand, if one assumes $\beta = 11/3$, the estimates are higher by $\approx 1-2$ orders of magnitude only (see Figure 6.12).

The mean square angular deviation ($\langle\theta^2\rangle$) of a ray propagating in a turbulent medium like the solar atmosphere in the limit $s << l_i(r)$ is [Bastian, 1995],

$$\langle\theta^2\rangle = \Gamma(1-\alpha/2)\frac{(2\pi)^{2-\alpha}\ r_e^2\lambda^4 C_N^2(r)\Delta z}{8\mu^4 l_i(r)^{2-\alpha}} \tag{6.20}$$

Refractive index (μ) of the medium is estimated using equation 6.21 for different plasma frequencies.

$$\mu = \sqrt{1-\frac{f_p^2}{f^2}} \tag{6.21}$$

where f is the frequency of observation in (MHz). Plasma frequency of the coronal layer close to the location of observation of Crab nebula is estimated using the equation 6.22

$$f_p = 8.97 \times 10^3 \times \sqrt{N_e(R)}\ \text{MHz} \tag{6.22}$$

and Δz is the thickness of the scattering medium. An inspection of Figure 6.9 indicates that a decrease in the flux density of the Crab nebula (due to scattering by density inhomogeneities) is noticeable only when it is within the heliocentric distance $r \approx 25\ R_\odot$. So we assumed $\Delta z \approx 50\ R_\odot$ in the present case. $\mu \approx 1$ since the plasma frequency (f_p) is much smaller (< 1 MHz) compared to the frequency of observation (f

= 80 MHz) in the range $r \approx 10 - 60\ R_{\odot}$ discussed in the present case [Leblanc et al., 1998a]. Substituting for the different parameters in equation 6.20 for the $\beta = 3$ case, θ on different days during June 2011 and June 2013 was calculated. The results are listed in Columns 5a and 5c in Table 6.1. The values are consistent with that reported earlier by Slee [1966], Harries et al. [1970] for similar observations at 80 MHz. The results for $\beta = 11/3$ case are listed in Columns 5b (June 2011) and 5d (June 2013) in Table 6.1. Note that in order to get a dimensionless values for $\langle\theta^2\rangle$ in equation 6.20, the values of $C_N^2(r)$ were substituted in units of m^{-6} and $m^{-20/3}$ for the $\beta = 3$ and $\beta = 11/3$ cases, respectively.

Figures 6.13 show the variation of $\langle\theta\rangle$ on different days in the month of June 2011 and June 2013, for the $\beta = 3$ case. The results for the $\beta = 11/3$ case is shown in Figure 6.14. The angular deviation seems to be slightly larger in June 2013 compared to June 2011 This is likely due to the higher values of $C_N^2(r)$ in June 2013 as compared to June 2011 in both the $\beta = 3$ and $\beta = 11/3$ cases. In Figures 6.13 and 6.14 we have also shown the $\langle\theta\rangle$ values obtained using the empirical relationship for angular broadening $50 \times (\lambda/r)^2$ derived by Erickson [1964] based on similar occultation observations of the Crab nebula by the solar corona. On an average, the latter seems to be slightly higher compared to our estimates for both the $\beta = 3$ and $\beta = 11/3$ cases. It is possible this discrepancy could be due to the reason that the observational data used by Erickson [1964] was obtained during 1961-1962, close to the maximum of a comparatively stronger solar cycle 19. The larger values of $\langle\theta\rangle$ in 2013 compared to 2011 and the correlation with the enhanced 10.7 cm flux in 2013 is consistent with the above argument.

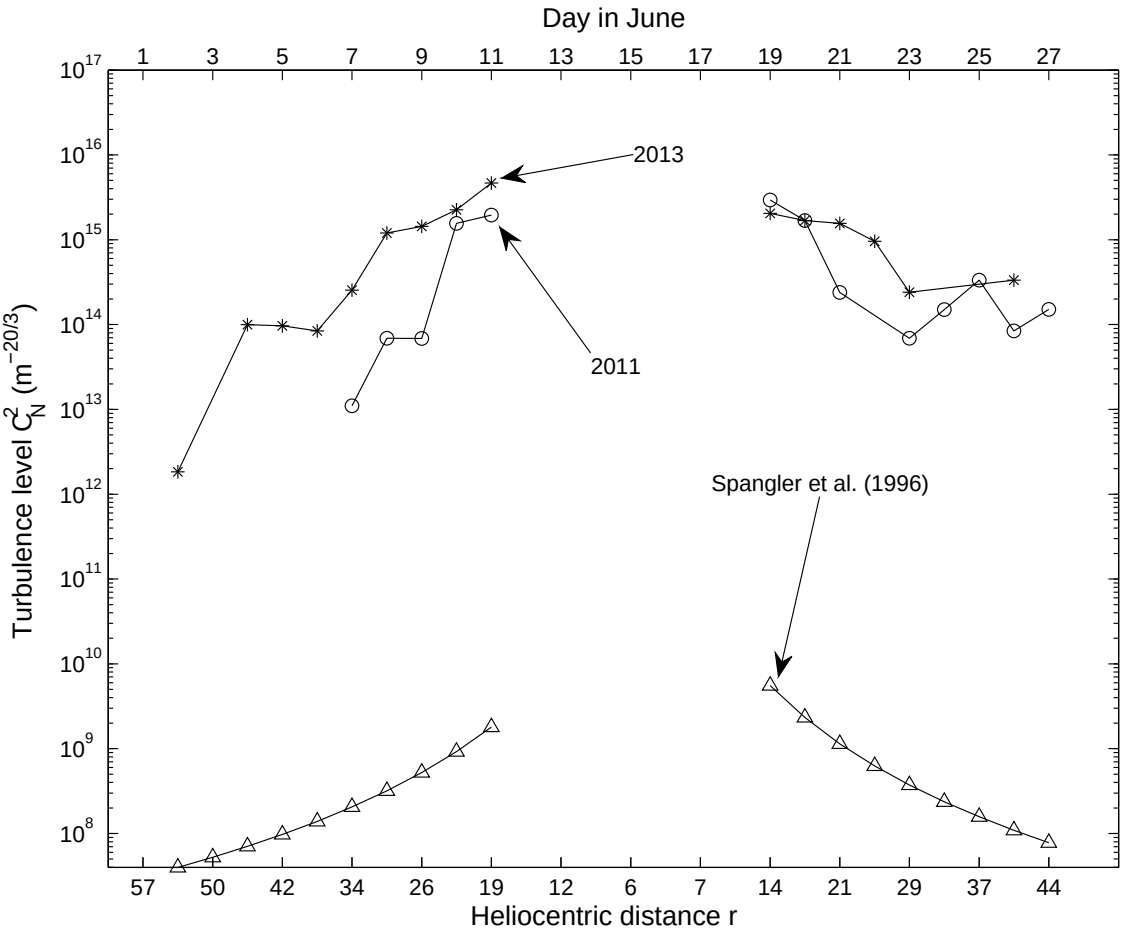

Fig. 6.11: Variation of the level of the turbulence in the near-Sun solar wind in the line of sight to the Crab nebula, with heliocentric distance ($\beta = 3$ case).

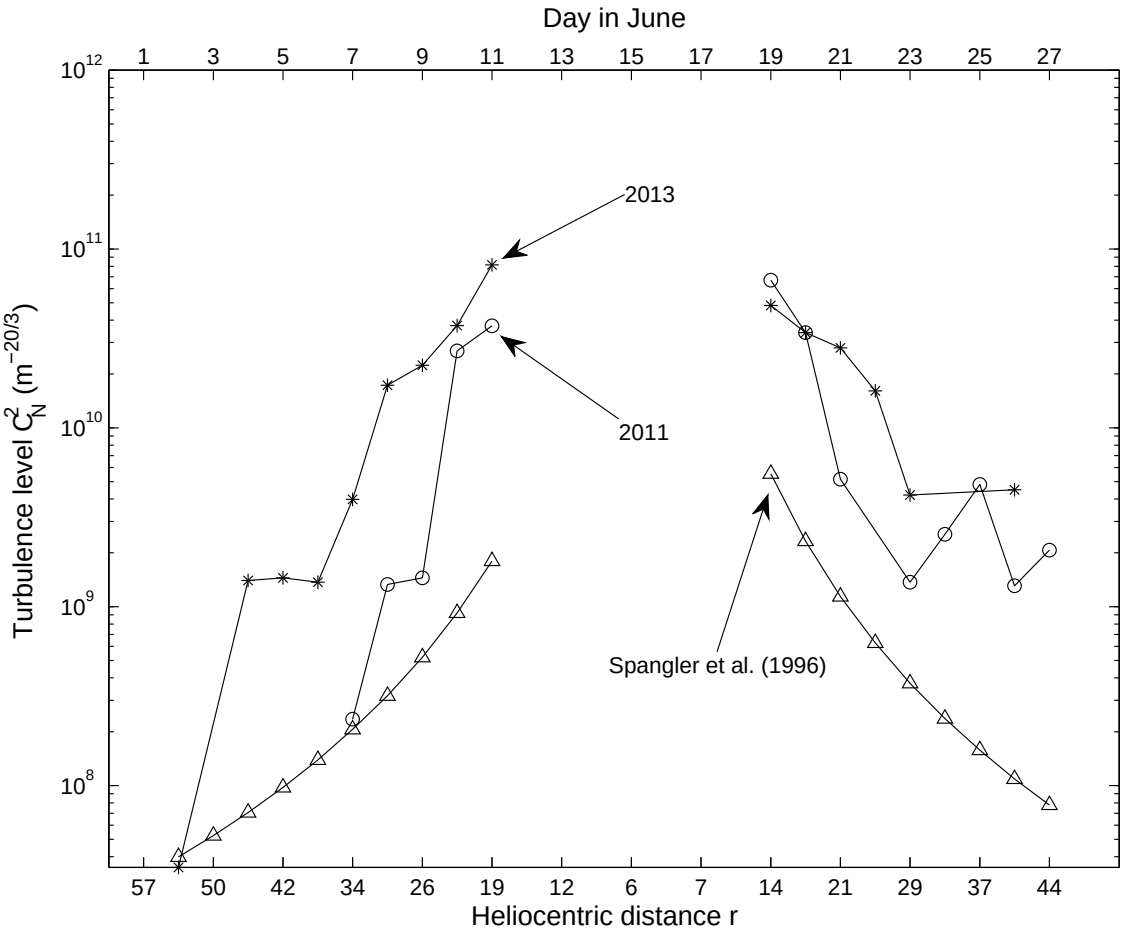

Fig. 6.12: Variation of the level of the turbulence in the near-Sun solar wind in the line of sight to the Crab nebula, with heliocentric distance ($\beta = 11/3$ case).

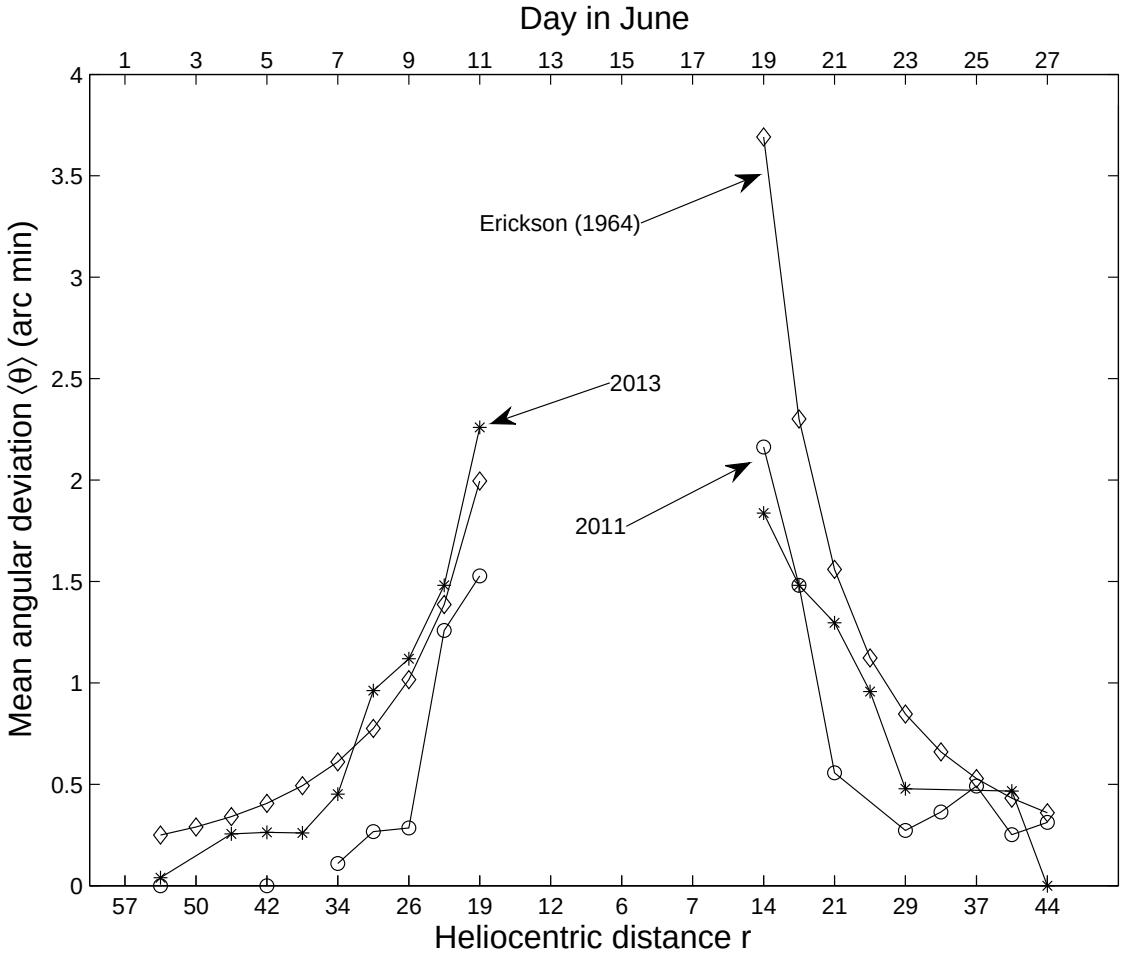

Fig. 6.13: Variation of the mean angular deviation $\langle\theta\rangle$ of the radio radiation from the Crab nebula with heliocentric distance ($\beta = 3$ case).

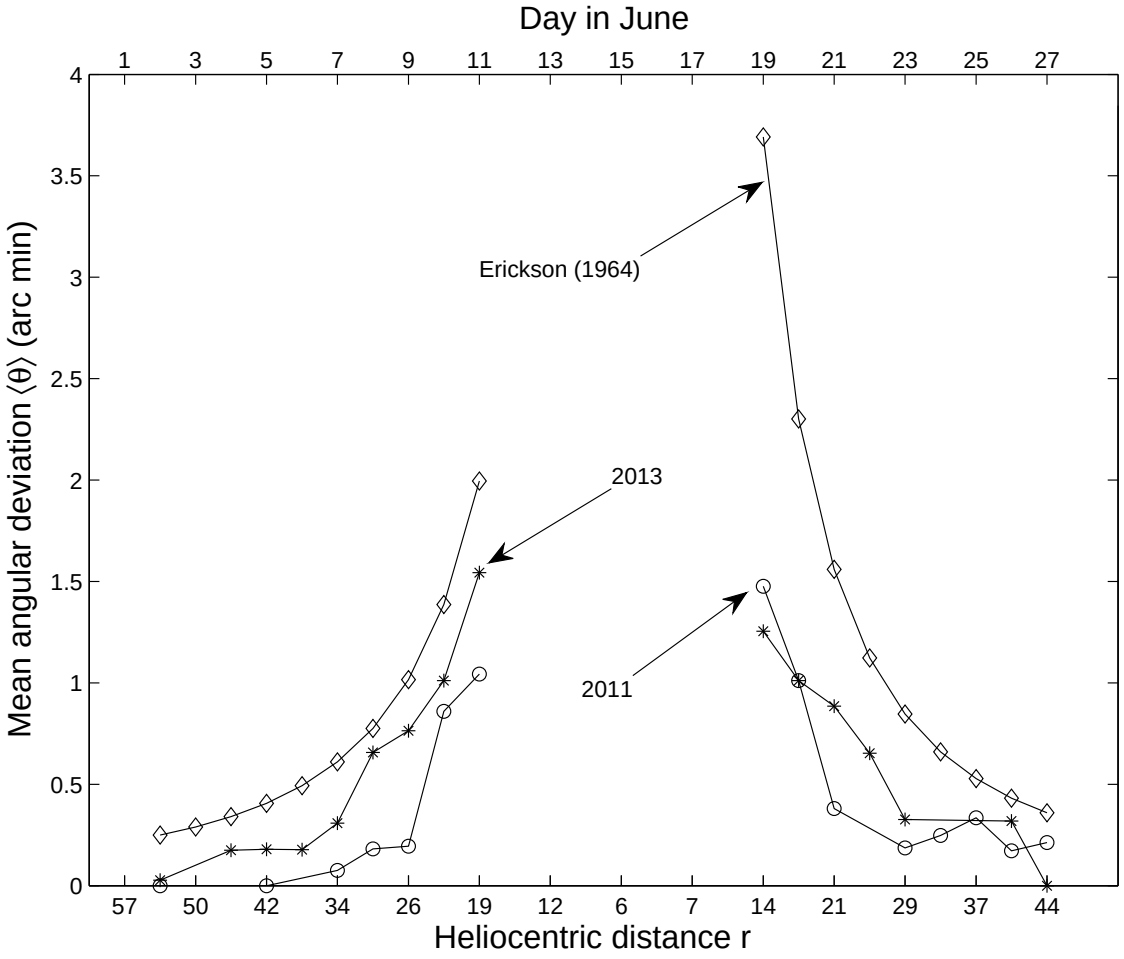

Fig. 6.14: Variation of the mean angular deviation $\langle\theta\rangle$ of the radio radiation from the Crab nebula with heliocentric distance ($\beta = 11/3$ case).

Table 6.1: Parameters estimated from the occultation observations of the Crab nebula

Day in June	r ($R_\odot$)	Flux density (Jy) 2011	Flux density (Jy) 2013	C_N^2 ($m^{-20/3}$) 2011 β=3	C_N^2 ($m^{-20/3}$) 2011 $\beta=\frac{11}{3}$	C_N^2 ($m^{-20/3}$) 2013 β=3	C_N^2 ($m^{-20/3}$) 2013 $\beta=\frac{11}{3}$	$\langle\theta\rangle$ (arc min) 2011 β=3	$\langle\theta\rangle$ (arc min) 2011 $\beta=\frac{11}{3}$	$\langle\theta\rangle$ (arc min) 2013 β=3	$\langle\theta\rangle$ (arc min) 2013 $\beta=\frac{11}{3}$
(1)	(2)	(3a)	(3b)	(4a)	(4b)	(4c)	(4d)	(5a)	(5b)	(5c)	(5d)
2	53	2015	2014	0	0	1.84e12	3.49e07	0	0	0.04	0.03
3	49	-	-	-	-	-	-	-	-	-	-
4	45	-	1979	-	-	9.96e13	1.40e09	-	-	0.26	0.17
5	42	2015	1980	0	0	9.65e13	1.45e09	0	0	0.26	0.18
6	38	-	1984	-	-	8.41e13	1.37e09	-	-	0.26	0.18
7	34	2010	1932	1.10e13	2.35e08	2.55e14	3.98e09	0.11	0.07	0.45	0.31
8	30	1989	1701	6.89e13	1.33e09	1.20e15	1.73e10	0.27	0.18	0.96	0.66
9	26	1989	1649	6.87e13	1.45e09	1.44e15	2.24e10	0.28	0.19	1.12	0.76
10	23	1622	1492	1.56e15	2.69e10	2.25e15	3.73e10	1.26	0.86	1.48	1.01
11	19	1544	1125	1.95e15	3.72e10	4.66e15	8.15e10	1.53	1.04	2.26	1.54
12	15	-	-	-	-	-	-	-	-	-	-
13	12	-	-	-	-	-	-	-	-	-	-
14	8	-	-	-	-	-	-	-	-	-	-
15	6	-	-	-	-	-	-	-	-	-	-
16	5	-	-	-	-	-	-	-	-	-	-
17	7	-	-	-	-	-	-	-	-	-	-
18	10	-	-	-	-	-	-	-	-	-	-
19	14	1361	1518	2.95e15	6.70e10	2.05e15	4.83e10	2.16	1.48	1.84	1.25
20	17	1596	1596	1.68e15	3.41e10	1.68e15	3.41e10	1.48	1.01	1.48	1.01
21	21	1936	1622	2.39e14	5.16e09	1.56e15	2.80e10	0.56	0.38	1.30	0.89
22	25	-	1753	-	-	9.58e14	1.61e10	-	-	0.97	0.65
23	29	1989	1936	6.88e13	1.37e09	2.40e14	4.21e09	0.27	0.19	0.48	0.33
24	33	1963	-	1.50e14	2.54e09	-	-	0.36	0.25	-	-
25	37	1910	-	3.33e14	4.82e09	-	-	0.49	0.34	-	-
26	40	1984	1910	8.42e13	1.31e09	3.33e14	4.51e09	0.25	0.17	0.47	0.32
27	44	1963	2015	1.51e14	2.07e09	0	0	0.31	0.21	0	0

6.9 Conclusions and summary

Based on two-element radio interferometer observations of the occultation of the Crab nebula by the solar corona during June 2011 and June 2013 at 80 MHz, the level of the coronal turbulence $C_N^2(r)$ in the heliocentric distance range $r \approx 10-60\ R_\odot$ was estimated. The spatial scale of the density inhomogeneities probed were ≈ 1.6 km, corresponding to the length of the interferometer baseline. Estimates of $C_N^2(r)$ for the $\beta = 3$ case are higher by $\approx 5-6$ orders of magnitude compared to the similar values reported previously for larger spatial scales ($\approx 200-2000$ km) from VLBI observations over the same heliocentric distance range [Spangler and Sakurai, 1995]. For $\beta = 11/3$, our estimates are higher by $\approx 1-2$ orders of magnitude. This indicates that $C_N^2(r)$ varies with the spatial scale of the density inhomogeneities irrespective of the power law index of their spatial spectrum. This could likely be the situation since: 1) according to Little [1971], the small scale density inhomogeneities form a distribution distinct from that of the larger scale inhomogeneities, 2) Armstrong et al. [1990] had noted that the mean axial ratio of angular broadened images on short baselines (< 3 km) is different from that on the long baselines ($\approx 3-30$ km); 3) based on simultaneous observations of density inhomogeneities on smaller spatial scales ($\approx 1-30$ km) with the VLA and larger spatial scales ($\approx 200-2000$ km) with the VLBI, Grall et al. [1997] concluded that the latter could not have come from the structure that has the same anisotropy as was observed with the VLA. Therefore it seems likely that the model of Spangler et al. [1996] might be applicable only in situations where the spatial scales are $\sim 200-2000$ km. We also find that the $C_N^2(r)$ varies with the phase of the solar cycle. In the present estimates for June 2013 are higher compared to those for June 2011. This correlates with the enhanced solar activity in June 2013 compared to June 2011, as revealed by the 10.7 cm solar radio flux. Also estimates of the angular deviation $\langle\theta\rangle$ during the corresponding epochs show a similar trend.

References

S. Ananthakrishnan, W. A. Coles, and J. J. Kaufmann. Microturbulence in solar wind streams. J. Geophys. Res., 85:6025, 11 1980.

K. R. Anantharamaiah, P. Gothoskar, and T. J. Cornwell. Radio Synthesis Imaging of Anisotropic Angular Broadening in the Solar Wind. *Journal of Astrophysics and Astronomy*, 15:387, December 1994. doi: 10.1007/BF02714823.

K. R. Anantharamaiah, P. Gothoskar, and T. J. Cornwell. Radio Synthesis Imaging of Scatter Broadening at Small Solar Elongations. *J. Astrophys. Astron.*, 16:265, June 1995.

J. W. Armstrong, W. A. Coles, B. J. Rickett, and M. Kojima. Solar wind observations near the sun. In R. G. Marsden, editor, *The Sun and the Heliosphere in Three Dimensions*, volume 123 of *Astrophysics and Space Science Library*, pages 59–64, 1986.

J. W. Armstrong, W. A. Coles, B. J. Rickett, and M. Kojima. Observations of field-aligned density fluctuations in the inner solar wind. ApJ, 358:685–692, August 1990. doi: 10.1086/169022.

J. W. M. Baars, R. Genzel, I. I. K. Pauliny-Toth, and A. Witzel. The absolute spectrum of CAS A - an accurate flux density scale and a set of secondary calibrators. A&A, 61:99–106, October 1977.

T. S. Bastian. Low-frequency solar radiophysics with LOFAR and FASR. *Planet. Space Sci.*, 52:1381, 12 2004.

T. S. Bastian. Angular scattering of solar radio emission by coronal turbulence. ApJ, 426: 774–781, May 1994. doi: 10.1086/174114.

T. S. Bastian. Angular scattering of radio waves: Implications for mode coupling in the solar corona. ApJ, 439:494–498, January 1995. doi: 10.1086/175190.

L. L. Bazelyan, S. Y. Braude, and A. V. Men'. Scattering of the Decameter Radio Emission of the Crab Nebula by the Solar Corona. Soviet Ast., 14:153, August 1970.

R. G. Blesing and P. A. Dennison. Coronal broadening of the Crab Nebula 1969-71. Observations. *Proceedings of the Astronomical Society of Australia*, 2:84, March 1972.

J. G. Bolton, G. J. Stanley, and B. G. Clark. A Solar Occultation of the Crab Nebula at a Wavelength of 12 Meters. PASP, 70:594, December 1958. doi: 10.1086/127302.

J.-L. Bougeret, J. H. King, and R. Schwenn. Solar radio burst and in situ determination of interplanetary electron density. Sol. Phys., 90:401–412, February 1984. doi: 10.1007/BF00173965.

R. N. Bracewell and G. W. Preston. Radio Reflection and Refraction Phenomena in the High Solar Corona. ApJ, 123:14, January 1956. doi: 10.1086/146125.

S. Y. Braude, O. M. Lebedeva, A. V. Megn, B. P. Ryabov, and I. N. Zhouck. Flux Densities of Some Radio Sources in the Frequency Range 1 2-25 MHZ. Astrophys. Lett., 5:129, 1970.

I. H. Cairns. Solar, interplanetary, planetary, and related extra-solar system science for LOFAR. *Planet. Space Sci.*, 52:1423, 12 2004.

M. H. Cohen and E. J. Gundermann. Interplanetary Scintillations.IV. Observations Near the Sun. ApJ, 155:645, February 1969. doi: 10.1086/149897.

W. A. Coles and J. K. Harmon. Propagation observations of the solar wind near the sun. ApJ, 337:1023–1034, February 1989a. doi: 10.1086/167173.

W. A. Coles and J. K. Harmon. Propagation observations of the solar wind near the sun. ApJ, 337:1023–1034, February 1989b. doi: 10.1086/167173.

W. A. Coles, B. J. Rickett, J. L. Codona, and R. G. Frehlich. Refractive scintillation in the interstellar medium. ApJ, 315:666–674, April 1987. doi: 10.1086/165168.

T. J. Cornwell, K. R. Anantharamaiah, and R. Narayan. Propagation of coherence in scattering - an experiment using interplanetary scintillation. *Journal of the Optical Society of America A*, 6:977–986, July 1989. doi: 10.1364/JOSAA.6.000977.

G. A. Dulk and D. J. McLean. Coronal magnetic fields. Sol. Phys., 57:279–295, April 1978. doi: 10.1007/BF00160102.

R. D. Ekers and L. T. Little. The Motion of the Solar Wind Close to the Sun. A&A, 10: 310, January 1971.

W. C. Erickson. The Radio-Wave Scattering Properties of the Solar Corona. ApJ, 139: 1290, May 1964. doi: 10.1086/147865.

G. B. Gelfreikh. Coronal Magnetic Field Measurements Through Bremsstrahlung Emission. In D. E. Gary and C. U. Keller, editors, *Astrophysics and Space Science Library*, volume 314 of *Astrophysics and Space Science Library*, page 115, September 2004. doi: 10.1007/1-4020-2814-8_6.

K. Golap and C. V. Sastry. The radio brightness of the undisturbed outer solar corona in the presence of a radial magnetic field. Sol. Phys., 150:295–304, March 1994. doi: 10.1007/BF00712891.

S. Gorgolewski, J. Hanasz, H. Iwaniszewski, and Z. Turlo. Interferometric Observations of the Outer Solar Corona at the 32.1 MHz Band. *Acta Astronomica*, 12(4):251, 00 1962.

R. R. Grall, W. A. Coles, S. R. Spangler, T. Sakurai, and J. K. Harmon. Observations of field-aligned density microstructure near the Sun. J. Geophys. Res., 102:421, 01 1997.

J. K. Harmon and W. A. Coles. Spectral broadening of planetary radar signals by the solar wind. ApJ, 270:748–757, July 1983. doi: 10.1086/161166.

J. R. Harries, R. G. Blesing, and P. A. Dennison. 80 MHz observations of the coronal broadening of the Crab nebula. *Proc. Astron. Soc. Aust.*, 1:319, 04 1970.

C B Haselgrove and Jenifer Haselgrove. Twisted ray paths in the ionosphere. *Proceedings of the Physical Society*, 75(3):357, 1960. URL http://stacks.iop.org/0370-1328/75/i=3/a=304.

J. Haselgrove. Ray Theory and a New Method for Ray Tracing. In *Physics of the Ionosphere*, page 355, 1955.

J. Haselgrove. The Hamiltonian ray path equations. *Journal of Atmospheric and Terrestrial Physics*, 25:397–399, July 1963. doi: 10.1016/0021-9169(63)90173-9.

A. Hewish. The Irregular Structure of the Outer Regions of the Solar Corona. *Royal Society of London Proceedings Series A*, 228:238–251, February 1955. doi: 10.1098/rspa.1955.0046.

A. Hewish, P. F. Scott, and D. Wills. Interplanetary Scintillation of Small Diameter Radio Sources. Nature, 203:1214–1217, September 1964. doi: 10.1038/2031214a0.

J. A. Högbom. The structure and magnetic field of the solar corona. MNRAS, 120:530, 1960.

A. Ishimaru. *Wave propagation and scattering in random media. Vol._1.* 1978.

K. Issautier, N. Meyer-Vernet, M. Moncuquet, and S. Hoang. Pole-To Solar Wind Density from ULYSSES Radio Measurements. Sol. Phys., 172:335–343, May 1997. doi: 10.1023/A:1004908601144.

T. Kakinuma and G. Swarup. A Model for the Sources of the Slowly Varying Component of Microwave Solar Radiation. ApJ, 136:975, November 1962. doi: 10.1086/147450.

J. D. Kraus. *Radio Astronomy (New York: McGraw-Hill).* 1966.

K. R. Lang and R.F. Willson. VLA observations of a solar noise storm. ApJ, 319:514, 08 1987.

Y. Leblanc, G. A. Dulk, and J. L. Bougeret. Tracing the Electron Density from the Corona to 1AU. Sol. Phys., 183:165, 11 1998a.

Y. Leblanc, G. A. Dulk, and J.-L. Bougeret. Tracing the Electron Density from the Corona to 1au. Sol. Phys., 183:165–180, November 1998b. doi: 10.1023/A:1005049730506.

H. Lin, M. J. Penn, and S. Tomczyk. A New Precise Measurement of the Coronal Magnetic Field Strength. ApJ, 541:L83–L86, October 2000. doi: 10.1086/312900.

L. T. Little. Small Scale Plasma Irregularities in the Interplanetary Medium. A&A, 10: 301, 01 1971.

K. E. Machin and F. G. Smith. A New Radio Method for Measuring the Electron Density in the Solar Corona. Nature, 168:599–600, October 1951. doi: 10.1038/168599b0.

K. E. Machin and F. G. Smith. Occultation of a Radio Star by the Solar Corona. Nature, 170:319–320, August 1952. doi: 10.1038/170319b0.

C. Mercier, P. Subramanian, A. Kerdraon, M. Pick, S. Ananthakrishnan, and P. Janardhan. Combining visibilities from the giant meterwave radio telescope and the Nancay

radio heliograph. High dynamic range snapshot images of the solar corona at 327 MHz. A&A, 447:1189, 03 2006.

G. Newkirk, Jr. Structure of the Solar Corona. ARA&A, 5:213, 1967. doi: 10.1146/annurev.aa.05.090167.001241.

G. Newkirk, Jr. The Solar Corona in Active Regions and the Thermal Origin of the Slowly Varying Component of Solar Radio Radiation. ApJ, 133:983, May 1961. doi: 10.1086/147104.

M. Pätzold, M.K. Bird, H. Volland, G.S. Levy, B.L. Seidel, and C.T. Stelzried. The mean coronal magnetic field determined from helios faraday rotation measurements. *Solar Physics*, 109(1):91–105, 1987. ISSN 0038-0938. doi: 10.1007/BF00167401. URL http://dx.doi.org/10.1007/BF00167401.

A. M. Prokhorov, F. V. Bunkin, K. S. Gochelashvili, and V. I. Shishov. Laser irradiance propagation in turbulent media. *IEEE Proceedings*, 63:790–811, May 1975.

R. Ramesh. Low frequency solar radio astronomy at the Indian Institute of Astrophysics (IIA). *Bull. Astron. Soc. India Conf. Ser.*, 2:55, 00 2011.

R. Ramesh and E. Ebenezer. Decameter Wavelength Observations of an Absorption Burst from the Sun and Its Association with an X2.0/3B Flare and the Onset of a "Halo" Coronal Mass Ejection. ApJ, 558:L141, 09 2001.

R. Ramesh and C. V. Sastry. Low Frequency (< 100 MHz) Thermal Radio Emission from the Solar Corona and the Effect of Radial Magnetic Field. In K. Sankarasubramanian, M. Penn, and A. Pevtsov, editors, *Large-scale Structures and their Role in Solar Activity*, volume 346 of *Astronomical Society of the Pacific Conference Series*, page 153, December 2005.

R. Ramesh and Ch. V. Sastry. Radio observations of a coronal mass ejection induced depletion in the outer solar corona. A&A, 358:749, 06 2000.

R. Ramesh, K. R. Subramanian, M. S. Sundararajan, and C. V. Sastry. The Gauribidanur Radioheliograph. Sol. Phys., 181:439–453, August 1998. doi: 10.1023/A:1005075003370.

R. Ramesh, K. R. Subramanian, and Ch. V. Sastry. Eclipse Observations of Compact Sources in the Outer Solar Corona. Sol. Phys., 185:77, 03 1999.

R. Ramesh, C. Kathiravan, and C. V. Sastry. Low-Frequency Radio Observations of the Angular Broadening of the Crab Nebula Due to a Coronal Mass Ejection. ApJ, 548:L229–L231, February 2001a. doi: 10.1086/319098.

R. Ramesh, C. Kathiravan, and C. V. Sastry. Low-Frequency Radio Observations of the Angular Broadening of the Crab Nebula Due to a Coronal Mass Ejection. ApJ, 548:L229–L231, February 2001b. doi: 10.1086/319098.

R. Ramesh, H. S. Nataraj, C. Kathiravan, and Ch. V. Sastry. The Equatorial Background Solar Corona during Solar Minimum. ApJ, 648:707, 09 2006a.

R. Ramesh, M. S. Sundara Rajan, and Ch. V. Sastry. The 1024 channel digital correlator receiver of the Gauribidanur radioheliograph. *Exp. Astron.*, 21:31, 02 2006b.

R. Ramesh, C. Kathiravan, M. S. Sundararajan, I. V. Barve, and C. V. Sastry. A Low-Frequency (30 - 110 MHz) Antenna System for Observations of Polarized Radio Emission from the Solar Corona. Sol. Phys., 253:319–327, December 2008. doi: 10.1007/s11207-008-9272-y.

R. Ramesh, C. Kathiravan, and C. V. Sastry. Estimation of Magnetic Field in the Solar Coronal Streamers Through Low Frequency Radio Observations. ApJ, 711:1029–1032, March 2010. doi: 10.1088/0004-637X/711/2/1029.

R. Ramesh, C. Kathiravan, I. V. Barve, and M. Rajalingam. High Angular Resolution Radio Observations of a Coronal Mass Ejection Source Region at Low Frequencies during a Solar Eclipse. ApJ, 744:165, 01 2012.

B. J. Rickett. Radio propagation through the turbulent interstellar plasma. ARA&A, 28: 561, 00 1990.

A. C. Riddle. On the Observation of Scattered Radio Emission from Sources in the Solar Corona. Sol. Phys., 35:153, 03 1974.

B. Ryabov. Coronal Magnetic Field Measurements Through Quasi-Transverse Propagation. In D. E. Gary and C. U. Keller, editors, *Astrophysics and Space Science Library*, volume 314 of *Astrophysics and Space Science Library*, page 135, September 2004. doi: 10.1007/1-4020-2814-8_7.

K. Saito, A. I. Poland, and R. H. Munro. A study of the background corona near solar minimum. Sol. Phys., 55:121–134, November 1977. doi: 10.1007/BF00150879.

T. Sakurai, S. R. Spangler, and J. W. Armstrong. Very Long Baseline Interferometer Measurements of Plasma Turbulence in th Solar Wind. J. Geophys. Res., 97(A11): 17141, November 1992.

C. V. Sastry. Polarization of the Thermal Radio Emission from Outer Solar Corona. ApJ, 697:1934–1939, June 2009. doi: 10.1088/0004-637X/697/2/1934.

C. V. Sastry and K. R. Subramanian. Observations on the occultation of the radio source Tauras A by the solar corona during June 1971. *Indian Journal of Radio and Space Physics*, 3:196–198, September 1974.

S. L. Scott. *Density spectrum and velocity of the solar wind inferred from scintillation observations*. PhD thesis, California Univ., San Diego., 1978.

S. L. Scott, W. A. Coles, and G. Bourgois. Solar wind observations near the sun using interplanetary scintillation. A&A, 123:207–215, July 1983.

K. V. Sheridan and D .J. McLean. *The quiet sun at metre wavelengths in Solar Radio*

Physics, ed. McLean, D. J. and Labrum, N. R. (London: Cambridge University Press), 443. 1985.

O. B. Slee. Occultations of the Crab Nebula by the Solar Corona in June 1957 and 1958. *Australian Journal of Physics*, 12:134, June 1959. doi: 10.1071/PH590134.

O. B. Slee. The outer solar corona during the declining portion of the solar activity cycle. Planet. Space Sci., 14:255–267, March 1966. doi: 10.1016/0032-0633(66)90125-5.

S. F. Smerd. Radio-Frequency Radiation from the Quiet Sun. *Australian Journal of Scientific Research A Physical Sciences*, 3:34, March 1950.

S. R. Spangler. *Plasma Turbulence in the Local Bubble*, page 277. 2009. doi: 10.1007/978-1-4419-0247-4_22.

S. R. Spangler. The Strength and Structure of the Coronal Magnetic Field. Space Sci. Rev., 121:189–200, November 2005. doi: 10.1007/s11214-006-4719-7.

S. R. Spangler and T. Sakurai. Radio interferometer observations of solar wind turbulence from the orbit of HELIOS to the solar corona. ApJ, 445:999–1016, June 1995. doi: 10.1086/175758.

S. R. Spangler, T. Sakurai, W. A. Coles, R. R. Grall, and J. K. Harmon. Radio interferometer observations of turbulence in the inner solar wind in Proc. of the Eighth International Solar Wind Conference, ed. Winterhatter, D., Gosling, J. T., Habbal, S. R., Kurth, W. S. and Neugebauer, M. (AIP Conf. Proc.) 382, 265. *Proc. of the Eighth International Solar Wind Conference, ed. Winterhatter, D., Gosling, J. T., Habbal, S. R., Kurth, W. S. and Neugebauer, M. (AIP Conf. Proc.), 382, 265*, 382: 265, 07 1996.

K. R. Subramanian. Multibaseline Observations of the Occultation of the Crab Nebula by the Solar Corona at Decameter Wavelengths. *Journal of Astrophysics and Astronomy*, 21:421, June 2000. doi: 10.1007/BF02702437.

P. Subramanian and I. Cairns. Constraints on coronal turbulence models from source sizes of noise storms at 327 MHz. *Journal of Geophysical Research (Space Physics)*, 116:A03104, March 2011. doi: 10.1029/2010JA015864.

G. Thejappa and M. R. Kundu. Unusually low coronal radio emission at the solar minimum. Sol. Phys., 140:19–39, July 1992. doi: 10.1007/BF00148427.

G. Thejappa and R. J. MacDowall. Effects of Scattering on Radio Emission from the Quiet Sun at Low Frequencies. ApJ, 676:1338–1345, April 2008. doi: 10.1086/528835.

G. L. Tyler, J. F. Vesecky, M. A. Plume, H. T. Howard, and A. Barnes. Radio wave scattering observations of the solar corona First-order measurements of expansion velocity and turbulence spectrum using Viking and Mariner 10 spacecraft. ApJ, 249: 318–332, October 1981. doi: 10.1086/159290.

V. V. Vitkevich. New Data on the Supercorona of the Sun. Soviet Ast., 2:45, February 1958.

B. Vršnak, J. Magdalenić, H. Aurass, and G. Mann. Band-splitting of coronal and interplanetary type II bursts. II. Coronal magnetic field and Alfvén velocity. A&A, 396: 673–682, December 2002. doi: 10.1051/0004-6361:20021413.

B. D. Ward. An Investigation of Radio-wave Scattering in the Interplanetary Medium. *Ph.D Thesis, University of Adelaide (http://hdl.handle.net/2440/20542)*, 15:387, 07 1975. doi: 10.1007/BF02714823. URL http://ebooks.adelaide.edu.au/dspace/handle/2440/20542.

S. M. White. Coronal Magnetic Field Measurements Through Gyroresonance Emission. In D. E. Gary and C. U. Keller, editors, *Astrophysics and Space Science Library*, volume 314 of *Astrophysics and Space Science Library*, page 89, September 2004. doi: 10.1007/1-4020-2814-8_5.

R. F. Willson, S. L. Redfield, K. R. Lang, B. J. Thompson, and St. Cyr O. C. First VLA Observations of Nonthermal Metric Bursts Associated with Coronal Mass Ejections Detected by the Solar and Heliospheric Observatory. ApJ, 504:L117, 09 1998.

R. Woo. *Mass Ejections Observed in Radio Propagation Measurements Through the Solar Corona, ed. Crooker, N. U., Joselyn, J. A. and Feynmann, J. (Washington DC: AGU), 235*, volume 99. 1997.

R. Woo and J. W. Armstrong. Spacecraft radio scattering observations of the power spectrum of electron density fluctuations in the solar wind. J. Geophys. Res., 84: 7288–7296, December 1979. doi: 10.1029/JA084iA12p07288.

R. Woo and R. Schwenn. Comparison of Doppler scintillation and in situ spacecraft plasma measurements of interplanetary disturbances. J. Geophys. Res., 96:21227, 12 1991.

P. Zlobec, M. Messerotti, G. A. Dulk, and T. Kucera. VLA and Trieste observations of type I storms, type IV and pulsations. Sol. Phys., 141:165, 09 1992.

Chapter 7

Cross-polarized log-periodic dipole antenna system to study the solar corona

7.1 Introduction

According to IEEE standards antenna is a means for radiating and receiving the radio waves. Although antenna can be of any shape, different requirements demand antennas of different kind and specifications. To design any antenna for a required purpose, the parameters have to be considered such as the material characteristics. The material has to be rigid to sustain the shape at all environmental conditions, free of oxidation or corrosion. It is preferred that the designing of an antenna has to be of low cost and weight and easy to fabricate. Different structures of antenna has different state of polarizations: linear, circular and elliptical. State of polarization of antenna is decided by current distribution in the antenna elements. If the current distribution is along one axis then it is said to be linearly polarized, and if there exists two orthogonal current distribution with 90^o phase

shift then antenna radiation can be circularly polarized [Huang and Boyle., 2008, pp.122]. Circular polarization will be elliptically polarized when there exists two orthogonal current distributions that are not in equal amplitudes. Therefore the linear, circular polarizations are special cases of elliptical polarization.

Linearly polarized antennas are preferred to measure the precise circular polarization and circularly polarized antennas to measure the linear polarization. Yagi-Uda antennas, simple log-periodic dipole antennas are linearly polarized. Circularly polarized radio radiation in the VHF range (30-300 MHz) can be received/transmitted using helical antennas, conical log-spiral antennas, cross-polarized Yagi-Uda antennas, cross-polarized log-periodic dipole antennas, etc. In some situations, where wider frequency coverage (10:1 or even more) is required, cross-polarized log-periodic dipole (CLPD) antennas are generally used. A CLPD consists of two linearly-polarized log-periodic dipole (LPD) antennas [Duhamel and Isbell, 1957] fixed to a common axis in a mutually orthogonal fashion. Log-periodic antennas are widely used in the field of radio astronomy, particularly where simultaneous multi-frequency observations of radio emission from the celestial radio sources are required [Erickson and Fisher, 1974, Boischot et al., 1980, Maan et al., 2013]. For example, in the case of solar corona, radio emission at different frequencies originate at different levels in the atmosphere. To obtain data on the activities related to a solar flare, which leads to the generation of transient radio emission almost around the same time at different levels in the solar corona, simultaneous multi-frequency observations are required [Ramesh et al., 1998]. However, the typical isolation between the two mutually orthogonal LPDs in the commercially available CLPDs is less, $\approx$ -20 dB [Pivnenko, 2006]. Because of this limit, an understanding of the polarization characteristics of the weak signals from celestial radio sources can be limited. Note that a 90^o hybrid is generally used in conjunction with the CLPD and the polarization strength is measured from the difference of the two outputs of the CLPD. The problem here is that the outputs from either LPD in a CLPD responds to the total intensity. So the observer encounters the problem of

measuring a small difference between two much larger quantities similar to polarization observations with circular feeds [Thompson et al., 2007]. Though dual-polarized antenna designs offering improved isolation have been mentioned in the literature, they are primarily at frequencies > 1 GHz [Pivnenko, 2006, Tran and Yagoub, 2007]. Our interest is to observe the polarized radio emission from the solar corona with high accuracy at low frequencies and use it to estimate the solar coronal magnetic field, one of the holy grails in solar astrophysics. Hence this paper is presented to achieve this goal. Note that low frequency radio emission originates from regions of the solar atmosphere where observations in white light and other regions of the electromagnetic spectrum are presently difficult.

7.2 Design and fabrication of the CLPD

7.2.1 Design of the LPD

In order to design a CLPD, first LPD has to be designed with required specifications. A step-by-step procedure for designing a LPD was first described by [Carrel, 1961]. In our efforts to construct a CLPD, we used the inputs mentioned in the above reference and fabricated a LPD. Figure 7.1 shows the schematic design of a LPD. It can be shown that the apex angle α is related to the length (L_n) of the adjacent arms and the spacing (S_n) between them as [Kraus, 1950, Balanis, 2005],

$$L_{n+1} = L_n + S_n \tan\alpha \tag{7.1}$$

Also, as mentioned previously, the length of the adjacent arms and the spacing between them follow the relationship,

$$\frac{L_{n+1}}{L_n} = \frac{S_{n+1}}{S_n} = k \tag{7.2}$$

where k is a constant called scaling factor (see section 2.2).

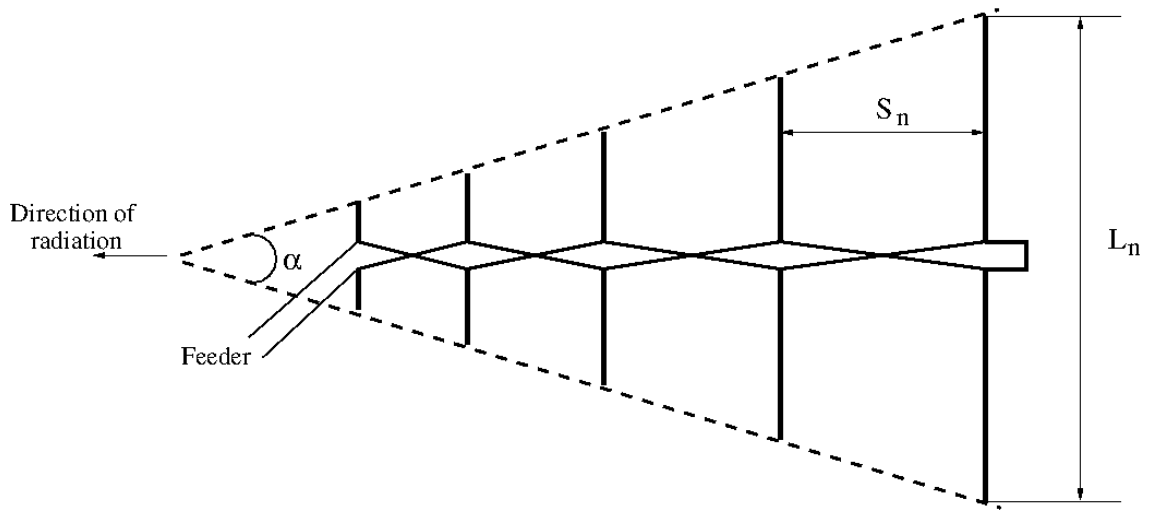

Fig. 7.1: Schematic design of a LPD. The direction of radiation is towards the direction of decreasing arm length.

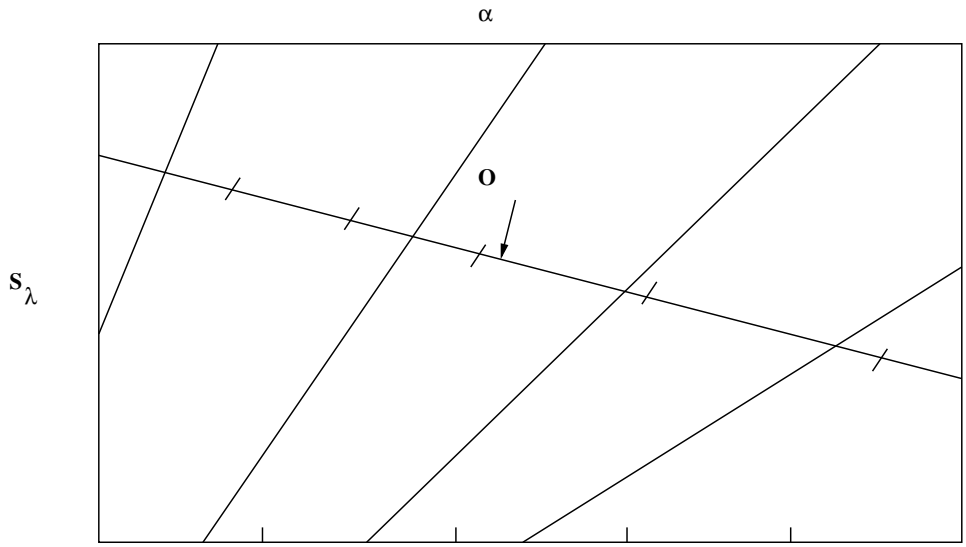

Fig. 7.2: Re-generated plot of the optimum design curve which is used to design the LPD. Original image credit: Kraus [1950]

Using equation 7.1 and by fixing the value of α, the length of the adjacent arms and the spacing between them are calculated iteratively. By knowing any of the two parameters: k, α and spacing in wavelength (s_λ) third one can be obtained using the optimum design line and gain values. The optimum design line is shown in the Figure 7.2. By making use of the optimum design curve of a LPD, the directional gain (G) of the LPD can be decided as a function of apex angle (α), inter-arm spacing (S) and the scale factor k. In the present case, parameters were chosen as: $G = 8$ dBi, $\alpha = 21^o$, $k = 1.14$, $S_\lambda = S/\lambda = 0.08$. In practice, by using the optimum gain curve, we can choose k for a required gain or vice-versa. The relationship between the bandwidth or the frequency ratio of a LPD is

$$F = f_{max}/f_{min} \tag{7.3}$$

where f_{max} and f_{min} are the expected maximum and minimum operating frequencies of the LPD and the design parameters are related as,

$$k^N = F \tag{7.4}$$

Equation 7.4 can be rewritten as follows

$$N = \frac{log(F)}{log(k)} \tag{7.5}$$

where N is the number of dipoles. Once the values of k and F are decided, the number of possible arms can be obtained using equation 7.5.

7.2.2 Design and fabrication of the CLPD

It is aimed to design a CLPD for its operation in the frequency range $\approx 65 - 95$ MHz since the existing radioheliograph at the GRO, operates primarily at 80 MHz [Ramesh et al., 1998, 1999, 2006, Ramesh, 2011]. The number of arms generally vary with the

frequency coverage of the antenna and in the present case, it was decided to fabricate the LPD with 4 arms, based on the values of F and k which are discussed above. The lengths of the different arms and inter element spacing of the LPD was calculated for the above frequency range and are tabulated in Table 7.1. The arms were designed using commercially available hollow cylindrical aluminium pipes of whose diameter $\approx$ 13 mm and they were fixed in pairs to two identical hollow rectangular aluminium pipes, (called as the booms) separated from each other by a non-conducting spacer in a criss-cross fashion as shown in Figure 7.1. The inter-boom separation (D) was calculated using the following equation [Wakabayashi et al., 1999].

$$Z_o = 138\ log_{10}\left(\frac{2\sqrt{2}D}{d}\right) \tag{7.6}$$

where Z_o is the characteristic impedance of the LPD and d is the width of each boom. In Figure 7.3, the d and D are shown which has to be carefully decided to design a CLPD to avoid mechanical and electrical characteristics.

Initially characteristic impedance (Z_o) was assumed to be 50 Ω and substituting the other values in equation 7.6, it was found that $D \approx 2$ cm. The two booms act like a 2-conductor transmission line. They were 'shorted' at one of their ends, close to where the arms with the longest length are fixed. The distance between the latter and the 'short' (stub) is $\approx$ 29 cm. This is $1/4^{\text{th}}$ of the length L_n of the longest arm in the CLPD, i.e. quarter wavelength loop which are shown in Table 7.1. The output was tapped using a RF coaxial cable connected to the other end of the two booms (close to where the arms with the shortest length are fixed). While the center conductor of the RF coaxial cable was connected to one of the booms, the shield (i.e. the 'ground') of the cable was connected to the other boom and the coaxial cable was drawn through the latter as described in Carrel [1961]. The 'shorting' of the two booms minimize the impedance mismatch that arise when directly connecting the 'unbalanced' RF coaxial cable to the 'balanced' LPD.

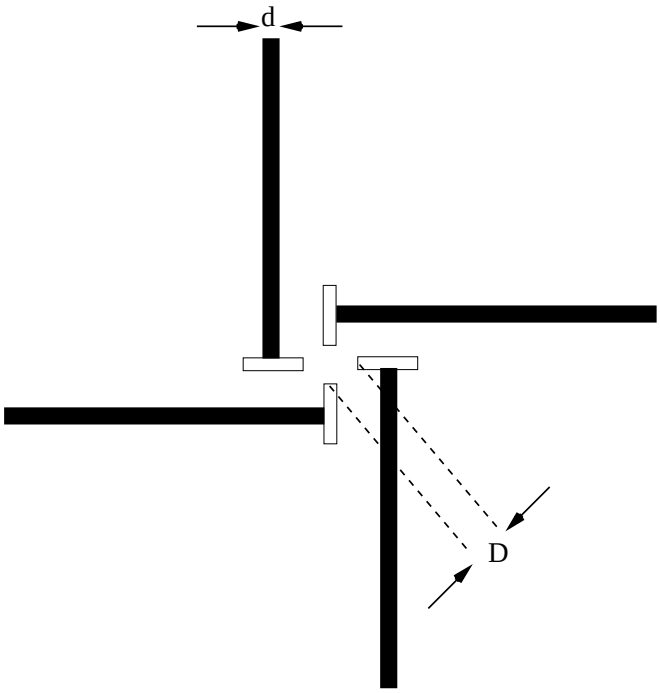

Fig. 7.3: Cross section view of the CLPD is shown in the Figure. The dark thick lines are the antenna arms and the white colored rectangles are the aluminium flats (booms).

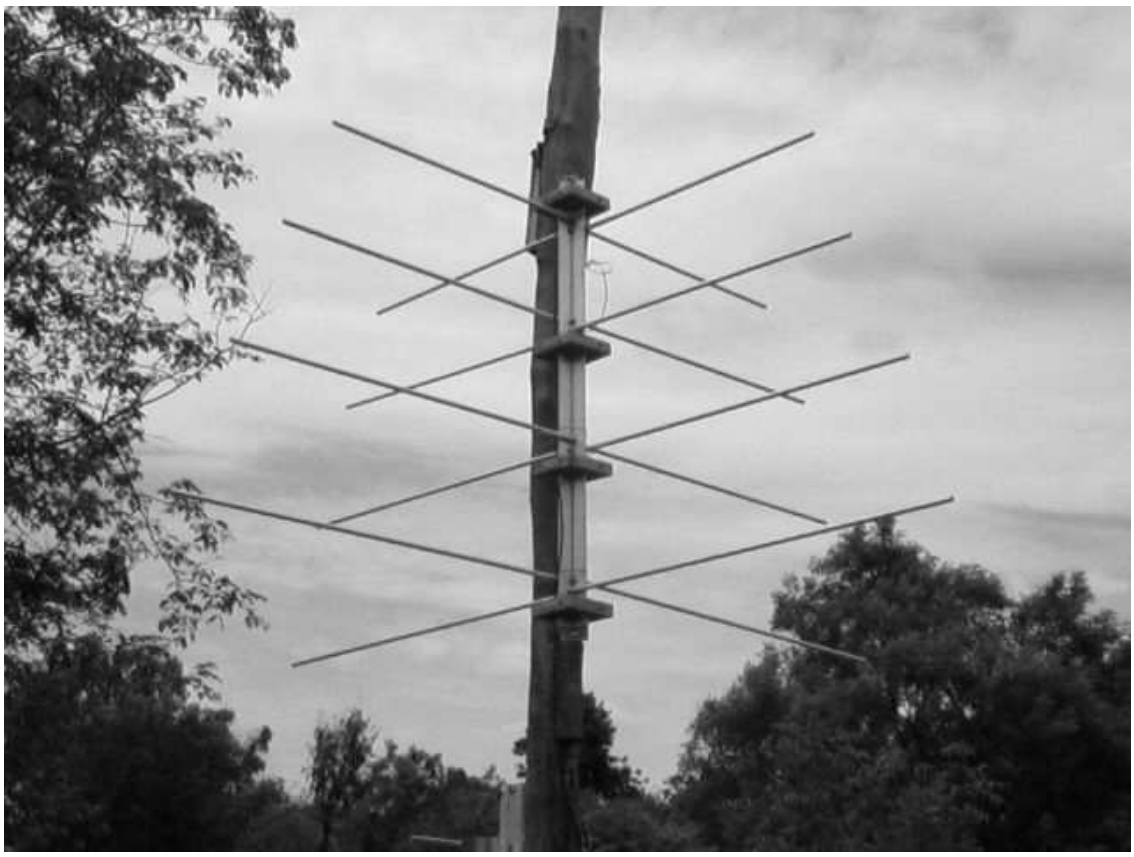

Fig. 7.4: A view of the low frequency CLPD designed and fabricated at the Gauribidanur radio observatory.

The approximately quarter wavelength of the coaxial cable in the boom acts as a 'balun' by presenting a high impedance to any common mode current [Kraus, 1950, Balanis, 2005]. Two LPDs with the above specifications were fabricated and combined them in a mutually orthogonal fashion to form a CLPD. Also the isolation of the CLPD was measured as discussed in section-7.3 and found that it is about ≈ -20 dBm, nearly the same as that of a commercial CLPD mentioned earlier.

It has been suggested that the isolation can be improved by decreasing the inter-boom spacing D to $\approx 1/100^{th}$ of the arm length [Pivnenko, 2006]. So, it was designed a LPD/CLPD with $D \approx 5$ mm (smaller than even $1/100^{th}$ of the shortest arm length in Table 7.1). Using commercially available rectangular aluminium flats as the booms instead of the rectangular hollow aluminium pipes mentioned above. All the other specifications

Table 7.1: Antenna Specifications

S.No	L_n (cm)	S_n (cm)	Frequency (MHz)
1	79	-	95
2	90	29	83
3	102	31	74
4	116	36	65

including the characteristic impedance were the same. The new CLPD mentioned above is shown in Figure 7.4. The RF cable was enclosed inside a small aluminium pipe fixed by the side of the aluminium flat that was 'grounded'. The isolation was measured to be $<$ -30 dBm. The details of the isolation and the other measurements carried out with the above CLPD are described in section-7.3. Trial observations with the CLPD are mentioned in section-7.5.

7.3 Measurement of antenna parameters of CLPD

After designing the antennas many characteristics of the antenna has to be studied. In this section, few antenna parameters like VSWR, radiation patterns, gain etc are measured for the designed CLPD. Measurement of the different antenna parameters are discussed as follows.

7.3.1 VSWR measurements

Important characteristic of an antenna is impedance matching. Reflection coefficient, return loss and VSWR are the terminologies which represents the similar property. These terms describe whether the load of the antenna matched with the transmission line so that the loss of the signal will be minimal. A complex quantity-reflection coefficient (Γ),

return loss (L_{rt}), voltage standing wave ratio (VSWR) are given in equations 7.7, 7.8 and 7.9 respectively.

$$\Gamma = \frac{Z_a - Z_o}{Z_a + Z_o} \tag{7.7}$$

$$L_{rl} = -20log_{10}(|\Gamma|) \tag{7.8}$$

$$VSWR = \frac{1 + |\Gamma|}{1 - |\Gamma|} \tag{7.9}$$

It is required for certain applications that L_{rt} has to be > 10 dB or VSWR should be < 2. The VSWR of the LPD/CLPD antenna mentioned above was measured using a vector network analyzer. The values were found to be $\lesssim 2$ for both the LPDs in the frequency range of $\approx 68 - 84$ MHz (see Figure 7.5). The VSWR remained nearly the same even after combining the two LPDs to form a CLPD. Due to the radio frequency interference generated by FM transmissions ($88 - 108$ MHz) the higher frequency cut-off in our VWSR measurements were limited to ≈ 84 MHz.

7.3.2 Radiation pattern measurements

Field or power response of the antenna for all azimuthal angles at any fixed distance is called radiation pattern. If the antenna is linearly polarized, it always describes the terms E-plane and H-plane. E-plane is a plane containing the electric field vector and the direction of the maximum radiation. Similarly H-plane is a plane which contains magnetic vector and the direction of maximum radiation. Always E-plane will be in the plane of the antenna arms mounted and H-plane will be perpendicular to that. However radiation pattern is classified in to three distinct regions: (1) far-field radiation pattern (2) near field pattern and (3) reactive near field pattern. The radiation pattern measurement of far-field and near field patterns are described in the following sub-sections.

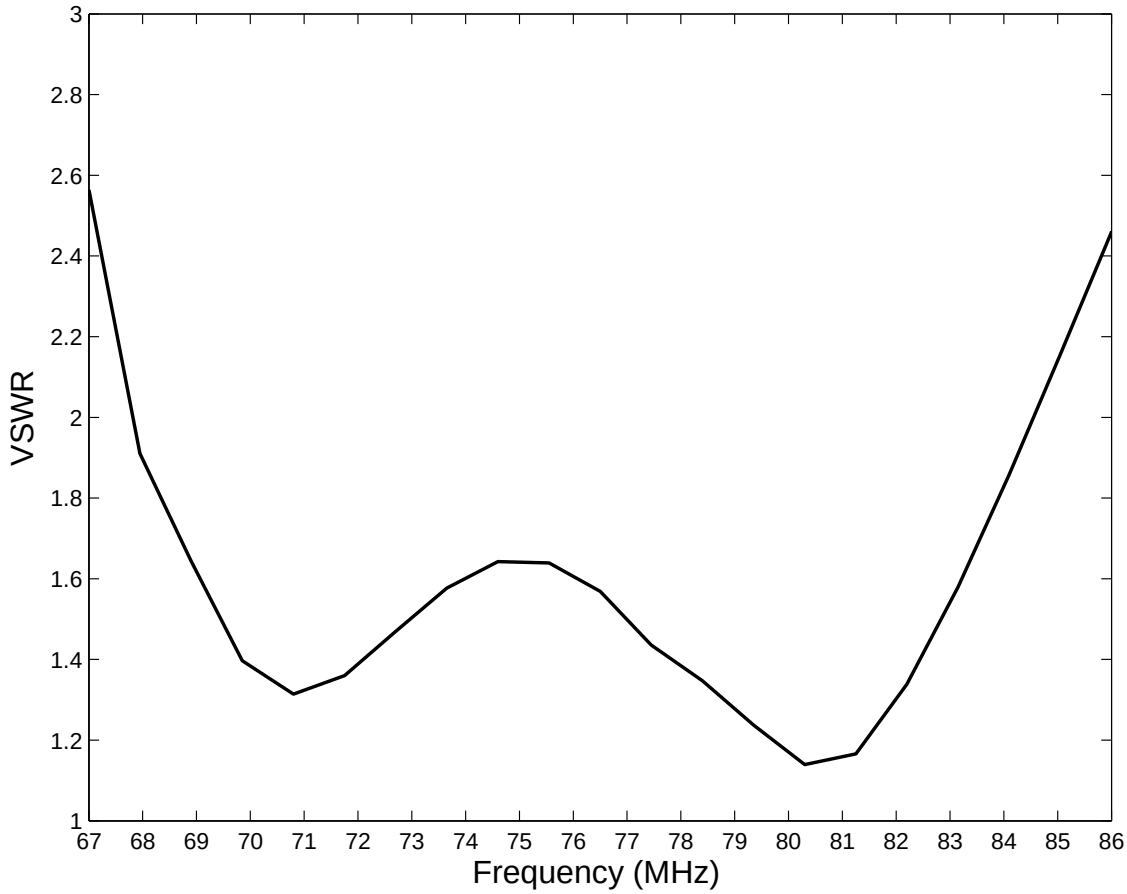

Fig. 7.5: VSWR of the CLPD in Figure 7.4.

7.3.2.1 Far field radiation pattern measurements

The region in which the angular field distribution is independent of the distance, then it is said to be a far-field (Fraunhofer region) region and the pattern in this region is called far-field radiation pattern. To measure the far field radiation pattern, the receiver antenna and the transmitter antenna were mounted at the height of $\approx$ 3 m above the ground level. The antennas were separated by a distance of $\approx$ 3 m consistent with the theoretical minimum observation distance for far-field measurements. The equation to measure the radius of the far-field region is shown in the equation 7.10

$$r_{ff} \gtrsim 2l^2/\lambda \tag{7.10}$$

where l is the length of the longest dipole in the CLPD and λ is the wavelength of the transmitted signal [Balanis, 2005]. At 80 MHz, $r_{ff} \approx 3$ m for $l \approx 2.32$ m (see Table 7.1). The signal was transmitted using a CLPD and the same was received by the arms of a LPD in the same plane. The measurements were carried out for different angle by rotating the transmitting LPD in the azimuth direction. This corresponds to the E-plane measurement. By mounting the transmitting and the receiving antennas in the vertical direction, the measurements were repeated which correspond to the H-plane measurement. Figure 7.6 shows the E-plane and H-plane far field patterns at 80 MHz for the CLPD in Figure 7.4. The half power beam width (HPBW) in the E-plane and H-plane are $\theta \approx 60^o$ and $\phi \approx 120^o$, respectively. The test was repeated at different frequencies and found that the E-plane and H-plane widths are similar. The above beam widths correspond to a solid angle, $\Omega = \theta\phi \approx 2.2$ sr. From this, the directional gain of the antenna with respect to an isotropic radiator is calculated using equation 7.11. The estimated gain is approximately 7.6 dBi.

$$G = 10\log_{10}(4\pi/\Omega) \tag{7.11}$$

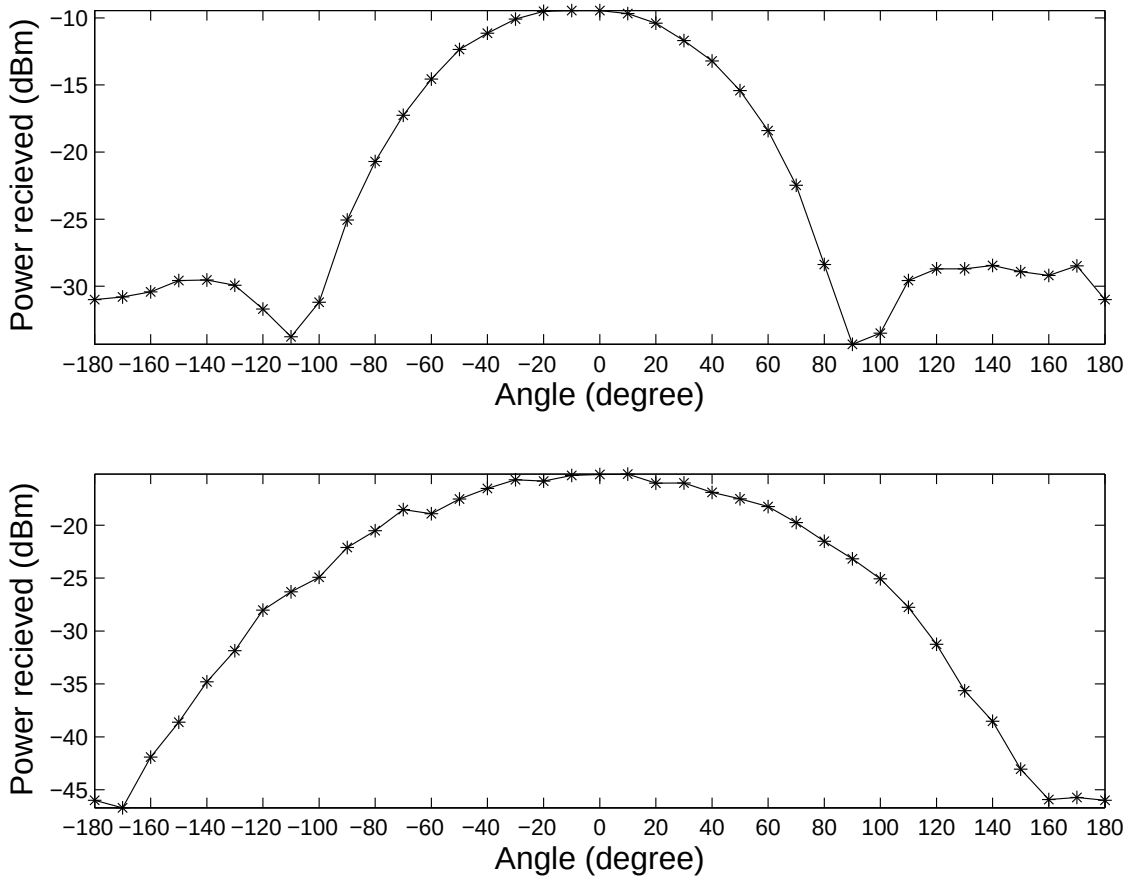

Fig. 7.6: Measured far field pattern of the CLPD is shown in Figure 7.4 at 80 MHz. The upper and lower panels correspond to the E-plane and H-plane, respectively.

Also the effective collecting area (A_e) of the one of the antenna of the CLPD is given in equation 7.12 and the estimated collecting area is $\approx 0.6\lambda^2$,

$$A_e = (G/4\pi)\lambda^2 \tag{7.12}$$

The various parameters of the CLPD are listed in Table 7.2. Note that little asymmetry in the E-plane and H-plane far field patterns in Figure 7.6. The presence of residual common mode currents could be a reason for this. They may be rejected to a large extent by adding clamp-on ferrite chokes to the coaxial cable.

7.3.2.2 Near field radiation pattern measurements

The region between the reactive near field and far field region is called the near field region or Fresnel region. Note that reactive near field region is the portion of near field region provided, it immediately surrounds the antenna where the reactive field predominates. The reactive near field region may be estimated using the formula-7.13

$$R < 0.62\sqrt{(l^3/\lambda)} \tag{7.13}$$

To obtain the radiating near field pattern, CLPD is mounted on a pole at a height of $\approx$ 3 m above the ground level and CW signal was transmitted from one of the LPDs in the CLPD. Using a monopole antenna, the signal strength was measured at different distances in the radiating near field range, i.e. $0.62\sqrt{l^3/\lambda} \lesssim r_{nf} \lesssim 2l^2/\lambda$, from the apex of the CLPD and also for different azimuth angles in the range $0^o - 180^o$. At 80 MHz, the radiating near field is in the distance range 1 m $\lesssim r_{nf} \lesssim$ 3 m for $l \approx 2.32$ m (see Table 7.1). The test was repeated for the same set of distances and angles by transmitting the signal through the other orthogonal LPD. The results were similar. Figure 7.7 shows the E-plane and H-plane radiating near field patterns at 80 MHz for the CLPD in Figure 7.4. One can notice that the measured power varies with the distance in the radiating near field range as expected.

7.3.3 Isolation measurements

By using the same set-up used to measure the far field pattern, cross-talk and isolation of the designed CLPD is estimated. The transmitting LPD was mounted in the horizontal orientation (0^o) and the signal was received by both 0^o and 90^o oriented arms of the CLPD. In principle, the signal has to be received in only the 0^o oriented arms of the CLPD. However, a finite amount of the signal was received in 90^o oriented arms of the

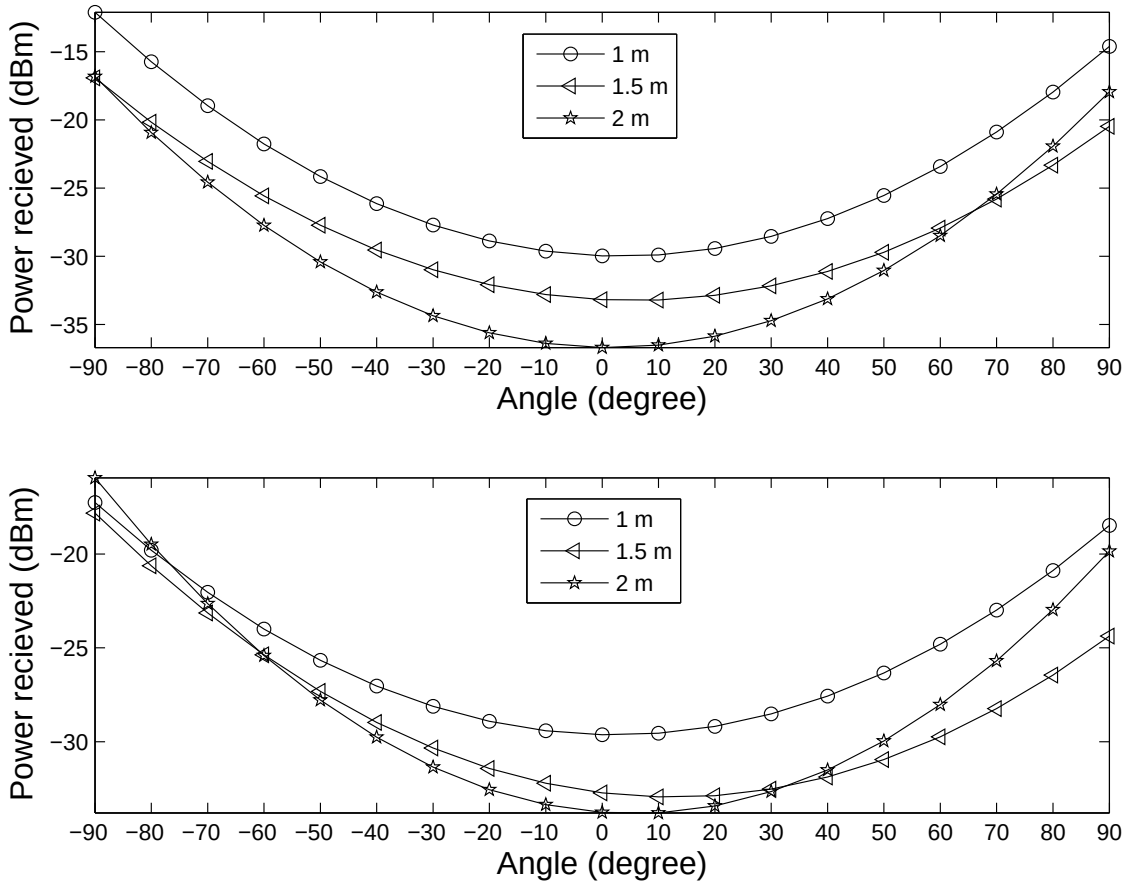

Fig. 7.7: Radiating near field pattern of the CLPD in Figure 7.4 at 80 MHz. The upper and lower panels correspond to the E-plane and H-plane, respectively. The numbers 1, 1.5 and 2 m in the rectangular box indicate the distances from the apex of the CLPD at which the measurements were obtained.

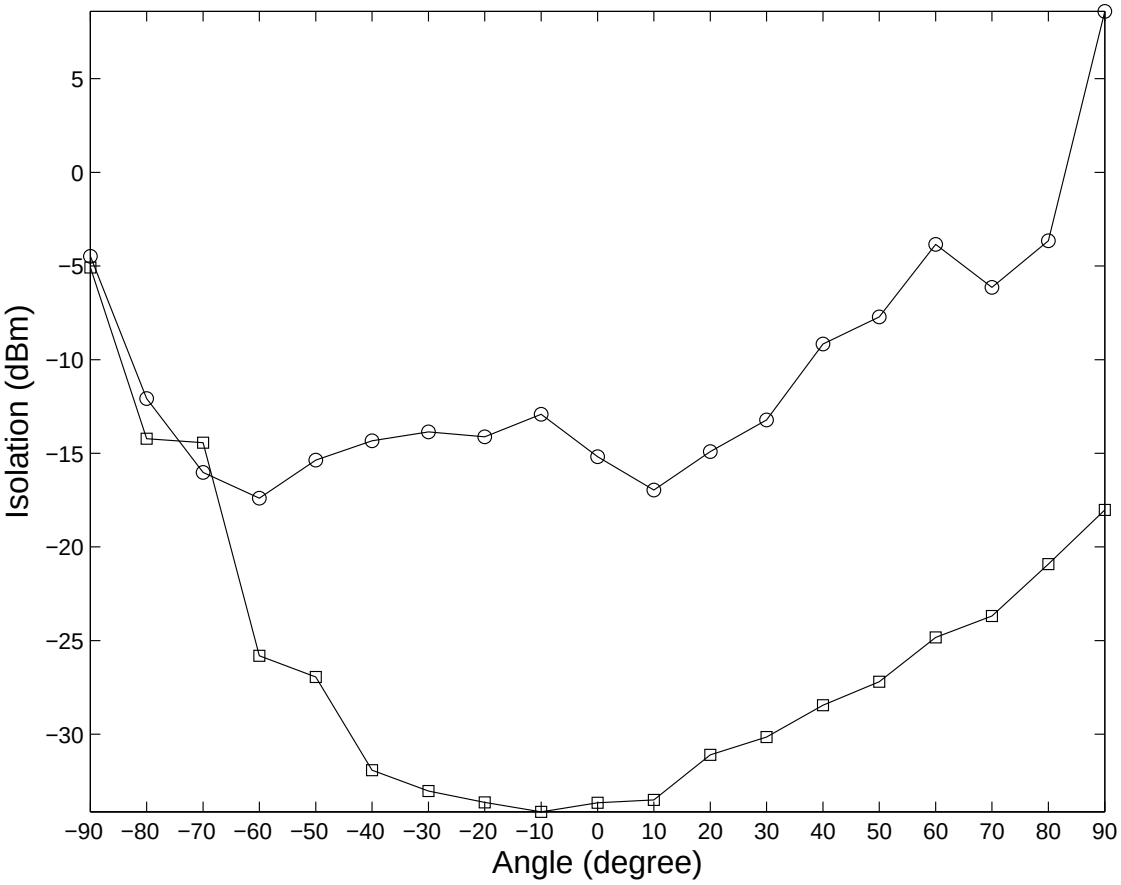

Fig. 7.8: Isolation between the orthogonal LPDs in the CLPD with inter-boom spacing $D = 5$ mm ('squares') and $D = 2$ cm ('circles') at 80 MHz.

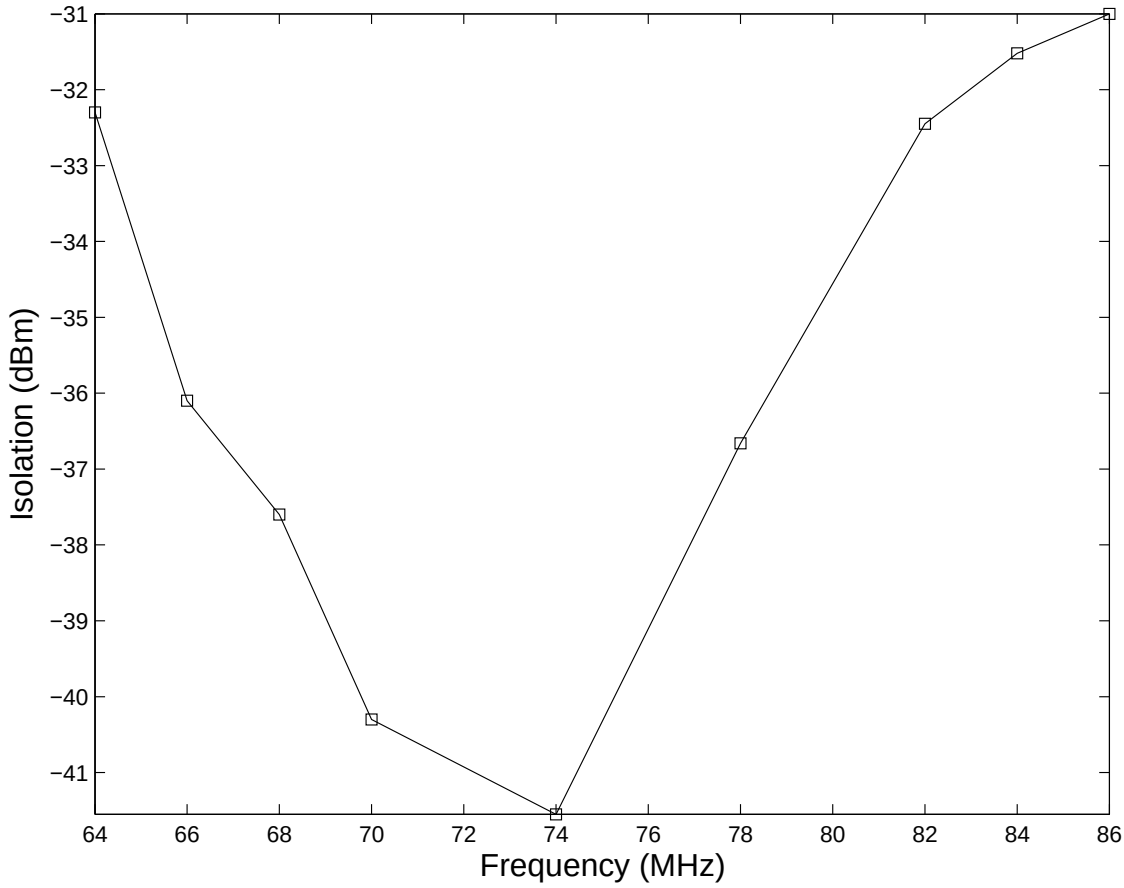

Fig. 7.9: Measured values of isolation (for an azimuthal angle of 0^o) at different frequencies for the CLPD in Figure 7.4 (inter-boom spacing $D = 5$ mm).

Table 7.2: Calculated parameters of the CLPD

S.No	Parameter	Value
1	HPBW in the E-plane (θ)	$\approx 60^o$
2	HPBW in the H-plane (ϕ)	$\approx 120^o$
3	Solid angle (Ω)	$\approx$ 2.2 sr
4	Directional gain (G)	$\approx$ 7.6 dBi
5	Effective collecting area (A_e)	$\approx 0.6\lambda^2$

CLPD. This is due to the cross-talk between the two orthogonal LPDs in the CLPD. The difference in the signal strength received by the two orthogonal LPDs in the CLPD which is a measure of the isolation. The measurements were repeated for different azimuth angles and the results are shown in Figure 7.8 for a frequency of 80 MHz. The two plots correspond to the CLPD designed with inter-boom spacing (D) of $\approx$ 2 cm and $\approx$ 5 mm mentioned earlier. While the isolation is $\approx$ -15 dBm for the former, it is $<$ -30 dBm for the latter. The variation of isolation with frequency is shown in Figure 7.9. Also isolation was estimated in an independent manner by transmitting the CW signal through one of the LPDs in the CLPD which is shown in Figure 7.4 and measured the received power near the other LPD using a monopole. The results obtained were similar to that in Figure 7.8. Note that the isolation bandwidth depends on the extent to which the residual common mode currents (see section-7.3.2.1) are rejected. It is possible that the limited bandwidth in Figure 7.9 could be due to the presence of such weak currents in the system.

7.4 Two element interference polarimeter

Two CLPDs similar to Figure 7.4 were designed and mounted with a separation of $\approx$ 40 m in the East-West direction. The CLPDs were at a height of $\approx$ 3 m above the ground. They were mounted vertically in such a manner that the length of the arms gradually increase from the top to the base. The schematic diagram of the antenna set-up is shown in Figure

7.10. RF output from the LPDs A, B, C and D were transmitted to a receiver room (about 500 m away) via low loss coaxial transmission lines buried under the ground at a depth of $\approx$ 1 m to minimize the phase variations. The set-up was operated as a correlation interferometer in the transit mode. The interferometer technique has the advantage of: 1) minimizing the contribution from the galactic background radiation and thereby the emission from discrete sources can be observed with better contrast; 2) spurious effects due to ground radiation are less [Morris et al., 1964]; and 3) calibration of the observations is also relatively simpler [Weiler, 1973, Sault et al., 1996, Ramesh et al., 2008]. In Figure 7.10, the multiplications $A \times C$ and $B \times D$ respond to the total intensity (Stokes I) and the multiplications $B \times C$ and $A \times D$ respond to the circularly polarized intensity (Stokes V). In principle, the multiplications $A \times C$ and $B \times D$ record only 50% of the total intensity. Since the situation is the same for observations on the target as well as the calibrator sources, the error will be minimal. Note that our interest is primarily on observations of the Stokes V emission from the solar corona since Stokes Q and U that contain information on the linear polarization of the signal, are considered to be extremely small at frequencies $<$ 100 MHz, particularly over observing bandwidths $\gtrsim$ 1 MHz. The Faraday rotation of the plane of linear polarization (during transmission through solar corona and the Earth's ionosphere) is considered to cancel the linear polarization generated at the source when the emission is summed over the observing band [Grognard and McLean, 1973]. There are reports of observations of high levels of linearly polarized radio emission from the Sun at frequencies $<$ 100 MHz, specifically over narrow bandwidths in the range of $\approx 0.1 - 10$ kHz [Bhonsle and McNarry, 1964, Chin et al., 1971]. This needs to be verified. Note that the interferometer method of measuring the Stokes V intensity described above differs from the conventional technique where a four-port 90^o hybrid is used in conjunction with a crossed dipole feed to extract the Stokes V from the difference of the two outputs from the hybrid. This method is also less sensitive to the cross-talk that arises in a hybrid [Cohen, 1958]. The analog and digital correlator receiver system used for the observations

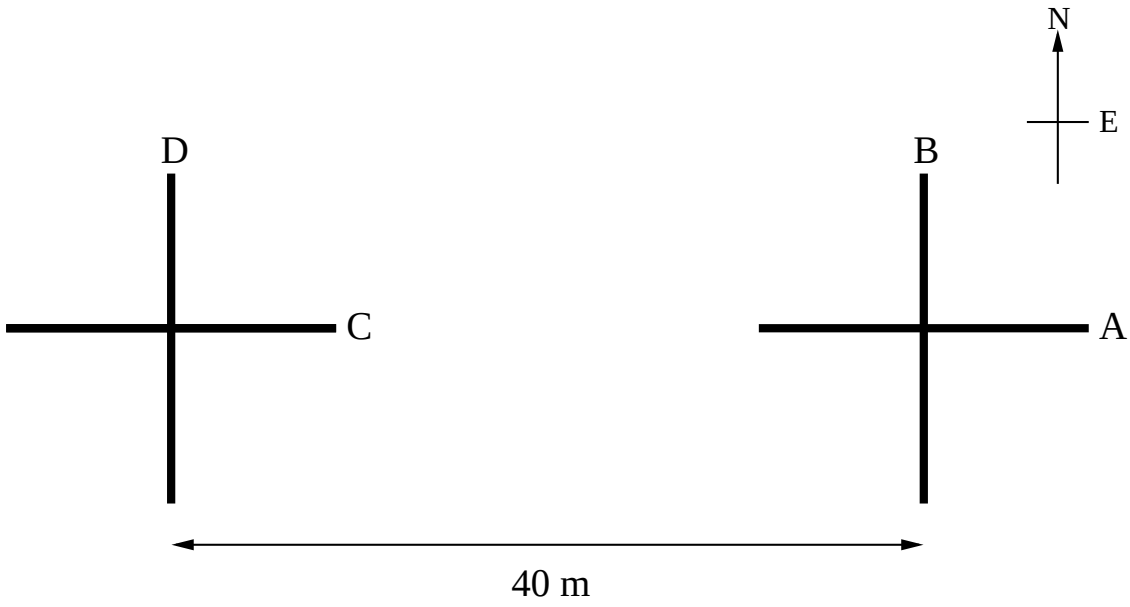

Fig. 7.10: Schematic of the two element interferometric polarimeter set up using the CLPDs at the Gauribidanur observatory.

is similar to that described in section-2.7 and Ramesh et al. [1998].

7.5 Observations of the solar corona

Observations of the solar corona is carried out and other unpolarized strong radio sources with constant flux density over a period of time (called calibrator sources) in both Stokes I and V using the above set-up. The frequency of observation was 80 MHz and the bandwidth was $\approx$ 1 MHz. Both the Sun and the calibrator sources can be treated as 'point' sources since the fringe spacing or the first-null beam width (FNBW) of the interference pattern at the above frequency is broad ($\approx 5^o$). Figure 7.11 shows the observations of the circularly polarized radio emission from the Sun on 5 October 2012 with the above set-up. The emission is primarily due to the presence of a noise storm source in the solar atmosphere which is known to be circularly polarized [Elgarøy, 1977, Ramesh et al., 2011, 2013]. Contribution to the Stokes V emission from the 'undisturbed' background solar corona is expected to be relatively small, particularly at 80 MHz [Sastry, 2009].

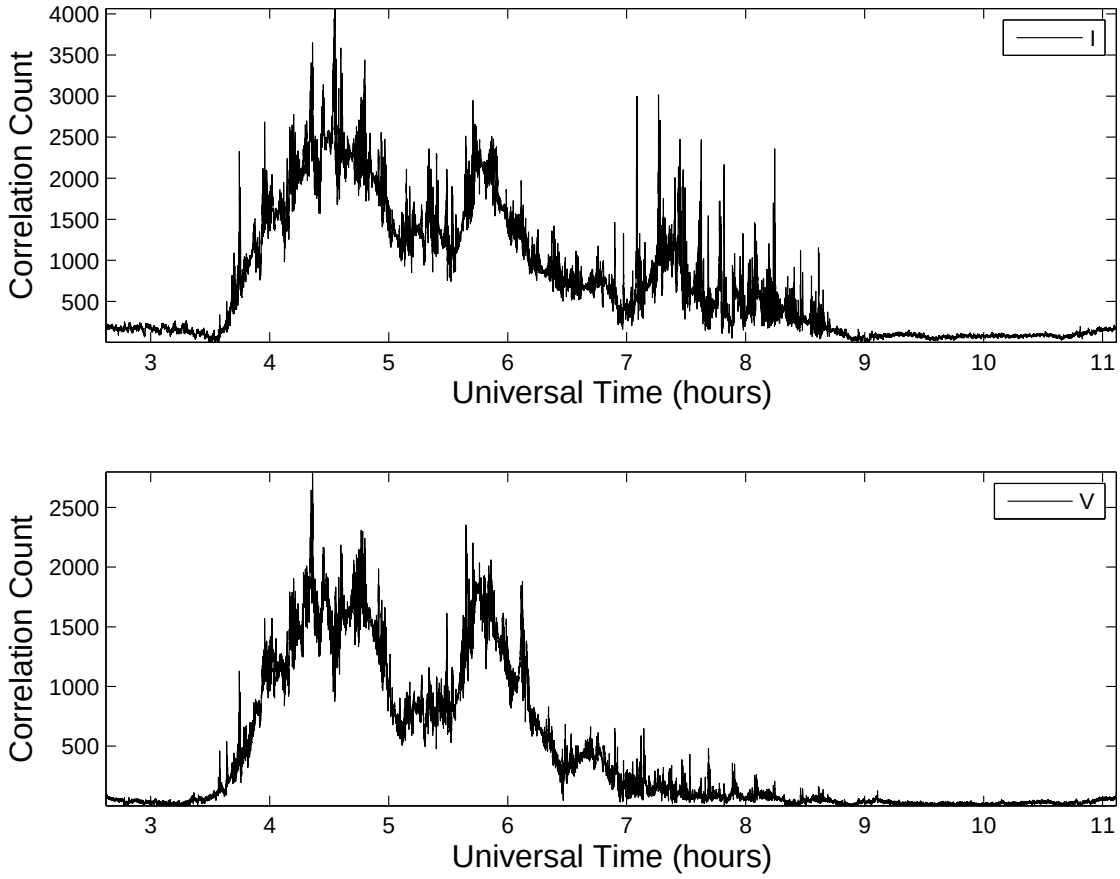

Fig. 7.11: Stokes I and V emission observed from the solar corona at 80 MHz on 5 October 2012. The top and the lower panel corresponds to Stokes I and V observations, respectively.

We would like to mention here that the effect of the instrumental circular polarization in our observations can be considered to be very small since the deflection in the Stokes V channel while observing some of the strong unpolarized calibrator sources was less than the 3σ level, where σ is the rms noise in the system.

7.6 Future scope and applications of the CLPD

Since the designed CLPD operates in the frequency range of $\approx 68 - 84$ MHz with VSWR < 2 and isolation $<$ -30 dBm between the two mutually orthogonal LPDs that constitute the CLPD. Trial observations indicate that the antennas can be used to effectively observe the circularly polarized radio emission from the solar atmosphere with minimal

instrumental polarization. It is possible that the CLPD described can also be used to transmit and receive circularly polarized radio waves by making use of the hybrid network, in applications involving transmission through the Earth's ionosphere which may produce rotation of the wave polarization (particularly at low frequencies). Note the polarization arriving at the receiver from a linearly-polarized transmitting antenna may be practically unpredictable due to reasons mentioned earlier. The compact size of the CLPD described also makes them suitable for use as a primary antenna (feed) that illuminates a parabolic reflector [Smith, 2001]. We intend to extend the bandwidth of the CLPD and simultaneously observe radio emission from different levels in the solar corona, with an array of CLPDs.

References

C. A. Balanis. *Antenna theory : analysis and design*. 2005.

R. V. Bhonsle and L. R. McNarry. Polarization Characteristics of Type III Solar Radio Bursts at 74 Mc/s. ApJ, 139:1312–1327, May 1964. doi: 10.1086/147866.

A. Boischot, C. Rosolen, M. G. Aubier, G. Daigne, F. Genova, Y. Leblanc, A. Lecacheux, J. De La Noe, and Moller-Pedersen. A New High-Gain, Broadband, Steerable Array to Study Jovian DEecametric Emission. *Icarus*, 253:399–407, September 1980. doi: 10.1016/0019-1035(80)90185-2.

R. Carrel. The design of log-periodic dipole antennas. In *IRE International Convention Record*, volume 9, pages 61–75, Mar 1961. doi: 10.1109/IRECON.1961.1151016.

Y. C. Chin, B. B. Lusignan, and P. C. W. Fung. Polarization Measurements of Solar Type III Radio Bursts at 25.3 MHz. Sol. Phys., 16:135–151, January 1971. doi: 10.1007/BF00154509.

M.H. Cohen. Radio astronomy polarization measurements. *Proceedings of the IRE*, 46 (1):172–183, 1958. ISSN 0096-8390. doi: 10.1109/JRPROC.1958.286729.

R. H. Duhamel and D. Isbell. Broadband logarithmically periodic antenna structures. In *IRE International Convention Record*, volume 5, pages 119–128, Mar 1957. doi: 10.1109/IRECON.1957.1150566.

E. Ø. Elgarøy. *Solar noise storms.* 1977.

W. C. Erickson and J. R. Fisher. A new wideband, fully steerable, decametric array at Clark Lake. *Radio Science*, 9:387–401, May 1974.

R. J. M. Grognard and D. J. McLean. Non-Existence of Linear Polarization in Type III Solar Bursts at 80 MHz. Sol. Phys., 29:149–161, March 1973. doi: 10.1007/BF00153446.

Yi. Huang and Kevin Boyle. *Antennas: From Theory to Practice*. August 2008.

J. D. Kraus. *Antennas*. 1950.

Y. Maan, A. A. Deshpande, V. Chandrashekar, J. Chennamangalam, K. B. Raghavendra Rao, R. Somashekar, G. Anderson, M. S. Ezhilarasi, S. Sujatha, S. Kasturi, P. Sandhya, J. Bauserman, R. Duraichelvan, S. Amiri, H. A. Aswathappa, I. V. Barve, G. Sarabagopalan, H. M. Ananda, C. Beaudet, M. Bloss, D. B. Dhamnekar, D. Egan, J. Ford, S. Krishnamurthy, N. Mehta, A. H. Minter, H. N. Nagaraja, M. Narayanaswamy, K. O'Neil, W. Raja, H. Sahasrabudhe, A. Shelton, K. S. Srivani, H. V. Venugopal, and S. T. Viswanathan. RRI-GBT Multi-band Receiver: Motivation, Design, and Development. ApJS, 204:12, January 2013. doi: 10.1088/0067-0049/204/1/12.

D. Morris, V. Radhakrishnan, and G. A. Seielstad. On the Measurement of Polarization Distributions Over Radio Sources. ApJ, 139:551, February 1964. doi: 10.1086/147784.

S. Pivnenko. Log-periodic dipole antenna with low cross-polarization. In *Antennas and Propagation, 2006. EuCAP 2006. First European Conference on*, pages 1–4, Nov 2006. doi: 10.1109/EUCAP.2006.4585044.

R. Ramesh. Low frequency solar radio astronomy at the Indian Institute of Astrophysics (IIA). In *Astronomical Society of India Conference Series*, volume 2 of *Astronomical Society of India Conference Series*, pages 55–61, 2011.

R. Ramesh, K. R. Subramanian, M. S. Sundara Rajan, and Ch. V. Sastry. The Gauribidanur Radioheliograph. Sol. Phys., 181:439–453, August 1998.

R. Ramesh, K. R. Subramanian, and Ch. V. Sastry. Phase calibration scheme for a "T" array. A&AS, 139:179–181, October 1999. doi: 10.1051/aas:1999387.

R. Ramesh, M. S. Sundara Rajan, and Ch. V. Sastry. The 1024 channel digital correlator receiver of the Gauribidanur radioheliograph. *Experimental Astronomy*, 21:31–40, February 2006. doi: 10.1007/s10686-006-9065-y.

R. Ramesh, C. Kathiravan, M. S. Sundara Rajan, Indrajit V. Barve, and Ch. V. Sastry. A Low-Frequency (30-110 MHz) Antenna System for Observations of Polarized Radio Emission from the Solar Corona. Sol. Phys., 253:319–327, December 2008. doi: 10.1007/s11207-008-9272-y.

R. Ramesh, C. Kathiravan, and A. Satya Narayanan. Low-frequency Observations of Polarized Emission from Long-lived Non-thermal Radio Sources in the Solar Corona. ApJ, 734:39, June 2011. doi: 10.1088/0004-637X/734/1/39.

R. Ramesh, K. Sasikumar Raja, C. Kathiravan, and A. Satya Narayanan. Low-frequency Radio Observations of Picoflare Category Energy Releases in the Solar Atmosphere. ApJ, 762:89, January 2013. doi: 10.1088/0004-637X/762/2/89.

Ch. V. Sastry. Polarization of the Thermal Radio Emission from Outer Solar Corona. ApJ, 697:1934–1939, June 2009. doi: 10.1088/0004-637X/697/2/1934.

R. J. Sault, J. P. Hamaker, and J. D. Bregman. Understanding radio polarimetry. II. Instrumental calibration of an interferometer array. A&AS, 117:149–159, May 1996.

A. A. Smith. *Radio Frequency Principles and Applications*. 2001.

A.R. Thompson, J. M. Moran, and G. W. Swenson. *Interferometry and Synthesis in Radio Astronomy*. 2007.

A. Tran and M. C. E. Yagoub. Interwined two-section dual-polarized log-periodic dipole antenna. In *PIERS Proceedings, Prague, Czech Republic*, pages 30–33, 2007.

R. Wakabayashi, K. Shimada, H. Kawakami, and G. Sato. Circularly polarized log-periodic dipole antenna for emi measurements. *Electromagnetic Compatibility, IEEE Transactions on*, 41(2):93–99, 1999. ISSN 0018-9375. doi: 10.1109/15.765096.

K. W. Weiler. The Synthesis Radio Telescope at Westerbork. Methods of Polarization Measurement. A&A, 26:403, August 1973.

Chapter 8

Summary and conclusions

The solar atmosphere can be broadly classified into four distinct regions - the photosphere, the chromosphere, the transition region and the corona. The photosphere is mainly observable at visible wavelengths, whose temperature is around ≈ 5800 K. Above the photosphere, a pink colored layer with thickness of ≈ 2000 km is called the chromosphere. In the chromosphere and transition region (a thin layer above the chromosphere) the temperature gradually raises and $\approx 10^4$ to 10^5 K respectively. Above the chromosphere and transition region, a tenuous plasma called solar corona, with temperature of 1 MK exists which extends outward and mix with inter-planetary media. The solar atmosphere is further divided into three layers: (1) lower corona which $< 1.2\ R_\odot$, (2) middle corona which extends from $1.3 - 3\ R_\odot$, and (3) outer corona starts above $3\ R_\odot$. The Sun and solar atmosphere can be observed at almost all wavelengths using different observing techniques. Each wavelength of observation corresponds to different layer of Sun. For example photosphere is observable at visual wavelengths, chromosphere is observable at H_α and microwave frequencies. Solar corona may be observed at soft X-ray (SXR), Hard X-ray (HXR), Extreme Ultra Violet (EUV) and radio frequencies. Ground based white light observations of solar corona is possible only during total solar eclipse which is a rare

phenomenon. Using coronagraphs the solar corona can be observed, in which photosphere is artificially occulted by a disk. Such observations has to be carried out from the space in order to avoid the scattering effects due to the Earth's atmosphere. Microwave and radio observations of the chromosphere and corona can be carried out from ground, X-ray and UV has to be carried out using a space borne instrumentation, since the Earth's atmosphere is opaque for these wavelengths. It is known that electron density decreases in the solar corona with increasing height. According to the dispersion equation, in a isotropic media different frequencies of observation correspond to different heights in the solar corona. Lower the frequency of observation higher the corona can be observed.

Low-frequency observations of the solar corona give many clues in understanding the long standing mysteries like coronal heating, coronal magnetic fields, coronal seismology, coronal mass ejections, solar influence on the space weather and Earth's climate etc. Also radio observations are useful in order to predict the sudden power grid disruptions, damages of satellites/spacecrafts, telecommunication/radar jams, geomagnetic storms, auroras, etc. Such kind of observations are possible from ground with low cost interferometric techniques. Since it is not possible to build a continuous large aperture size telescopes, interferometric techniques are used in which one can synthesize the aperture to improve resolution and sensitivity. Such kind of interferometric arrays build with broad band antennas are suitable to observe the solar corona.

Magnetism plays a crucial role in evolution and dynamics of a solar corona. But, there is no direct method to estimate the magnetic field in the solar corona. Zeeman effect and Hanle effect are used to estimate the magnetic field of the photosphere and chromosphere respectively but not in corona. So estimation of the magnetic fields are highly difficult and it is essential to understand the mysteries of the corona. At radio frequencies magnetic fields can be estimated using the polarization observation of the corona. At me-

ter wavelengths linear polarization get canceled out due to the Faraday rotation of solar corona and Earth's ionosphere. So in very high frequency (VHF) band i.e., 30-300 MHz, only Stokes I and V measurements are possible from the ground. From the Stokes I and V, the degree of circular polarization (dcp) can be calculated, from which magnetic fields are estimated by adopting different techniques. With this motivation we build a polarimeter (henceforth Gauribidanur Radio Interference Polarimeter, GRIP) in Gauribidanur Radio Observatory (GRO), which is 100 km from Bangalore, India. Longitude of the place is $77^o27'07''$ East and latitude is $13^o36'12''$ North.

GRIP consists of 40 linearly polarized log periodic dipole (LPDs) antennas along East-West direction with every adjacent antenna is separated by 10 m. The frequency of operation of LPD is 30-150 MHz. LPDs characteristic impedance is 50 Ω with VSWR < 2.5 in the frequency of operation. Effective collecting area of the individual LPD is $\approx 0.6\lambda^2$ and the directional gain is 7 dBi. Half power beam width of the antenna in E-plane (along the arms of LPD) and H-plane (perpendicular to arms of the LPD) are 75^o and 105^o respectively, which enables to carryout the observations of the Sun through out the year for all declinations. In GRIP there exists a 5 groups and each group consists of 8 antennas. Length of each group is 70 m and the total length of the GRIP is $\approx$ 400 m. Output of each LPD taken from top side of the antenna using coaxial cable, which passes through a hollow aluminum square shaped boom of LPD. The RF signal from antenna pass through a high-pass filter (cut-off frequency is 50 MHz) and then amplified using a pre-amplifier (with gain 28 dB). The signals from 8 antennas are brought to the group center using a 50 m cable and added using a 8-way power combiner. The 8-way power combiner outputs of group 1 and 2 are added using a 2-way combiner and then amplified using a wide-band amplifier called a group amplifier (with gain 34 dB). In the same fashion, the group 4 and 5 are combined and amplified with a group amplifier. The former combination forms a major group A and the latter one is called a major group C. In

group 3, output of 8 antennas are added using a 8-way combiner and then amplified using a group amplifier and the output is named as B. Note that in the present configuration, the major groups A and C outputs are contributed by 16 antennas where as group B is by 8 antennas. The LPDs in group A are oriented in 0^o (arms of the LPD are oriented in North-South fashion) and in the case of group B and C, the LPDs are mounted in 90^o orientation (arms of the antennas are oriented along East-West direction). The signal from A, B and C are brought to the receiver building using a low-loss RF cables which are about 500 m in length and buried under ground at around one meter depth to avoid fluctuations of phase due to temperature gradient.

The RF signals from group A, B and C are processed separately in the receiver room. Firstly, signals are high-pass filtered and then amplified to ≈ 28 dBm. The amplified output is further up-converted using a mixer to 170 MHz (intermediate frequencies, IF1) using a variable local oscillator. Output of the mixer is further amplified and pass through a band-pass filter with a center frequency (f_c) of 170 MHz and bandwidth of 4 MHz to suppress the signal at other frequencies. The signal is then down-converted to 10.7 MHz (IF2) using a fixed frequency mixer and second local oscillator (LO2) of frequency of 180.7 MHz. The output is further amplified and pass through a band-pass filter with $f_c \approx 10.7$ MHz and bandwidth of 1 MHz. The output voltage of the analog receiver is maintained (V_{pp}) ≈ 100 mV. The IF signal from every receiver is further divided into in-phase (cosine) and quadrature (sine) components using a analog quadrature hybrid and those are finally given to the digital correlator. The digital receiver does the correlations of all channels, which has custom-built chips that use CMOS gate array technology. The correlator accepts inputs from antennas and give four complex correlations. The IF signals of each channel is separately quantized to two levels, then sampled with 2 MHz to avoid aliasing effects. The sampled signal is correlated and counted the number of correlation counts using a counter. The stored output in memory over an integration cycle of 256 ms

is read to the personal computer.

The correlated output between B and C gives the information of total intensity (Stokes I) and A and C corresponds to the circularly polarized intensity (Stokes V). The collecting area of the group B is $\approx 5\lambda^2$ and group A or C is $\approx 10\lambda^2$. The calculated minimum detectable flux (5σ level) of the array for both Stokes I and V is ≈ 0.05 sfu (1 sfu $= 10^{-22}$ Watts m^{-2} Hz^{-1}). Baseline length of the phase centers of the group B and any major group is 120 m so that angular resolution (1.8^o) and collecting area (12 λ^2) for both Stokes I and V are same. Half power beam-width (HPBW)/ field of view (FOV) of group A or C is $\approx 1.3^o$ and for group B $\approx 2.6^o$. Since HPBW of the group A and C is within the HPBW of group B, correlated output of A and B or B and C will not produce any artifacts in the correlation interferometry. In such interferometers to observe the polarized radio emission precisely from the Sun and other celestial sources, the instrumental errors has to be minimized. In order to do that, the RF cables used in the GRIP were maintained with equal lengths for all channels to avoid gain variations. The phase equalization of the RF cables was done and maintained constant for all the channels to suppress the coherence loss. Observations of the randomly/linearly polarized sidereal sources give deflection in Stokes I where as no deflection in Stokes V. During the solar activity the deflection in both Stokes I and V is often observed with the GRIP. Such observations proves that the instrumental errors of the GRIP was minimal. The actual flux density of the solar corona was found with the observations of the calibrator sources whose flux density is constant over a long period. Since dcp is proportional to the the magnetic field of corona, by using different methodologies the magnetic field of the solar corona is estimated.

Signature of the weak, transient energy releases in the solar atmosphere related to the non-thermal emissions are frequently observed at low-frequencies. Such kind of tran-

sient weak energy observations which are related to the flares were reported at SXR, HXR, EUV, microwave and radio wavelengths. Depending on the energy released, the events were classified as microflares and nanoflares which was postulated by Parker. According to Parker, larger flares are superposition of the microflares and microflares are the superposition of the nanoflares. A typical large flare energy release is $\approx 10^{33}$ erg. If the solar flare energy is in the range of $10^{26} - 10^{28}$ erg, then associated flares are called microflares and if the energy range is $10^{23} - 10^{25}$ erg then they are defined as nanoflares. Earlier reports says that large flares are reported in SXR, HXR and EUV wavelength regimes, where as microflares are detected in SXR and EUV, and nanoflares in EUV only. Recently signature of the weak energy events are reported even in microwave and radio regimes. It is suspected that microscopic magnetic reconnection processes exist virtually everywhere on the solar surface, which can reveal themselves as tiny non-thermal transients. In this scenario, noise storms are often observed using GRIP in both Stokes I and V. The noise storms are the broad-band continuum emissions lasting for few hours to days over which narrow-band short duration (0.1-1 s) spikes (called type I bursts) were superposed. These emissions are highly circularly polarized and circular polarization arises due to the propagation effects in the solar corona in the presence of magnetic field. These bursts are considered to be evidence of successive electron accelerations unlike the transient acceleration associated with flares. The radiation is due to the fundamental plasma emission due to the coupling of the Langmuir plasma waves and low-frequency waves (either lower-hybrid or ion-acoustic). The type I bursts are related to the non-flaring sunspot active regions and point to an exceedingly restless corona even during the non-flaring times. Such kind of signatures occur in many small steps and the cumulative effect is the 'gradual' evolution of the solar corona. Analysis of the few such noise storms observed using the polarimeter reveal that the energy correspond to the each burst is around 10^{21} erg which is 10^{-12} times of the large flare. These are the weakest energy release events in the solar atmosphere reported till date and they are called 'picoflares'. The occurrence rate

of the narrow-band bursts are ≈ 1 s^{-1}, so the power emitted by the type I bursts in our observation was $\approx 10^{21}$ erg s^{-1}. The distribution of the number of bursts (dN) in the flux density range of S to $S + dS$ follows a power law. The estimated index of the power-law (γ) is ranging from ≈ -2.2 to -2.7. From the EUV, UV, and X-ray observations, it was found that γ is ≈ -2.3 for the events with the energy range $\approx 10^{24} - 10^{26}$. [Litvinenko, 1994] showed that the weak events with $\gamma < -2$ can be explained by assuming the reconnecting current sheet model for energy accumulation and release. So the type I bursts originate due to the small-scale reconnections in the solar atmosphere with low energy. Also Crosby et al. [1996] suggested that flare-like energy released in the active region is necessary condition for the onset of the type I bursts. Mercier and Trottet [1997] reported the $\gamma \approx -3$ for type I bursts at 164, 237 and 327 MHz. Such results are justified because of the high flux density of the events ($\approx 10^7$ Jy) where as using polarimeter we observed the events whose flux density is $\approx 10^4$ Jy. Observed brightness temperature of the events are $\approx 10^9$ K. Magnetic fields estimated near the source region was in the range of $\approx 200 - 900$ mG.

Whether the observed picoflares will contribute for the coronal heating or not? In this regard several authors pointed out that the corona maintaining high temperature due to the magnetic flux emergence on the plasma. For example, Spicer et al. [1982] predicted coronal heating prior to the onset of the type I storms. Melrose et al. [1980] pointed out that the required level of low-frequency turbulence for the generation of the type I emission is likely to be present in the region where the corona is heated. Raulin and Klein [1994] mentioned that the common features in the time profile of SXR brightenings and noise storms point to a physical link between the heating of the plasma in the active region and the noise storm emission. However to heat the corona required power is $10^{27} - 10^{28}$ erg s^{-1}. In the present observations the estimated power of the noise storms are smaller ($\approx 10^{21}$ erg s^{-1}). It is possible that given type I bursts are one of the weak energy releases

in the corona mentioned by Aschwanden [2004], and all these weak events together heat the solar corona.

Direct measurement of the magnetic field in solar atmosphere is not there till now. But there are indirect methods to estimate the magnetic field in the solar atmosphere as mentioned earlier. Polarization measurements are one of the methods to estimate the magnetic field in the atmosphere. Magnetic field of the type III bursts was estimated in different approaches at 80 MHz plasma layer. In general type III solar radio bursts are the signatures of the accelerated electrons streaming outward through the corona and inter planetary medium aftermath of flares and weak chromospheric brightenings. The electron streams along the open magnetic field lines with speeds $\approx c/3$ will cause type III bursts. The radio emission occurs in the following two step process: (1) the excitation of the high levels of plasma oscillations (Langmuir plasma waves) by the propagating electron streams and (2) subsequent conversion of these Langmuir waves into electromagnetic waves at the fundamental (F) and the second harmonic (H) of the local plasma frequency. The coalescence of the two Langmuir plasma waves produces the H emissions. Depending on the drifting speeds of the radiation type III bursts are identified in the spectrum observed using existing spectrometers at GRO, Gauribidanur LOw-Frequency solar Spectrograph (GLOSS) and the Compound Astronomical Low-cost Low-frequency Instrument for Spectroscopy and Transportable Observatory (CALLISTO). Type III bursts has the drifting speed from high to low frequencies is ≈ 100 MHz s^{-1}. These bursts occurs from ≈ 1 GHz - 10 kHz, corresponding distance range extends from lower corona to beyond the Earth's orbit. Type III bursts can occur in general as isolated bursts, groups or storms. These bursts are classified based on the life time of the occurrence of the bursts. Isolated bursts occur as a single spike whose life time is of few seconds. If such type of bursts occurs as a bunch which lasts for few minutes they are called type III groups and if it continues for hours they are called type III storms.

It is believed that each burst corresponding to the beam of the electrons streaming outwards in the diverging open magnetic field lines. Such kind of occurrence of non-thermal bursts is the clear evidence of the particle acceleration during the event. Type III bursts are weakly, circularly polarized with dcp $\approx$ 0.15, however few bursts which are identified due to the F emissions have dcp $\approx$ 0.5. Harmonic emissions in general are observed at low-frequencies. The net dcp of the type III bursts observed in the source region are the ordinary o-mode for the escaping radiation. Polarization observation of the H emissions are the better diagnostic tool to estimate the solar coronal magnetic field. Both F and H emissions of type III bursts are observed if the events are near to the center of the solar disk. Elsewhere emission should be purely harmonic, because F emission is more directive than the H emission. According to the Caroubalos and Steinberg [1974], the ground-based observations of the type III radio bursts associated with the Sunspot regions located $\gtrsim 70^o$ to either East or West of the central meridian of the center of the solar disk are primarily H emission. The directivity of the F emission component has a limiting directivity of $\pm 65^o$ from the central meridian of the Sun at 80 MHz. Therefore if the heliographic solar longitude of the event is $\gtrsim 70^o$ and the dcp is $\approx$ 0.15 then emission is purely H component. Under such circumstances the magnetic field near the source position was calculated.

The group of type III bursts are quasi-periodic in nature. Such kind of quasi-periodicities are also a diagnostic tool of estimating the coronal magnetic field. The quasi-periodicity or pulsation refers to the quasi-periodic amplitude variations in the time profile of the observed radio flux density at a observing frequency. Associated physical mechanisms have been classified into the three categories: (1) modulation of the emission by coronal loop oscillations, (2) intrinsic oscillations of the emission created by oscillatory wave-wave interactions and wave-particle interactions, and (3) modulation of the

electron acceleration/injection process responsible for the emission. The point (2) can be ruled out because such kind of emission occurs primarily for the fundamental o-mode and harmonic extra-ordinary (e-mode) emissions, where as in the present work harmonic o-mode emissions are considered. According to the Kliem et al. [2000], the temporal variations in the radio burst flux are caused by modulations of the particle acceleration by the highly dynamic reconnection process. A similar model, quasi-periodic reconnection and particle injection, was reported by Zlotnik et al. [2003]. It is known that even a very small ($\approx 2\%$) quasi-periodic modulations of the magnetic field is sufficient for the periodic electron acceleration. Many authors reported that such kind of modulations are related to the magneto hydrodynamic (MHD) oscillations. Based on the above discussion by knowing the periodicity of the quasi-periodic bursts the alfvén speeds and magnetic fields are estimated.

Interestingly, the estimated magnetic field in both methods yields consistent results. For example, on 20 September 2012, estimated magnetic fields using the dcp and quasi-periodicity were $\approx 4.7 \pm 1$ and $\approx 4.8 \pm 0.3$ G respectively. The empirical relation given by Dulk and McLean [1978] gives the magnetic field of 3.1 G at 1.3 $R_\odot$. The results estimated using these methods has reasonable agreement with the earlier reports. For example, at 77 MHz estimated magnetic field was B $\approx 5 \pm 1$ G reported by Ramesh et al. [2010] for the sources associated with the coronal streamers at 1.5 $R_\odot$. Lin et al. [2004] has measured B ≈ 4 G at 1.1 $R_\odot$ using the Zeeman splitting observations of the Fe XIII 1075 nm coronal emission line from the active region which is close to the limb. Such kind of radio observations indicated the significance of the low-frequency observations to estimate the coronal magnetic field in the middle corona ($1.2 \lesssim r \lesssim 2$ $R_\odot$). Note that such kind of measurements at other wavelength bands are currently difficult.

Type IV bursts are broadband quasiâĂŞcontinuum features that occur during the

decay phase of large solar flares. They were first reported by Boischot [1957] at meter wavelengths. The bursts are considered to be an useful tool to understand the solar terrestrial relationship because of their statistical association with energetic particles detected in the Earth environment. But they are not as common as the other radio bursts from the Sun. Imaging observations at metric wavelengths tend to show that most type IV bursts are stationary in the corona. A subclass of type IV bursts, known as moving type IV, is of great interest because they are seen to move in images at speed similar to speeds of the mass ejections in the solar atmosphere. But they are difficult to separate from stationary type IV events just from their spectral characteristics alone. Moving type IV bursts are predominantly a low-frequency phenomenon, occurring at frequencies below 100 MHz, The enhanced continuum emissions other than the noise storms are called type IV bursts. Type IV and noise storms looks alike but different in few characteristics discussed as follows, duration of the former is few minutes to hours where as the latter continued for few hours to days. Type IV bursts are observable over all frequencies (broad-band continuum emissions) with a smoothly varying continuum with free of type I and type III bursts superposed over the continuum unlike the noise storms. These bursts are associated with the microwave outbursts where as noise storms are observable only at meter-wavelengths. On 15 March 2013, a moving type IV bursts which was associated with a coronal mass ejection was recorded in Stokes I and V using GRIP. The observations were carried out at 80 and 40 MHz. Peak flux density of the event in Stokes I and V were $\approx 170,000$ Jy and $50,000$ Jy respectively at 80 MHz. Simultaneously observed peak flux density of the event in Stokes I and V at 40 MHz were $\approx 181,000$ Jy and $62,000$ Jy respectively. Calculated dcp of that event for 80 and 40 MHz were $\approx 0.29 \pm 0.1$ and 0.34 ± 0.1. Brightness temperature of the event by assuming the source sizes of the event $\approx 4'$ was of the order of $\approx 10^7$ K. Since the event is observed in two different frequencies, spectral index was calculated. The spectral index found for that event was -0.1. Spectrogram obtained with GLOSS reveal that the recorded event was a moving type IV burst. Assuming the emission mech-

anism of the type IV bursts observed is due to the gyrosynchrotron emission mechanism based on the spectral index estimates, the associated magnetic field was estimated using the corresponding equations mentioned in the literature [Dulk and Marsh, 1982, Dulk, 1985]. The values at 80 and 40 MHz were 2.2 ± 0.4 G and 1.4 ± 0.2 G respectively. The estimated magnetic fields were agreeing with the earlier reports.

Propagation of the radio waves in the solar corona get scattered due to the non-uniform distribution of the electron density from point to point. The radio waves undergo irregular refraction which modulates the radio structure of the actual distant cosmic source when the latter is observed through the solar corona. Such a modulation gives information about the density distribution in the solar corona. Crab nebula (Taurus-A) is a supernova remnant and a strong radio source at lower frequencies with constant flux density. It gets occulted by the solar corona during the mid-June in every year. This phenomenon was first time observed by Machin and Smith [1951]. Later Hewish [1955], Slee [1959], Blum and Boischot [1957], Bolton et al. [1958], Sastry and Subramanian [1974], Ramesh et al. [2001] observed the occultation at longer wavelengths.

Right ascension (RA) of the Crab nebula is 05 : 35 : 04 and Declination (Dec) is 22^o. Note that the above values are close to the ecliptic. Due to the movement of the Sun in both RA and Dec, the distance between the Sun and Crab nebula decreases to $\approx 5\ R_\odot$ during June 15 of every year. Polarimetric observations of the Crab nebula occultation at 80 MHz was carried out in June, 2011, 2012 and 2013. It was expected that when the Crab nebula radiation passes through the density irregularities of the corona there may be a possibility of circular polarization, because of the splitting of the randomly/linearly polarized radiation into magneto-ionic modes. However there was no deflection seen in Stokes V channel but the observations lead to scattering studies. Crab nebula was not identified in the observations of occultation during 2012, due to the strong solar activity.

The fortuitous lull of Sun enabled us to observe the same in the year 2011 and 2013. During 2011 and 2013, flux density of the Crab nebula is decreased when it approached the solar disk and increased when it moves away. Using those observations, the level of the coronal turbulence ($C_N^2(r)$) over the range 10 $R_\odot \lesssim r \lesssim$ 60 $R_\odot$ was estimated on a baseline length of $\approx$ 1.6 km, are larger than the similar estimates from VLBI observations on baseline lengths $\approx 200 - 2000$ km. Based on the estimated C_N^2 values, angular broadening of the Crab nebula at those distances were estimated. Both C_N^2 values and angular broadening measured using this technique are compared with the empirical relations. It was found that the estimates of $C_N^2(r)$ for the $\beta = 3$ case are higher by $\approx 5 - 6$ orders of magnitude compared to the similar values reported previously for larger spatial scales ($\approx 200 - 2000$ km) from VLBI observations. For $\beta = 11/3$, the estimated are higher by $\approx 1 - 2$ orders of magnitude. Also the angular broadening estimates are matching with the earlier empirical equations.

Better understanding of the Universe is only possible with the improved instrumentation. While developing the instruments, efficiency, lifetime, compactness, cost etc have to be considered. At GRO, the basic antenna element used in heliograph (Gauribidanur RAdio HeliograPH, GRAPH), GRIP, GLOSS etc is log-periodic dipole antenna, which is a linearly polarized antenna. GRAPH gives the two-dimensional maps of the solar corona, GRIP measures the dcp of the event and spectrograms of the solar corona is made with GLOSS and Callisto instruments. To measure the polarization of the weak bursts one need the polarimeter with improved sensitivity, resolution and less instrumental errors. Always interferometric arrays suffers with gain variations, phase fluctuations, off axial effects etc. Such variations are different for different channels since the hardware used (RF amplifiers, RF filters, RF cables, analog and digital receivers etc) are different. In order to minimize such effects one has to calibrate the instrument thoroughly. Unfortunately there are no circularly polarized calibrator sources available in the GRO in the frequency of operation. So we intend to build Cross-polarized Log Periodic Dipole (CLPD) antenna

in which, two linearly-polarized log-periodic dipole (LPD) antennas are fixed to a common axis in a mutually orthogonal fashion. Circularly polarized radiation in VHF band can be received/transmitted using helical antennas, conical log-spiral antennas, cross-polarized Yagi-Uda antennas, CLPDs etc. In situation where 10:1 or even more wider bandwidth is required, CLPD are preferred. Log-periodic antennas are widely used in the field of radio astronomy, particularly where simultaneous multi-frequency observations of radio emission from the celestial radio sources are required. Since different frequencies originates at different heights in the solar atmosphere, CLPD is preferred to observe the polarized radio emissions. However, in commercially available CLPD the isolation is ≈ -20 dBm. Because of such CLPDs, polarization characteristics of the weak cosmic signals can be limited. Though, dual polarized antenna designs with improved isolation exists, they are primarily at frequencies > 1 GHz. Our aim is to observe the polarized radiation from the solar corona with high accuracy at meter wavelengths and use them to estimate the coronal magnetic field.

Since GRAPH is operating at 80 MHz, we intend to design CLPD which works in the range $\approx 65 - 95$ MHz. To begin with we designed LPD with inter-boom spacing of 2 cm. Using such two LPDs, a CLPD was fabricated and found that the isolation was ≈ -20 dBm. Experimentally, it was found that isolation not improves by shifting the vertical arms of the CLPD with respect to the horizontal arms (by maintaining apex angle). It has been suggested by the Pivnenko [2006] that isolation can be improved by decreasing the inter-boom spacing to 1/100th of the arm length of the antenna. For such kind of design aluminum flats are used instead of the rectangular hallow aluminum pipes. The output of the antennas was taken from the top using a co-axial cable, which was passing through a aluminum pipe fixed to grounded boom of the antenna. After maintaining the inter-boom spacing of 5 mm, the isolation improved to $\lesssim -30$ dBm. We measured the voltage standing wave ratio (VSWR) of the designed CLPD using vector network ana-

lyzer. The values are found < 2 for both the LPDs in the frequency of 68-84 MHz after combining them to form a CLPD.

Far-field (Fraunhofer region), near-field (Fresnel) radiation patterns and isolation measurements of the antennas were carried out. To measure far field pattern, the receiving and transmitting antennas were mounted on a pole at a height of ≈ 3 m above the ground level. The transmitting and receiving antennas are separated by a 3 m distance which is a theoretical minimum far field distance. The signal was transmitted using a CLPD and the same was received by the arms of the LPD in the same plane. The measurements were taken for all the azimuthal angles by rotating the transmitted antenna. This corresponds to the E-plane measurements. With the same setup by keeping the transmitting and receiving antennas in vertical directions the experiment is repeated. Such measurement corresponds to the H-plane pattern. Half power beam width of the antenna in both E-plane and H-plane are $\approx 60^o$ and 120^o respectively. Measured beamwidths correspond to a solid angle of 2.2 sr. From solid angle, calculated directional gain was ≈ 7.8 dBi and the effective collecting area of the antenna was $\approx 0.6\lambda^2$. Near field measurements were performed by mounting a CLPD on a pole at a height of ≈ 3 m above the ground level and the test (CW) signal was transmitted from one of the LPD of the CLPD. Using a monopole antenna the signal strength is measured at different distances in the radiating near field range from the apex of the CLPD and also for different azimuthal angels in the range $0^o - 180^o$. At 80 MHz, the radiating near field region range calculated theoretically was $1 \lesssim r_{nf} \lesssim 3$ m. In this fashion both E-plane and H-plane near field radiation pattern measurements were carried out and the variation of the power with distance was observed as expected.

By using the similar setup used for far field measurements cross-talk levels and isolation was measured as follows. The transmitting LPD was mounted in horizontal ori-

entation (0^o) and the signal was received by both the 0^o and 90^o oriented arms of the CLPD. In principle one has to receive signal only in the 0^o oriented arms of the CLPD. However, a finite amount signal was received in the 90^o oriented arms also. This is called cross-talk between the two orthogonal LPDs in a CLPD. Difference in the signal levels of the two LPDs in a CLPD is called isolation. Such kind of measurements were carried out for both the 2 cm and 5 mm CLPD. The isolation for former case was ≈ -15 dBm and for the latter was $\lesssim -30$ dBm.

Two similar CLPDs were fabricated and mounted them in 40 m apart in East-West direction. The antennas were mounted to a pole at 3 m height above the ground. The antennas are mounted such that the length of the arms in increasing fashion from top to the base. The RF signals from the antennas (2 from each CLPDs) are transmitted to the receiver room using a low-loss coaxial cable which are buried under the ground at 1 m depth to avoid the phase variations. Using the analog receivers similar to the one used in GRIP the signals are down-converted. The intermediate frequency signal whose bandwidth is 1 MHz is sampled with 2 MHz rate and correlated using the digital correlator, which is similar to the one used in GRIP. The signal from the 0^o oriented antenna (arms along East-West direction) of the two CLPDs was correlated which corresponds to Stokes I. Similarly correlation of the 0^o oriented signal from one CLPD and 90^o orientation of other CLPD give the information of the Stokes V. Literally observed intensities are the 50% of the intensity, since this is the case for the calibrator sources, the error will be minimal after calibration of the target source. Linear polarization measurements are not possible to measure because of the Faraday rotation which is mentioned earlier. Stokes I and V can be measured using the 4 port quadrature hybrid in conjunction with the crossed dipole feed. Polarization measurement with latter techniques will be affected by the cross-talk due to the quadrature hybrid but not the former technique. Using the established two-element correlation interference polarimeter, observations of the solar atmosphere was

carried out and noise storms as well as few radio bursts were successfully recorded in both Stokes I and V at 80 MHz. Because of the compact structure of the CLPD makes them suitable to use as a feed that illuminate the parabolic reflector. It is also possible that the CLPD described can be used to transmit/receive circularly polarized waves in applications involving especially transmission through the Earth's ionosphere which may produces the rotation of the plane of the polarization. In future we intend to design the CLPD in wider bandwidth so that simultaneously observe the radio emission from different layers in the solar atmosphere, with the array of CLPDs.

8.1 Future scope

Ancient civilization began to understand the Sun many centuries back. In last few decades many space born instruments at different wavelengths with sophisticated technology were developed. Even then it is required to setup high resolution and sensitive telescopes along with innovative research to resolve the uncleared issues of the Sun. Few of the outstanding research issues which are not clearly known are listed below: coronal heating mechanism, coronal-seismology, coronal magnetic fields, helio-seismology, solar influence on space weather and Earth's climate changes, solar cycle, origin and driver mechanisms of the solar flares, coronal mass ejections, emission mechanism and evolution of radio radiation from the solar corona, polarization properties of the solar events at different wavelengths, turbulence/scattering properties of the solar corona, propagation of radio waves in the solar corona, precise density models, properties of the thermal emissions, chromospheric heating mechanism etc. Some of the scientific/technical goals to be done using the low-frequency radio observations of the solar corona is discussed below.

It is known that radio bursts are the frequently observed events in the solar atmosphere. However their origin, propagation, emission mechanisms, their different characteristics and their association with CMEs are not fully known. These bursts provide the clue

in understanding the many mysteries of the corona. Polarization properties of these events are useful in understanding the plasma characteristics and magnetic field information. By using the imaging, spectroscopic and polarization observations of these bursts at meter wavelengths, different phenomenon of the radio bursts have to be studied thoroughly. Also, it is believed that the CMEs originate at chromospheric levels and propagates to heliospheric distances. The driver mechanism, propagation effects in plasma, kinematics and dynamics of the CMEs are not clear. Therefore the CMEs have to be studied by making use of different radio instruments along with the space based observations. A rigorous research on the discussed aspects can be further continued using the instruments: GRIP, GLOSS and GRAPH. Also by developing the designed cross polarized log periodic dipole antenna with larger bandwidth and improved isolation, two-dimensional polarized imaging instrument has to be developed. Note that such facility at these frequency of operation is not available at present.

References

M. J. Aschwanden. *Physics of the Solar Corona. An Introduction*. Praxis Publishing Ltd, August 2004.

E. J. Blum and A. Boischot. Occultation of the Crab nebula by the solar corona. *The Observatory*, 77:205–206, October 1957.

A. Boischot. Caractères d'un type d'émission hertzienne associé à certaines éruptions chromosphériques. *Academie des Sciences Paris Comptes Rendus*, 244:1326–1329, 1957.

J. G. Bolton, G. J. Stanley, and B. G. Clark. A Solar Occultation of the Crab Nebula at a Wavelength of 12 Meters. PASP, 70:594, December 1958. doi: 10.1086/127302.

C. Caroubalos and J. L. Steinberg. Direct Measurements of the Directivity of Type i and Type III Radiation at 169 MHZ (presented by C. Caroubalos). In G. A. Newkirk, editor, *Coronal Disturbances*, volume 57 of *IAU Symposium*, page 239, 1974.

N. Crosby, N. Vilmer, N. Lund, K.-L. Klein, and R. Sunyaev. Deka-KeV X-Ray Emission Associated with the Onset of Radio Noise Storms. Sol. Phys., 167:333–348, August 1996. doi: 10.1007/BF00146343.

G. A. Dulk. Radio emission from the sun and stars. ARA&A, 23:169–224, 1985. doi: 10.1146/annurev.aa.23.090185.001125.

G. A. Dulk and K. A. Marsh. Simplified expressions for the gyrosynchrotron radiation from mildly relativistic, nonthermal and thermal electrons. ApJ, 259:350–358, August 1982. doi: 10.1086/160171.

G. A. Dulk and D. J. McLean. Coronal magnetic fields. Sol. Phys., 57:279–295, April 1978. doi: 10.1007/BF00160102.

A. Hewish. The Irregular Structure of the Outer Regions of the Solar Corona. *Royal Society of London Proceedings Series A*, 228:238–251, February 1955. doi: 10.1098/rspa.1955.0046.

B. Kliem, M. Karlický, and A. O. Benz. Solar flare radio pulsations as a signature of dynamic magnetic reconnection. A&A, 360:715–728, August 2000.

H. Lin, J. R. Kuhn, and R. Coulter. Coronal Magnetic Field Measurements. ApJ, 613: L177–L180, October 2004. doi: 10.1086/425217.

Y. E. Litvinenko. An explanation for the flare frequency-energy dependence. Sol. Phys., 151:195–198, April 1994. doi: 10.1007/BF00654092.

K. E. Machin and F. G. Smith. A New Radio Method for Measuring the Electron Density in the Solar Corona. Nature, 168:599–600, October 1951. doi: 10.1038/168599b0.

D. B. Melrose, G. A. Dulk, and D. E. Gary. Corrected formula for the polarization of second harmonic plasma emission. *Proceedings of the Astronomical Society of Australia*, 4:50–53, 1980.

C. Mercier and G. Trottet. Coronal Radio Bursts: A Signature of Nanoflares? ApJ, 474: L65, January 1997. doi: 10.1086/310422.

S. Pivnenko. Log-periodic dipole antenna with low cross-polarization. In *Antennas and Propagation, 2006. EuCAP 2006. First European Conference on*, pages 1–4, Nov 2006. doi: 10.1109/EUCAP.2006.4585044.

R. Ramesh, C. Kathiravan, and C. V. Sastry. Low-Frequency Radio Observations of the Angular Broadening of the Crab Nebula Due to a Coronal Mass Ejection. ApJ, 548: L229–L231, February 2001. doi: 10.1086/319098.

R. Ramesh, C. Kathiravan, M. S. Sundararajan, I. V. Barve, and C. V. Sastry. A Low-Frequency (30 - 110 MHz) Antenna System for Observations of Polarized Radio Emission from the Solar Corona. Sol. Phys., 253:319–327, December 2008. doi: 10.1007/s11207-008-9272-y.

R. Ramesh, C. Kathiravan, and C. V. Sastry. Estimation of Magnetic Field in the Solar Coronal Streamers Through Low Frequency Radio Observations. ApJ, 711:1029–1032, March 2010. doi: 10.1088/0004-637X/711/2/1029.

J. P. Raulin and K.-L. Klein. Acceleration of electrons outside flares: Evidence for coronal evolution and height-extended energy release during noise storms. A&A, 281:536–550, January 1994.

C. V. Sastry and K. R. Subramanian. Observations on the occultation of the radio source Tauras A by the solar corona during June 1971. *Indian Journal of Radio and Space Physics*, 3:196–198, September 1974.

O. B. Slee. Occultations of the Crab Nebula by the Solar Corona in June 1957 and 1958. *Australian Journal of Physics*, 12:134, June 1959. doi: 10.1071/PH590134.

D. S. Spicer, A. O. Benz, and J. D. Huba. Solar type I noise storms and newly emerging magnetic flux. A&A, 105:221–228, January 1982.

E. Y. Zlotnik, V. V. Zaitsev, H. Aurass, G. Mann, and A. Hofmann. Solar type IV burst spectral fine structures. II. Source model. A&A, 410:1011–1022, November 2003. doi: 10.1051/0004-6361:20031250.